Instituto Andaluz de Geofísica
y Prevención de Desastres Sísmicos

Departamento de Física Teórica
y del Cosmos

Seismic anisotropy in the Iberian Peninsula

Anisotropía sísmica en la Península Ibérica

TESIS DOCTORAL

Memoria presentada por la Licenciada en Ciencias Geológicas Dña. Luisa Buontempo para optar al Grado de Doctor con mención de ''Doctor Europeo'' por la Universidad de Granada.

Esta Tesis Doctoral ha sido dirigida por el Dr. José Morales Soto, Investigador en el Instituto Andaluz de Geofísica y Profesor Titular de Universidad del departamento de Física Teórica y del Cosmos.

En Granada, Noviembre de 2008

Vº Bº del Director

Fdo. Dr. José Morales Soto

La Doctoranda

Fdo. Luisa Buontempo

UNIVERSIDAD DE GRANADA
2008

Editor: Editorial de la Universidad de Granada
Autor: Luisa Buontempo
D.L.: GR. 2742-2008
ISBN: 978-84-691-8243-7

Luisa Buontempo
Instituto Andaluz de Geofísica y Prevención de Desastres Sísmicos
Universidad de Granada- Campus Cartuja s/n, 18071 - Granada (Spain)
Departamento de Física Teórica y del Cosmos
e-mail: luisa@iag.ugr.es

Alla mia famiglia

''Ci sono soltando due possibili conclusioni: se il risultato conferma le ipotesi, allora hai appena fatto una misura. Se il risultato è contrario alle ipotesi, allora hai fatto una scoperta''

Enrico Fermi

AGRADECIMIENTOS

Quiero agradecer a José Morales por haberme ofrecido la oportunidad de realizar esta tesis doctoral en el Instituto Andaluz de Geofísica (IAG) de la Universidad de Granada.

El empuje más significativo a este trabajo fue en abril de 2006, durante mi primera estancia en la Université de Montpellier. Donde las ayudas de los profesores Götz Bokelmann y Andreas Wüstefeld fueron decisivas en la orientación de la presente tesis y a partir de ellas también se ha llevado acabo un artículo.

Quisiera agradecer al doctor Jesús Ibáñez por haberme ofrecido la posibilidad de vivir la experiencia de una campaña antártica….. *tantissime grazie!*

A lo largo de este camino, varios amigos han compartido la misma experiencia de realizar una tesis; quiero recordar con mucho cariño a Enrique Carmona, Elena Ocaña y Mabel Rodríguez, que siempre han tenido palabras de apoyo y ánimo. Así como al resto del personal del IAG que me ha hecho sentir como una compañera más.

También quisiera reconocer el apoyo y el cariño de las demás personas que he conocido a lo largo de estos años en España, y de las personas que he dejado en mi Italia. No puedo hacer un listado específico pero las llevo a todas en mi corazón.

I'd like to thank you, Miss Anita Sandoval, for correcting this Thesis.

Vull donar-li moltes gràcies a la Teresa Teixidó per la seva ajuda i paciència en llegir tota la meva tesis, en corregir i donar suggerenciès. A més, a segut un punt de apomo en aquestos mesos de faena i amargós tragos, me ha donat ànim en els moments dolents donant sempre un somriurà. Moltes gràcies.

Esta Tesis Doctoral ha sido subvencionada por los proyectos: CGL2005-04541-C03-01-BTE, REN2002-04198-C02-01, NEAREST (Global Change and Ecosystem Contract Nº 037110) y por último Geociencias en Iberia: Estudios integrados de topografía y evolución 4D. Topo-Iberia CSD2006-00041

Contents

Prefacio

Esta tesis versa sobre la anisotropía sísmica como método de reconstrucción de las tendencias de deformación en el manto litosférico de la Península Ibérica, principalmente en la parte meridional. Se han estudiado los telesismos registrados en las estaciónes de banda ancha de distintos organismos, en dos dominios geológicos de la Península: el Macizo Varisco y las Cordilleras Béticas. Los patrones de deformación medidos se han comparado con otros parámetros geofísicos y se han enmarcado en los contextos geodinámicos de las áreas de estudio.

La Península Ibérica y en particular el dominio de Alborán, constituyen desde siempre una región donde muchas cuestiones todavía quedan abiertas. Hemos elegido la anisotropía sísmica como método para el estudio dado que su origen estructural proporciona información sobre el comportamiento a gran escala y ayuda a formular reconstrucciones geodinámicas y estructurales. La anisotropía sísmica obtenida a partir de fases SKS de telesismos es el instrumento más apropiado para el estudio del manto superior, donde la anisotropía sísmica refleja el flujo plástico activo o congelado, dependiendo de que se las ondas sísmicas penetren en la astenósfera o se queden en la litósfera.

Prefazione

L'obiettivo di questa tesi dottorale è stato ricostruire lo stile di deformazione nel mantello litosferico della Penisola Iberica. Sono stati studiati i telesismi registrati da stazioni di banda larga appartenenti a diversi organismi, e situate in due domini geologici della Penisola: il Macizo Varisco e la Cordilleras Beticas. Il modello di deformazione ottenuto è stato confrontato con altri parametri geofisici ed inquadrato nell'ambito dell'evoluzione geodinamica che ha interessato l'area di studio.

La Penisola Iberica ed in particular il domino di Alboran, sono da sempre una regione dove restano aperte molte questioni. Abbiamo scelto la anisotropia sismica come tema per questo studio, in quanto avendo l'anisotropia un'origine strutturale, si presenta come lo strumento più idoneo per poter fornire informazioni circa il comportamento strutturale a grande scala e, di consequenza contribuire all'interpretazione in chiave geodinamica e strutturale dei processi deformativi che hanno modellato la zona. A tal fine sono state studiate le fasi SKS di telesismi, dato che la SKS è una fase che viaggia attraveso tutto il mantello, per cui la anisotropia registrata per tale fase riflette il flusso plastico mantellico active o frozen, dipendendo se le onde sismiche viaggiano attraverso l'astenosfera o la litosfera.

Preface

This Thesis includes a study of means by which the tendencies of deformation have been reconstructed in the lithospheric mantle of the Iberian Peninsula. We studied telesismic events recorded in broadband seismic stations of different network in two geologic domains of the Peninsula: the Variscan Massif and the Betic Cordillera. The measured trends of deformation have been compared with other geophysical parameters and they have been explained in geodynamic contexts related to the events that have forged the studied areas. The Iberian Peninsula and in particular the Gibraltar arc, constitute regions where many questions are still open. We have chosen the seismic anisotropy as instrument for the study because its structural origin can bring information on large-scale about the behaviours of structures on long scale and contribute to geodynamic and structural reconstructions. The calculated seismic anisotropy from SKS phases of teleseismic event is the instrument for the study of the upper mantle where the seismic anisotropy reflects plastic flow either active or frozen, depending on whether seismic waves penetrate the asthenosphere or remain in the lithosphere.

I. Resumen extendido de la Tesis

Introducción

Las ondas sísmicas representan sin duda la fuente de información más potente para estudiar el interior de la Tierra, dado que éstas son sensibles a los cambios físicos y químicos de los materiales que encuentran en su camino. De modo que una onda registrada en una estación sísmica contiene la historia de todo aquello que le ha sucedido; desde información concerniente a su génesis (fuente sísmica) hasta información debida a su propagación (trayectoria). El estudio de las interacciones entre los distintos materiales y la propagación del frente de onda sísmico nos permite interpretar la estructura interna de la Tierra.

La relación entre estructuras superficiales e internas de la Tierra representa un punto clave para comprender la naturaleza de los procesos geodinámicos que han forjado una región, y así mismo conocer cómo éstos están actuando en la actualidad. Uno de los aspectos básicos de la geodinámica es determinar cómo los procesos de deformación alteran la estructura de la litosfera y la del manto sub-litosferico, y saber cuando estos eventos han ocurrido. En este contexto, el estudio de la anisotropía sísmica representa uno de los instrumentos de la Sismología que puede proporcionar información acerca de la deformación en el manto. De hecho la anisotropía es uno de los parámetros físicos que afectan a las ondas sísmicas debido a que su propagación es función de las propiedades elásticas del manto, que a su vez dependen de otros factores como temperatura, presión, mineralogía y

composición. La relación entre anisotropía y deformación, requiere además el conocimiento de las relaciones entre la estructura de los agregados cristalinos de los minerales del manto y el tipo de deformación que sobre ésta ha actuado.

Muchas rocas que componen la corteza y el manto presentan características anisótropas, ya que están compuestas por cristales cuya estructura y organización condiciona una dependencia de la dirección y de la velocidad de propagación del frente de onda sísmico (Savage, 1999). De los minerales que componen el manto superior, el más anisótropo es el olivino que también es el mineral más abundante en el manto, formando aproximadamente el 90% de su composición.

La presente memoria se enmarca dentro de los estudios de anisotropía sísmica que en esta última década han ido intensificándose coincidiendo con el aumento del número de estaciónes sísmicas de banda ancha emplazadas por todo el planeta. Entre estos estudios, la técnica más empleada para estudiar la anisotropía en el manto es la que utiliza las fases convertidas de las ondas de cizalla (ondas S) en la discontinuidad núcleo – manto, como son las ondas SKS, SKKS, PKS (Vinnik et al., 1992; Silver and Chan, 1988). Específicamente, esta tesis versa sobre la anisotropía sísmica en el manto litosférico bajo la Península Ibérica y Arco de Gibraltar calculada a partir del estudio de ondas SKS.

Los estudios de anisotropía sísmica se han aplicado en el conocimiento de distintas regiones tectónicas, como por ejemplo en zonas de subducción, en zonas de *rift* o de fallas de desgarre (*strike-slip)*.

Las zonas de subducción presentan una estructura 3D bastante compleja del flujo del manto que motiva controversias en la interpretación de la anisotropía dado que intervienen varios factores (e.g. Pozgay et al., 2007; Ando et al., 1983; Russo and Silver, 1994; Fouch and Fischer, 1996; Sandvol and Ni, 1997; Fischer et al., 1998; Smith et al., 2001; Anderson et al., 2004; Currie et al., 2004). Entre ellos está la geometría de la zona de subducción que en las regiones de *slab rollback* puede generar un flujo toroidal del manto, como en el caso del Arco Calabria en Italia (Civello and Margheriti, 2004). Otro factor que juega un papel importante en estas zonas es el contenido en agua de los materiales implicados; de hecho la presencia de

agua (y también de elementos volátiles) puede alterar la estructura cristalina del olivino y en consecuencia, la dirección de la anisotropía que se detectará.

En zonas de subducción se obtienen tanto orientaciones de anisotropía paralelas a las zonas de trincheras (*trench*), como orientaciones perpendiculares (Figura 2.13); aunque las primeras parecen ser las más comúnes. Principalmente se han registrado en Nueva-Zelanda (Marson-Pidgeon et al., 1999), en las Aleutianas (Yang et al., 1995; Mehl et al., 2003), en Japón (Fouch and Fischer, 1996) y en Tonga (Fischer and Wiens, 1995). Mientras que las anisotropías perpendiculares se han registrado en las Kuriles y en el noroeste Pacifico (Russo and Silver, 1994).

Cabe mencionar que ninguno de los modelos utilizados para interpretar la anisotropía sísmica en zonas de subducción considera la posibilidad de recristalización del olivino que se produce en situaciones de grandes esfuerzos, debido a las dificultades que implica su interpretación.

Estudios realizados en regiones de *rift* evidencian que la dirección de anisotropía puede ser paralela o sub-paralela a su dirección de apertura. Cuando el *rift* es activo, va erosionando la litosfera causando una elevación de la astenosfera, de modo que la presencia de anisotropía se relaciona con la aparición de finas lentes de magma en estado de fusión parcial situadas por debajo de él (Kendall and Silver, 1996).

En regiones con fallas de desgarre también se ha detectado anisotropía fuerte debido a la presencia de foliación vertical; en estas situaciones la dirección de anisotropía resulta ser casi paralela a la dirección del movimiento de desgarre (Figura 2.16); ejemplos de ello son el Rift de Maoma en Siberia (Vinnik et al., 1992), el norte del Tibet (Holt, 1997) y la falla Alpina de Nueva Zelanda (e.g. Gledhill and Stuart, 1996). Una situación distinta se presenta en la falla de San Andrés donde se registran medidas contradictorias de dirección anisótropa (Vinnik et al., 1989; Vinnik et al., 1992; Savage and Silver, 1993; Ansel et al., 1989; Ozalaybey and Savage, 1995) que pueden ser explicadas con la presencia de dos capas anisótropas, una superior relacionada con la deformación litosférica asociada a la falla y otra inferior relacionada con el flujo astenosférico.

Anisotropía Sísmica

La anisotropía sísmica se manifiesta como la variación de las propiedades físicas dependiendo de la dirección de propagación de las ondas sísmicas debido a las orientaciones preferentes que adquieren los minerales que componen las rocas. Los dos factores principales que causan la anisotropía son la orientación preferente de la estructura externa cristalina (*shape preferred orientation,* SPO) y la orientación preferente de la estructura interna (*lattice preferred orientation,* LPO). Ambas orientaciones constituyen las respuestas al esfuerzo al cual han sido sometidos los cristales (Figuras 2.4 y 2.5).

Los estudios de anisotropía poco profunda (primeros 10-15 km de la corteza) indican como principales causas de anisotropía la presencia de fracturas rellenas de fluido (Crampin, 1984; Kendall et al., 2006) y la variabilidad estructural, como puede ser la presencia de finas capas alternantes cada una con sus propiedades elásticas (Backus, 1962).

Mediciones de laboratorio realizadas para calcular las propiedades sísmicas de los agregados cristalinos muestran que por debajo de los 10-15 km no puede detectarse anisotropía ya que la presión supera los 200-300 MPa y las fracturas empiezan a cerrarse en respuesta al aumento de la presión litostática (e.g. Kern, 1990; Kern, 1993). De modo que la anisotropía más profunda debe relacionarse con otros fenómenos; entre éstos la LPO de los cristales de los minerales anisótropos del manto (Christensen and Salisbury, 1984; Nicolas and Christensen, 1987; Karato et al., 1995). En estos casos, se asume que la LPO viene dada por el eje cristalográfico [100] del olivino como consecuencia de los procesos tectónicos al que ha sido sometido; siendo el olivino el mineral principal y también el más anisótropo de las fases peridotíticas (Nicolas and Christensen, 1987).

La interpretación de la anisotropía sísmica a otras profundidades es más difícil. En la astenósfera se considera que la anisotropía es una manifestación del flujo convectivo actual, por lo tanto se asume que la dirección de anisotropía sísmica debe ser paralela al flujo del manto. Ribe, 1989, demostró que las direcciones de LPO y del flujo del manto están relacionadas sólo en las zonas de cuña mantélica

(above subducted slab), por debajo de la litosfera, y en las capas fronterizas (*boundary layers*. Mientras que en los otros lugares de la astenósfera interviene un factor más que complica los cálculos: el contenido de agua en los cristales de olivino que es capaz de modificar la relación entre la geometría del flujo y las direcciones LPO (Jung and Karato, 2001).

La anisotropía sísmica en el manto superior se mide en la superficie terrestre mediante el desdoblamiento de las ondas S de los telesismos. Una onda S que se propaga en un medio anisótropo se separa en dos componentes polarizadas ortogonales que viajan a diferente velocidad dependiendo de su dirección. Este fenómeno se define como desdoblamiento de la onda de cizalla (*shear wave splitting)* y fue observado por primera vez en la calcita (Figura 1.2a); en óptica este fenómeno se conoce como birrefringencia (Figura 1.2b).

La anisotropía sísmica puede cuantificarse como el porcentaje de la variación de velocidad entre la dirección más rápida y la más lenta (Birch, 1960; Kern and Richter, 1981), mediante la expresión:

$$\mathbf{A = [\ (V_{max} - V_{min})/V_{mean}\ ] * 100} \qquad \text{(en porcentaje)}$$

donde V_{max} y V_{min} son las velocidades sísmicas máxima y mínima respectivamente.

En el caso del olivino las velocidades máximas y mínimas de las ondas P son de 9.89 km/s y 7.72 km/s respectivamente, y de 5.53 km/s y 4.42 km/s para las ondas S, de modo que los porcentajes de anisotropía son A_P=25% en el caso de onda P, y A_S=22% en el caso de la onda S (Figura 2.1). Es de notar que el olivino tiene un porcentaje de anisotropía bastante similar para ambos tipos de onda, mientras que hay otros minerales que tienen valores muy distintos; por ejemplo la mica presenta valores de A_P> 16% y A_S>116%. En el otro extremo estaría el granate, que es un mineral isótropo, cuyos valores de A_P y A_S son inferiores al 1%.

El desdoblamiento de las ondas S ocurre en todos los tipos de medios anisótropos, ya sean estos altamente o poco anisótropos y poco importa que sistema de simetría cristalina tengan.

El estudio del desdoblamiento de las ondas S consiste fundamentalmente en la búsqueda de los dos parámetros causantes de la anisotropía (Figura 1.3):

a) El retraso temporal (δt) entre la fase rápida y la lenta, que está relacionado con el espesor y la anisotropía intrínseca del medio anisótropo.
b) La orientación (ϕ) de los planos de polarización, que está relacionada con la orientación de la estructura del medio.

En los sismogramas, la presencia de desdoblamiento se manifiesta como un aumento de energía en las ondas S (Figura 3.3). Actualmente, la mayoría de los algoritmos existentes para calcular δt y ϕ se basan en este aumento energético de las fases de cizalla polarizadas, y su estrategia consiste en buscar los valores de los parámetros que mejor eliminen el efecto del desdoblamiento. Es decir, corrigiendo el efecto de anisotropía mediante la reducion de la energia en la componente transversal del sismograma.

En la corteza el desdoblamiento está típicamente causado por las tensiones horizontales (*horizontal stress)* que alinean paralélamente las micro fracturas verticales (Crampin 1984; 1994; Crampin et al., 1999; Crampin et al., 2006) de modo que a partir de los dos parámetros ϕ y δt se puede evaluar respectivamente la alineación de las fracturas y su grado de fracturación (Crampin and Gao, 2006). En la mayoría de los casos, la anisotropía relacionada con la orientación preferente externa (SPO) se detecta bajo las regiones de dorsales oceánicas, en zonas de *rift* continentales y bajo las zonas continentales estables con delgada litosfera.

En teoría, la fuente de la anisotropía debe estar localizada en cualquier punto a lo largo de la trayectoria del frente de ondas. Aunque los sismólogos apuntan al manto superior como zona principal de anisotropía, siendo ambiguo precisar si su localización está en la astenosfera o en la litosfera. Cuando la anisotropía está localizada en la litosfera entonces los parámetros de desdoblamiento (δt y ϕ) se pueden relacionar con una deformación, fósil o activa (Figura 2.10), mientras que si la anisotropía ocurre en la astenosfera, δt y ϕ pueden atribuirse al flujo actual producido por el movimiento diferencial entre las placas tectónicas y el manto subyacente, es decir a la dirección absoluta de movimiento de placa (APM) (Figura 2.9). Estudios realizados en diferentes regiones del mundo permiten concluir que

muchas veces una combinación de ambas situaciones (litosférica y sub-litosférica) es la responsable de la mayor parte de las anisotropías sísmicas observadas.

Desdoblamiento de las Ondas de Cizalla

Una simplificación que se realiza en determinados estudios sismológicos para simplificar los cálculos es considerar la Tierra como un medio isótropo; ya que para un medio anisótropo deben considerarse más constantes elásticas que complican la formulación.

Para cualquier cuerpo, la ley de Hooke $\sigma_{ij} = c_{ijkl}\varepsilon_{kl}$ relaciona el esfuerzo aplicado (*stress) c*on la deformación resultante (*strain)* mediante un tensor elástico c_{ijkl} compuesto de 81 variables. Un medio donde son necesarias más de dos variables para describirlo y éstas varían con la dirección se define como medio anisótropo. De lo contrario, un medio isótropo viene definido cuando las propiedades son las mismas en cualquier dirección, de modo que $c_{ijkl} = c_{jikl} = c_{ijlk} = c_{klij}$ y las 81 variables se reducen a 2.

Para medios anisótropos, el caso más simple es un cuerpo con simetría triclínica, donde se cumple que el esfuerzo y la deformación son simétricos igualándose $c_{ijkl} = c_{jikl} = c_{ijlk} = c_{klij}$ de modo que las 81 variables se reducen a 21. La introducción de ulteriores simetrías hace que el número de constantes elásticas se pueda reducir aún más. En base a ello, la mayoría de los estudios de anisotropía consideran dos tipos de simetrías: la hexagonal, que considera 5 constantes elásticas, y la ortorrómbica que posee 9 constantes (Tabla 2.1).

Como ya se ha mencionado anteriormente, uno de los efectos más remarcables de la anisotropía es la separación de la onda S en sus componentes ortogonales (*shear wave splitting)*, cuyas velocidades dependen de los respectivos ángulos entre las trayectorias desdobladas y cada uno de los ejes de simetría del medio.

Cuando el eje de simetría de un medio es vertical, que es la situación más común de las estructuras internas de la Tierra, se produce la denominada como **isotropía**

transversal o anisotropía radial y se detecta en un medio formado por capas estratificadas, donde cada capa es isótropa con propiedades diferentes entre sí. En caso de que el eje de simetría sea X_3 (perpendicular a la estratificación) y la propagación sea a lo largo de la dirección de estratificación X_1, (Figura 2.2a), las ondas S se desdoblan en dos ondas, donde la SH viaja con velocidad S_1 más rápida que la SV con velocidad S_2.; dado que el desplazamiento de SH está favorecido en las capas rápidas. La misma situación se verifica cuando la propagación es a lo largo de la dirección X_2. En cambio cuando la propagación es a lo largo de la dirección de simetría X_3 ambas velocidades de las ondas S son iguales a S_1 (Figura 2.2b). Además se cumple que $P_1>P_2$, o sea que la velocidad de las ondas P es más rápida en la dirección X_1 que el la X_3.

Cuando el eje de simetría de un medio es horizontal, se produce la denominada **anisotropía azimutal**, donde las velocidades varían en función de la dirección horizontal de simetría. Una forma de visualizar este caso es considerar la situación expuesta para la anisotropía transversal pero con el eje X_3 rotado de 90˚ respecto al plano horizontal (Figura 2.3a y b). En esta situación las velocidades de las ondas S desdobladas en dirección X_3 son distintas.

El desdoblamiento de la onda S se puede medir en todos los tipos de ondas de cizalla y para determinar la anisotropía en el manto es necesario utilizar la fase S de telesismos que ocurren a una distancia epicentral mayor de 60°. Las ondas SKS constituyen la fase más popular para esta tipología de estudio, ya que son fácilmente detectables. Estas ondas se propagan inicialmente como ondas S, luego se convierten en ondas P en su propagación en el núcleo externo y vuelven a convertirse en ondas S cuando pasan otra vez al manto. En este contexto, todas las informaciones de anisotropía producidas por la fuente se pierden en cuanto las ondas se propagan a través del núcleo externo. Por lo tanto, la anisotropía que se registra en la estación se refiere al recorrido de la onda en el tramo entre la discontinuidad núcleo-manto y la superficie.

El desdoblamiento en la onda SKS puede atribuirse a cualquier punto del trayecto que éstas recorren entre la discontinuidad núcleo-manto y la estación donde se registra. De manera que, a priori, es difícil establecer a qué profundidad hay que referir la anisotropía. Los numerosos análisis de desdoblamiento indican

que la anisotropía se localiza en general en los primeros 410 km de litosfera. Para algunas regiones continentales se propone un modelo de desdoblamiento coincidente con las estructuras geológicas superficiales; sugiriendo que la anisotropía sísmica predomina en la litosfera (Silver, 1996, Barruol et al., 1997a) y es coherente con la deformación sub-litosférica (Silver, 1996) (Figura 2.10). Mientras que para otras regiones se ha propuesto un modelo de anisotropía sísmica más parecido a la dirección local del movimiento absoluto de placas (APM) (Vinnik et al., 1992) situando la anisotropía en el manto astenosférico y generada por las estructuras resultantes del flujo mantélico (Figura 2.9).

Técnicas de inversión

El estudio del desdoblamiento de la onda S de eventos regionales o telesismicos, es, de entre las metodologías sismológicas, la técnica más empleada y la que mejor detecta la presencia de anisotropía ya que puede reflejar la anisotropía azimutal bajo el área investigada (Silver and Chan, 1991). Basándose en cáculos teóricos y medidas de laboratorio, el cálculo asume un medio de anisotropía transversal con ejes de simetría horizontal.

Los métodos de análisis que se utilizan para caracterizar el efecto de la anisotropía pueden agruparse en dos categorías: las que consideran telesismos individuales y las que consideran múltiples eventos sísmicos (Figura 3.4).

Las técnicas que utilizan **eventos individuales** se basan en determinar los parámetros de anisotropía a partir de un solo evento. En general el cálculo se realiza definiendo una malla (*grid*) en el subsuelo donde los distintos bloques van modificándose para devolver los valores δt y ϕ que mejor eliminan el efecto del desdoblamiento. Una onda S al cruzar un medio isótropo sólo estaría polarizada en su componente radial, sin embargo al viajar en un medio anisótropo se produce también una componente transversal, que resulta ser la derivada temporal de la componente radial. Dentro de este grupo, se consideran los siguientes métodos:

Método de la energía mínima de Silver and Chan (1991): Es el método más utilizado. En caso de anisotropía débil, cuando el tiempo de retardo δt es pequeño comparado con el período dominante de la señal, la componente transversal es idéntica a la derivada del tiempo de la componente radial. Entonces, si se detecta una polarización inicial, como es en el caso de las fases reflejadas y refractadas en el núcleo (e.g., PC, SKS, SKKS, PKS,…) se busca la combinación δt y ϕ que reduce al mínimo la energía de la componente transversal. Lo cual corresponde a "eliminar" el efecto de la anisótropa de los datos.

Método de la correlación cruzada de Bowman and Ando (1987): Consiste en maximizar la semejanza de las formas del pulso de las fases S rápidas y lentas, que en teoría deben ser idénticos y que sólo uno está retrasado con respecto al otro. Se realiza una malla (*grid)* con los valores de δt y ϕ y se buscan los que mejor maximizan la correlación cruzada entre las componentes rápida y la lenta.

Método del autovalor *(eigenvalue)* de Silver and Chan (1991): Considera valores de δt y ϕ de sismogramas no desdoblados como valores propios para crear las componentes radial y transversal corregidas. Entonces, las componentes del tensor que minimice la energía serán aquellas que contengan los valores propios ϕ y δt favoritos. La evaluación del mínimo de energía consiste en calcular para distintos ángulos de rotación el movimiento de la partícula a partir de minimizar la razón de los autovalores de la matriz de covariaza.

Otro método recientemente desarrollado es el **algoritmo de la convolución cruzada de Menke and Levin (2003)**, que se diseña para reducir al mínimo el ajuste entre un modelo de Tierra anisotrópico dado y los datos de forma de onda observados.

Las técnicas que utilizan **múltiples eventos** analizan simultáneamente un conjunto de registros provenientes de distintos *azimuths* y considerando diferentes estaciónes sísmicas. De entre ellas, las más empleadas son:

Apilamiento energético **(*stacking energy*) de Wolfe and Silver (1998):** Se basa en normalizar la energía E (ϕ, δt) de todas las componentes desdobladas y calcular para cada una de ellas los parámetros de desdoblamiento. De esta manera se aumenta la

razón señal-ruido en un sistema anisótropo para obtener resultados de anisotropía fiables. Esto depende de todas formas de la existencia de una buena cobertura azimutal. Una vez realizado este cálculo, se procede a sumar estos lóbulos energéticos para obtener la distribución de "energía final" en una determinada estación. Cuando esta energía final es mínima, puede decirse que el efecto de anisotropía ha quedado reducido y el resultado son los parámetros δt_i y ϕ_i utilizados en la última iteración. Este método es eficaz en estaciónes con un alto nivel de ruido ambiental, como el caso de las islas oceánicas, puesto que las características colectivas del conjunto de registros ayudan a mejorar las estimaciones. Otra ventaja del metodo es que puede calcularse un error formal. Sin embargo, su limitación es que asume una sola capa de anisotropía horizontal, de modo que se pierde toda la información sobre la variación acimutal de los parámetros de desdoblamiento y las estructuras anisotrópicas mas complejas quedan sin identificar.

Vector e intensidad del desdoblamiento de Chevrot (2000): Este método considera variaciones azimutales de la energía transversal para las fases del núcleo y proyecta las amplitudes de las componentes transversales sobre las amplitudes de las derivadas del tiempo de las componentes radiales, para obtener un solo conjunto que proporcione el mejor ajuste de los parámetros δt y ϕ en una estación sísmica. Este método aporta una estimación de la intensidad del desdoblamiento lo que significa una medida adicional de la escala de la anisotropía, pero requiere una amplia gama de cobertura azimutal.

Hartog and de Schwartz (2000) y Walker et al. (2004) utilizan una aproximación similar para predecir los parámetros de desdoblamiento (*splitting)*. Parten por realizar una búsqueda en base a dividir el medio mediante una malla regular, en donde para cada bloque se va definiendo y variando el *back-azimuth* del eje rápido hasta encontrar la orientación óptima del tensor que reduce al mínimo la diferencia entre los parámetros de desdoblamiento calculados y los observados. Esta estrategia permite examinar capas múltiples de anisotropía.

Vinnik et al. (1989): esta metodología es bastante similar a la de Silver and Chan anteriormente explicada, pero en este caso se aplica al caso de múltiples eventos. Los autores construyen una traza transversal ideal a partir de la componente radial observada y asumiendo valores determinados de δt y ϕ. A partir de este modelo

inicial, se van modificando los valores de desdoblamiento hasta dar con aquellos que mejor reproducen la traza de la componente transversal observada. La diferencia con la metodología de Silver y Chan consiste en que este método carece de la posibilidad para calcular los errores de las medidas.

A parte de estos métodos que son de ensayo-error, Teanby et al. (2004) han introducido recientemente una forma de análisis más automatizada para calcular el desdoblamiento de los ondas S. Parten por ir evaluando las distintas formas de onda que se van generando para una gama elegida de longitudes de onda. Mediante un análisis cluster se selecciona la ventana final de los datos basándose en la forma de onda que proporciona el error más bajo del cluster.

Una limitacion de todos estos métodos expuestos, es que asumen una sola capa de anisotropía, con los ejes rápido y lento orientados horizontalmente. Esta limitación puede ser superada considerando que las medidas obtenidas como "aparentes" (Silver and Savage, 1994) y por lo tanto provenientes de distintos *back-azimuths*, pueden ser invertidas para evaluar la presencia de más capas anisótropas (Silver et al., 1994) o de una sola capa con buzamiento (Babuska et al., 1993).

Tanto en tratamientos de eventos individuales como de eventos múltiples, los análisis de desdoblamiento de las ondas S poseen varias ventajas; esto explica su popularidad desde su introducción en los años 80. A parte de que las metodologías aplicadas son relativamente simples, permiten calcular el error de cada medida y de esta forma se pueden comparar los resultados de anisotropía con los obtenidos mediante otros grupos de datos y metodologías. Otra ventaja es que la resolución lateral de la anisotropía calculada mediante los parámetros de desdoblamiento es generalmente buena y por lo tanto el análisis proporciona una información bastante exacta de las estructuras a gran escala.

Una desventaja de estos cálculos de anisotropía es que se realizan con metodologías muy diversas y con distintos grados de calidad de los datos, de modo que existe una gama de resultados bastante heterogénea donde no siempre es fiable comparar los resultados. Otra limitación que conlleva cuando se trabaja con el desdoblamiento de las fases del núcleo (SKS) es que no se obtiene una información fiable de la profundidad a la cual se detecta la anisotropía, pudiéndose ésta originarse en el manto (e.g. Kendall, 2000), en la parte inferior del manto superior

(Wookey et al., 2002; Wookey et al., 2004), o por dispersiones en la corteza y/o en el manto (Hedlin and Shearer, 2000).

Finalmente, cabe comentar que la fiabilidad de los parámetros de desdoblamiento depende en gran medida de la distribución *back-azimuthal* de los registros utilizados, de manera que una cobertura *azimutha*l pobre introduce un error grande obstaculizando la valoración final de la anisotropía. Por otra parte, también se requiere que las estaciónes sísmicas estén registrando durante largos períodos (por lo menos más de año y medio) para lograr un volumen suficiente de datos.

Cálculo de los Parámetros δt y ϕ para la Península Ibérica

La instalación de numerosas estaciónes de banda ancha por parte del Instituto Andaluz de Geofísica (IAG) en los últimos años ha hecho posible la realización de este estudio de anisotropía de la Península Ibérica. Así mismo, el creciente número de proyectos de investigación que se están llevando a cabo en el Sur de la Península y en el dominio de Alborán (IBERSEIS, TOPOIBERIA, TOPOMED, etc.) son un indicativo del interés que suscita esta zona geológica. La Península Ibérica se encuentra en la proximidad de límites de placa activos (Euroasiatica y Africana) en sus márgenes meridionales, y está delimitada al Norte por los Pirineos y en el margen Este por una cuenca extensional neógena. Tanto por sus dimensiones, como por estas condiciones de contorno, la Península es un excelente laboratorio natural para el análisis de la litosfera subyacente y el estudio de los procesos de deformación que han estado, y están actuando sobre ella.

En esta tesis, el análisis del desdoblamiento de las ondas SKS se ha efectuado utilizando el programa SplitLab (Wüstefeld et al., 2008). Este programa se circunscribe dentro de las técnicas que utilizan un solo telesismo y calcula los parámetros anisotrópicos aplicando tres de los métodos anteriormente citados: el método de correlación cruzada, el método de mínima energía y el método de los autovalores. De forma que cuando la fase SKS del telesismo analizado posee una

alta relación señal/ruido (S/R), entonces las tres metodologías deben proporcionar valores de δt y ϕ parecidos y se obtiene una buena fiabilidad de los parámetros de anisotropía. Adicionalmente, la comparación entre los tres resultados proporciona una herramienta muy útil para discriminar los telesismos que no presentan evidencia de desdoblamiento de la fase SKS (*null measurement*) de los que presentan un desdoblamiento muy bajo, es decir una baja anisotropía (*weak anisotropy*).

En este trabajo se han analizado datos de telesismos registrados en 19 estaciones sísmicas de banda ancha desplegadas por la Península Ibérica (Figura 4.1). De estas estaciones, 13 pertenecen al Instituto Andaluz de Geofísica de la Universidad de Granada (IAG), 3 al Real Observatorio de la Armada-Universidad Complutense de Madrid-GEOFON (ROA-UCM-GEOFON), 1 al Instituto Geográfico Nacional (IGN), 1 al IRIS/USGS, y 1 a GEOFON.

Los datos analizados varían en un espacio temporal que va desde los 9 años (estación PAB) a los 5 meses (estación JAND). Esta variabilidad depende de la fecha en que se empezó a almacenarse los telesismos de forma continua. Otro aspecto a tener en cuenta es que la calidad de los registros también varia dependiendo de donde esté ubicada la estación sísmica; por ejemplo las estaciónes de CEUT y SFS presentan registros con mucho ruido y por lo tanto se han obtenido pocas medidas de anisotropía para estas estaciónes.

En total se han identificado 106 telesismos con desdoblamiento SKS ocurridos a distancias mayores de 85° y con magnitud (Mw) superior a 5.5. En el Capítulo 4, la Figura 4.4 muestra los eventos seleccionados con una proyección terrestre centrada en la España meridional, donde se pone de manifiesto que el mayor número de telesismos procede del cuadrante NE y hay pocos que llegan del cuadrante SE; lo que va a suponer una dificultad a la hora de establecer el número de capas anisótropas debido a la cobertura *back-azimuthal* irregular. Para las distancias comprendidas entre 130° y 165° también se ha considerado la fase SKKS.

Para las fases SKS su frecuencia dominante está entre 0.125 Hz - 0.1Hz. Siempre que ha sido posible, se ha priorizado no filtrar los datos, y cuando la relación señal-ruido ha sido alta se han aplicado filtros paso-banda que respeten el ancho de las

frecuencias SKS; siendo las bandas más comunes utilizadas: 0.01 Hz -1 Hz, 0.02 Hz - 0.2 Hz, 0.02 Hz - 0.3 Hz.

Las localizaciones epicentrales de los telesismos utilizados se han extraído del catálogo Harvard (http://www.seismologyharvard.edu/CMTsearch.html) y los tiempos teóricos de llegadas de las fases SKS a las estaciónes se han calculado usando el modelo de Tierra IASP91 (Kennett, 1995) y el software de IASP91TTIM (Buland and Chapman, 1983; Kennett and Engdahl, 1991).

A cada pareja de parámetros de anisotropía calculados (δt y ϕ), se le ha asignado un parámetro de calidad que tiene en cuenta la relación señal/ruido de las fases SKS (Barruol et al., 1997a). En la Tabla 5.20 se recogen las coordenadas de las estaciones sísmicas utilizadas y los valores medios de la anisoropía obtenida, con sus errores.

Evaluación de la Anisotropía mediante fases SKS en la Península Ibérica

Si bien el ámbito general del estudio de la anisotropía SKS realizado en esta tesis es toda la Península Ibérica, los dos dominios geológicos principales sobre los que se focaliza son el Macizo Varisco y la Cordillera Bética. Por tanto, antes de proceder a la presentación de la anisotropía obtenida a partir de los parámetros de desdoblamiento δt y ϕ presentados en la Tabla 5.20, es conveniente efectuar una breve descripción geológica dado que su compleja estructura va a determinar la interpretación.

La orogenia Varisca comenzó en el Devónico medio y terminó en el Carbonífero (Ribeiro et al., 1979) como resultado de la colisión oblicua entre los grandes continentes Laurentia-Báltica y Gondwana. El macizo Varisco es el mejor fragmento expuesto en la Península y ocupa su mitad occidental. Al Este y Sur está delimitado por cuencas que se han dividido en cinco zonas principales, en base a las características paleogeográficas, al estilo estructural, al metamorfismo y al magmatismo (Julivert et al., 1980; Ribeiro et al., 1979). Éstas son: Zona Cántabra (CZ), la zona Astur-Ocidental-Leonesa (WAIZ), la zona Galicia-Tras-OS-Montes

(GTMZ), la zona Centro-Ibérica (CIZ), la zona de Ossa Morena (OMZ) y zona Sud-Portuguesa (SPZ), (Figura 6.3).

El otro dominio geológico es la Cordillera Bética conectada al Rif a través del arco de Gibraltar, y que representan el tramo de la orogenia Alpina situado más a Sur de Europa (Figura 6.4). Junto con la cuenca de Alborán constituye una de las más complejas regiones geológicas del mediterráneo occidental.

Un desafío importante es explicar cómo la cuenca de Alborán, que está en régimen extensional (Comas et al., 1999) puede coexistir dentro de un régimen de colisión continente-continente, es decir por la convergencia de la placa Africana y de Eurasia que estuvo funcionando desde el Cretácico al Paleógeno (Dewey et al., 1989).

Se han propuesto diversos modelos geodinámicos para explicar la formación y evolución Neógena de la región de Alborán y del Arco de Gibraltar. En las Figuras 6.5, 6.6 y 6.7, se recogen los principales.

El **colapso extensional post-orogénico (*convective renoval*)** (e.g. Dewey, 1988; Platt and Vissers, 1989; Platt et al., 2003) considera que el hundimiento litosférico es el resultado de la convergencia entre placas que creó un *ridge* colisional con una gruesa corteza cuya raíz fría penetra en el manto litosférico. A partir del Eoceno y hasta el Oligoceno, los esfuerzos tectónicos debidos a la convergencia entre las placas Euroasiática y la Africana, favorecen el engrosamiento de la litosfera en el dominio de Alborán. Como consecuencia, se forma un trozo grueso de corteza cuya base es una raíz litosférica fría e inestable. La remoción de esta raíz provoca la extensión de la región orogénica y la exhumación rápida de los niveles corticales más profundos, mientras que los esfuerzos horizontales generados describirían un patrón radial, que combinado con la convergencia continuada de África y Eurasia, determinaran además un acortamiento en las zonas externas del orógeno (Figura 6.5).

El modelo propuesto por **Seber et al.** (1996a; Mezcua and Rueda, 1997; Calvert et al., 2000) está basado en un proceso de **delaminación** litosférica y comparte algunas características con el modelo de anterior. La diferencia reside en el estilo de eliminación de la espesa raíz litosférica y en la magnitud del proceso. Los autores

proponen que como consecuencia de la compresión, una gruesa porción de litosfera descendió por gravitación convirtiéndose en una raíz inestable que progresivamente fue desprendiéndose en la dirección Oeste y Noroeste, a la vez que era substituida por material astenosférico caliente. Como consecuencia del flujo ascendente astenosférico se produjo un calentamiento en la base de la corteza que indujo la elevación y la extensión del área de Alborán (Figura 6.6).

El modelo de r**etroceso (*roll-back*)** de Royden (1993; Lonergan and White 1997; Frizon de Lamotte et al., 1991) se basa en la subducción de litosfera oceánica debajo la zona interna. Cuando la velocidad de subducción excede la tasa de la convergencia, la zona de subducción empieza a migrar hacia el Oeste mientras que la corteza del *ridge* de colisión (zonas internas) sufre un intenso adelgazamiento. En la porción norte y sur de la zona de subducción, la migración hacia el Oeste se ralentiza debido al contacto con las cortezas de Iberia y África; y las zonas internas sufren un acortamiento en los márgenes continentales. Mientras que en la porción central de la subducción, continua la migración hacia Oeste con mayor velocidad, determinando la extensión bajo el mar de Alborán (Figura 6.7).

El modelo propuesto por **Zeck (1996) *slab break-off*** (Wortel and Spakman, 2000) sugiere la existencia de una lámina que subduce hacia el NO bajo la parte SE de la Península, originada por el movimiento relativo entre la placa Africana (hacia el Oeste) y la Península Ibérica (hacia Eurasia) que estuvo funcionando desde el Cretácico hasta el Paleógeno. Durante el Mioceno esta lámina subducente se rompe y actualmente está orientada verticalmente bajo la parte Sur de la Península. Este modelo es capaz de explicar la subducción de una gran cantidad de material litosférico en una zona de limitada convergencia. Aunque cabe notar que el movimiento hacia el Este de África respecto de la Península ocurrió con anterioridad en el Cretácico medio, lo que implicaría que otra porción de lámina subducente debería estar residente en el manto 60 millones de años antes de desprenderse y descender hacia el manto (Figura 6.8).

Existen otros modelos que consideran diferentes geometrías y direcciones de la subducción: hay modelos que sugieren procesos de subducción hacia el Este (Gutscher et al., 2002); otros consideran matices distintos en cuanto a la dirección y de la lámina que subduce (e.g., Blanco and Spakman, 1993; Spakman et al., 1993; Zeck, 1996, 1998; Morales et al., 1999; Jolivet et al., 2000); incluso hay modelos que

predicen la evolución espacial y temporal del vulcanismo que tendría asociado la subducción (e.g., El Bakkali et al., 1998; Duggen et al., 2004, 2005; Gill et al., 2004).

La mayoría del territorio ibérico está afectado por una sismicidad media superficial (h<30 km) (Stich et al., 2006); donde destacan algunos sismos profundos localizados cerca de Granada (h≈ 640 km; Buforn et al., 1991). Al estar cerca de los límites de placa activos, el margen meridional de Iberia está caracterizado por un alto nivel de sismicidad y es donde se concentra el mayor número de terremotos grandes; sobre todo en el golfo de Cádiz y en el Norte de África. Los terremotos recientes más grandes registrados en estas zonas han sido en Marruecos en 2004 con Mw=6.3 (Stich et al., 2005), en Argelia en Octubre de 1980 con Mw=7.1 (Deschamps et al., 1982) y en el golfo de Cádiz el 15 de Marzo de 1964 con Mw=6.1 (Buforn et al., 1988).

Mientras que la geometría cortical de la Península Ibérica está bien caracterizada por los numerosos estudios sísmicos, geológicos, topográficos, tomográficos y gravimétricos que se han realizado; las estructuras sub-corticales y del manto superior sólo se han investigado mediante estudios de tomografía sísmica. Dentro de este conjunto, son aún más escasos los trabajos que tratan aspectos anisotrópicos, de entre ellos destacar los desarrollados por Díaz et al. (1998), Calvert et al. (2000a, 2000b), Schmid et al. (2004) y Serrano et al. (2005). Los objetivos de esta tesis se emarcan en esta línea de investigación: en el estudio de la anisotropía en regiones con deformación actual.

En concreto, esta tesis se centra en el estudio de la anisotropía en el manto litosférico. Para ello se ha utilizado una metodología geofísica y se ha pretendido conciliar las informaciones geodinamicas con los resultados obtenidos mediante datos sismológicos, proporcionando de esta forma una visión general de los factores que controlan la deformación en la Península Ibérica y arco de Gibraltar. En este contexto, ha sido posible caracterizar el manto litosférico en terminos anisotrópicos y establecer un patrón general de las direcciones de anisotropía en toda el área de estudio. De forma que ha podido deducirse el tipo de deformaciones que han actuado en la zona y ajustar el modelo geodinámico más coherente con las direcciones de anisotropía observadas.

La aportación de estos nuevos datos de anisotropía sísmica en la Península Ibérica y arco de Gibraltar, constituye una ayuda en la investigación de los patrones de deformación que han modelado esta región tan debatida.

En la Figura 5.22 se presentan los resultados de anisotropía SKS de la Península Ibérica, donde se aprecia como la anisotropía en la zona Galaica-Astúrica, en los Pirineos y en la parte más septentrional del Macizo Varisco presenta una dirección aproximadamente Este-Oeste. Esta misma tendencia se mantiene en la parte Norte-Central (estaciónes ECAL, MTE y PAB) que presentan una dirección media de polarización rápida de N77°W, N89°E y N83°E respectivamente.

Las direcciones de anisotropía de las estaciónes situadas en la zona Centro-Ibérica, (PAB y MTE, Figura 5.22) y de la zona Galicia-Tras-OS-Montes (ECAL, Figura 5.22) son aproximadamente similares. Estas dos áreas se consideran como parte de un único bloque geológicamente estable de litosfera continental de modo que cabe esperar que la deformación sea la misma y, por ende, la dirección de anisotropía.

En el supuesto que la anisotropía estuviese relacionada con el flujo astenosférico debido al movimiento de placa absoluto actual (APM), entonces debería encontrarse un paralelismo entre las direcciones de la anisotropía y las direcciones de APM. Sin embargo nuestras observaciones sugieren que no es este el caso (Figura 6.13).

Por otro lado, las anomalías magnéticas aportan otra comparación útil dado que reflejan cambios de composición y/o estructurales en la corteza. De forma que un paralelismo entre la dirección rápida de anisotropía y los alineamientos magnéticos corticales indica que hay deformación vertical coherente entre la corteza y el manto. En nuestro caso, las estaciónes presentan dirección casi sub-vertical respecto a la tendencia de las anomalías magnéticas (Figura 6.14) y, por tanto, puede suponerse que la deformación que ha actuado en la corteza es diferente a la del manto. Circunstancia que indica un desacople entre estas dos partes y que coincide con estudios de sísmica de reflexión realizados en proximidad de la sierra de Aracena (Simancas et al., 2003); donde se encuentra la estación ARAC.

Además, las direcciones rápidas deducidas para las estaciónes PAB, MTE y ECAL (Figura 5.22) coinciden con la tendencia E-O de la deformación Hercínica acaecida en esta zona (Banda et al., 1981). Estas observaciones implican que la

anisotropía detectada debe estar "congelada" en la litosfera (Silver et al., 1991), de modo que el último episodio orogénico significativo que ha afectado indujo la LPO que estamos registrando.

Esta tendencia Este-Oeste, cambia para las estaciónes situadas en el contacto entre el Macizo Ibérico y la Cordillera Bética, o sea para las estaciónes ARAC, HORN, JAND y SESP (Figura 5.22), donde la dirección de anisotropía preferente es NNE-SSO. Al mismo tiempo se detecta una dependencia clara de los parámetros de desdoblamiento con el back-azimut de los eventos que puede explicarse como una variación vertical de la anisotropía; debido a la presencia de dos (o más) capas anisotrópicas, o a variaciones laterales de la anisotropía. Esta variación de la dirección de anisotropía respecto a la parte Norte y Centro también podría reflejar una deformación posterior a la hercínica, relacionada con las principales etapas de la evolución tectónica de esta parte (etapa transpresional, transtensional y de acortamiento), o bien podría deberse a una deformación relacionada con la orogenia Alpina. - De hecho hay evidencias de la deformación Alpina en la parte SW de la Península; cerca de la sierra de Aracena hay fallas que han sido reactivadas por esta orogenia, detectándose un moderado levantamiento regional (Stapel, 1999).

A diferencia de la parte situada más al sur del Macizo Varisco que exhibe una compleja anisotropía, la parte Este de las Béticas es más homogénea detectándose una anisotropía donde la dirección rápida tiene una tendencia ENE-OSO, que cambia a E-O hacia el Oeste y llega a ser de N-S en la zona del estrecho de Gibraltar. En efecto, la mayoría de las estaciónes situadas en la Béticas (CART, VELZ, ACBG, GORA, ACLR y ASCB, Figura 5.22) muestran esta tendencia homogénea con dirección aproximadamente N70°E y unos tiempos de retardo alrededor de 1.5 segundos. Una tendencia similar se detecta en la estación MELI en el Norte de África, donde la dirección es N68°E y el retraso temporal de 0.95 sec. Probablemente esta anisotropía observada esté originada por una sola capa.

La parte Este de la Béticas presenta una leve variación de anisotropía que concuerda con las características geológicas superficiales. Lo que indicaría que las estructuras de la corteza y del manto están reflejando el mismo movimiento, es decir, la litosfera entera ha sufrido la misma deformación convirtiéndose en un todo anisótropo.

Un caso interesante ocurre en las estaciónes SFS y CEUT (Figura 5.22) donde la dirección de anisotropía es paralela a la tendencia del arco de Gibraltar; aunque el número de datos disponibles en estas dos estaciónes sea bastante exiguo. Pero la comparación de estas anisotropías SKS con las anisotropías obtenidas a partir de las ondas Pn (Calvert et al., 2000b; Figura 6.16) muestra que hay buena coincidencia entre ambos resultados, de modo que puede validarse las direcciones de rotación halladas alrededor del arco.

El hecho de que la dirección de anisotropía cambie alrededor del arco de Gibraltar parece ser el resultado de una rotación gradual desde ENE de la zona interna de las Béticas hacia el NE. Ello estaría en correspondencia con la estación de ANER, a NS en las estaciónes de CEUT y SFS. Tal y como se ha mencionado anteriormente, para esta zona se han propuesto varios modelos geodinámicos, que difieren esencialmente en la forma como el material litosférico ha sido removido y reemplazado por material astenosférico. En este contexto, nuestras medidas de anisotropía SKS son difíciles de reconciliar con los modelos geodinámicos basados en colapso extensional post-orogénico o en la delaminación, ya que se daría el caso de la existencia de un flujo radial que no se observa en nuestras medidas. De manera que nuestras observaciones favorecen más los modelos que proponen una subducción no activa en la actualidad con un *roll-back* en el Mediterráneo Occidental.

1. Introduction

Since Hess' (1964) pioneering work on the existence of seismic anisotropy in the oceanic lithosphere, studies of seismic anisotropy in the upper mantle have been routinely carried out on a global scale. These studies have established that much of the upper mantle, above 400 km, is seismically anisotropic. Thus, measurements of shear wave birefringence, or splitting, are an important tool for providing information on the geometry of deformations associated with tectonic and geodynamic processes.

Seismic anisotropy is an ubiquitous feature of most geological materials. This is because rocks are composed of intrinsically anisotropic crystals (for instance, olivine) that generally exhibit fabric or order, which leads to a directional dependence in seismic velocities (Savage, 1999).

When a polycrystal is subjected to an external deformation, the resulting intracrystalline slip will be function of the orientation of the grains relative to the externally imposed stress and will depend on the compatibility of deformation between neighboring grains (Kaminski and Ribe, 2002). Laboratory experiments can be used to predict anisotropic scenarios in the upper mantle, though all likely factors remain to be tested. All these experiments predict that the lattice preferred orientation (LPO) of an initially isotropic aggregate deformed uniformly follows the finite strain ellipsoid (FSE), with the fast axis of olivine aligned with the longest axis of the finite strain ellipsoid (Wenk et al., 1991; Ribe, 1992). These predictions coincidewell with experimental observations made by Zhang and Karato (1995), who found that at small strain the fast axis follows principal extension in modestly deformed olivine aggregates (<100% strain), but aligns with the direction of flow for large deformation. This result suggests that modest simple shear, such as may occur

at the base of a moving plate, will produce anisotropy with a dipping axis of symmetry; modest pure shear in the horizontal plane, associated with rifting extension or orogenic compression, would align the symmetry axis with the flow direction. Accumulated simple-shear flow from thermal convection would also align the symmetry axis with the flow direction (Parker and Levin, 2002). LPO is the first possible cause of anisotropy and, as explained above, it can result from mineral alignment during strain (e.g. Christensen, 1984; Zhang and Karato, 1995; Kaminski, 2002), and is inferred to be the dominant cause of upper mantle anisotropy (Figure 2.5). The second possible cause of anisotropy is the shape-preferred orientation (SPO) (Figure 2.4) that can result from cracks in the crust, melt-filled cracks, or lenses in the mantle (Savage, 1999). SPO may exist in areas beneath mid-ocean ridges and subduction zones in the uppermost mantle, as well as in the lowermost mantle (e.g. Garnero et al., 1998).

Most minerals composing the bulk of the crust and mantle are anisotropic to some degree (Babuska and Cara, 1991), while the majority of crustal anisotropy in the upper 10-15 km is caused by cracks and microcracks and presence of fluid in them (Crampin, 1984). On the other hand the proprieties of olivine dominate the upper mantle anisotropy.

Vinnik and Montagner (1996) model the mantle as anisotropic above 320 km, as isotropic between 320 and 580 km, and with 3% anisotropy between 580 and 620 km.

However, the origin of anisotropy beneath continental regions is currently a topic of much debate and is still unresolved. Two competing hypotheses have been proposed to explain shear-wave splitting pattern in continental settings. The first hypothesis considers that the possible source can be in the asthenosphere, and the observed splitting parameters should be related to the present-day flow induced by the differential motion between tectonic plate and underlying mantle (Vinnik et al., 1992); in this case, the absolute plate motion direction will be parallel to anisotropic directions. The second hypothesis predicts that the source of anisotropy can be in the lithosphere and the splitting parameters should be related to frozen or active deformation (Silver and Chan, 1991), or in both layers.

Measurement and interpretation of shear wave splitting for phases that traverse the upper mantle has shed light on past and present deformation processes in a

variety of tectonic settings, including subduction zone, rift zones, strike-slip faults and other tectonic setting (Figure 1.1).

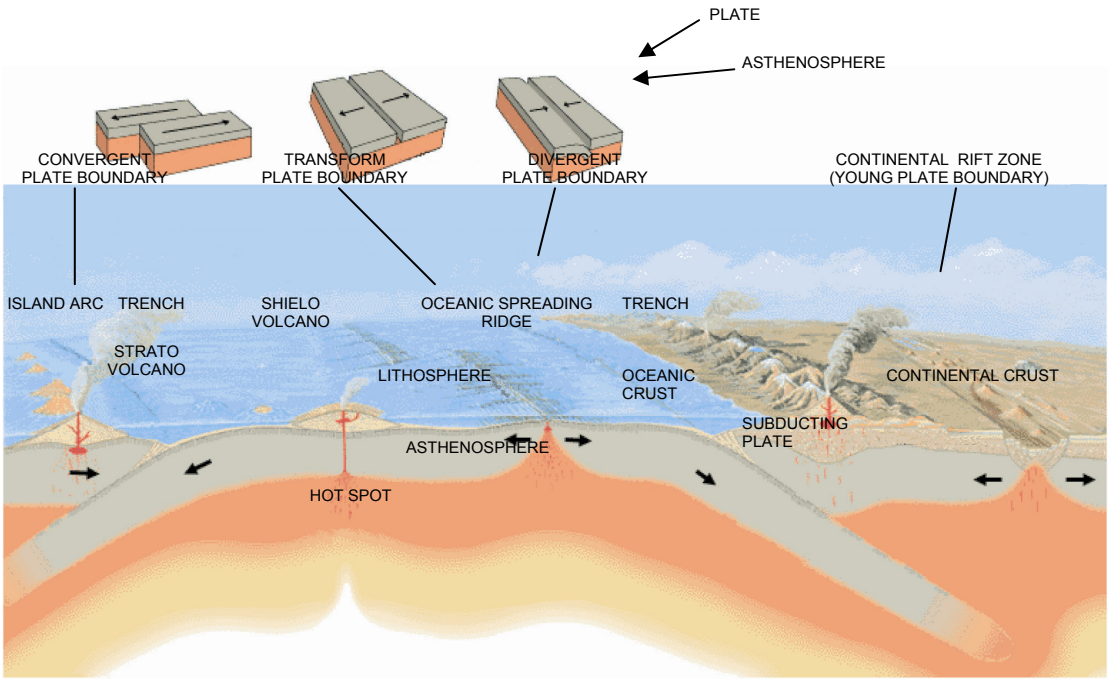

Figure 1.1 – The main regions where anisotropic measurements can be carried out are summarized in this cartoon

Figura 1.1 – Esquema de las principales zonas donde se pueden obtener mediciones de anisotropía sísmica.

In subduction zones (e.g. Pozgay et al. 2007; Ando et al., 1983; Russo and Silver, 1994; Fouch and Fischer, 1996; Sandvol and Ni, 1997; Fischer et al., 1998; Smith et al., 2001; Anderson et al., 2004; Currie et al., 2004), a complex 3D patter of mantle flow is present, so the interpretation of anisotropy can be controversial since different factors, such can be considered. For examples, the geometry of the zone or other factors as the presence of water and perhaps other volatiles, which can alter the relative strengths of olivine slip planes and change how it deforms. These factors will be further explained in the Chapter 2 and references to study areas and their observed anisotropy will be given

Shear wave splitting in rift zones, revels for the most case, that fast direction is observed parallel or sub-parallel to the rift opening (Figure 2.15). On the other hand, there are cases where the fast direction is neither parallel nor perpendicular to the rift opening as in the Basin and Range (Savage and Silver, 1993; Sheehan et al., 1997) and Iceland (Bjarnason et al., 1996).

Whereas, in oceanic ridge the shear wave splitting is interpreted mainly as an effect of structural anisotropy due to the presence of ridge-parallel cracks in the shallow crust, as for example is in the Juan Fuca Ridge (Almendros et al., 2000). In the case of Pacific plate (Shimamura et al., 1983; Ishikawa, 1984), the anisotropic alignments are assumed that represents the plate absolute motion at the time this layer was accreted to the lithosphere (Figure 2.15) (Babuska and Cara, 1992).

Anisotropic studies in strike-slip regions show that foliation influences on the orientation of anisotropy. San Andreas Fault is a clear example of strike-slip region, a proposed two layers model foallows (Savage and Silver, 1993).

As discuss above, seismic anisotropy is usually attributed to the alignment of crystal orientations, which in turn can be related to the strain history of the rock (Zhang and Karato, 1995; Christensen and Salisbury, 1984). Thus seismic anisotropy can provide information about tectonic deformations and dynamic processes occurring in the upper mantle. Preferred orientation of component minerals in the mantle with strong intrinsic anisotropy, particularly olivine, is regarded as the main candidate for generating the seismic anisotropy seen in the observations.

Core-mantle refracted waves, such SKS and SKKS, have been used systematically to measure seismic anisotropy. This is because their initial polarization is well known, they have a near-vertical incidence at the receiver and are well-recorded at a large distance interval far away from the source, so these phases are affected only by anisotropy located along the path between the core-mantle-boundary and the receiver. It is not clear whether the splitting is originated within the lithosphere or the sublithosphere, and/or in the asthenospheric mantle. Therefore, this technique does not have a vertical resolution, and thus does not provide an answer as to where the anisotropy is located unsolved.

Other seismic waves used to detect anisotropy are the Pn phase, surface phase and seismic phases converted from P to S below the receiver. All these waves sample different depths (Figure 2.17) so the comparative uses of them help to better constrain the depth where anisotropy occurs.

An anisotropic elastic system can be characterized by its elastic tensor, which relates the stress to the strain and is intimately related to the seismic velocities. A homogeneus system is described by Hooke's law (Chapter 2). The assumption of

symmetry systems can reduce its initial 81 independent elastic constants required. In fact, most anisotropy studies have concentrated on two types of symmetry: hexagonal symmetry, which has 6 elastic constants and the orthorhombic system, which has 9 elastic constants.

When a shear wave propagates through an anisotropic medium with a horizontal symmetry axis, an up-going shear wave will split into orthogonally fast and slow waves which have similar waveforms. This property is referred to as shear-wave splitting, or sometimes birefringence and it was observed for the first time in the calcite mineral.

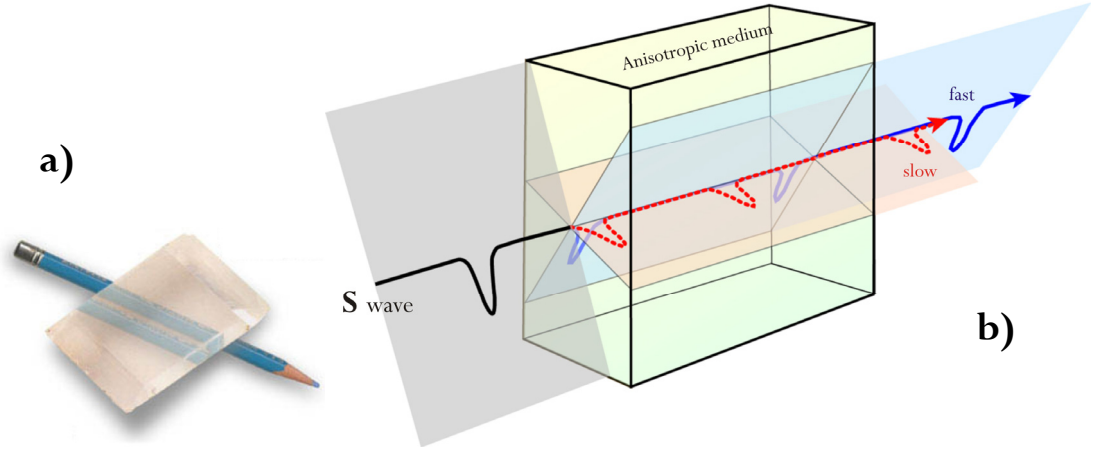

Figura 1.2 – a) Birefringence in a crystal of calcite. b) Schematic cartoon of splitting of S wave in an anisotropic medium. Polarization is along symmetric axis of the anisotropic medium; the difference in velocity propagation produces a difference in the speed giving fast and slow waves: http://garnero.asu.edu/research_images/images_all.html.

Figura 1.2 – a) Fenómeno de la birrefringencia observado en un cristal de calcita. b) Esquema del desdoblamiento de una onda S al atravesar un medio anisótropo. Además de la polarización según los dos ejes de simetría del cuerpo anisótropo, se produce un cambio en la velocidad de las ondas desdobladas. Normalmente uno de los ejes de anisotropía favorece una mayor velocidad (cortesia de Garnero http://garnero.asu.edu/research_images/images_all.html).

Shear wave birefringence, or splitting, is the most popular tool for investigating seismic anisotropy. Splitting can be described in terms of two parameters: the fast polarization direction (ϕ) and delay time (δt) between fast and slow polarized S waves.

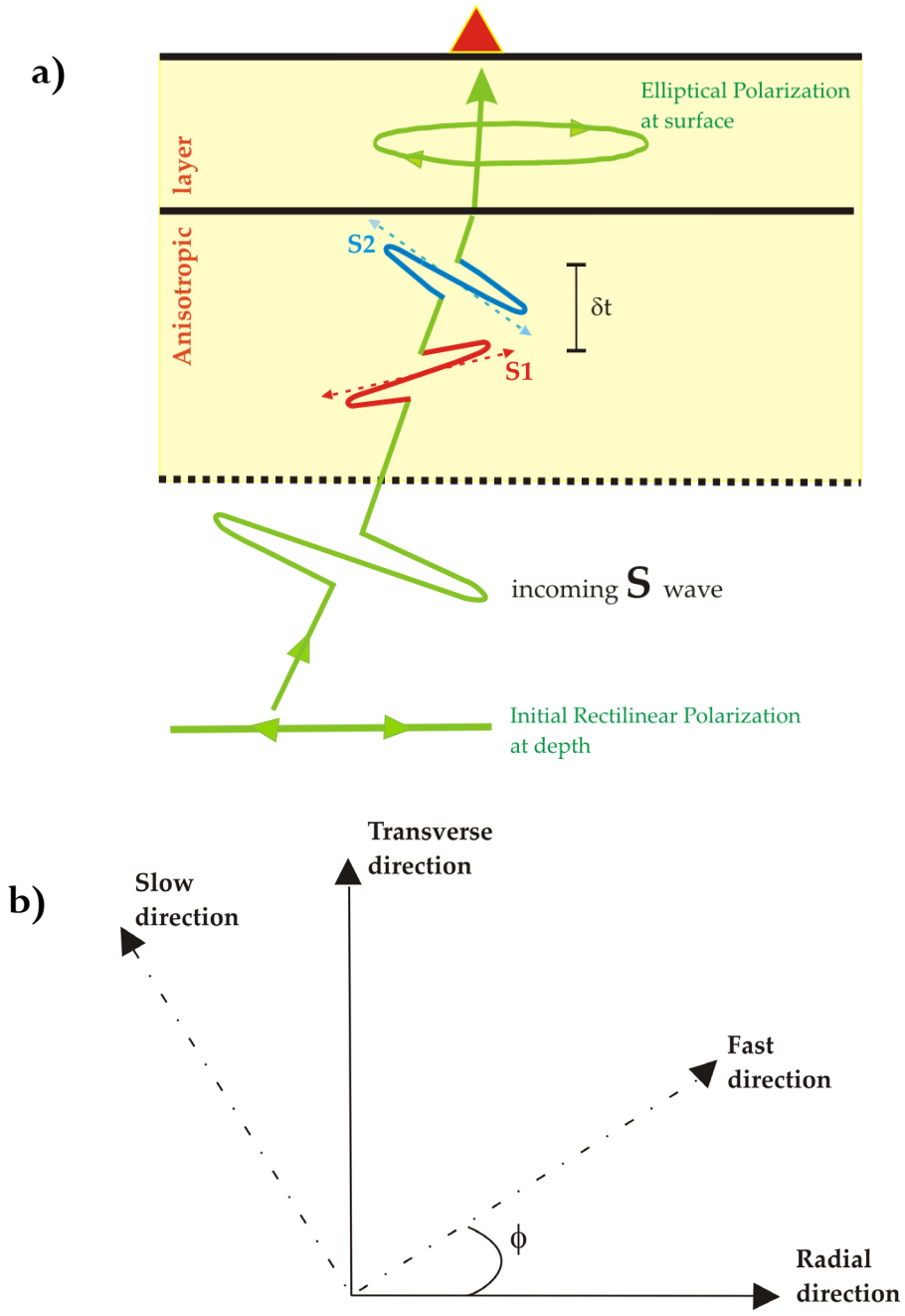

Figure 1.3 – a) Splitting of incoming S wave in anisotropic medium oriented along the fast (S2) and slow (S1) direction of anisotropy. δt is the time difference between the split pulses. b) the fast polarization angle ϕ, gives the rotation of the fast axis relative to the radial propagation direction.

Figura 1.3 – a) Onda S entrante en un medio anisótropo que se desdobla en dos ondas S orientadas según la dirección rápida (S2) y lenta (S1) de anisotropía. δt es la diferencia de tiempo entre los dos pulsos. b) Orientación del ángulo de polarización ϕ, que define la rotación de la dirección rápida respecto a la dirección radial de propagación.

Shear wave splitting parameters are most often measured using grid search methods that seek to remove or compensate for the effect of splitting from a single measurement of an incoming shear wave. A review of techniques used to find the anisotropic parameters is described in Chapter 3.

In this study, we have utilized the SplitLab program (Wüstefeld et al., 2008) that offers the possibility to calculate the anisotropic parameters with three methodologies whose comparison help to better constrain the observed anisotropic measurements.

In our shear wave splitting analysis, we used teleseismic core phases including SKS and SKKS, pSKS and sSKS of waveforms recorded at nineteen stations deployed in the Iberian Peninsula. Results from these stations are presented in Chapter 5.

The majority of stations are deployed in the Betic Cordillera, within a network managed by the Instituto Andaluz de Geofisica, Universidad de Granada, and the density of distributions is related to the referred interest for this zone.

The areas of interest in this Thesis, the Iberia Peninsula and the Gibraltar arc, represent a key area of geodynamic interest for the Africa-Eurasia collision and for the various stages of the openings and closures of the Mediterranean basins. Various geodynamic models and mechanisms have been proposed to explain the large-scale structures and timing constraints in the Gibraltar arc, based on regional-scale recycling of lithosphere into the mantle, such as active continental subduction (Morales et al., 1999), delamination (Seber et al., 1996a) or active oceanic subduction (Lonergan and White, 1997; Gutscher et al., 2002). These models are presented and discussed in detaile in Chapter 6.

In Chapter 5, new shear-wave splitting measurements, obtained at permanent stations located in the Variscan Iberian Massif and in the Betic and Rif Cordillera, are presented and compared to previous results from Iberia (Silver and Chan, 1988; Vinnik et al, 1989; Diaz et al., 1998; Schmid et al., 2004), as well as from Pn phase anisotropy (Serrano et al., 2005; Calvert et al., 2000b). In the light of tomographic models for this region and other geophysics data set, we propose that these anisotropy observations may help to constrain and to better understand the geodynamic setting of this complex area and to allow us to map lateral variation of

apparent mantle anisotropy. The lateral variations of the shear wave splitting parameters, as well as their dependence on the direction of propagation within the upper mantle, reflect a general complexity orientation of anisotropic structures in the mantle lithosphere, expecially for the boundary between Iberian Hercynian Massif and Betic Cordillera.

The existence of variations in splitting parameters with back azimuth may be a characteristic of dipping layers of anisotropy, multiple layers of anisotropy with different geometries or lateral variations in anisotropy. However, sampling in back azimuth is limited for such stations. We therefore cannot rule out the possibility of models with complex geometries of anisotropy, such as the ANER stations, where two layer case of anisotropy is present.

While, the oldest interior portions of the Iberian Massif lithosphere have remained stable for more than ≈ 250 Ma, regions to the south-east are much younger in age. In regions which are currently tectonically stable, the fast shear wave polarization will reflect the last episode of deformation, as the case of the Iberian Variscan Massif. On the other hand, several aspects of the observed splitting patterns in the southern part of Iberian Massif are clearly not consistent with the last episode of major lithospheric deformation that occurred in that zone and require more complex model to explain the data. However, in active tectonic regions such as the Betic Cordillera and Gibraltar arc, fast shear wave polarizations will be related to the present deformation, of which the geology of the overlying plate used as an indicator.

2. Seismic Anisotropy

Continental plates are much older than oceanic plates and form complex areas involving innumerable tectonic processes. Thus, continental interiors offer a unique window into past and present processes of Earth development. Using this information, seismological techniques have been developed throughout recent decades to study the relation between plate tectonics and mantle flow as well as the internal deformation of the plate (Silver and Chan, 1988).

One of the best ways to obtain a image of deformation in the Earth's interior is through the detection and interpretation of seismic anisotropy, meaning the study of the dependence of seismic velocities on the direction of wave propagation and polarization. The use of anisotropy as a measure of deformation requires knowledge of its various seismological manifestations, its relation with the properties of crystalline aggregates and the style of orogenic deformation (Silver, 1996). Therefore it is essential to know how deformational processes alter the fabric of both the lithosphere and the sub-lithospheric mantle, and the identification of when certain deformational events occurred to accurately interpret the anisotropy. There is growing evidence suggesting that seismic isotropy - an important and common assumption in seismological studies - may actually be a rarity, rather than the rule in the shallow earth.

The majority of minerals and rocks that form the crust and upper mantle display seismic anisotropy in laboratory measurements (Babuska et al., 1992). Seismic anisotropy is a characteristic feature of the Earth; it is present in the crust due to aligned cracks (e.g. Crampin, 1984a), and in the upper and lower mantle due to mineral preferred orientation (e.g. Mainprice et al., 1989; Karato, 1998).

Most minerals composing the crust and mantle are anisotropic. If they are randomly oriented, then the bulk material appears isotropic. If there is a preferred orientation, the bulk material appears anisotropic (Savage, 1999).

2.1 Isotropic and Anisotropic media

In most seismological models, the Earth is usually assumed to be isotropic, that is, its physics properties do not vary with direction. However, the evidences that individual crystal and most common materials are observed to be anisotropic, with elastic properties that vary with orientation, yielded to the conclusion that the Earth was not completely isotropic. This assumption is made for seismological convenience because to consider the full effects of anisotropy, great computational complexity is required for anisotropic calculation. Therefore, the difficulty in inverting data for a greater number of elastic constants and, in many cases, the lack of compelling evidence for the existence of anisotropy are other complexity factors.

Anisotropy is responsible for the largest variation in seismic velocities: changes in the preferred orientation of mantle minerals or in the direction of seismic waves cause larger changes in velocity that can be accounted for by change in temperature, composition or mineralogy. Thus, the anisotropy is present in many parts of the Earth, making anisotropy studies an increasingly important part of seismology research.

We will start with an overview of the elastic system and follow with a discussion on the anisotropic system. A considerable number of books written on this topic exist. We are basing our information about the stress-strain relation and the seismic anisotropy on Stein and Wysession, 2003; Lay and Wallace, 1995, Shearer, 1999; Babuska and Cara, 1992.

An anisotropic elastic system can be characterized by its elastic tensor, which relates the stress to the strain. The stress-strain relationship is expressed by Hooke's law, for which the general form in a homogeneous system is: $\sigma_{ij} = c_{ijkl}\varepsilon_{kl}$

with $i, j, k, l = 1, 2, 3$, where σ_{ij} is the stress tensor for the system, ε_{kl} is the strain tensor, and c_{ijkl} is the elastic tensor which consists of 81 entries.

Following Voigt's representation of the c_{ijkl} tensor, we can transfer the 3x3x3x3 tensor as a 6x6 matrix c_{mn}, where the indices *m* and *n* vary from 1 to 6 if the pairs of indices (i,j) or (k,l) of the elastic tensor c_{ijkl} take the values of (1,1), (2,2), (3,2), (1,3) and (1,2) respectively:

$$c_{mn} = \begin{bmatrix} c_{1111} & c_{1122} & c_{1133} & c_{1123} & c_{1113} & c_{1112} \\ c_{2211} & c_{2222} & c_{2233} & c_{2223} & c_{2213} & c_{2212} \\ c_{3311} & c_{3322} & c_{3333} & c_{3323} & c_{3313} & c_{3312} \\ c_{2311} & c_{2322} & c_{2333} & c_{2323} & c_{2313} & c_{2312} \\ c_{1311} & c_{1322} & c_{1333} & c_{1323} & c_{1313} & c_{1312} \\ c_{1211} & c_{1222} & c_{1233} & c_{1223} & c_{1213} & c_{1212} \end{bmatrix} = \begin{bmatrix} c_{11} & c_{12} & c_{13} & c_{14} & c_{15} & c_{16} \\ c_{21} & c_{22} & c_{23} & c_{24} & c_{25} & c_{26} \\ c_{31} & c_{32} & c_{33} & c_{34} & c_{35} & c_{36} \\ c_{41} & c_{42} & c_{43} & c_{44} & c_{45} & c_{46} \\ c_{51} & c_{52} & c_{53} & c_{54} & c_{55} & c_{56} \\ c_{61} & c_{62} & c_{63} & c_{64} & c_{65} & c_{66} \end{bmatrix}$$

For most media stress and strain are symmetric, so $c_{ijkl} = c_{jikl} = c_{ijlk} = c_{klij}$ and these symmetries reduce the number of independent elastic constants in c_{ijkl} from 81 to 21, in the most general case. The latter is the most complex symmetry and is described as triclinic symmetry.

For isotropic material, the c_{ijkl} tensor can be written in terms of two independent elastic constants:

$$c_{ijkl} = \lambda\delta_{ij}\delta_{kl} + \mu\left(\delta_{ik}\delta_{jl} + \delta_{ij}\delta_{kl}\right)$$

Where λ and μ are called the Lamé parameters and δ is the Kronecker symbol (1 if i=j, 0 if i≠j), and for which the matrix form is:

$$c_{mn} = \begin{bmatrix} \lambda+2\mu & \lambda & \lambda & 0 & 0 & 0 \\ \lambda & \lambda+2\mu & \lambda & 0 & 0 & 0 \\ \lambda & \lambda & \lambda+2\mu & 0 & 0 & 0 \\ 0 & 0 & 0 & \mu & 0 & 0 \\ 0 & 0 & 0 & 0 & \mu & 0 \\ 0 & 0 & 0 & 0 & 0 & \mu \end{bmatrix}$$

However, the crystal structures of many earth materials require additional independent elastic coefficients.

Additional symmetries can be considered to further reduce the number of elastic constants. For example, crystals with 13 elastic constants have monoclinic symmetry; those with 9 have orthorhombic symmetry; those with 7 or 6 have tetragonal symmetry; those with 5 have hexagonal symmetry; those with 3 have cubic symmetry; and those with 2 have isotropic symmetry (see Table 2.1).

Type of symmetry	Number of independent elastic coefficients	Typical mineral
Triclinic	21	plagioclase
Monoclinic	13	hornblende
Orthorhombic	9	olivine
Tetragonal	6	stishovite
Trigonal	I 7	ilmenite
Trigonal II	6	quartz
Hexagonal	5	ice
Cubic	3	garnet
Isotropic solid	2	volcanic glass

Table 2.1 - Number of independent elastic coefficients for type of symmetry of typical mineral or Earth's material (from Bakuska and Cara 1992).

Tabla 2.1 – Número de coeficientes elásticos independtientes para cada tipo de simetría de los minerales más comunes de la Tierra (extraida de Babuska and Cara, 1992).

Any material in which more than two parameters, which may vary in direction, are needed is called anisotropic. In contrast, the properties of an isotropic medium are the same in every direction. However, while a number of symmetry systems exist, most anisotropy studies have concentrated on two types: hexagonal symmetry and orthorhombic symmetry.

For example, the olivine, which is the most abundant and anisotropic mineral in the Earth's mantle, requires 9 constants and belongs to the orthorhombic class system. Thus, the anisotropic seismic velocities have a complex behaviour (Figure

2.1). The maximum and minimum S velocities are 5.53 km/s and 4.42 km/s, so the percent of anisotropy can be calculated by the equation (2.1):

$$(2.1) \qquad A = (V_{max} - V_{min})/V_{max} * 100 \qquad \text{(in percent)}$$

where V_{max} and V_{min} are the maximum and minimum seismic velocities, respectively.

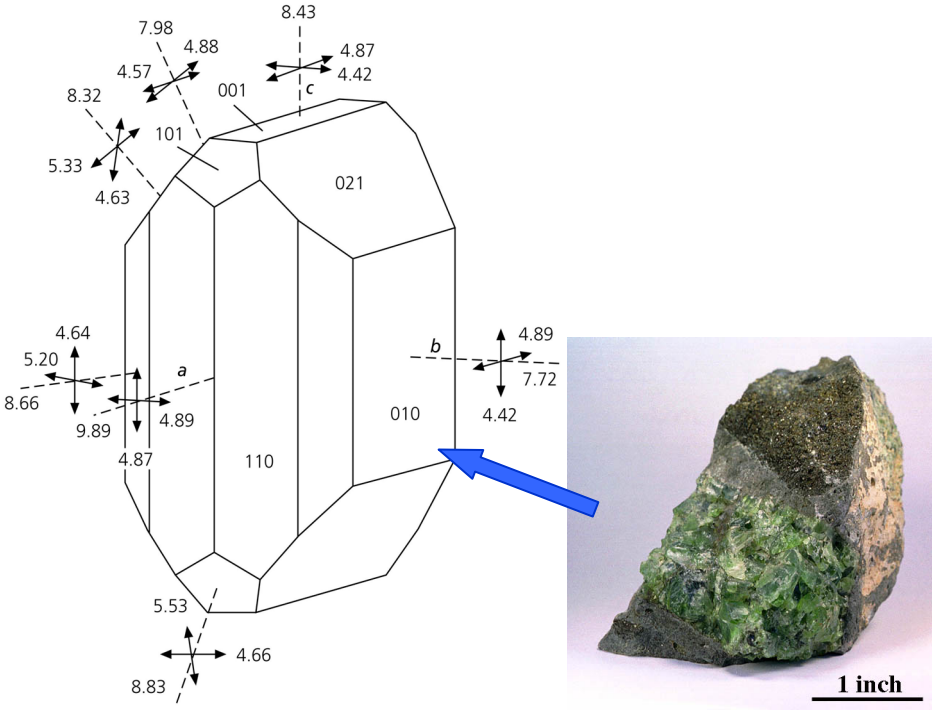

Figure 2.1 – Compressional and shear-wave velocities in a monocrystal of olivine. P velocities are in the directions of the dashed lines, and the S velocities are shown by the adjacent pairs of perpendicular lines. The *a* axis, corresponding to the [100] crystal face, is the fastest direction through the crystal (from Babuska and Cara, 1992).

Figura 2.1 – Velocidades de las ondas P y S en un monocristal de olivino. Las velocidades de las ondas P se corresponden con las direcciones marcadas por las líneas discontinuas y las velocidades de las ondas S vienen dadas por los dobletes de líneas perpendiculares. El eje a corresponde a la dirección más rápida a través del cristal y coincide con la cara [100] de éste (según Babuska and Cara, 1992).

For the S-wave A_S=22%, while for the P-wave A_P=25%. Although for olivine the anisotropy of P and S waves are similar, they can differ greatly for the other minerals. Other important minerals range from nearly isotropic to extremely anisotropic. One of the most isotropic minerals is garnet, where A for both P and S

waves is ≤ 1%. At the other extreme, mika has an A value of up to 60% for P waves and 116% for S waves.

Transverse isotropy and azimuthal anisotropy

The S-wave behaviour in isotropic homogeneous media is remarkably simple, but greater complexity arises in anisotropic media. In an anisotropic, homogeneous medium, two independent body waves, that have orthogonal planes of particle motions, are generated. These are usually called quasi-compressional waves (qSV and qSH). In general, the propagation direction of these waves is not perpendicular to their wavefronts, so the particle motions differ from isotropic behaviour. The velocities of these waves vary with the trajectory of the wave through the medium with respect to any axes of symmetry in the structure.

When the symmetry axis is vertical, which is the common situation in Earth structures, it results in the so-called transverse isotropy (also known as radial anisotropy, axisymmetry, and cylindrical symmetry), that occurs for a stack of layered materials. Transverse isotropy may be referred to as an hexagonal symmetry systems with five independent elastic constants, and for which the matrix form is:

$$c_{mn} = \begin{bmatrix} A & A-2N & F & 0 & 0 & 0 \\ A-2N & A & F & 0 & 0 & 0 \\ F & F & C & 0 & 0 & 0 \\ 0 & 0 & 0 & L & 0 & 0 \\ 0 & 0 & 0 & 0 & L & 0 \\ 0 & 0 & 0 & 0 & 0 & N \end{bmatrix}$$

The matrix gives the velocities' waves propagating in different directions. In the case of propagation in X_1 direction, analogue to isotropic case, A corresponds to $\lambda + 2\mu$ for the X_1 direction, N corresponds to μ for the X_2 direction and L corresponds to μ for the X_3 direction. Thus the velocities for P-waves and S-waves are expressed as:

$$P_1 = \sqrt{\frac{A}{\rho}}\ , \qquad S_1 = \sqrt{\frac{N}{\rho}}\ , \qquad S_2 = V\sqrt{\frac{L}{\rho}}$$

However, for S-wave propagation the speed depends not only on the polarization, but also on the propagation direction. So, in the case in which the propagation is along the X_1 direction in the plane of layering, the S waves split into two waves, one travelling faster than the other. The same situation occurs when the propagation is along the X_2 direction. In contrast, when the propagation is along the X_3 direction, both S velocities are equal to S_1 (Figure 2.2a and b).

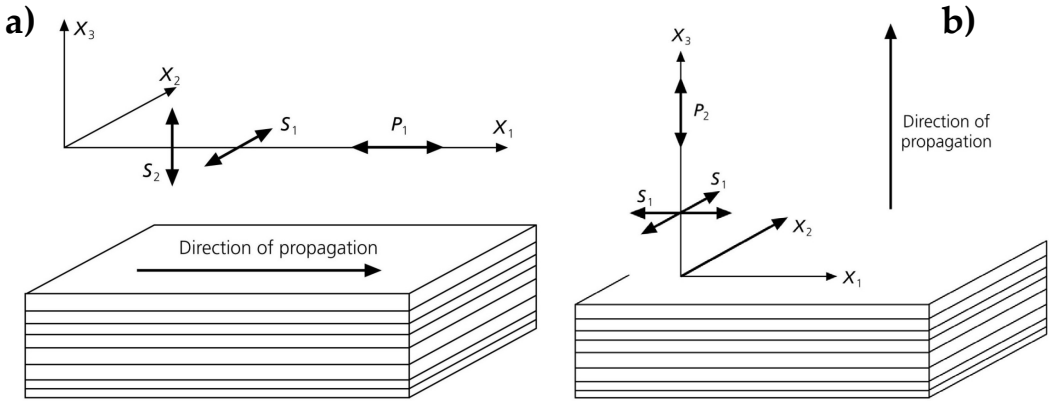

Figure 2.2 - The effects of transverse isotropy due to layering (a) In the case of P and S wave propagating in the X_1 direction, parallel to the plane of layering, the velocity S_1 is faster than S_2. (b)By contrast in the case of direction of propagation in X_3 direction, perpendicular to the plane layering, the velocity P_2 is generally less than P_1 and both shear waves have the same velocity S_1 (after Stein and Wysession, 2003).

Figura 2.2 – Esquema del efecto de la isotropía transversal en un medio estratificado. a) En el casoen el que la dirección de propagación de las ondas P y S es según X_1, paralela al plano de estratificación, la onda S se separara en dos componentes que viajarán con velocidad S_1 más rápida que la S_2. b) En el caso que la propagación sea según X_3, perpendicular al estratificación; entonces las dos ondas S tendrán velocidad S_1, mientras que la onda P_2 será mas lenta que la P_1 (Stein and Wysession, 2003).

If the medium exhibits direction dependence of velocity in the horizontal surface, the behaviour is called azimuthal anisotropy. One way to obtain this is to have transverse isotropy with the X_3 axis turned horizontally (Figure 2.3a and b). Azimuthal anisotropy can result in crystal structures or in macroscopic effects as layering or fluid-filled cracks.

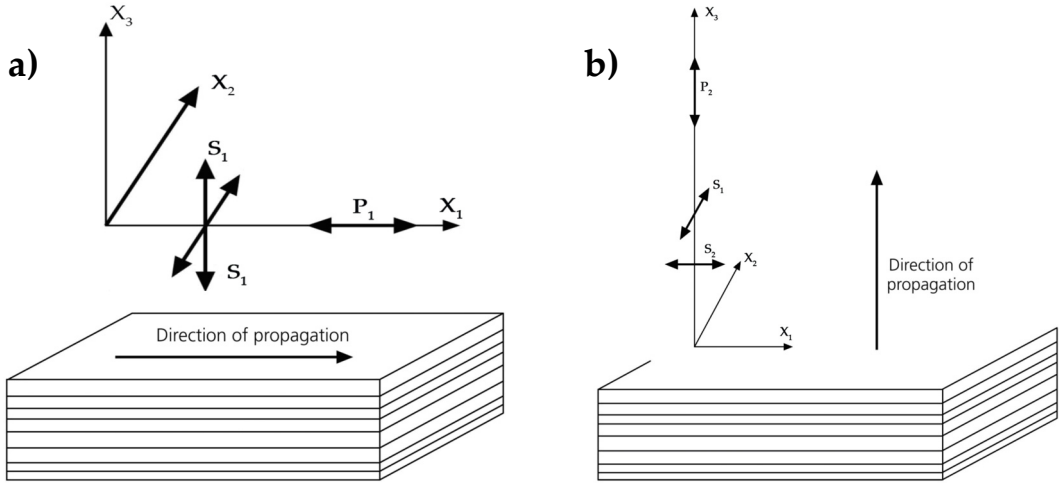

Figure 2.3 – The effects of azimuthal anisotropy due to layering with horizontal symmetry axis. It is the same situation as Figure 2.2 but rotated 90°. a) In the case of P and S waves propagating in the X_1 direction, parallel to the plane of layering, the velocity S_1 is faster than S_2. By contrast, in the case of propagation in X_3 direction, perpendicular to the plane layering, the velocity P_2 is generally less than P_1 and both shear waves have the same S_1 velocity (modified after Stein and Wysession, 2003).

Figura 2.3 - Esquema del efecto de anisotropía azimutal en capas estratificadas con eje de simetría horizontal. Es la misma situación de la Figura 2.2 rotada 90°. a) En el caso que la dirección de propagación de las ondas P y S sea según la dirección horizontal X_1. Entonces, la onda S se separara en dos componentes que viajaran con velocidad S_1 más rápida que la S_2. b) En el caso que la propagación sea según X_3, perpendicular a la estratificación, entonces las dos ondas S tendrán velocidad S_1, mientras que la onda P_2 será mas lenta que la P_1 (modificado de Stein and Wysession, 2003).

For fluid-filled cracks in a region with significant melt which are parallel to the X1 axis, the anisotropy is given by the matrix

$$c_{mn} = \begin{bmatrix} \lambda+2\mu & \lambda & \lambda & 0 & 0 & 0 \\ \lambda & \lambda+2\mu & \lambda & 0 & 0 & 0 \\ \lambda & \lambda & \lambda+2\mu & 0 & 0 & 0 \\ 0 & 0 & 0 & \mu & 0 & 0 \\ 0 & 0 & 0 & 0 & \mu(1-\varepsilon) & 0 \\ 0 & 0 & 0 & 0 & 0 & \mu(1-\varepsilon) \end{bmatrix}$$

Where ε is the crack density given by $\varepsilon = Na^3/V$, N is the Number of cracks in the volume V, and a is the half-width of a crack. If the cracks become infinitely small, ε=0, yielding the isotropic case.

2.2 What cause the seismic anisotropy: SPO and LPO

The causes of seismic anisotropy in the crust and mantle are still under significant debate. The two primary candidates are the shape-preferred orientation (SPO) and the lattice-preferred orientation (LPO) of Earth material, created as a consequence of tectonic forces, both of which have also been used to explain anisotropy in the lower mantle (e.g. Garnero, 2000; Kendall, 2000).

2.2.1 Shape-preferred orientation - SPO

The shape preferred orientation is anisotropy taking the form of aligned inclusions or periodic layering of material with contrasting elastic properties. SPO is the primary mechanism for crustal anisotropy and can result from fluid-filled cracks due to responses to stress (e.g. Crampin et al., 1984); while in the mantle, SPO may be generated by melt-filled cracks or lenses or compositional lamellae (Figure 2.4) (e.g. Kendall, 1994, 2000; Walker et al., 2004).

In seismic context, when a seismic wavefront (mainly shear waves) passes through a SPO medium, a splitting wave phenomena occurs, where the fast polarization direction coincides along the long axis or plane of structures, such as tubules or lenses (Figure 2.4). According to the direction of faster velocity material (Fermat's principle), the degree of anisotropy is proportional to the magnitude of velocity contrasts and the relative volumes of fast and slow components in the matrix material (Kern et al., 1981).

In Figure 2.4, there are two situations of SPO materials with strongly varying seismic velocities (e.g. Kendall and Silver, 1996; Wysession et al., 1999). SPO can involve a great variety of geometries as in the Figure 2.4 from sheets to lenses.

SPO is thought to be a significant cause of seismic anisotropy beneath mid-ocean ridges and perhaps some portions of subduction systems. Similarly, continental rift zones contain a range of evidence suggesting that SPO due to decompression melting plays an important role in the development of seismic anisotropy. Beneath stable continental interiors with thick lithospheres, however, SPO is usually

perceived as a local crustal phenomenon with less broad-scale influence in most seismic anisotropy observations.

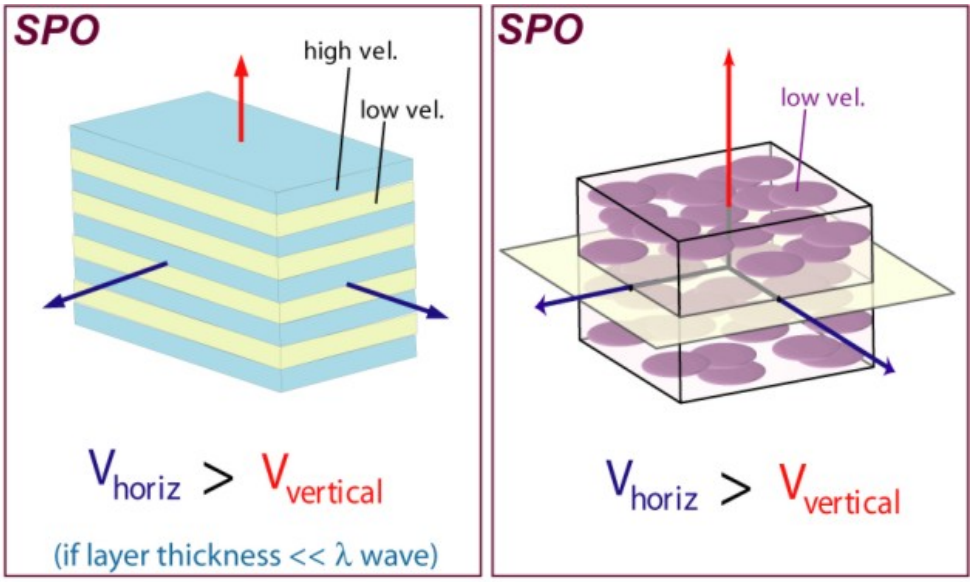

Figure 2.4 - Different causes of anisotropy SPO and wave velocity propagation in the medium, where $V_{vertical}$ represents the shear velocity in the vertical direction and V_{horiz} represents the velocity in the horizontal (after Moore et al., 2004)

Figura 2.4 – Anisotropías SPO y velocidades de propagación de las ondas de cizalla polarizadas. $V_{vertical}$ representa la velocidad de la onda de cizalla en al dirección vertical y V_{horiz} representa la velocidad de la onda de cizalla en la dirección horizontal (según Moore et al., 2004)

2.2.2 Lattice preferred orientation - LPO

Lattice preferred orientation, or alignment of intrinsically anisotropic crystals, is due to deformation. LPO of olivine is well-documented as the primary mechanism for upper mantle anisotropy.

Figure 2.5 shows the crystals with a vertical hexagonal symmetry axis, oriented by shear flows, to have lattice-preferred orientation (LPO). This situation can produce splitting in a similar way to SPO splitting. In the case in which $V_{horiz} > V_{vertical}$, radial anisotropy occurs; where $V_{vertical}$ represents the shear velocity in the vertical direction and V_{horiz} represents the velocity in the horizontal.

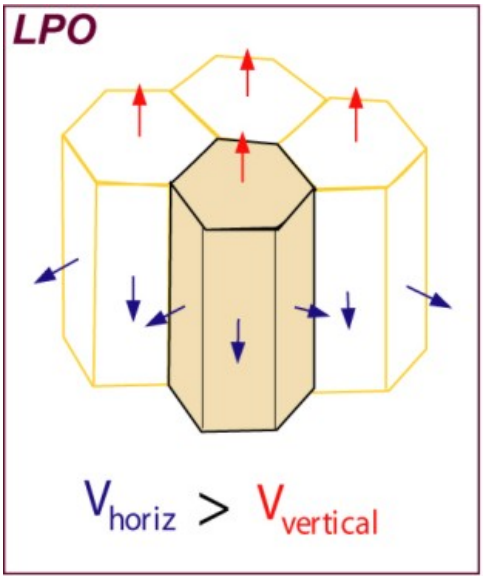

Figure 2.5 – LPO anisotropy and wave velocity propagation in the medium, where $V_{vertical}$ represents the shear velocity in the vertical direction and V_{horiz} represents the velocity in the horizontal direction (after Moore et al., 2004)

Figura 2.5 – Anisotropía LPO y velocidades de propagación de las ondas de cizalla polarizadas. $V_{vertical}$ representa la velocidad de la onda de cizalla en al dirección vertical y V_{horiz} representa la velocidad de la onda de cizalla en la dirección horizontal (según Moore et al., 2004)

LPO anisotropy requires low temperature and high stress. The type and extention of strain influence the anisotropic fabric, therefore, the relation between strain and mineral is quite complicated. It is generally believed that a key cause of seismic anisotropy in the crust and the mantle is the LPO, and the main mechanism causing the LPO is the dislocation creep, which is the motion of crystalline dislocations within grains (e.g. Nicolas and Christensen, 1987; Karato, 1987). This orientation is a consequence of deformation mechanisms which acted, deforming a rock depending on mineral type and conditions of deformation.

Observation of large scale seismic anisotropy at shallow depths is commonly explained as a preferred orientation of the [100] crystallographic axis of olivine crystals by tectonic processes.

The interpretation of seismic anisotropy at other depths is more difficult. In the asthenosphere it is often taken as a manifestation of present day convective flow, as opposed to frozen in anisotropy at shallower depths.

The detection of seismic anisotropy should, however, not be taken as a direct estimation of mantle flow as the fast axis of the anisotropy is not necessarily aligned

with the flow direction. Ribe (1989) demonstrated that flow direction and LPO are only simply related in a few places: above subducted slab, beneath the lithosphere and in boundary layers. Montagner (1998) therefore proposed to associate the layers of the mantle where seismic anisotropy is observed with boundary layers. Further complications can also arise from the water content of olivine-rich crystals, since it can modify the relation between flow geometry and seismic anisotropy (Jung and Karato, 2001).

2.3 Where the anisotropy is located in the Earth

The upper mantle probably contributes most to the delay times observed in teleseismic phases. Debate continues over whether anisotropy is confined to the upper 200 km beneath the mantle or continues through to the transition zone (Savage, 1999). Montagner (1994) defined that much of the upper mantle, above 400 km, is known to be anisotropic.

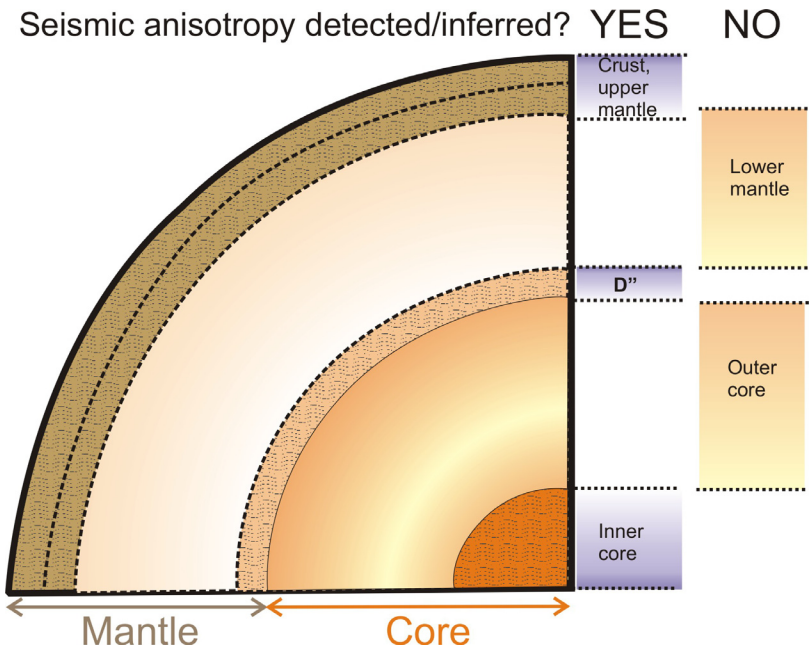

Figure 2.6 - In this scheme are represented in which parts of the Earth the seismic anisotropy is inferred: http://garnero.asu.edu/research_images/images_all.html.

Figura 2.6 – En este esquema se representa las zonas del interior de la Tierra donde se detecta anisotropía. (Garnero http://garnero.asu.edu/research_images/images_all.html).

Petrophysical analyses of mantle minerals and rocks (Mainprice et al., 2000; Mainprice et al., 2005) suggest that anisotropy lies in the uppermost 400 km of the Earth. Recent theoretical studies using finite-frequency sensitivity kernels provide similar conclusions since SKS splitting are shown to be more sensitive to the upper mantle above the transition zone than to the lower mantle (Sieminski et al., 2007). Samples of the Earth's mantle rocks are found in the surface in forms of ultramafic massif, xenolithis in basaltic or kimberlitic volcanics and as inclusions in diamonds (Mainprice et al., 2000) (Figure 2.6). However, samples from depths greater than 220 km are extremely rare.

A good knowledge of the distribution of the anisotropy with depth is essential to understand its origin, although determining the vertical location of the anisotropic layer(s) is always challenging since the splitting of SKS phases may occur somewhere between the core-mantle boundary and the station. Other phases such as local S (e.g. Bowman et al., 1987) may help to constrain the anisotropy distribution beneath a station, but they require the presence of nearby seismogenic zones. If one assumes that the crust may contribute only a few tenths of a second to the total SKS splitting (Barruol et al., 1993; Crampin and Booth, 1985), these arguments suggest that the anisotropy lies primarily in the subcrustal upper mantle. On the other hand, variations in the splitting parameters often observed on a scale of a few hundred kilometres (Vinnik et al., 1989; Makeyeva et al., 1992; Sandvol et al., 1992; Savage and Silver 1993; Helffrich et al., 1994) appear to rule out the contribution of the lower mantle (Alsina et al., 1995). The causes of anisotropy at the D'' layer and in the solid core remain controversial.

It is, however, not clear whether the anisotropy lies within the lithosphere and is related to a 'frozen' deformation (Silver and Chan, 1988), or within the asthenosphere and is thus related to present-day plate motion (Vinnik et al, 1992). This question can be addressed by SKS splitting only indirectly since these observations only weakly constrain the depth of anisotropy within the upper mantle. On the other hand, this question can in principle be resolved combining SKS observations with other geophysics observations.

However, the origin of anisotropy beneath continental regions is currently a topic of much debate and is yet to be resolved. It is still a matter of controversy as to whether the observed effects of anisotropy are primarily an effect of present-day

asthenospheric flow beneath an isotropic plate (Vinnik et al., 1992), are due mainly to 'fossil' lithospheric fabric formed in past tectonic events (Silver and Chan, 1991; Silver, 1996) or arise from a combination of processes.

Measurement and interpretation of shear wave splitting for phases that traverse the upper mantle has shed light on past and present deformation processes in a variety of tectonic settings, including subduction zone, rift zones, strike-slip faults and among other tectonic settings.

2.3.1 Anisotropy in the D" layer

Most of the lower mantle seems to be isotropic except the D'' layer (Vinnik et al., 1989; Maupin, 1994). The D'' layer, extending 250- 300 km above the boundary between the core and mantle in some regions, was only recently discovered (Lay and Helmberger, 1983) and is therefore just beginning to be characterized.

Shear wave splitting measurements have been undertaken across a very wide range of tectonic environments across the continents using data from both permanent and portable stations and, with a more limited range of measurements, on oceanic islands. The presence of such shear wave splitting indicates passage through a zone of anisotropy on the way to the receiver, but does not provide direct evidence of the location of this zone. The most likely scenarios are then at the base of the mantle (in the D'' layer) or in the upper part of the mantle.

There are a number of studies that suggest the presence of anisotropy in D'', but only for waves which have spent a long time in this region, e.g., diffracted waves (Maupin, 1994) or wide-angle ScS reflections (Young and Lay, 1990). SKS and SKKS pass through D'' nearly vertically and so do not spend long periods of time in this region.

As shown in Figure 2.7 the anisotropy in the D'' layer is related to the SPO, where the flow oriented the melt pocket of the medium.

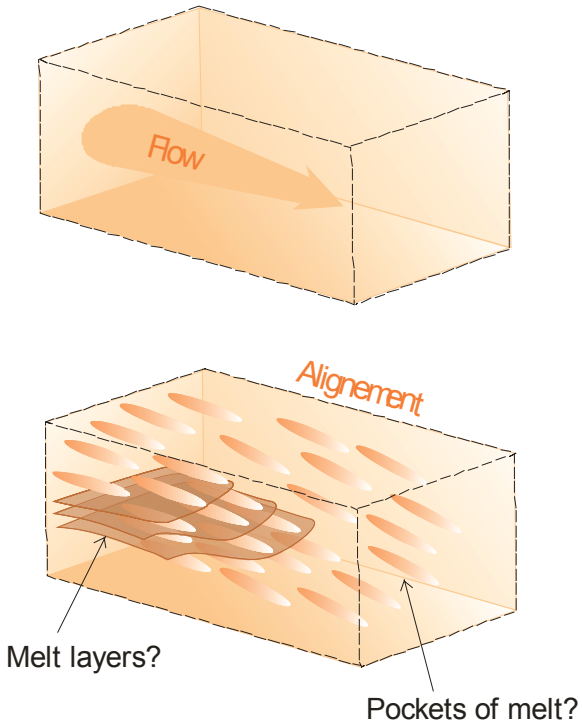

Figure 2.7– SPO in a medium. Flow direction oriented the structure inside the medium (Garnero web http://garnero.asu.edu/research_images/images_all.html)

Figura 2.7– Esquema de formación de SPO. La dirección de flujo orienta la estructura en el medio (Garnero web http://garnero.asu.edu/research_images/images_all.html).

2.3.2 Anisotropy in the upper mantle

Most of the lower mantle (below 660km) appears to be isotropic. A transition zone, which plays a key role in mantle dynamics, exists above it. This zone is described for a discontinuity which might inhibit the passage of matter between the upper and lower mantle (Montagner, 1998). Vinnik and Montagner (1996) modelled the upper mantle as anisotropic above 320 km, as isotropic between 320 and 580 km, and as low anisotropy (with 3%) between 580 and 620 km.

The upper mantle (up to 410 km from the surface) is composed primarily of three anisotropic and volumetrically important phases: olivine, enstatite (orthopyroxene) and diopside (clinopyroxene). Olivine ($(Mg_{0.9}Fe_{0.1}O)_2\ SiO_4$) is more strongly anisotropic than other minerals and it aligns under the prevalent deformation of dislocation-creep type (Nicolas and Christensen, 1987), hence mantle anisotropy results primarily on the lattice preferred orientation of olivine (Figure 2.8).

A common assumption in anisotropy studies is that the crystallographic symmetry axis is either vertical or horizontal. On the other hand, a number of studies indicate that an axis with a tilted orientation is needed to explain observations of teleseismic waves (Babuska et al., 1993; Levin et al., 1996; Grésillaud et al., 1996). Crustal overthrusting is another likely cause of tilted-axis anisotropy. So shear wave splitting measurements can characterize the orientation and the depth extent of the mantle strain field (Savage, 1999), the fast direction relating to the orientation of the mantle strain field.

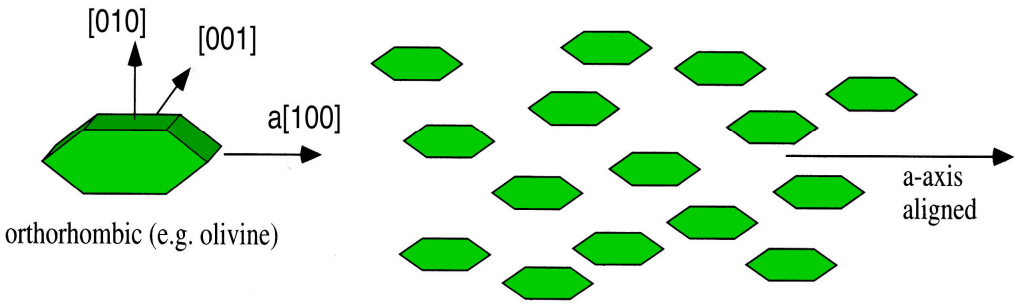

Figure 2.8 – Hexagonal anisotropy can result from aligned olivine crystals (Shearer, 1999)

Figura 2.8 – La anisotropía hexagonal puede resultar de la alineación de los cristales del olivno

2.3.3 Anisotropy in the asthenosphere

Paragraph 2.2.2 discussed how LPO in olivine aggregates generate by relative motion between the Earth's surface plates and underlying mantle. Thus as this fabric is developed with the evolving mantle flow field, observations of seismic anisotropy can constrain asthenospheric flow patterns if the contribution of fossil lithospheric anisotropy is small (Conrad et al., 2007).

The simplest model to explain the development of olivine crystal preferred orientations (CPO), invokes shearing of the sublithospheric mantle in response to a velocity gradient between the plate, rigid lithosphere and the asthenosphere. Progressive cooling of the plate freezes the CPO within the plate and results in deepening of the shear zone. This process aligns the olivine [100] axes, parallel to the flow direction of the mantle, and therefore the fast polarization of the split shear waves will be parallel to the absolute plate motion (APM) direction (Figure 2.9). In

this model, the observed delay time should thus increase with lithospheric age (Tommasi, 1998).

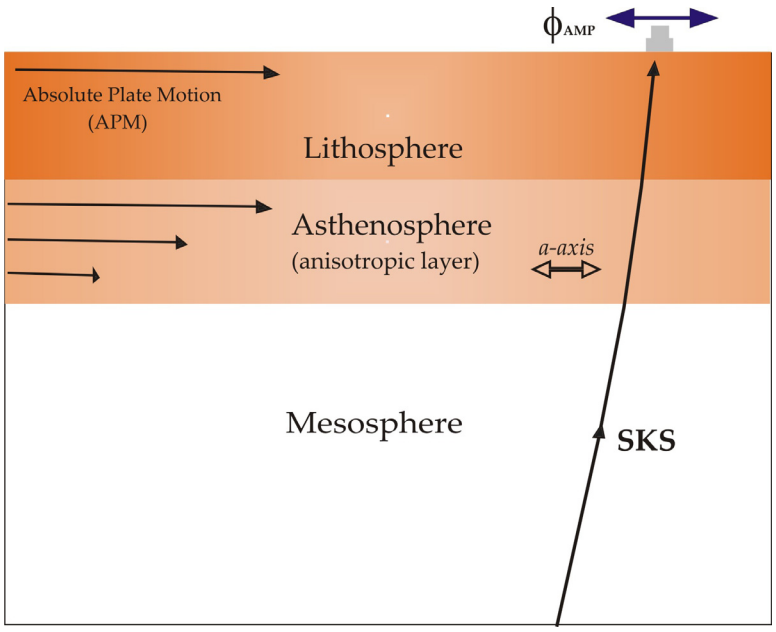

Figure 2.9 - Simple asthenospheric flow (after Silver, 1996)

Figura 2.9 – Flujo astenosférico simple (según Silver, 1996)

2.3.4 Anisotropy in the lithosphere

Many continental regions exhibit splitting patterns that appear closely related to superficial geologic features. On the basis of this observation, some studies suggest that anisotropy exists largely in the lithosphere and is related to surface features that were generated by the most recent significant tectonic event (Silver, 1996; Barruol et al., 1997b). In this model, the most recent significant tectonic event controls the character of splitting in the lithosphere.

When crust and subcontinental mantle are deformed coherently in orogenies it results in the so-called case of Vertical Coherent Deformation (VCD). In that case, the last penetrative episode prevails. Spatial variation of splitting parameters on a small scale should track geological variations, and in that case, fast directions are close to the surface's geological features such as faults and regional foliation trend (Figure 2.10).

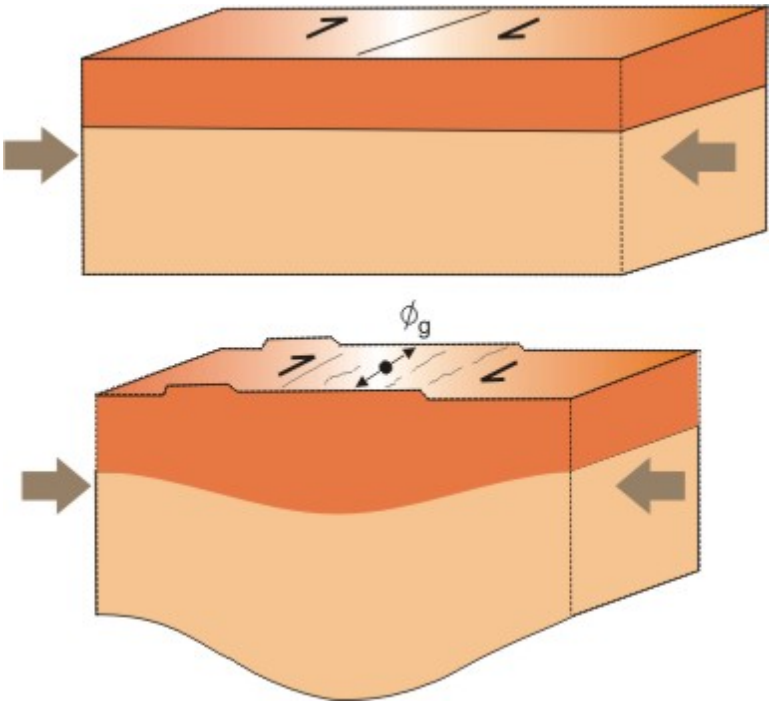

Figure 2.10 - Vertical Coherent Deformation of crust (orange) and mantle (salmón) by transpression event (after Silver, 1996).

Figura 2.10 - Deformación coherente vertical de la corteza (anaranjada) y del manto (salmón) debido al efecto de transpression (modificado de Silver, 1996).

Vauchez and Nicolas (1991) suggested that the coherent deformation of the subcontinental lithospheric mantle acquired during tectonic episodes, such as mountain building or continental disruption, may therefore explain the observed delay times.

2.3.5 Anisotropy in the crust

The vast majority of crustal anisotropy is caused by cracks, and microcracks, and the presence of fluid in them in the upper 10- 15 km of the crust (e.g. Kaneshima et al., 1988; Crampin, 1994), with a contribution from 0.04 to 0.2 sec to the splitting. Alternating thin isotropic layers of higher and lower velocity can also produce an overall anisotropic efect (Backus, 1962; Helbig, 1993), with the velocities normal to bedding are slower than along it (Figure 2.11). The strongest influence is believed to be that of aligned cracks and/or pore spaces (Babuska and Pros, 1984; Crampin, 1991b; Crampin, 1994). The aspect ratio of pore/cracks and the presence of fluid in

them determine the extent and proportion of anisotropy (Hudson, 1991; Crampin, 1984; Crampin, 1991a). Between 10 and 15 km depth, the pressure is like 200-300 MPa and measurements in a laboratory have shown that anisotropy disappears due to the closure of cracks in response to increasing overburden pressure (e.g. Babuska and Pros, 1984; Kern, 1990; Kern, 1993). Below this depth, crustal anisotropy is probably caused by other phenomena, for example minerals aligned during ductile flow of the lower crust.

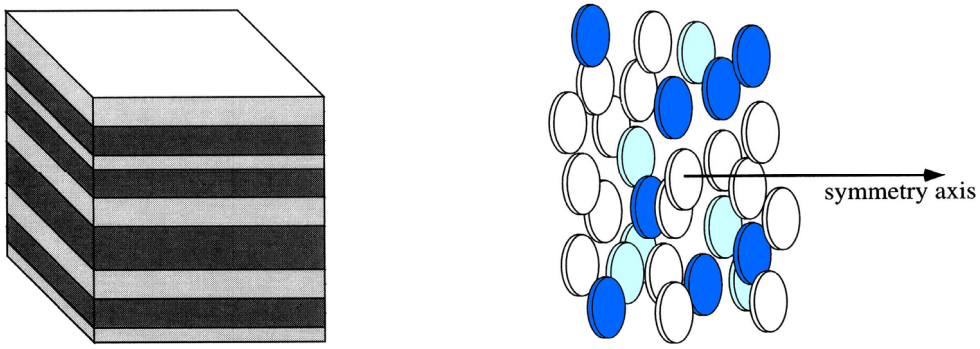

Figure 2.11 - a) Horizontal alternating layers of fast and slow material, and b) randomly distributed cracks with a preferred orientation (after Shearer, 1999).

Figura 2.11 - a) Alternancia de capas horizontales entre materiales rápidos y lentos y b) grietas distribuidas aleatoriamente con una orientación preferente (según Shearer, 1999*).*

For teleseismic shear wave splitting, crustal rocks may contribute little to splitting because foliation planes within the crust are usually horizontal, and with vertical propagation of teleseismic phases, the splitting is expected to be small (Barruol et al., 1996). Barruol (1993) and Barruol and Mainprice (1993) noticed a strong correlation between the orientation of the foliation and the amplitude of the delay time. Maximum delay time is systematically observed for waves propagating parallel to the foliation. Furthermore, the fast shear wave is polarized parallel to the foliation plane.

2.3.6 Anisotropy in subduction zone

In subduction zones (e.g. Pozgay et al. 2007; Ando et al., 1983; Russo and Silver, 1994; Fouch and Fischer, 1996; Sandvol and Ni, 1997; Fischer et al., 1998; Smith et al., 2001; Anderson et al., 2004; Currie et al., 2004), a complex 3D pattern of mantle flow

is present, and so the interpretation of anisotropy can be controversial since different factors can be considered. That is, for example the geometry of the zone, a slab rollback may cause toroidal mantle flow beneath the region as is in the Calabrian arc (Civello and Margheriti, 2004; Baccheschi et al., 2007) (Figure 2.12).

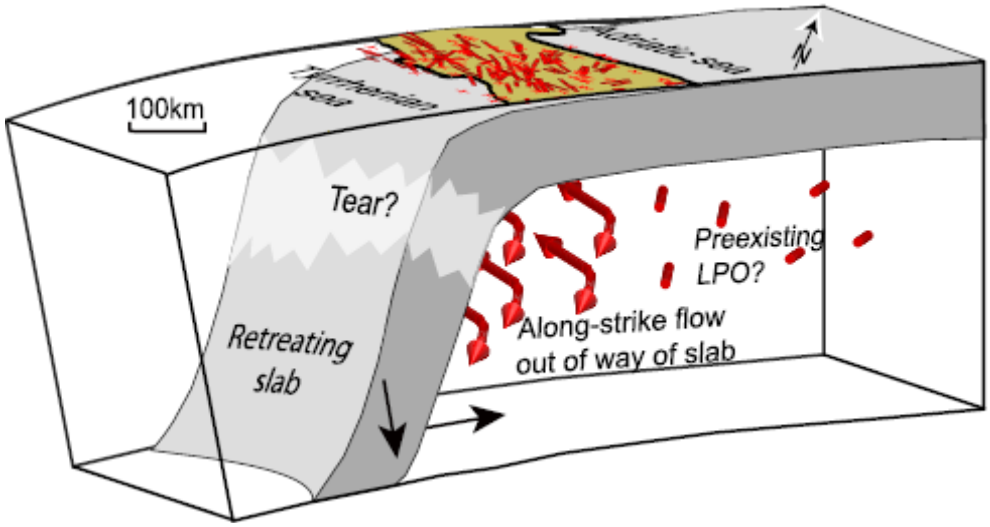

Figure 2.12 - Model presented by Baccheschi et al. (2007) to explain the inferred anisotropic directions.

Figura 2.12 – Modelo presentado por Baccheschi et al. (2007) para explicar las direcciones de anisotropías.

Another factor that can be a key cause of anisotropy in subduction zones is the presence of water, and perhaps other volatiles, which can alter the relative strengths of olivine slip planes and change how it deforms. Thus, interpreting seismic anisotropy in regions of abundant volatiles, such as in the mantle wedge of island-arc subduction zones, may be complicated (Jung and Karato, 2001; Karato, 1987). Nevertheless, laboratory results have shown that when olivine aggregates are deformed under high-stress, low-temperature and water-rich conditions, the fast axes of individual olivine crystals tend to align 90° from the flow direction (Jung and Karato, 2001). These B-type olivine fabrics, in conjunction with trench-perpendicular flow in the mantle wedge, may explain trench-parallel fast directions in some regions (Karato, 2003; Kneller et al., 2005). It is not clear, however, if the stresses, temperatures and volatile concentrations, needed to produce B-type olivine fabric, are relevant to large volumes of the mantle wedge. Moreover, the commonly used assumption of infinite strain (and thus the neglect of strain history) may not

always be adequate (Kaminski and Ribe, 2002). Consequently, interpretations of splitting measurements are non-unique and rarely uncontroversial (e.g. Park et al., 2002; Wiens and Smith, 2003).

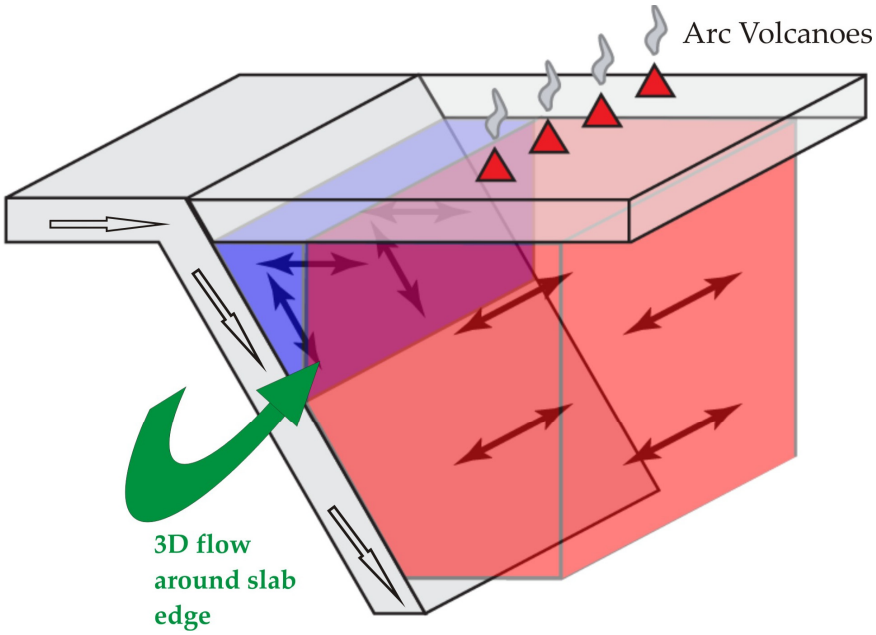

Figure 2.13 - General trend of anisotropy in subduction-zone. Blue arrows show arc-normal a-axes in the shallow wedge corner, red arrows show arc-parallel a-axes deeper and beneath the arc (modified after Abt).

Figura 2.13 - Esquema general de orientación de la anisotropía en zonas de subducción. Las flechas situadas en la banda azul representan la situación cuando la orientación de anisotropía es perpendicular a la zona de contacto y las situadas en la banda roja cuando es paralela (modificado de Abt).

Both trench-parallel and trench-perpendicular fast directions (Figure 2.13) have been observed in subduction zone settings, but trench-parallel fast directions (that is, perpendicular or at a large angle to the convergence direction) seem to be more common and have been observed or inferred in New-Zealand (Marson-Pidgeon et al., 1999), in Aleutians (Yang et al., 1995; Mehl et al., 2003), in Japan (Fouch and Fischer, 1996), in Tonga (Fischer and Wiens, 1995) and in South America, among other regions. Trench-normal fast polarization has been recorded in the back-arc of the Kuriles and Pacific Northwest (Russo and Silver, 1994) (Figure 2.14). However, many of the measurements used lack depth resolution because the pertinent waves propagate nearly vertically through the upper mantle.

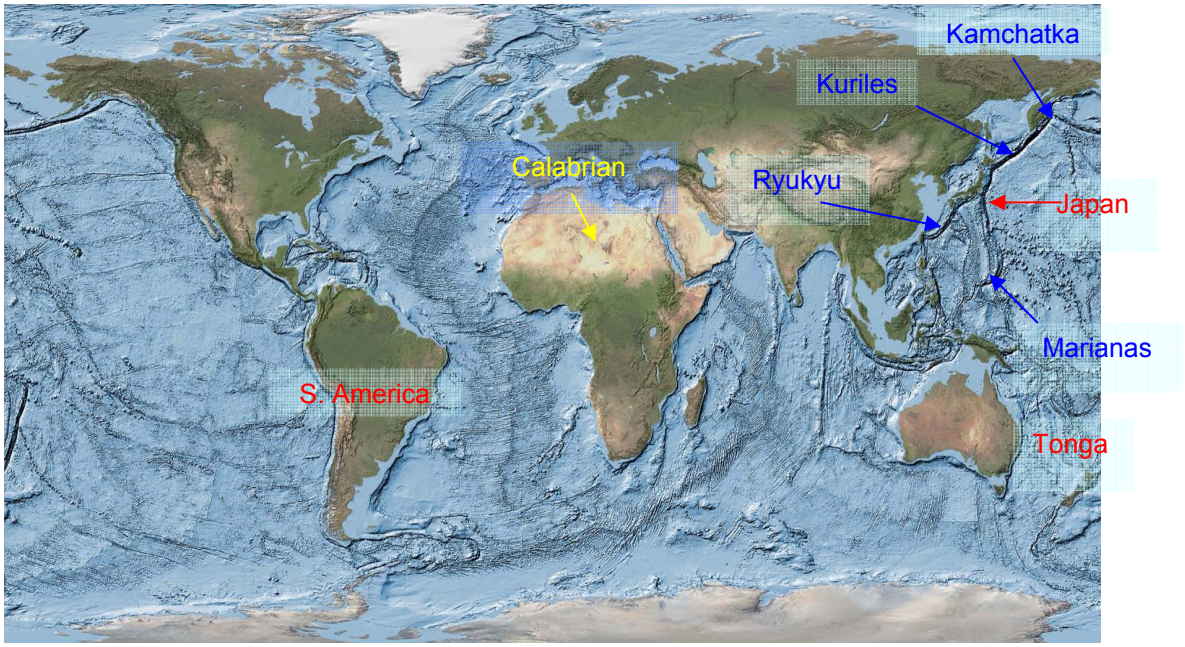

Figure 2.14 – Summary of the main regions where shear wave splitting measurements have been obtained, the name marked in red are related to trench-parallel ϕ, the white are trench-normal ϕ and yellow is region with toroidal geometry.

Figura 2.14 – Principales regiones donde se han hecho medidas de desdoblamiento de las ondas de cizallas, los nombres en rojo indican las zonas donde la dirección de ϕ es paralela al surco, los nombre en azul donde la dirección de ϕ es perpendicular al surco, en amarillo la región con geometría toroidal.

Because of the ambiguity of which processes are contributing to the observed anisotropy and because shear wave splitting is a path-integrated measurement with generally poor depth resolution, the interpretation of shear wave splitting measurements in subduction zone settings remains an area of controversy. Regardless, the dynamic recrystallization of olivine, that is required for interpreting observations of anisotropy in terms of mantle flow, is neglected in these models. In fact, experiments conducted by Zhang and Karato (1995) show that at a large strain, the mean of axis orientation no longer follows the finite strain ellipsoid, but rotates more rapidly toward the shear direction. This evolution is accompanied by intensive dynamic recrystallization, sub-grain rotation (SGR) and grain boundary migration (GBM) (Zhang et al., 2000). The experiments of Nicolas et al. (1973) similarly indicate that the evolution of the lattice preferred orientation at large strains is controlled by dynamic recrystallization. In the convecting mantle, dynamic recrystallization is likely to control the lattice preferred orientation because the finite strains present are large (McKenzie, 1979).

2.3.7 Continental rift zone

Rifting processes have been classified as either passive or active based on the nature of the casual processes, which actually drive the lithospheric extension relative importance of the lithospheric versus sub-lithospheric events and the source of the extensional driving force. In passive rifting, extension and lithospheric thinning result from tensional stresses arising from the force distribution at plate boundaries (White and McKenzie., 1989). Whereas in active rifting, the interaction of actively upwelling asthenosphere with the lithospheric plates, and in this situation, the anisotropy is perhaps controlled by thin melt pockets directly beneath the rift zone (Kendall and Silver., 1996) rather than olivine alignment. Some examples are the Rio Grande Rift (Sandvol et al., 1997), the Basin and Range (Savage and Silver, 1996; Sheehan et al., 1997) and the East African Rift (Gao et al., 1997). Evidence for an active role of the structure of the lithosphere in the rifting process also comes from the observation that rift propagation is not random, but tends to follow the trend of the preexisting orogenic fabric of the plates, systematically reactivating ancient lithospheric structures (e.g. the Atlantic and West Indian Oceans, and the Rio Grande, Baikal, East African and Northeast China rifts) (Tommasi and Vauchez, 2001).

Indeed, seismic anisotropy beneath rifts may result from various processes: the pre-rift deformation may be responsible for an inherited crystallographic fabric in the lithospheric mantle; the deformation associated with the rifting may modify the older fabric and generate a new, rift-related crystallographic fabric in the lithosphere; the flow of asthenospheric mantle beneath the rift may also produce a preferred orientation of mantle minerals; and oriented melt pockets may develop in the asthenospheric wedge beneath the rift. To evaluate the respective contribution of these various processes and, hence, to predict the seismic anisotropy that may be observed beneath a continental rift, one needs to predict the effect of each of them. In addition, it is necessary to evaluate how efficient the upper mantle "memory" is, i.e., how long an anisotropic structure formed in the upper mantle may be preserved before being erased by subsequent processes (Vauchez et al., 2000).

2.3.8 Mid oceanic ridge

Upper mantle beneath mid-ocean ridge is also known to exhibit anisotropy at depths shallower than 200 km (Gu et al., 2005). Measurements of shear wave splitting in rift zones reveal, in most cases, that fast direction is observed to be parallel or sub-parallel to the spreading direction.

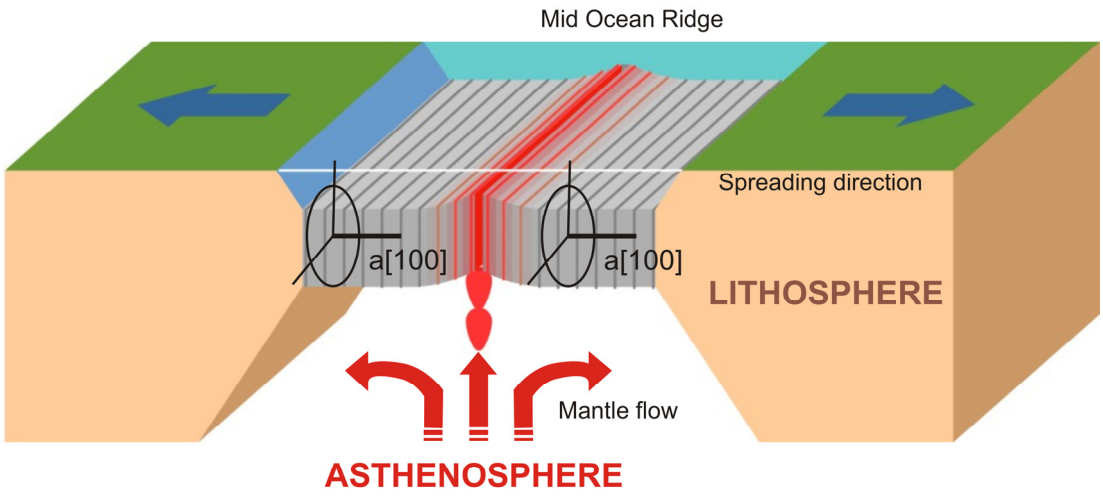

Figure 2.15 – Illustration of how the spreading process yields a preferred orientation of olivine crystals in the oceanic lithosphere, the fast axis velocity [100] is in the spreading direction (modified after Gu et al., 2005).

Figura 2.15 – La figura indica como el proceso de expansión produce la orientación preferencial de la estructura de los cristales de olivino en la litosfera oceánica. La dirección de eje rápido [100] está en la misma dirección que la expansión (modificado de Gu et al., 2005).

In the case of Pacific plate (Shimamura et al., 1983; Ishikawa, 1984), the anisotropic alignments are assumed to form at the interface between the lithosphere and the astenosphere (Babuska and Cara, 1992). The olivine orientation, in this model, vary with depth and the direction of [100] olivine axes in each layer represents the plate absolute motion at the time this layer was accreted to the lithosphere (Figure 2.15) (Babuska and Cara, 1992).

While, in the shallow crust, shear wave splitting is interpreted as an effect of structural anisotropy due to the presence of ridge-parallel cracks. In fact, in a study on the Juan de Fuca Rigde (North America), carried out for Almendros et al. (2000), it is shown that anisotropy is concentrated in the upper 1- 2 km.

2.3.9 Strike-slip faults

Strike-slip regions show that anisotropy should be particularly strong because the foliation will be vertical and ϕ direction should be near-horizontal and parallel to the strike-slip motion (Savage, 1999) (Figure 2.16). This situation is present for example in the Maoma Rift in Siberia (Vinnik et al., 1992), the northe of Tibet (Holt, 1999) and in the Alpine fault of New Zeland (e.g. Gledhill and Stuart, 1996).

The results along the San Andreas Fault are even more contradictory, where a model with two layers will explain the anomalous trend (Savage and Silver, 1993).

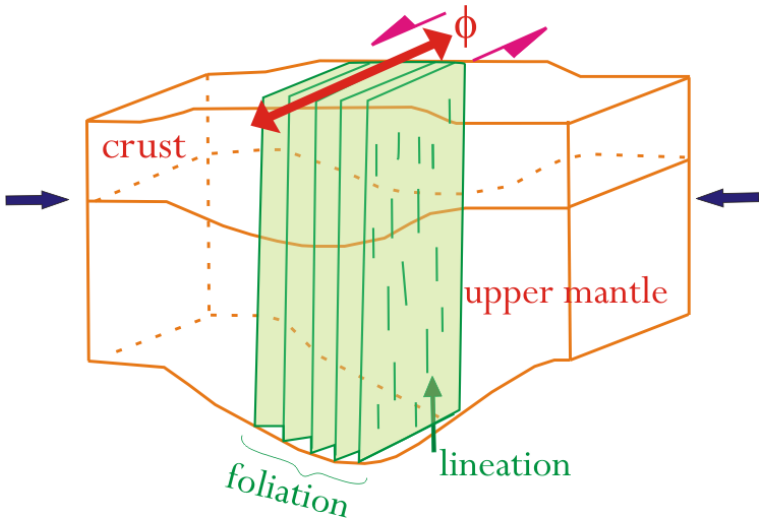

Figure 2.16 – Definitions of foliation and lineation and S wave splitting in orthorhombic and hexagonal media (modificated after Silver (1996) and Savage (1999)).

Figura 2.16 – Esquema de foliación y de alineación, y del desdoblamiento de la onda S en un medio ortorrómbico y hexagonal (modificada de Silver (1996) y Savage (1999)).

2.4 How detect seismic anisotropy

This section presents main wave-methods currently used to investigate seismic anisotropy in continental areas, which have better control on the depth distribution of anisotropy.

Figure 2.17 shows a sketch of raypaths and sampling regions for Pn, Ps receiver functions, body wave delay time, body wave shear wave splitting and surface wave (Fouch and Rondenay, 2006). Shaded areas represent sampling areas, including

Fresnel zone volumes, but are not to scale. We can note that Pn and surface waves sample lateral structure and therefore have better depth resolution, while body waves sample predominately vertical structure and therefore have better lateral resolution.

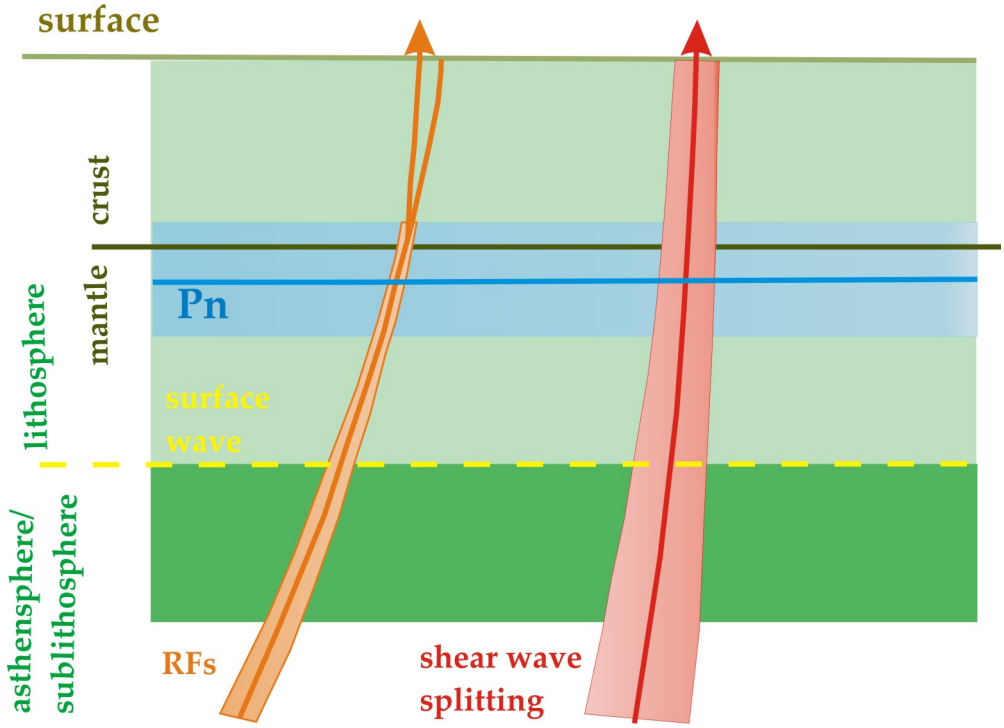

Figure 2.17 - Schematic raypaths and sampling regions for seismic phases (modificated after Fouch and Rondenay, 2006). For the explication see the main text.

Figura 2.17 – Esquema del trazado de rayos y zonas recorridas por las fases sísmicas (modificado de Fouch and Rondenay, 2006). Véase el texto.

2.4.1 P wave

The P*n* phase is a head wave which travels along the boundary between the crust and uppermost mantle (Moho) with a velocity close to 7.9 km/s. Variation in P*n* velocities are caused by changes in the physical parameters of uppermost mantle rocks, and can be changes in temperature and composition or the presence of water and volatiles. Hence, P*n* wave velocity is often used to infer uppermost mantle rheology. P*n* velocities are generally the highest in oceanic lithosphere and could reach up to 8.4 km/s (Walker, 1977). Continental lithosphere P*n* velocities, however, vary significantly depending on the rheology of the mantle lid. Generally, regions of

slower Pn (7.5-7.9 km/sec) are associated with regions of warm or absent mantle lithosphere or the presence of melt (e.g. Hearn 1999; Calvert et al., 2000).

With this type of analysis, information is obtained on two factors, the fast polarization direction of the P wave and the magnitude of anisotropy. The azimuthal variations in the time arrival are used to deduce the lateral variation in seismic anisotropy below the oceanic basin. This anisotropy is interpreted as being caused by deformation during the most recent thermotectonic event, and thus provides information on the process of mountain building, whereas tectonic stress and many structural features in the upper crust are usually oriented perpendicular to the structural axis of mountain belts and P*n* anisotropy is aligned parallel to the structural axis. These alignments are interpreted to indicate mountain-parallel ductile (i.e. creeping) deformation in the uppermost mantle, which is a consequence of mountain-perpendicular compressive stress (Meissner et al., 2002). Furthermore, fast orientations from the P*n* polarization tend to align parallel to the subduction zones and transform faults. Under continental cratons there is a general alignment of the fast orientation with absolute plate motion direction, comparable to that found in SKS splitting studies. Taking into account the sampling of the long-period P waves, these results are consistent with anisotropy influenced by lithospheric deformation at shallow depths as well as flow induced by plate motion at greater depth.

The advantage of Pn anisotropy analysis is that it provides a direct estimate of seismic anisotropy in the uppermost mantle, with limited uncertainty as to the depth location of the layers surveyed (Fouch and Rondenay, 2006).

The limitation of P*n* anisotropy analysis is not easily discernible if the anisotropy is due to seismic heterogeneity or to the aligned fabric.

Figure 2.18 shows an example of results obtained with the Pn method in the central of the Apennines (Italy). The SKS anisotropic results are also shown.

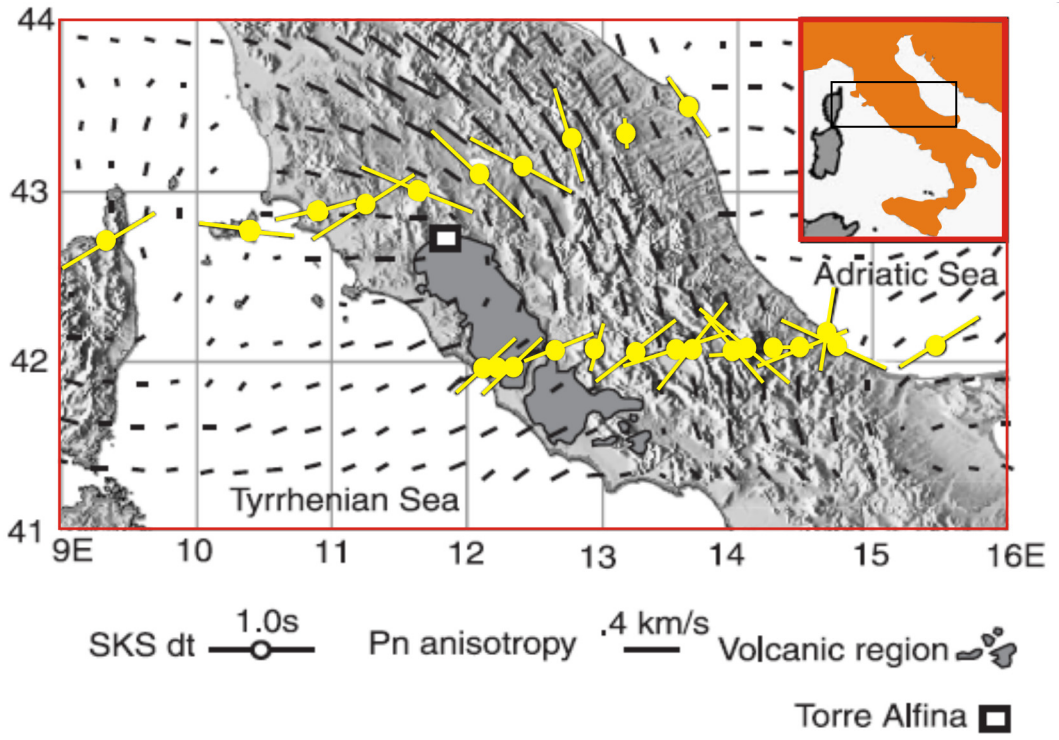

Figure 2.18 – Fast directions of Pn and SKS calculated in the north of Apennines (Pera et al., 2003).

Figura 2.18 – Direcciones rápidas de la fase Pn y SKS medidas en el Norte de los Apeninos (Pera et al., 2003).

2.4.2 S waves

The most common teleseismic shear waves used to measure seismic anisotropy are the S (e.g. Bowman and Ando, 1987) and the ScS (e.g. Ando, 1984), but both are not very useful in the continental areas as they require a nearby seismogenic zone (Silver and Chan, 1988) and the SKS result in a phase more useful and less ambiguous than the others. This phase travels through the mantle as an S wave, then is converted to a P wave at the outer core and converted back to an S wave when it passes back into the mantle, so there is no contribution from the source-side of the path (Figure 2.19 and Figure 2.20) Thus, it keeps information between the core-mantle boundary and the surface and has a near vertical mantle path so its initial polarization (radial) is known and is easier to interpret (Savage, 1999).

When an S-wave travels in an anisotropic medium, it will split into orthogonally fast and slow waves. This property is referred to as shear wave splitting or birefringence (Figure 3.1) and will be discussed in Chapter 3.

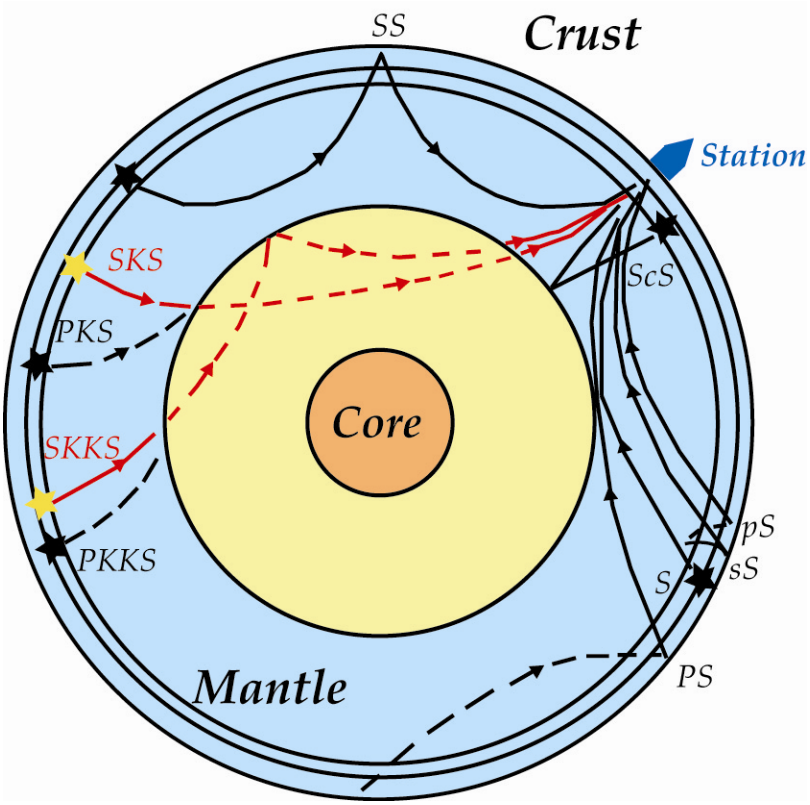

Figure 2.19 – Waves propagation in the Earth's interior (modified after Garnero web http://garnero.asu.edu/research_images/images_all.html).

Figura 2.19 – Propagacion de las principales fases de ondas sísmicas en el interior de la Tierra (modificado de Garnero web http://garnero.asu.edu/research_images/images_all.html *).*

Information about seismic anisotropy in the upper mantle just below a seismic station is obtained from the shear wave splitting, analog to the optical birrefringence. This phenomenon occurs when a shear wave travels in an anisotropic medium and it splits into two shear waves that are polarized orthogonally to each other and have different speeds.

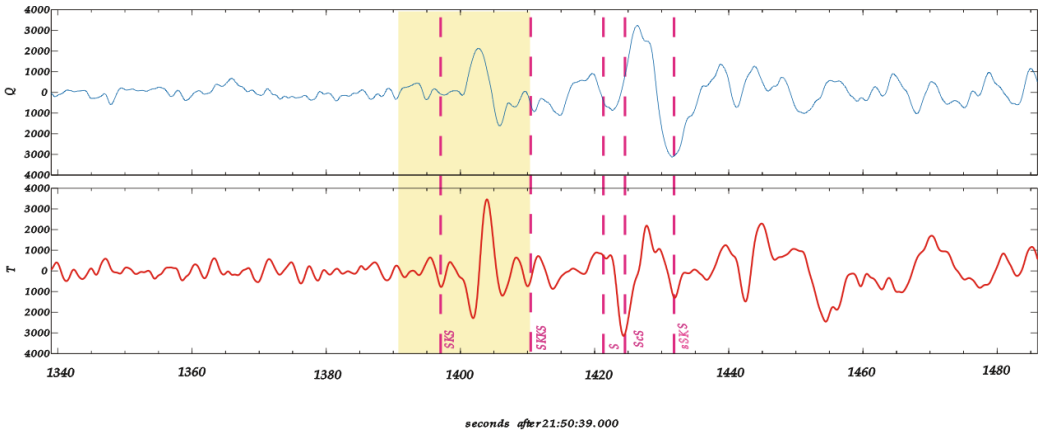

Figure 2.20 - Seismograms for PAB station, rotated in the radial and transversal (QT) components, utilized in this study, where the main phases shown in Figure 2.19 are presented.

Figura 2.20 - Sismogramas registrados en la estación PAB,rotados en las componentes radial y transversal (QT), utilizada en este trabajo, donde se pueden ver algunas de las fases presentadas en la figura 2.19.

2.4.3 Surface waves

Initial studies on upper mantle anisotropy could be observed on surface wave dispersion (e.g. Anderson and Harkrider, 1962; Anderson, 1966; Nataf et al., 1984; Montagner and Tanimoto, 1990), which have confirmed that azimuthal and SH/SV polarization anisotropy are global phenomena in the Earth's upper mantle, particulary in the top 200 km of the sub-continenatl mantle (Mainprice et al., 2000). Measurements on Love and Rayleigh wave dispersion curves showed that they could not be compatible with a unique isotropic model.

Surface waves propagate horizontally in the Earth's crust and upper mantle from a source to a receiver and are therefore sensitive to primarily shear wave structure at depths of approximately 1/3 of a given wavelength (Fouch and Rondenay, 2006). However, the long wave lengths limit the lateral solution (~400km) (Debayle at al., 2005).

Surface waves are also well suited for investigating upper mantle anisotropy. The azimuthal variation of phase velocity of surface waves led to the azimuthal anisotropy, it was observed initially on Rayleigh waves by Forsyth (1975) in the

Nazca plate. As example of this kind of studies, in Figure 2.21 a global map of anisotropic model at 200 km depth for Montagner and Tanimto (1991) is presented.

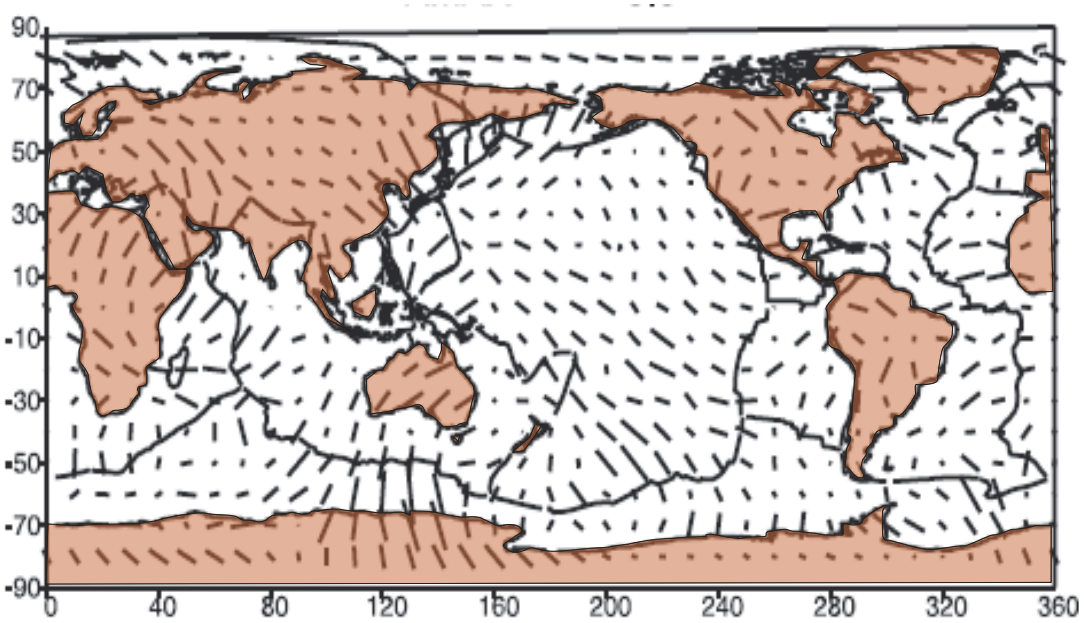

Figure 2.21 - Map of global anisotropic model for the SV wave velocity (Montagner and Tanimoto, 1991).

Figura 2.21 – Mapa del modelo anisotrópico del globo terrestre calcualdo mediante la onda sísmica SV (Montagner and Tanimoto, 1991).

2.4.4 Receiver functions

Seismic phases converted from P to S below the receiver are particulary useful in studies of the crust and mantle. The receiver function technique (RFs) has been used to investigate discontinuities in material proprieties of the subsurface, especially in the crust and upper mantle structure at a regional scale (e,g. Vinnik et al., 1997, Sandvol et al., 1998), given that the RFs present a response of the Earth's medium near a seismograph station to the excitation by either a P or S wave.

Generally, the signals in the transverse component of the receiver function are usually explained by lateral heterogeneity of the isotropic medium, and in particular, by dipping layers (Savage, 1998). By stacking receiver functions from different distances and directions, effects of lateral structural variation are suppressed and an average crustal model is obtained.

An example of the application of this method is presented by Roselli et al. (2008). They study teleseismic receiver functions in the northern Apennines, Italy, to distinguish the effects of azimuthal anisotropy from those of lateral heterogeneity, to finally reveal the crustal structure variations across the mountain chain. They identify the crustal-mantle transition located almost everywhere in the study area, and they record an S wave velocity, with velocity values typical for the sub-crustal mantle, that may indicate the locus where the subducting Adriatic plate starts to dip into the mantle.

3. Shear Wave Splitting of SKS phase: methods

During the last decades, seismological techniques have been developed to analyze the deep deformation of the Earth, and particularly the relation between plate tectonics and mantle flow as well as the internal deformation of the plate (e.g., Silver and Chan, 1988). The most popular technique uses the birefringence in anisotropic media that induces the splitting of shear waves and allows one to obtain quantitative information about seismic anisotropy in the upper mantle below a seismic station. The most useful seismological phase for studying shear-wave splitting is the SKS phase. From three-component seismic records, two parameters can be measured to quantify the: 1) the difference in arrival time δt between the two split waves anisotropy (that depends on thickness and the intrinsic anisotropy of the medium, and 2) the ϕ of the faster split shear wave polarization plane azimuth that is related to the orientation of the anisotropic structure. These parameters provide information on the nature of the rocks that the wave propagated through, and are highly dependent upon the geometry of the anisotropic material. Shear-wave splitting measurements can therefore characterize the orientation and to a lesser degree the depth extent of the mantle strain field (Savage, 1999).

Shear-wave splitting is routinely measured in teleseismic data and is used to probe the fabric of crust and mantle rocks (Silver, 1996; Savage, 1999; Kendall, 2000). The length scales of these observations vary from hundreds of kilometers for teleseismic SKS and direct S phases (Park et al., 2001; Wookey et al., 2002) to

kilometer scales for local shear-waves (Gledhill and Stuart, 1996) and meter scales for micro-seismic events (Bokelmann et al., 2000; Teanby et al., 2004). Hence, splitting measurements can be used to interpret LPO, fracturing and geodynamical processes over a large range of length scales.

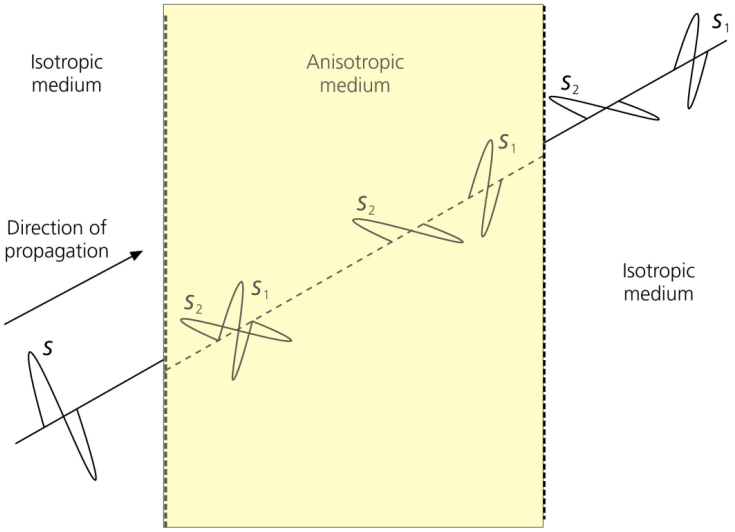

Figure 3.1 –Propagation of an S-wave from an isotropic medium into an anisotropic medium with the generation of the shear-wave splitting phenomena.

Figura 3.1 – Propagacion de una onda S desde un medio isótropo a uno anisótropo con la consiguiente generación del desdoblamiento de la onda de cizalla.

Reliable calculations of teleseismic shear-wave splitting parameters are needed to study anisotropic structures of the upper mantle. The SKS phase and the internal core multiple SKKS have been extensively used in analyses of shear-wave splitting (Vinnik et al., 1992; Silver,1996), and there has been an occasional use of PKS (e.g. Barruol et al., 1998). All of these phases have a P leg in the core so that the expected polarization before S-wave passage through the mantle to the receiver is only in a vertical plane, so no such transverse component is possible. For a stratified medium, in the absence of anisotropy, the only expected signal on the horizontal components would be on the radial component. This is the same for the simplest case of a vertically propagating S-wave within an isotropic medium. This situation can be described by the relation of the anisotropic system to the geographic system or the wave-path system (Figure 3.2). The associated displacements in the wave coordinate system (Radial, Transverse and Vertical) are:

$$u_{iso}(z,t) = \begin{cases} u_R = a_0 \exp(i\omega(t - \dfrac{z - z_o}{Vs_0})) \\ u_T = 0 \\ u_z = 0 \end{cases} \qquad [3.1]$$

where a_0 is a constant, ω is the angular frequency and $Vs_0(z)$ is the S-wave velocity in the isotropic medium.

In a geographic coordinate system, the displacements are

$$u_{iso}(z,t) = \begin{cases} u_E = a_0 \cos\alpha \exp(i\omega(t - \dfrac{z - z_o}{Vs_0})) \\ u_N = a_0 \sin\alpha \exp(i\omega(t - \dfrac{z - z_o}{Vs_0})) \\ u_z = 0 \end{cases} \qquad [3.2]$$

where α is the angle between the North and the Radial axis.

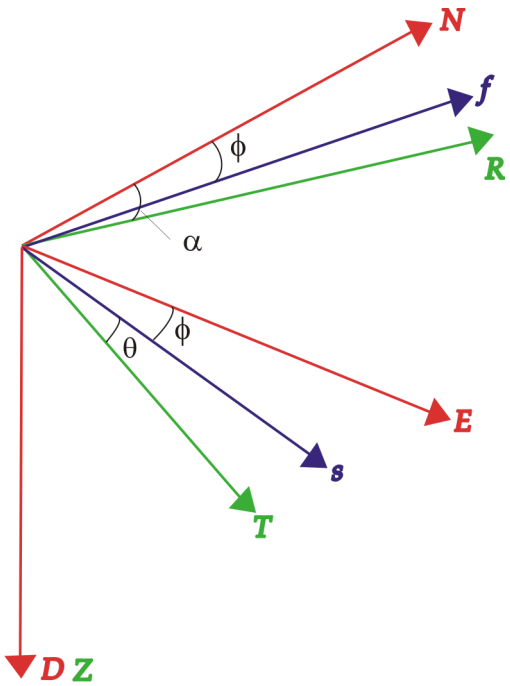

Figure 3.2 – Coordinate systems used to describe the anisotropic propagation: the wavepath system (R,T,Z) is rotated in the geographic system (N,E,D) by the azimuth α, and the anisotropic system is represented by f and s axes.

Figura 3.2 – Sistema de coordenadas usados para describir la propagación anisotrópica: el sistema de propagacion (R, T, Z) se gira en el sistema geográfico (N, E, D) por el azimuth α, y el sistema anisotrópico está representado por los ejes f y s.

According to Montagner et al. (2000), *f* and *s* are considered to lie in the horizontal plane so that b is vertical (Figure 3.2). In this situation, the angle θ between f and R directions is $\theta = \alpha - \phi$

The presence of a transverse component associated with SKS, PKS or SKKS phases, is an indication of local heterogeneity or the presence of an anisotropic structure somewhere in the mantle traversed by the S-wave. The presence of anisotropy imposes a systematic structure on the nature of the transverse component, and so the analysis of arrivals from multiple azimuths can provide a discrimination against the influence of heterogeneity (Figure 3.3).

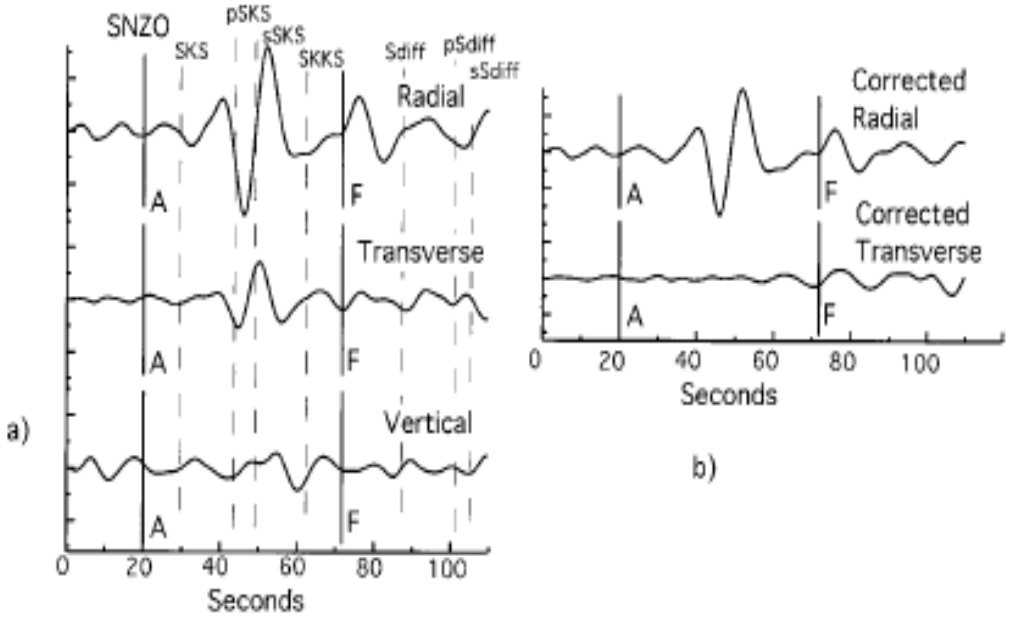

Figure 3.3 - (a) Seismic example of a telesismic event recorded in New Zeland where the SKS phase show the presence of anisotropy in transversal component. (b) the same event is corrected for anisotropy thus the obtained δt y ϕ reduce the energy on the transversal component. (Stein and Wysession, 2003)

Figura 3.3 - (a) En la figura se muestra el registro de un telesismo registrado en Nueva Zelanda donde la llegada de la fase SKS indica la presencia de anisotropía en las componentes transversal. (b) El mismo registro corregido por anisotropía, donde se aprecia como la aplicación de los valores específicos de δt y ϕ en la componente transversal ha conseguido reducir la energía de desdoblamiento de las fases de cizalla. (Stein and Wysession, 2003).

Now we assume that at depth $z = z_0$, the wave enters an anisotropic medium with horizontal (fast and slow) symmetry axes. This reduces the problem to two dimensions, since the vertical axis is identical to all appearing systems:

$$u_{aniso}(z,t) = \begin{bmatrix} u_f \\ u_s \end{bmatrix} = \exp(i\omega t) \begin{bmatrix} e^{i+} & 0 \\ 0 & e^{i-} \end{bmatrix} \times \begin{bmatrix} \cos\phi & \sin\phi \\ -\sin\phi & \cos\phi \end{bmatrix} \begin{bmatrix} a_R \\ a_T \end{bmatrix} \quad [3.3]$$

where $e^{i+} = \exp(-i\omega \frac{z - z_0}{V_{S0} + \delta V_S / 2}$ and $e^{i-} = \exp(-i\omega \frac{z - z_0}{V_{S0} - \delta V_S / 2}$ [3.4]

with θ being the angle between the radial and the fast axis

Considering propagation along the vertical axis, the S-wave is split into two components travelling at velocities of: $q_f = V_{S0} + \delta V_S / 2$ and $q_s = V_{S0} - \delta V_S / 2$

This represents the delay time accumulated and is expressed with the matrix:

$$H = \begin{bmatrix} e^{i+} & 0 \\ 0 & e^{i-} \end{bmatrix} \quad [3.5]$$

and the elements $e^{i\pm}$ can be written as

$$e^{i\pm} = e^{i\omega(z - z_0/V_{S0})} e^{\mp i\omega\left((z - z_0)\delta V / 2V^2_{S0}\right)} \quad [3.6]$$

When an S-wave, radially polarized, passes through a region of uniform anisotropy, then the combination of both the fast and the slow polarizations on both the radial and the transverse components, can be represented as:

$$u_R(t) = u(t_f)\cos^2\theta + u(t_s)\sin^2\theta \quad [3.7a]$$

$$u_T(t) = \left\{ u(t_f) - ut_s \right) \frac{1}{2} \sin 2\theta \right\} \quad [3.7b]$$

where t_f and t_s are the times of passage for the fast and slow components, and ϕ is the angle between the fast and radial direction.

For a uniform anisotropic zone, we expect the pulse shapes to be the same for the faster and slower S contributions, but there could be some differences introduced in the presence of anisotropic gradients. For propagation along the fast direction, ϕ =0, there would be no transverse component and this forms the basis of the methods,

introduced by Silver and Chan (1991) and Wolfe and Silver (1998), to estimate anisotropic parameters.

For SKS the aim is to seek a rotated coordinate system in which the new transverse component is minimized, and thereby determine the time shift δt =tf-ts , which is found from the correlation of the fast and slow pulses in the rotated frame. The energy $E_t(\phi,\delta t)$ on the reconstructed transverse component $\widetilde{u}_t(t)$ is expressed as:

$$E_t(\phi,\delta t) = \frac{1}{T}\int_0^T \widetilde{u}_t(t)^2 dt \sim \frac{1}{N}\sum_{n=1}^{N} (\widetilde{u}_t{}^n)^2 \Delta t \qquad [3.8]$$

For an N point digital time series, Et is evaluated from many candidate values of ϕ and δt (increments of 1 degree and 0,05 sec respectively) (Silver and Chan, 1988).

3.1 Shear wave splitting: inversion techniques

Analysis of shear-wave splitting on local and teleseismic shear-waves has evolved into a very commonly used tool for constraining continental seismic anisotropy.

The most common technique is to assume an anisotropic symmetry system and orientation or, alternatively, a thickness can be assumed and a percentage of anisotropy can be calculated. These assumptions are based on theoretical and laboratory measurements. Often a 4% anisotropy and the symmetry system of transverse anisotropy with a horizontal symmetry axis are assumed (Savage, 1999).

Techniques of shear-wave splitting analysis, that seek to best remove the anisotropy, can be divided into general groups, those that consider single events and those that consider multiple events (Figure 3.4).

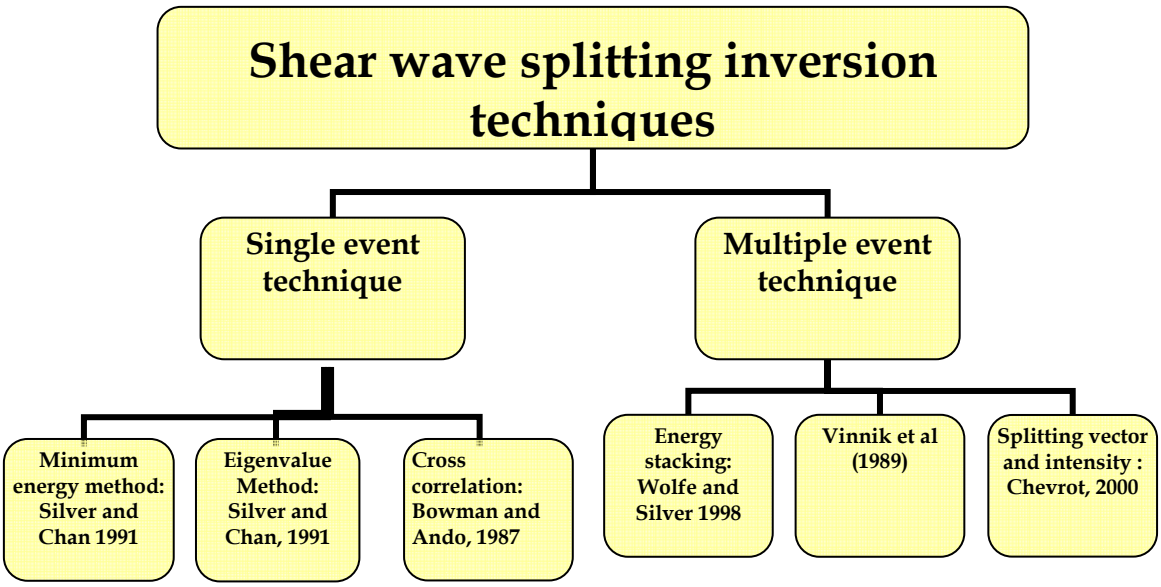

Figure 3.4 – This block diagram presented by Wüstefeld, 2007, summarizes all the techniques that are used to calculate shear-wave splitting.

Figura 3.4 - El diagrama de bloque ha sido presentado por Wüstefeld (2007) reasume todas las técnicas que se utilizan para calcular el desdoblamiento de la onda de cizalla.

3.1.1 Single event technique:

This first type of technique determines the anisotropy parameters based on a single event. When an S-wave travels through an isotropic medium, it is radially polarized and thus there is no transverse component. In contrast, in the passage through an anisotropic medium, a transverse component is present and it will be approximately proportional to the time derivative of the radial component (equation 3.7b). Thus, these techniques performed a grid search for the splitting parameters ϕ and δt which best remove the effect of splitting.

In this group are included the follows methods:

Minimum energy method by Silver and Chan (1991): This method is arguably the most popular method in shear-wave splitting. For weak anisotropy (small delay time compared to the dominant period of signal), the transverse component is identical to the time derivative of the radial component. If the initial polarization is known, as in core reflected and refracted phases (e.g., is assumed to unsplit the δt and ϕ PcS, SKS, SKKS, PKS, …), the value of seismogram, searching for a combination of fast direction and delay time which

minimizes the energy on the transverse component and which corresponds to the t. The corrected radial and transverse components areδ and ϕpreferred values of contoured and the error bars are based on energy contours. This corresponds to "removing" the effect of the anisotropic layer from the data.

Cross-correlation method by Bowman and Ando (1987): This method attempts to maximize the similarity in pulse shapes of the fast and slow components, which should ideally be identical, one delayed with respect to the other. It is performed on a grid search to find the values that maximize the δt and ϕ over possible values for δt and ϕ that produces the smallest cross-correlation to find the best pair of root-mean-square misfit to the individual measurements.

Eigenvalue method by Silver and Chan (1991): The eigenvalue method discussed in the work of Silver and Chan (1991), can be visualized by searching for the most linear particle motion, minimizating the ratio of covariance matrix eingenvalues.

Another recently developed method is the cross convolution algorithm by Menke and Levin (2003), which is designed to minimize the misfit between a given anisotropic earth model and observed waveform data.

3.1.2 Multiple events technique:

This type of technique analyse simultaneously a set of records coming from different azimuths. In this group are included the follows methods:

Energy stacking by Wolfe and Silver (1998): This is a stacking method devised to find the optimum splitting parameters and 95% error region for teleseismic shear-waves phases from a set of earthquake events. Here, the energy $E(\phi,\delta t)$ on the transverse component of each measurement is computed for each candidate set of splitting parameters. The stacking of these (then normalized) energy distributions gives a global energy at the station, whose minimum then gives its splitting parameters. This approach is helpful for stations with a high ambient noise level, such as ocean islands, because the noise proprieties vary for different earthquake events, however, stacking events with a similar polarization

will also improve the final result. This technique effectively averages out splitting signal variation, and provides the best model parameters for a single-layer anisotropy model with a horizontal fast axis.

Vinnik et al, 1989: This methodology is equivalent to the Silver and Chan method. This method allows values, that best reproduce the observed transverse component, to be found. However, this method lacks the possibility to constrain measurement errors, which is the main difference when compared to the Silver and Chan method.

Several techniques utilize backazimuthal variations in shear-wave splitting parameters to detect the effects of dipping or multiple layers of anisotropy. For example, the splitting vector and intensity by Chevrot (2000) takes into consideration backazimuthal variations in transverse energy of core phases and projects the amplitudes of transverse components to the amplitudes of the time derivatives of radial components to obtain a single set of best-fitting splitting parameters for a seismic station. This method provides an estimate of the splitting intensity that provides an additional measure of anisotropy scales, but requires a broad range of backazimuthal coverage.

For instance, Hartog and Schwartz, 2000) and Walker et al. (2004) use similar approaches to solve the Christoffel equation to predict splitting parameters. Then a grid search is performed to find the optimum orientation (including fast axis azimuth and dip) of the tensor that minimizes the difference between the trial and observed splitting parameters. This type of analysis is easily extended to examine multiple layers of anisotropy.

3.1.3 Vantages and limitations of shear wave splitting tecniques

Shear-wave splitting analyses possess a number of advantages. Standard methodologies typically used are relatively simple and computationally inexpensive, which likely explains their popularity since their introduction in the 1980s, and thus the rich database of thousands of measurements currently available.

Furthermore, an important constraint provided by shear-wave splitting analysis is the formal estimation of measurement error, which is critical to the interpretation of similarities and differences in data sets, as well as comparisons of data sets using different methodologies. Moreover, the lateral resolution of structure is generally good and provides important constraints on broad-scale fabric.

The popularity of shear-wave splitting analyses, growing in the last decade, has led to having a considerable number of published shear-wave splitting studies, but with results obtained from very different methodologies and thus with varying levels of quality control. A related problem is that splitting parameters for core phases, such as SKS and SKKS, using the same source–receiver pair are not always compatible with one another (James et al., 1996; Ozalaybey et al., 1999; Niu et al., 2004), suggesting that the extraction of shear-wave splitting parameters is not always as simple as assumed. Furthermore, methods of error estimation vary, limiting a complete comparison of shear-wave splitting studies in many cases. Finally, the reliability of the splitting parameters estimated depends strongly on the azimuthal distribution of the record used, and poor coverage may introduce a large error hindering the estimation of the final parameters. Moreover, stations must record for periods of more than two years to attain sufficient data coverage (Fouch and Rondenay, 2006) and a considerable number of SKS measurements.

In all the methods presented in this Chapter, the shear-wave analysis window is selected manually and the δt and ϕ that best correct the splitting in this window are calculated by means of a grid search. A problem often encountered when using this approach is that the calculated parameters are sensitive to the choice of the shear-wave analysis window. This means that the manual selection of the shear-wave analysis window is subjective and can heavily influence the results. In that case, automated window selection could avoid this problem and give an objective measurement.

Teanby et al. (2004) have recently introduced an automated shear-wave splitting analysis tool. With this tool, shear-wave splitting is evaluated for a range of waveform window lengths and the stability of the measurement is evaluated using cluster analysis and a final data window is selected based on the lowest cluster error. Fast polarization orientation and splitting time estimates are therefore objective and internally consistent (Fouch and Rondenay, 2006).

Regardless, the techniques in which measurements depend on visual examination of rotated seismograms and polarization diagrams, or those of almost fully automatic processes, have their disadvantages as well. Visual techniques are subjective and, although arguably the most accurate, are tedious and time-consuming. More automated techniques are preferred because of objectivity, consistency and repeatability, but they work well on noise-free impulsive near-classic examples of shear-wave splitting, but on typical records either require visual checking or need to pass stringent selection criteria which may severely limit the data and bias the results.

Therefore, the typical complexity of the shear-wave signals is the justification for developing a combined visual and semi-automatic technique.

Measurements of shear-wave splitting analyses using core phases do not provide any constraint on the depth location of the anisotropy since the splitting could originate in the lowermost mantle (e.g., Lay et al., 1998; Kendall, 2000), the uppermost lower mantle (Wookey et al., 2002), or scatterers in the crust and/or mantle (Hedlin and Shearer, 2000). Also, shear-wave splitting measurements should be made for as many azimuths as possible since this allow the recognition of effects due to dipping symmetry axes (Babuška et al., 1993) or where more than one anisotropic layer is present (Silver and Chan, 1991). In fact, methods such as these assume a single layer of anisotropy, with fast and slow axes oriented horizontally. This limitation can be overcome by regarding the obtained measurements as "apparent" (Silver and Savage, 1994). The backazimuthal variations of these apparent splitting parameters are then characteristic and can be inverted for two layers or even dipping layers (Brechner et al., 1998).

4. Seismic Data selection and Analysis

In the Iberian Peninsula are deployed a considerable number of permanent broad-band stations, belonging to several network. The Topo-Iberia project, started in July 2006, has enforced the existent red with the installation of broad-band stations every 50 km in the last two years, so we cont on for future work with this new network.

4.1 Seismic Network Data.

We analyzed the shear wave splitting of 19 permanent broad-band stations (Figure 4.1), management by different organisms:

- Instituto Andaluz de Geofisica- Universidad de Granada, IAG-UGR (IG) : ACBG, ACLR, ANER, ARAC, ASCB, CEUT, ESTP, GORA, HORN, JAND, SELV, SESP and VELZ;
- Real Observatorio de la Armada- Universidad Complutense- GEOFON, ROA-UCM-GEOFON (WM) : SFS, CART and MELI;
- GEOFON Program, GFZ Postdam, Germany (GE): MTE;
- Incorporated Research Institution for Seismology IRIS (IU) Geological Survey, IRIS/USGS (IU) : PAB;
- Instituto Geografico Nacional, IGN (ES) : ECAL.

The majority of data utilized in this work are events recorded by seismic station of the Instituto Andaluz de Geofisica - University of Granada (IAG-UGR). The main

characteristics of these networks are presented as well as of the other in the next Chapters.

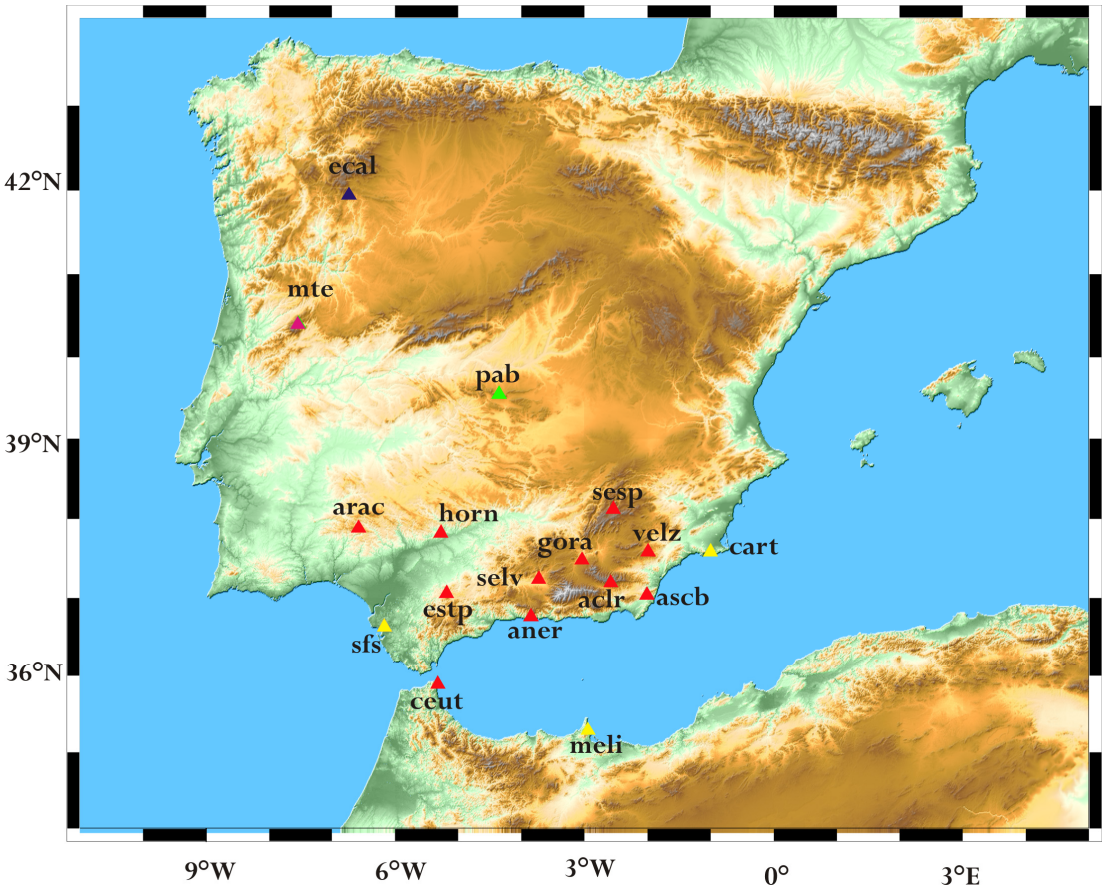

Figure 4.1 – Distributions of seismic station utilized in this work (red triangles is IG network; yellow triangles is WM network; green triangle is IU network; magenta triangle is GE network; blu triangle is ES network).

Figura 4.1 – Distribución espacial de las estaciónes utilizadas en este trabajo (triangulos rojos es la red IG; triangulos amarillos es la red WM; triangulo verde es la red IU; triangulo magenta es la red GE; triangulo azul es la red ES).

4.1.1 The IAG- UGR (IG) Broadband Seismic network

The broadband seismic network of the IAG-UGR present the following characteristics (Morales et al., 2007):

- A three-component Streckeisen-STS2 broad band seismometer with flat ground velocity response between 120 s and 50 Hertz.

- Earth Data digitizer of 24-bit of resolution that digitizes the signal of the seismometer to 50 samples per second. In addition it synchronizes the signal through the time coming from a GPS Garmin.

- A PC interface where the data in continuous format and by events are stored

- A modem-router for for the communication with the data center via Internet, ADSL, cellular telephony or basic telephony.

In the figure (Figure 4.2a) an example of the electronic component of a seismic station of the IAG-UGR network with its some of the mentioned modules is showed (digitizer, PC, router etc..). All the stations are isolate of the ground by a granite slab of about 6 cmts of thickness with the purpose to avoid abrupt changes of temperature in the interphase soil-seismometer that can introduce distortions in the signal to long periods. In addition, seismometer is isolated of fluctuations of external temperature through a "metallic jacket" formed by: polyurethane foam including in a box of aluminium, fiber glass and a covering of aluminium paper (Figure 4.2b). For the acquisition, interrogation and management of the data are used three programs:

- Seislog: it is a package of programs (Utheim and J.Havskov, 2001), installed in the station of field for the acquisition that runs under operating system QNX and that manages the acquisition of the data and the state of receiver GPS.

- Seisnet: it is a set of programs (Ottemoller and Havskov, 1999) that allows the communication and interrogation of the seismic stations in field using different communication protocols. It is installed in a work station Sun. The data transmission in the interrogation phase, it is realised via RTB and GPRS (by modem) or by protocol TCP/IP (ADSL and Internet).

- Seisan: (Havskov and Ottemöller, 1999), it is a developed system to organize data of different types from seismic stations in a data base and provides with tools for routine processing and also to facilitate different dedicated calculations from the investigation. The data are stored in two data bases, one of events and another one of continuous. The first corresponds with the events declared by the system of data acquisition (seislog) and that usually corresponds with local, regional earthquakes, explosions of quarries etc., and for the first minutes of telesismic records. The data base of continuous corresponds with the waveform in its continuous form.

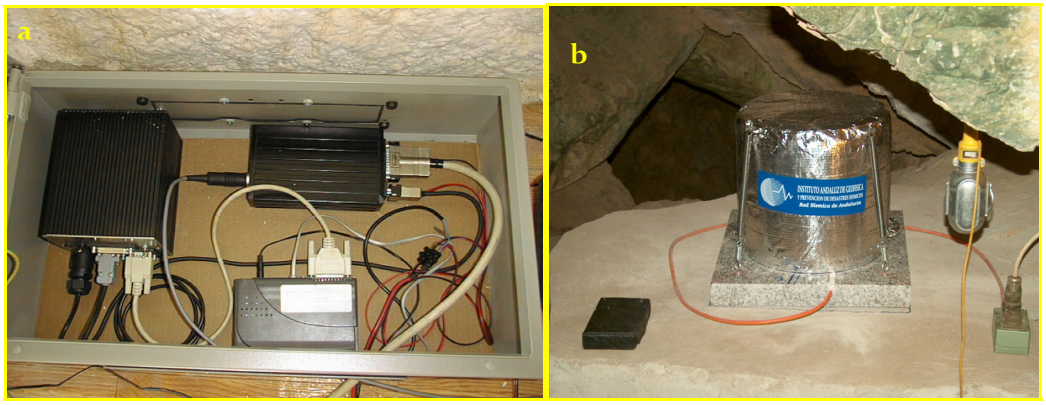

Figura 4.2- (a) Example of electronic components of seismic station of the Instituto Andaluz de Geofísica-Universidad de Granada. It is showed the conversor A/D de 24 bits of the Earth Data with the incoming of the seismometer STS-2 and of the GPS, the interface SEISCOMP where the data are stored in a hard disc and where seislog is installed. Also it is showed the modem for the communication/interrogation with the data center situated in the Observatorio de Cartuja. (b) Example of the "metallic jacket" to isolate the broad band seismometer by fluctuations of external temperature. Ii is also showed the granite slab of about 6 cmts of thickness to avoid abrupt changes of temperature in the interphase soil-seismometer.

Figura 4.2- (a) Componentes electrónicos de una estación sísmica del Instituto Andaluz de Geofísica-Universidad de Granada. Se aprecia el conversor A/D de 24 bits, las entradas provenientes del sismómetro STS-2 y del GPS, la internase SEISCOMP donde se graban los datos en el disco duro y donde reside el programa de adquisición (seislog). También se aprecia un modem para la comunicación/interrogación con la central de registro, localizada en el Instituto.(b) *Sismómetro de banda ancha con protección metálica al objeto de evitar perturbaciones producidas por las variaciones de temperatura ambiente. El equipo también se sitúa sobre una losa de granito de unos 6 cm de espesor para aislarlo térmicamente del suelo.*

4.1.2 The Western Mediterranea Broadband Seismic network of the ROA-UCM-GEOFON (GE/WM).

The broadband stations of the seismic network of the western Mediterranean are managed by the Real Observatory of the Navy of San Fernando (ROA), the University Complutense de Madrid (UCM) and GeoForschungsZentrum - GFZ of Postdam. The selected stations, SFS, CART and MELI (Figure 4.1), have all broadband sensors Streckeisen STS-2, system of acquisition Quanterra Q380 and Q4120 or Earth Data digitizer on a Seiscomp interface. The stations are connected with the data center that receives the data in real time (Internet) or with a slight delay (those that uses telephone modem). The stations that have been used for the

analysis of seismic anisotropy have been Sn Fernando (SFS), Cartagena (CART) and Melilla (MELI)

4.1.3 The GEOFON (GE) broadband seismic network

The station of Manteigas (Portugal) is managed by network GEOFON (Hanka et al., 2000), of the GeoForschungsZentrum-GFZ de Postdam http://www.gfz-potsdam.de/geofon, and consists of sismometer broadband STS-2 and an acquisition system Quanterra Q380. The transmission of this station is in real time and it is received in different websites where seismic data are stored.

4.1.4 The Global Seismograph network, IRIS/USGS (IU)

The station of San Pablo of Montes (Toledo) belongs to the global seismic network managed by IRIS and the USGS (http://www.iris.edu/hq/programs/gsn/). This station this composed by sismómetro STS-1 and acquisition system Quanterra. In addition the station has an accelerograph FBA Kinemetrics.

4.1.5 The National Seismic network, IGN (ES)

Of the stations that conforms the national seismic network managed by Instituto Geográfico Nacional (IGN), we have selected the station of ECAL (Calabor) in Zamora. The station has a broadband sismometer, a digitizador of three channels (24 bits), a transmission VSAT, a receiver GPS, a transmitting antenna VSAT. The seismic station settled in 2001 and the telesísmicos data were obtained through the page of Virtual European Broadband Seismograph Network (VEBSN) managed by ORFEUS (http://www.orfeus-eu.org/Data-info/vebsn.html).

4.2 Shear Wave Splitting of SKS phase: stations' data analysis

We selected events occurring at epicentral distances larger than 85°, as for these distances the SKS phase is both well isolated from S and Scs and sufficiently energetic (Figure 4.3) and for the distance range between 130 and 165 degrees we also selected SKKS phases. Also the events are chosen with magnitude Mw≥ 5.5.

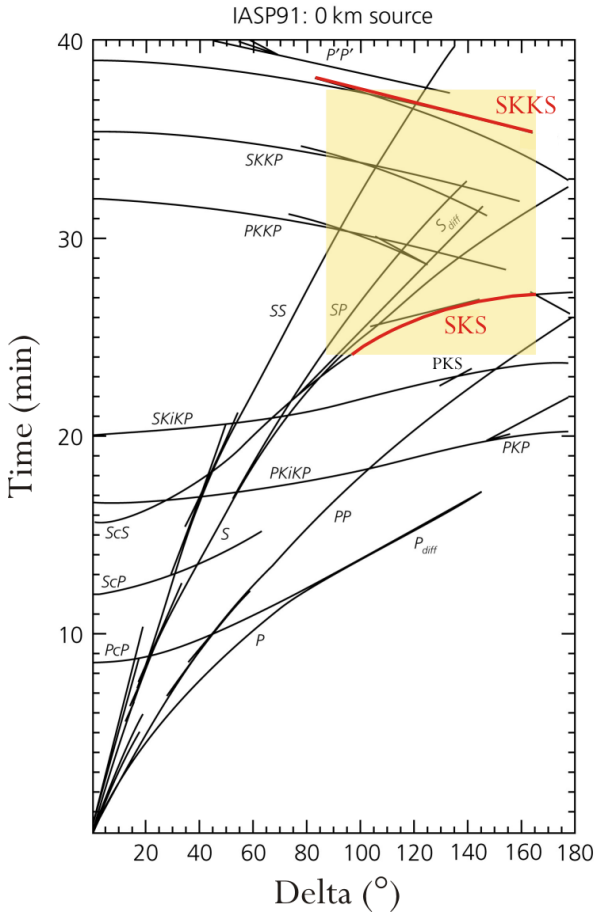

Figure 4.3 – Travel times for the main seismic phases for theIASP91 model. The selected window for the SKS ans SKKS is shown in yellow.

Figura 4.3– Dromocronas de las principales fases sísmicas para el modelo IASP91. La ventana de selection de la fase SKS y SKKS es mostrada en amarillo.

The geographic distribution of the selected events are shown in Figure 4.4, with a global projection centered on southern Spain and preserving the azimuths, and a table with earthquakes location is in the Table 4.1.

Date	lat	long	depth	Mw	region
1996.163	12.74	125.41	28.5	7.1	SAMAR, PHILIPPINE ISLAND
1996.198	1.27	120.35	21	6.5	MINAHASSA PENINSULA
1996.204	1.34	120.65	28.2	7.0	MINAHASSA PENINSULA
1996.249	21.78	121.45	30.8	6.8	TAIWAN REGION
1996.249	-22.32	-113.28	16	6.8	EASTER ISLAND REGION
1996.293	31.73	131.78	22	6.7	KYUSHU, JAPAN
1996.357	43.29	138.78	244.7	6.5	EASTERN SEA OF JAPAN
1996.162	51.38	-176.49	36.5	7.2	ANDREANOF ISLANDS, ALEUTIAN
1997.288	-31.03	-71.42	69.8	7.1	NEAR COAST OF CENTRAL CHILE
1997.329	1.37	122.71	29.4	7.0	MINAHASSA PENINSULA
1998.030	-24.02	-70.62	41	7.0	NEAR COAST OF NORTHERN CALIF.
1998.123	22.37	125.53	22.9	7.4	SOUTHEAST OF TAIWAN
1998.232	28.99	139.47	425.5	7.0	BONIN ISLANDS REGION
1998.246	-29.56	-71.97	34.0	6.5	NEAR COAST OF CENTRAL CHILE
1998.271	-8.36	112.40	153	6.5	JAVA
1998.301	1.00	125.98	15.0	6.5	MOLUCCA PASSAGE
1998.313	-7.05	128.75	15.4	6.7	BANDA SEA
1999.028	52.86	-169.10	51.1	6.6	FOX ISLANDS, ALEUTIAN
1999.079	51.67	-177.30	43.0	6.9	ANDREANOF ISLANDS, ALEUTIAN
1999.098	43.66	130.47	575.4	7.1	E. USSR-N.E. CHINA BORDE
1999.263	24.15	120.80	21.2	7.6	TAIWAN
1999.319	-1.21	88.89	15.0	6.9	SOUTH INDIAN OCEAN
1999.344	-36.38	-97.52	15.0	6.5	WEST CHILE RISE
1999.345	15.87	119.64	35.1	7.2	LUZON, PHILIPPINE ISLAND
2000.028	43.08	146.81	50.0	6.8	KURIL ISLANDS
2000.114	-28.41	-63.04	607.9	6.9	SANTIAGO DEL ESTERO PROV.
2000.125	-1.29	123.59	18.6	7.5	SULAWESI
2000.156	-4.73	101.94	43.9	7.8	SOUTHERN SUMATERA
2000.312	-55.34	-29.24	16.0	6.7	SOUTH SANDWICH ISLANDS
2001.055	1.55	126.42	42.8	7.0	MOLUCCA PASSAGE
2001.083	33.97	132.52	47.4	6.8	SOUTHERN HONSHU, JAPAN
2002.010	-3.21	142.68	18.0	6.7	NEAR N COAST OF PAPUA N.G.
2002.090	24.19	121.96	39.0	7.1	TAIWAN REGION
2002.116	13.15	144.67	69.1	7.0	MARIANA ISLANDS
2002.169	-31.04	-71.63	57.0	6.4	NEAR COAST OF CENTRAL CHILE
2002.179	43.74	130.45	581.5	7.3	E. USSR-N.E. CHINA BORDER
2002.306	2.89	96.05	27.0	7.2	NORTHERN SUMATRA, INDONESIA
2002.319	-55.91	-35.51	15.0	6.6	SOUTH GEORGIA ISLAND REGION
2002.321	47.81	146.45	479.8	7.3	NORTHWEST OF KURIL ISLAN
2003.027	-45.43	35.28	15.0	6.4	PRINCE EDWARD ISLANDS REG.
2003.084	-8.28	120.75	32.0	6.4	FLORES REGION, INDONESIA
2003.146	38.94	141.57	61.0	7.0	NEAR EAST COAST OF HONSHU
2003.146	2.61	128.88	34.0	6.9	HALMAHERA, INDONESIA
2003.166	51.57	176.72	22.0	6.5	RAT ISLANDS, ALEUTIAN
2003.171	-30.88	-71.97	35.0	6.8	NEAR COAST OF CENTRAL CHILE
2003.174	51.55	176.60	28.8	6.9	RAT ISLANDS, ALEUTIAN ISLAND
2003.208	46.99	139.23	477.2	6.7	PRIMOR'YE, RUSSIA
2003.216	-60.80	-43.21	15.0	7.6	SCOTIA SEA
2003.268	41.75	143.62	47.3	7.3	HOKKAIDO, JAPAN REGION

2003.272	42.29	144.62	35.0	6.4	HOKKAIDO, JAPAN REGION
2003.321	51.14	177.86	21.7	**7.7**	RAT ISLANDS, ALEUTIAN ISLAND
2003.322	12.11	125.58	36.6	6.5	SAMAR, PHILIPPINES
2004.052	-58.62	-14.90	17.3	6.6	EAST OF SOUTH SANDWICH ISLAND
2004.124	-37.95	-73.75	24.0	6.6	NEAR COAST OF CENTRAL CHILE
2004.150	34.20	141.87	12.0	6.3	OFF EAST COAST OF HONSHU
2004.207	-2.68	104.38	600.5	7.3	SOUTHERN SUMATRA, INDONE
2004.249	32.94	137.00	16.0	7.2	NEAR S. COAST OF WESTERN
2004.249	33.13	137.22	12.0	7.4	NEAR S. COAST OF HONSHU
2004.250	-55.43	-28.79	12.0	6.7	SOUTH SANDWICH ISLANDS
2004.250	33.14	137.28	12.0	6.6	NEAR S. COAST OF HONSHU
2004.282	-10.87	162.27	40.0	6.7	SOLOMON ISLANDS
2004.289	24.48	122.74	102.1	6.6	TAIWAN REGION
2004.297	37.31	138.83	13.0	6.6	NEAR WEST COAST OF HONSHU
2004.316	-7.87	125.12	17.0	7.5	TIMOR REGION
2004.333	42.88	145.36	47.0	7.0	HOKKAIDO, JAPAN REGION
2004.341	42.82	145.41	36.0	6.7	HOKKAIDO, JAPAN REGION
2005.036	5.47	123.67	530.6	7.1	MINDANAO, PHILIPPINES
2005.046	4.80	126.66	56.8	6.5	TALAUD ISLANDS, INDONESIA
2005.050	-5.52	122.23	12.0	6.4	SULAWESI, INDONESIA
2005.061	-6.54	129.99	196.1	7.1	BANDA SEA
2005.079	33.72	130.15	12.0	6.6	KYUSHU, JAPAN
2005.080	-24.88	-63.54	572.3	6.8	SALTA PROVINCE, ARGENTIN
2005.132	-57.57	-138.91	12.0	6.5	PACIFIC-ANTARCTIC RIDGE
2005.134	0.42	98.24	39.0	6.7	NORTHERN SUMATRA, INDONESIA
2005.139	1.88	96.74	12.0	6.8	NORTHERN SUMATRA, INDONESIA
2005.164	-20.02	-69.23	94.5	7.8	NORTHERN CHILE
2005.165	51.15	179.52	18.0	6.8	RAT ISLANDS, ALEUTIAN ISLAND
2005.207	-15.41	-73.15	107.6	5.9	SOUTHERN PERU
2005.228	38.24	142.05	37.0	7.2	NEAR EAST COAST OF HONSH
2005.288	25.29	123.43	194.6	6.4	NORTHEAST OF TAIWAN
2005.321	-22.46	-68.13	155.3	6.8	CHILE-BOLIVIA BORDER REG
2006.002	-61.12	-21.39	20.2	7.4	EAST OF SOUTH SANDWICH ISLAND
2006.034	11.83	92.17	12.0	6.1	ANDAMAN ISLANDS, INDIA
2006.055	-17.94	-179.42	640.9	6.1	FIJI ISLANDS REGION
2006.109	2.70	93.22	17.2	6.2	OFF W COAST OF NORTHERN
2006.136	0.01	96.98	13.5	6.8	NORTHERN SUMATRA, INDONE
2006.173	45.37	149.52	104.8	5.9	KURIL ISLANDS
2006.189	51.04	-179.12	28.0	6.6	ANDREANOF ISLANDS, ALEUTIAN
2006.197	-28.71	-72.84	12.0	6.2	OFF COAST OF CENTRAL CHILE
2006.204	-17.97	-178.42	597.9	5.8	FIJI ISLANDS REGION
2006.209	23.91	122.49	39.2	5.9	TAIWAN REGION
2006.218	26.23	144.13	19.2	5.8	BONIN ISLANDS, JAPAN REGION
2006.219	-15.76	167.63	157.7	6.8	VANUATU ISLANDS
2006.223	2.10	96.18	20.6	6.2	NORTHERN SUMATRA, INDONESIA
2006.232	-61.27	-34.52	17.2	7.0	SCOTIA SEA
2006.232	49.58	156.87	35.6	6.0	KURIL ISLANDS
2006.236	50.92	158.17	50.2	6.5	NEAR EAST COAST OF KAMCH
2006.237	-24.44	-67.18	185.8	6.6	CHILE-ARGENTINA BORDER
2006.249	-61.09	-34.09	13.2	5.7	SCOTIA SEA
2006.273	46.29	153.45	12.8	6.6	KURIL ISLANDS

2006.274	46.38	153.64	12.8	6.5	KURIL ISLANDS
2006.282	20.69	119.98	12.3	6.3	PHILIPPINE ISLANDS REGION
2006.285	23.88	122.54	35.2	5.8	TAIWAN REGION
2006.286	46.14	153.73	12.0	5.8	KURIL ISLANDS
2006.335	3.83	125.10	215.3	6.3	CELEBES SEA
2006.356	10.70	92.11	22.0	6.2	ANDAMAN ISLANDS, INDIA

Table 4.1 – Earthquakes locations used in this work.

Tabla 4.1 – Localizacion de los terremotos utilizados en este trabajo.

As visible in the Figure 4.4, the bulk of data are arriving from NE, very few data are available from SE, this make more difficult constrain the results in the case of more anisotropic layers.

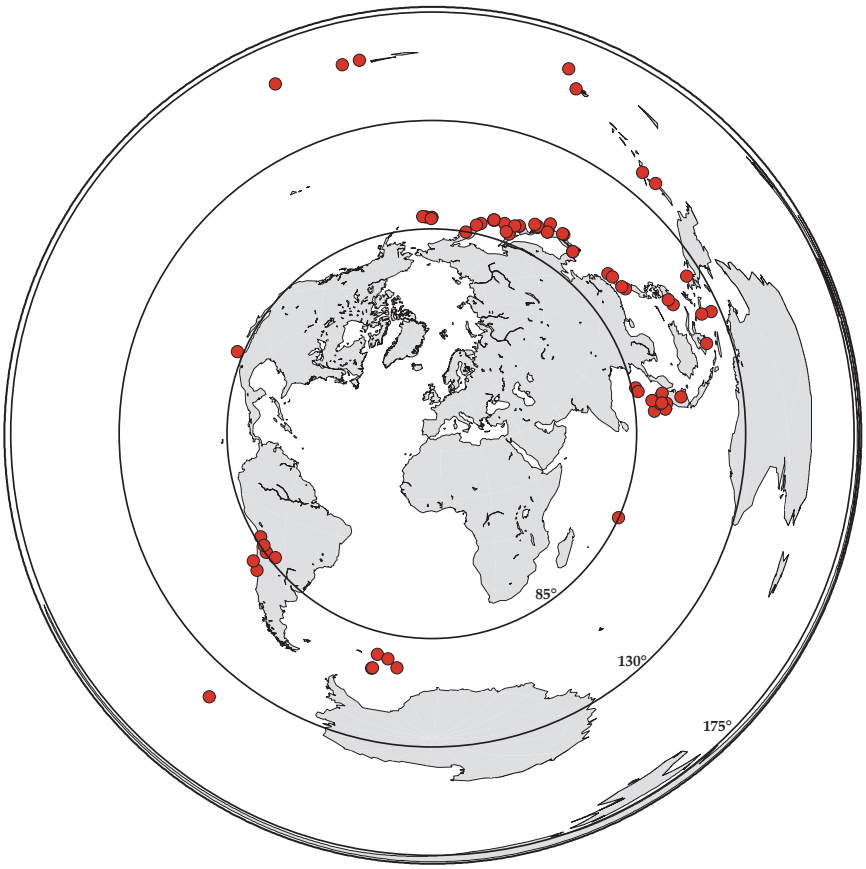

Figure 4.4 - Spatial distribution of earthquakes used in this study in a projection that preserves backazimuths, centered in the Alboran Sea. Epicentral distances of 85° (minimum distance for SKS splitting measurement), 130° and 175° are also shown**.**

Figura 4.4 - Distribución espacial de los terremotos usados en este estudio, la proyección esta centrada en la Península Ibérica. Están además representados los círculos de la distancia epicéntrica a 85° (distancia mínima a la cual se registran la fases SKS para el estudio de splitting), 130° y 175°.

Locations and centroid times of teleseismic events used to extract the data from the continuous record were taken from the Harvard catalogue, http://www.seismologyharvard.edu/CMTsearch.html and arrival times of theoretical SKS phases at the stations were calculated using the theoretical Earth model IASP91 (Kennett, 1995) with the IASP91TTIM software (Buland and Chapman, 1983; Kennett and Engdahl, 1991).

The continuous records for the telesismic events are obtained in different matter: for the IG stations we download from IAG data base the continuous records; for the WM and GE stations we obteine data by e-mail to geofon_dc@gfz-potsdam.de, and we obtain the data in SAC format; for the IU station we obtain data by e-mail to dmsque@iris.washington.edu and we convert to SAC format; and for the IGN stations we obtain data by ftp to the web http://www.orfeus-eu.org/Data-info/available.html.

We present results related to data analyzed until December 2006. The data are available for various time spans, ranging from 10 years (PAB) to few months (JAND). The data quality is also variable, some stations as CEUT and SFS provided few events for shear-wave splitting measurements, for the high ratio signal to noise relation.

Thus, we visually inspected each event, and only those with a relative good signal-to-noise ratio were subsequently analysed. In total we were able to identify 106 SKS shear-wave splitting events. Waveforms with good or fair quality generally give similar results with or without filtering, so that results do not depend overly on choice of filter parameters. The dominant period of SKS is around 0.125-0.1Hz. Where possible, we used either raw data or a weak band-pass filter (0.01-1Hz, it is when the S/N ratio is high. We apply a third-order Butterworth filter twice to produce zero phase distortion. The strongest filter we applied to the data was a 0.02-0.3, 0.01-1.0, 0.02-0.2 Hz band-pass, data with high S/N ratio give similar results for these passbands as the dominant period of SKS is included. Some studies show a dependence of the splitting parameters on frequency (Marson-Pidgeon and Savage, 1997) anyway in our study the small number of significant results do not allow to make meaningful conclusions about the frequency dependence.

For each SKS phase selected, we calculated the two splitting parameters δt and ϕ using SplitLab program (Wüstefeld et al., 2008), which utilizes three different

techniques simultaneously: the rotation correlation method (e.g. Bowman and Ando, 1987), that is maximizing the cross-correlation between the radial and transverse component of the SKS phase, the minimum energy method (Silver and Chan, 1991) that is minimizing the energy on the transverse component, and the minimum eigenvalue method (Silver and Chan, 1991). Relative to the quality of the data, given good or fair events, these methodologies give similar splitting results. The comparison is helpful for discriminating cases where seismograms did not show SKS splitting (also known as *null* measurements) from cases of existent, but weak, splitting. Null measurements occur when the SKS phase is not split. This may happen when the medium is isotropic or when the backazimuth of the incoming SKS wave is parallel to either the slow or the fast directions in the anisotropic layer. In the case of a simple anisotropic medium, Null and non-Null measurements have to be consistent with each other.

Figure 4.5 shows the processing work flow used to calculate the anisotropy.

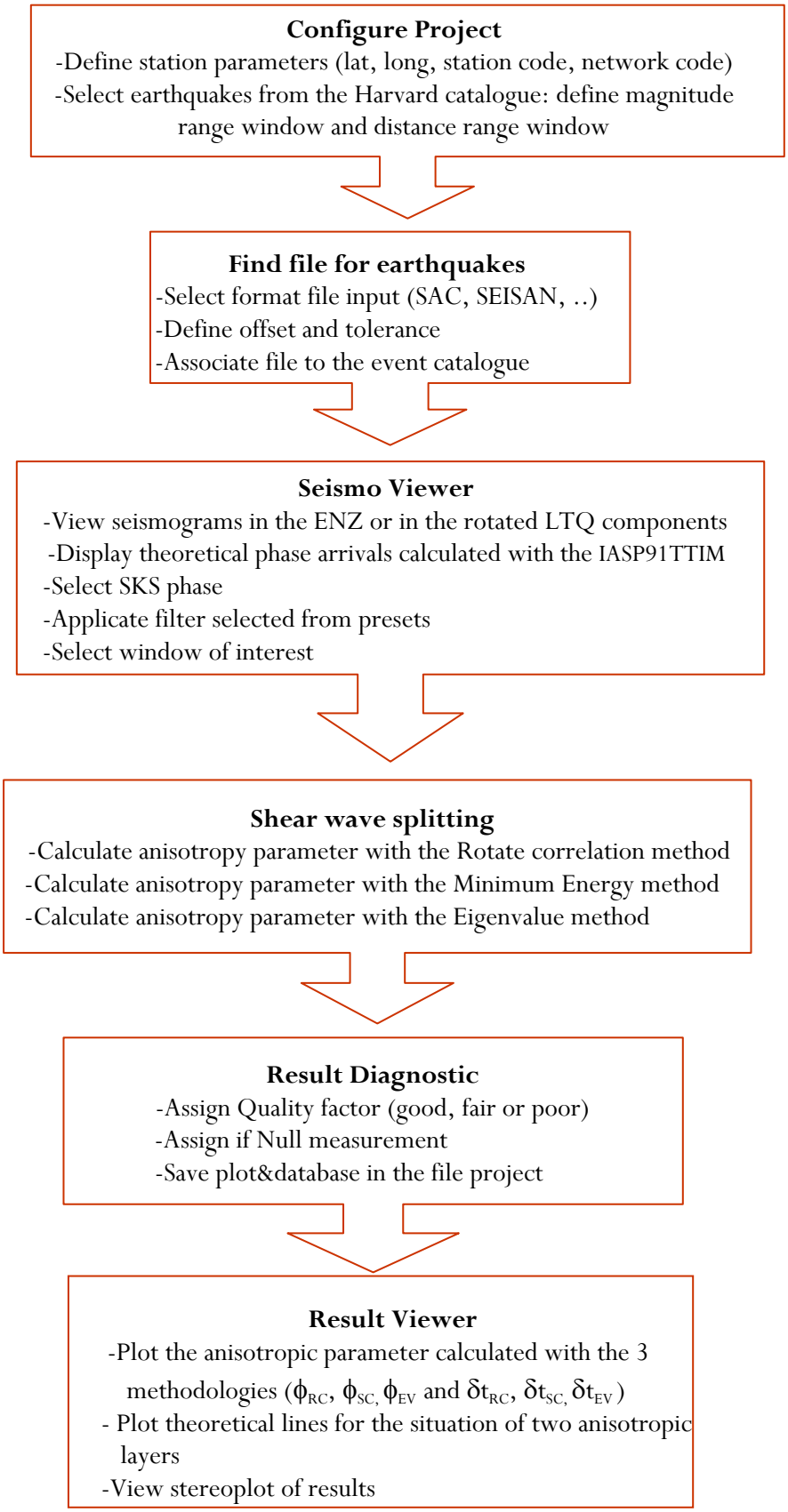

Figure 4.5 – Workflow utilized to calculate the anisotropy parameters with SplitLab program (Wustefeld et al., 2008).

Figura 4.5– Diagrama de flujo utilizado para el calculo de los parametros de anisotropia con el programa SplitLab (Wustefeld et al., 2008).

In the Chapter 5, we present the tables with the results for splitting parameters for each seismogram at each station. The comparison with the results for the 3 methodologies, is also helpful to qualify the results, as we qualified splitting results as "good", "fair", and "poor", as proposed by Barruol et al. (1997), i.e., depending on: the quality of the seismograms, the signal-to-noise ratio of the initial phase, the amount of energy on the transverse component, on the correlation of the two split waveforms, and on the elliptical particle motion before anisotropy correction and its linearization after correction. Figures 4.6, 4.7 and 4.8 we present some example of these cases. In the upper panel is showed the event information and the initial radial and transverse components. Dashed lines are the predicted phase arrival times from IASP91 and the shaded area is the selected window for the shear-wave splitting processing. (middle) Figures for inspecting the performance are shown with four plots for the rotation-correlation method in panel a) and four plots for the minimum energy method in panel b). From left to right: 1) fast and slow components (dashed and continuous lines, respectively), corrected for the calculated splitting delay time; 2) corrected radial and transverse components (dashed and continuous lines, respectively), note that the energy on the transverse component is well removed after anisotropy correction; 3) the particle motion in the horizontal plane (dashed) becomes linear after the correction for anisotropy (solid); 4) contour plot for the maximum value of correlation coefficient and for the energy on transverse component as function of delay time and fast polarization angle. The shaded area marks the 95% confidence interval. (bottom) Numerical values that summarize the results for the three methodologies are given at the bottom, with their respective error ranges.

For simplicity in the discussion and pictures, we present in the Chapter 6, only measurements obtained with the minimum energy method.

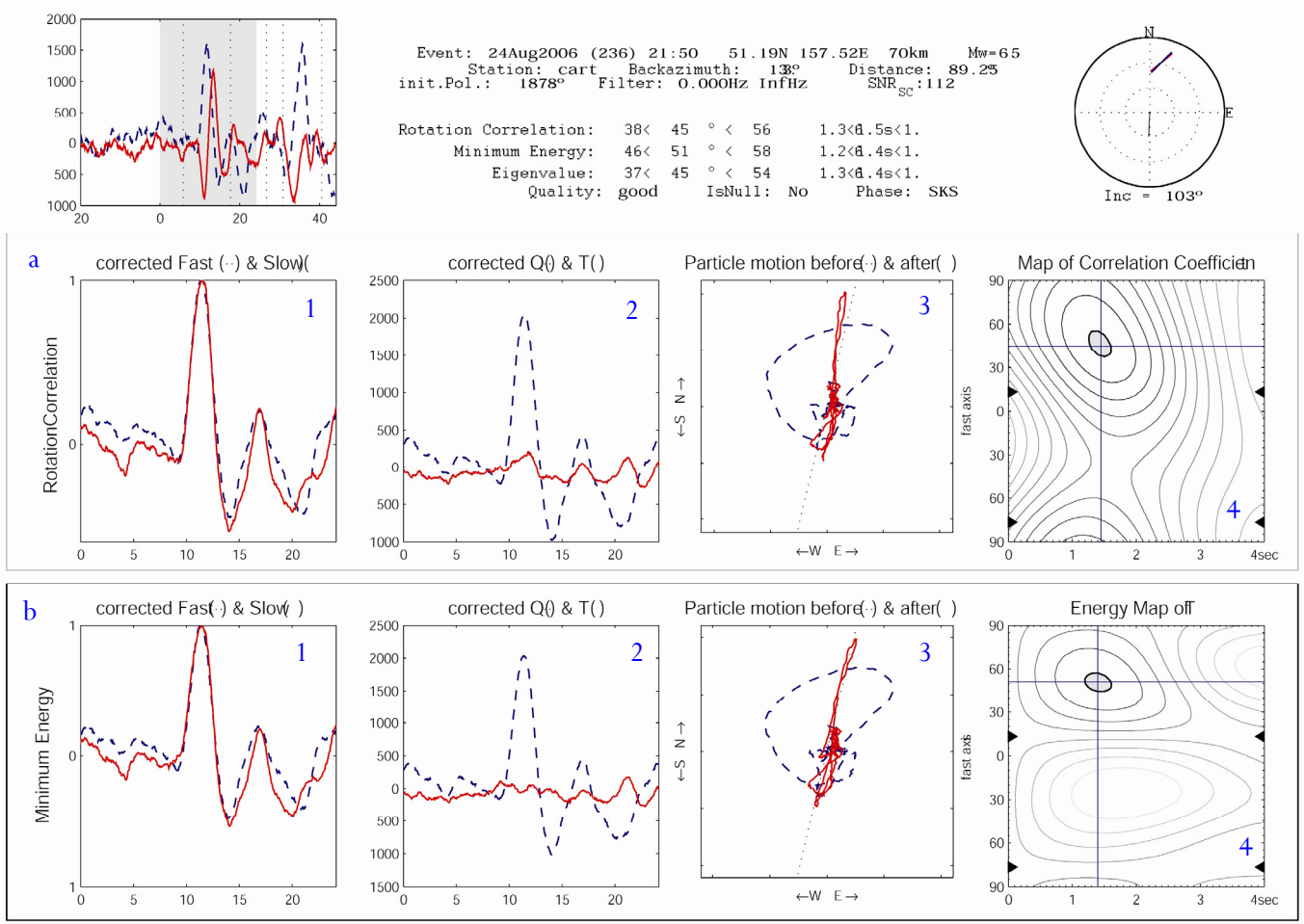

Figure 4.6 – Example of an event recorded for CART station which we considered as good value.

Figura 4.6 - Ejemplo de evento registrado en la estación de CART, clasificado como good.

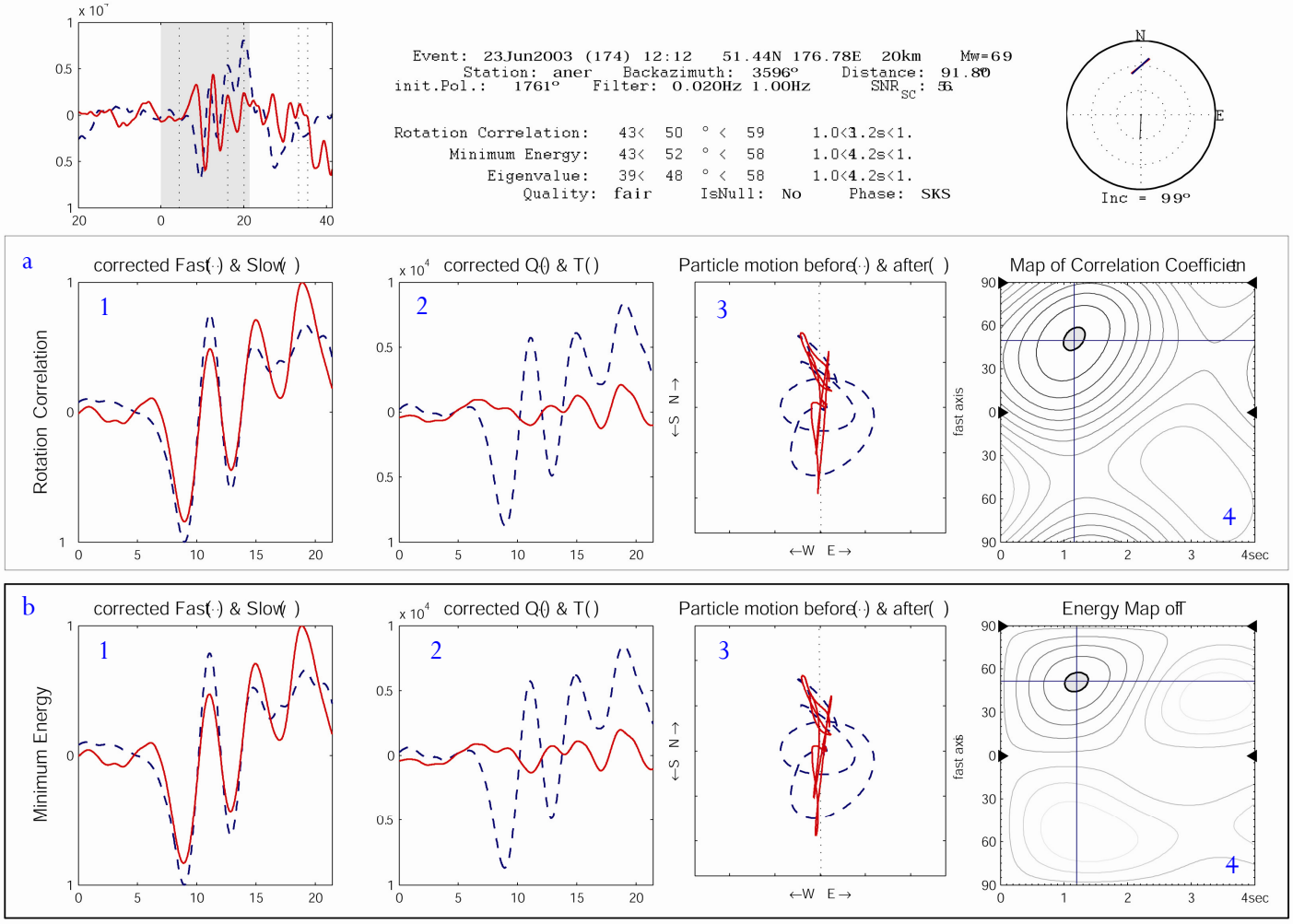

Figure 4.7 – example of an event recorded for station ANER which we considered as fair value.

Figura 4.7 – Ejemplo de evento registrado en la estación de ANER, clasificado como fair

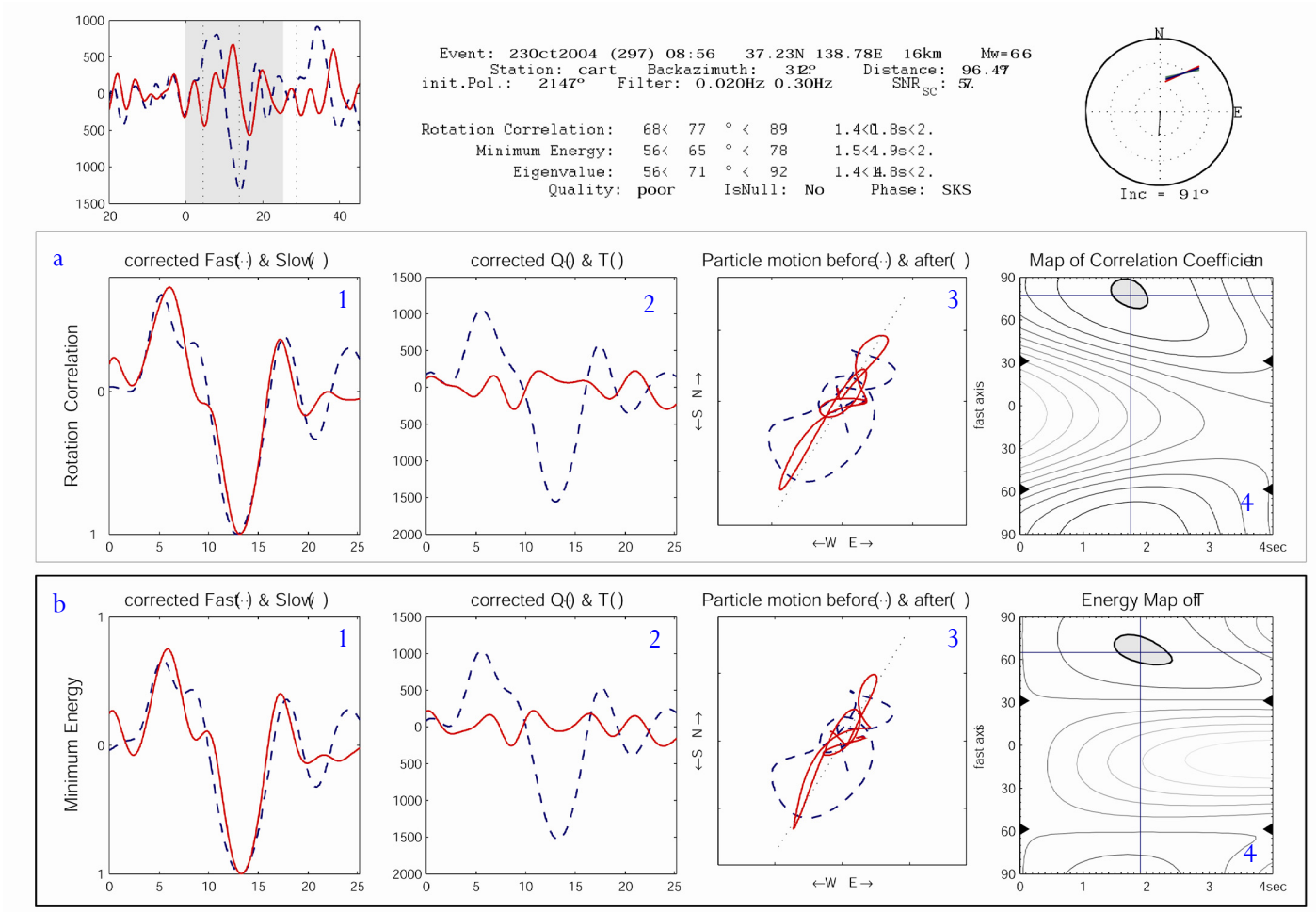

Figure 4.8 – example of an event recorded for CART station which we considered as poor value.

Figura 4.8 - Ejemplo de evento registrado en la estación de CART, clasificado como poor.

5. Measurements and Results

We have analyzed the shear wave splitting at 19 broad band seismograph stations on the Iberian Peninsula.

The splitting measurements exhibit large variations, the fast polarization directions range between N359°E and N96°E and delay times range between 0.8 and 2.1 seconds. This variation is related with the different geological domains where we have calculated the anisotropy.

Now, we will start introducing the main characteristic for each station and the relative anisotropic observations.

5.1 ECAL

ECAL station is in Calabor (Zamora), in the north-west of Iberian Peninsula in the geological domain of Galicia-Tras-Os-Montes Zone (Figure 5.1). This station is management by IGN and it is running since December 2001. We obtained few data even if we check 5 years, in fact finally we analyzed 25 SKS events of which we finally have only 8 availabled and which we classified 1 good, 1 poor, 3 good Null, 1 fair Null and 2 poor Null (Figure A-1). For 2006 we note that a considerable number of events are bad recorded. We utilize a filter of 0.01-1.0 Hz for the majority of events, where poor quality is present we elect to use a filter of 0.02-0.3 Hz.

Westerly events resulted solely in Null measurements. Events from the east give ambiguous results since Nulls and non-Nulls are observed from similar backazimuths (Figure 5.2). This kind of effect can be observed if either two layers of

anisotropy with mutually perpendicular are present (e.g., Silver and Savage, 1994; Heintz et al., 2006) or if the anisotropy is only weak. Short delay times of non-Null measurements indicate only weak anisotropy, which causes Null measurements in case of only weak signal on the initial radial component. The deduced ϕ = -72° and δt=0.8 sec for the one good event.

We are confident that our weak anisotropy is real, due to comparing the results with the other two techniques.

We have for ECAL only one good data which give preliminary information about the anisotropic direction for this station; unfortunately we can not able to make such conclusion, the lack of events hinders a clear interpretation at this moment, but might become clearer with a growing dataset over the next years.

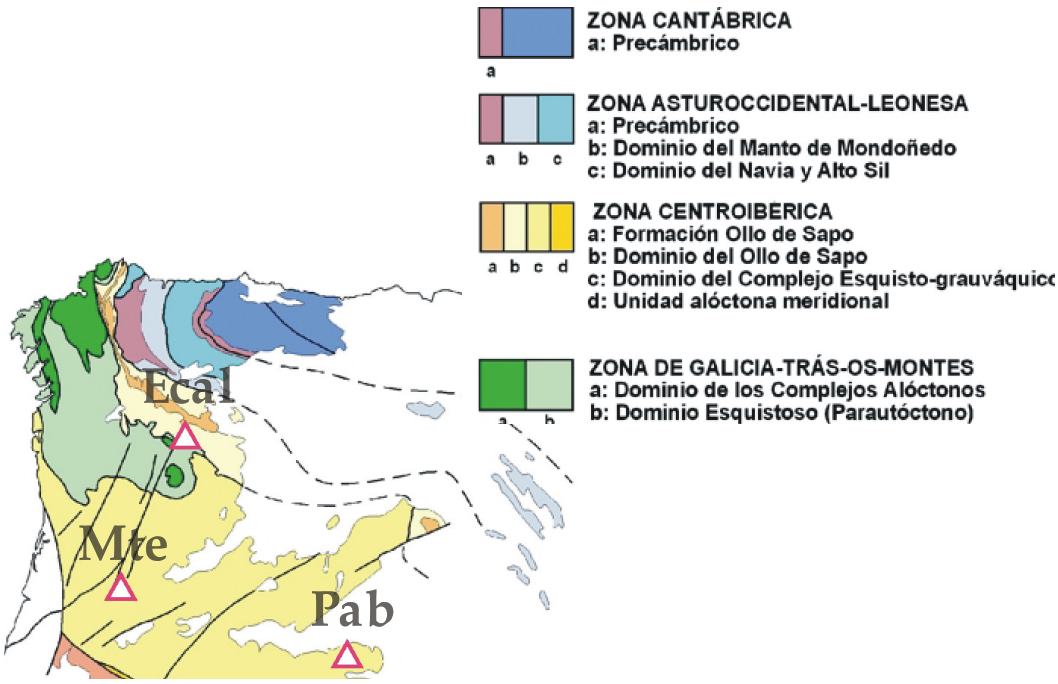

Figure 5.1 – Geological sketch for the north-west part of Iberian Peninsula, we show station location of ECAL, MTE and PAB (after Pérez-Estaún et al., 2004).

Figura 5.1 – Mapa geológico de la parte noroeste de la Península Ibérica, se reresenta la localización de la estación de ECAL, MTE y PAB (según Pérez-Estaún et al., 2004).

In Figure 5.2 we show in the panel ***a*** the station location; in ***b*** the individual splitting measurements are plotted at the various stations to evaluate the coherence of the results. Lines show the fast anisotropy directions ϕ, obtained from the minimum energy method, and their lengths are proportional to the splitting delay

time δt. Good data are shown by red lines, and fair data by blu lines; poor data are not plotted. In panel ***c***, in order to better visualize the lateral sampling of the anisotropy measurements and the regional-scale stability of the anisotropy parameters beneath the stations, we choose to project the individual splitting measurements of good and fair quality along their incoming rays to a depth of 150 km. Although the splitting of the SKS waves is not well-located vertically, this representation is helpful since it plots the splitting parameters closer to the location where they were acquired. The measurements with well-constrained anisotropy, good, are presented as red lines while measurements of lower quality, fair, are shown blu lines. In addition, Figure 5.2***c*** presents the Null measurements by open circles.

We utilized this same matter to represent the results for the other stations too.

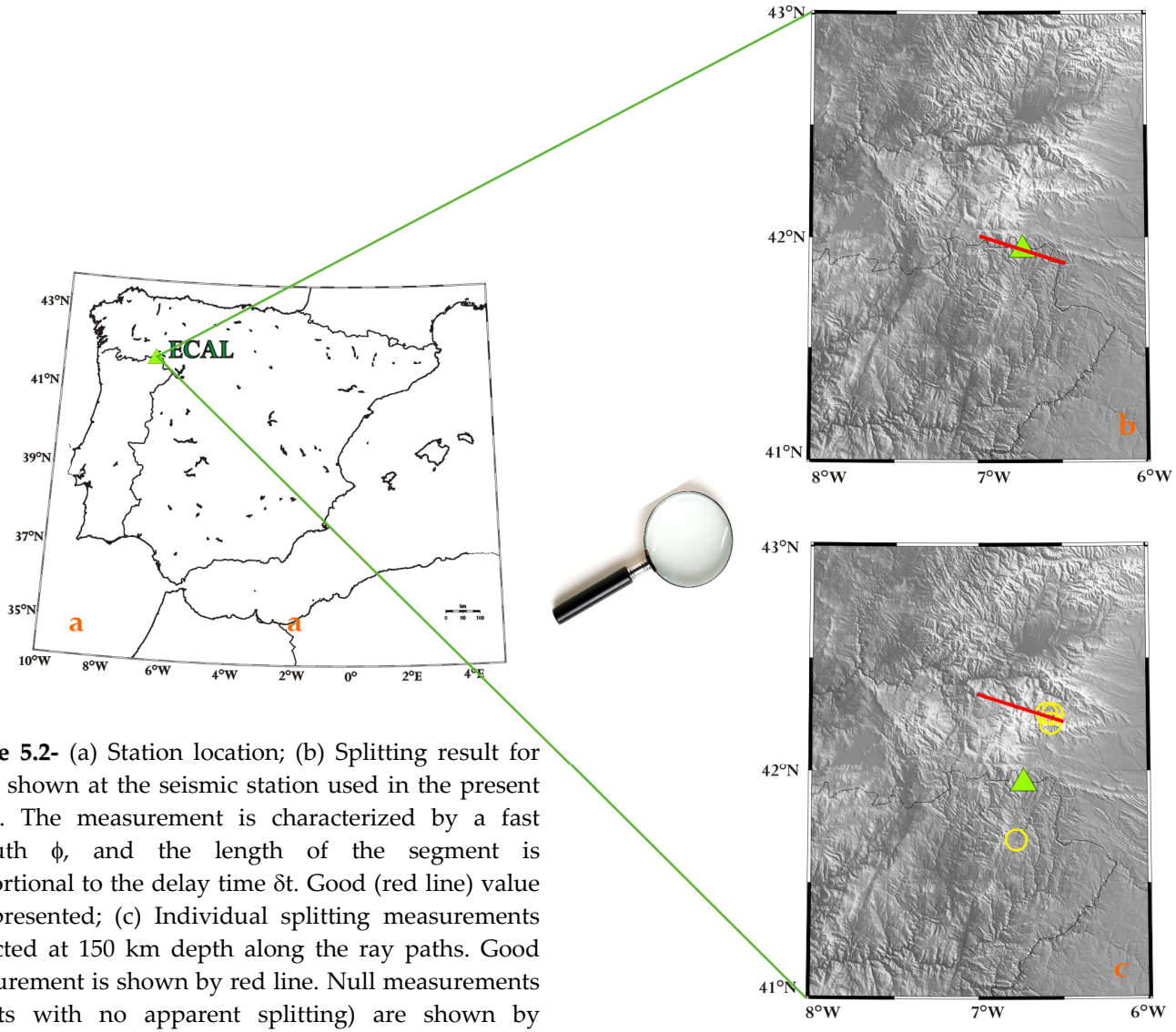

Figure 5.2- (a) Station location; (b) Splitting result for MEM shown at the seismic station used in the present study. The measurement is characterized by a fast azimuth ϕ, and the length of the segment is proportional to the delay time δt. Good (red line) value is represented; (c) Individual splitting measurements projected at 150 km depth along the ray paths. Good measurement is shown by red line. Null measurements (events with no apparent splitting) are shown by yellow circles.

Figura 5.2- (a) Localización de la estación; (b) Resultado del splitting obtenido con el MEM projectado a la estación. La medida está caracterizada por la dirección rápida ϕ, y la longitud del segmento es proporcional al retraso δt. El valor good está representado por la línea roja; (c) Las medidas individuales del splitting están proyectadas a 150 km de profundidad a lo largo del recorrido del rayo. La medida good se muestra con una línea roja. Las medidas Null (eventos con aparente no splitting) están mostrados con círculos amarillos.

Date	phase	baz°	Δ°	Mw	ϕ ° ME	δt ME(s)	ϕ° RC	δt RC (s)	ϕ°EV	δt EV(s)	quality	Null
2003.174	SKS	357,80	86,57	6,88	-84<-72<-62	0,5<0,8<1,2	-51<-44<-38	0,3<0,4<0,5	-56<-26<-11	0,4<0,6<0,8	good	No
2003.272	SKS	20,89	91,69	6,44	41<51<66	0,6<0,8<1,1	65<69<75	0,4<0,5<0,7	41<53<70	0,5<0,8<1,1	poor	No
2002.321	SKS	17,81	87,11	7,28	-	-	-	-	-	-	good	Yes
2003.146	SKS	24,22	94,22	7,00	-	-	-	-	-	-	good	Yes
2003.166	SKS	357,72	86,45	6,50	-	-	-	-	-	-	poor	Yes
2003.208	SKS	22,42	85,95	6,71	-	-	-	-	-	-	good	Yes
2003.268	SKS	21,68	92,11	7,34	-	-	-	-	-	-	poor	Yes
2006.002	SKS	187,32	103,45	7,36	-	-	-	-	-	-	fair	Yes

Table 5.1 – ECAL results. We present the data events in Julian format, the analized phase, the backazimuth of the event, its epicentral distance and the magnitud. Then, the results for ϕ and δt and their error obtained with the three methodologies and the quality factor assigned. In the grey column are null measurements data.

Tabla 5.1 – Resultados de ECAL. Presentamos la fecha de los eventos en formato Juliano, el tipo de fase analizado, el backazimuth del evento, su distancia epicentral y la magnitud. Además de los resultados por ϕ y δt y sus errores obtenidos con las tres metodologías y el parámetro de calidad asignado. Las columnas en gris son los valores null.

5.2 MTE

The MTE Geofon station is in Manteigas in Portugal, within the Iberian Massif domain and has been operating since October 1997 (Figure 5.1). We analyze data from 1997 to 2006, with a total of 156 events which gave 40 SKS measurements. All the results obtained are shown in table 5.3. We utilize a filter of 0.01-1.0 Hz for the majority of events, where poor quality is present we elect to use a filter of 0.02-0.3 Hz.

Upper mantle anisotropy beneath MTE has been previously studied by Schmid et al. (2005), who report a mean average for ϕ=89.63° and δt=1.03 sec, which are consistent with our results.

Since we noticed (Figure 5.3) homogeneous distributions of measurement, we propose a one layer model with splitting parameters of ϕ =N93˚E and δt = 1.3 sec for MTE station.

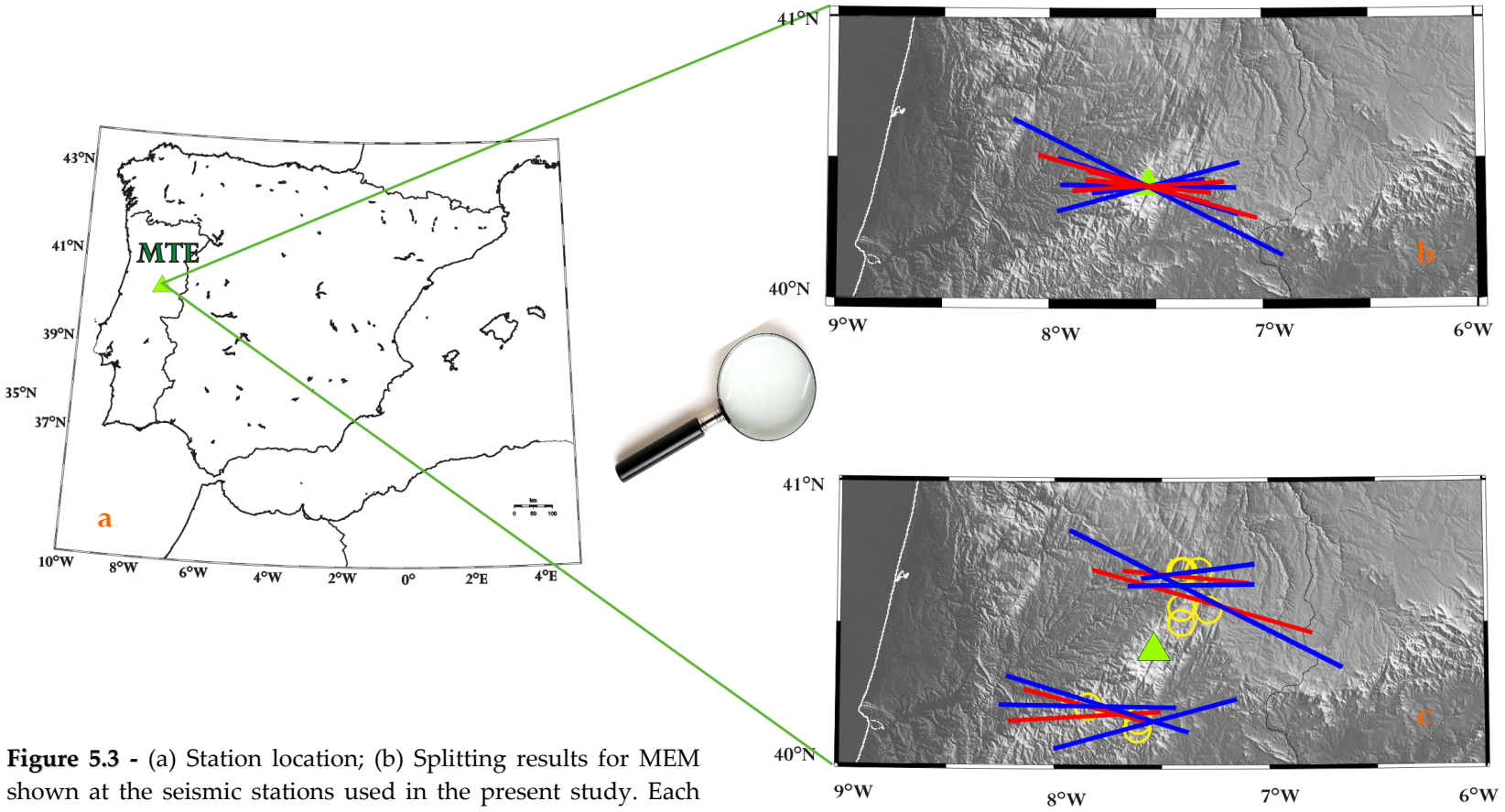

Figure 5.3 - (a) Station location; (b) Splitting results for MEM shown at the seismic stations used in the present study. Each measurement is characterized by a fast azimuth ϕ, and the length of the segment is proportional to the delay time δt. Good (red lines) and fair (blu lines) are represented; (c) Individual splitting measurements projected at 150 km depth along the ray paths. Good measurements are shown by red lines, fair measurements by blu lines. Null measurements (events with no apparent splitting) are shown by yellow circles.

Figura 5.3 - (a) Localizacíon de la estación; (b) Resultados del splitting obtenidos con el MEM projectados a la estación. Las medidas están caraterizadas por la direccíon rápida ϕ, y la longitud del segmento es proporcional al retraso δt. Se representan los valores good (líneas rojas) y los valores fair (líneas azules); (c) Las mediciones individuales del splitting estàn proyectadas a 150 km de profundidad a lo largo del recorrido del rayo. Las medidas good se muestran con líneas rojas y las fair con líneas azules. Las medidas Null (eventos con apparente no splitting) se muestran con círculos amarillos.

Date	phase	baz°	Δ°	Mw	ϕ ° ME	δt ME(s)	ϕ° RC	δt RC (s)	ϕ°EV	δt EV(s)	quality	null
1997.329	SKS	59.74	117.67	7.01	86<-84<-78	1.1<1.4<1.7	-86<-78<-71	1.1<1.3<1.5	88<-82<-74	1.1<1.4<1.7	poor	no
1998.123	SKS	43.98	102.37	7.44	48<-74<-52	0.2<1.6<4.0	60<85<-70	0.0<1.1<2.3	31<-76<-43	0.2<1.5<4.0	good	no
1998.246	SKS	231.69	92.66	6.53	84<-80<-66	0.8<1.1<1.6	73<88<-75	0.9<1.3<1.6	82<-74<-56	0.8<1.2<1.7	Poor	no
1999.344	SKS	241.31	113.11	6.49	72<77<84	2.0<2.5<3.1	-67<-49<-34	0.0<0.2<0.5	60<75<-90	1.9<2.5<3.1	poor	no
2000.114	SKS	226.57	86.88	6.93	82<87<-92	1.0<1.1<1.3	78<82<-91	1.0<1.2<1.2	76<81<88	1.1<1.2<1.3	good	no
2000.125	SKS	60.57	120.13	7.53	-88<-57<-43	0.5<1.0<1.8	-86<-75<-64	0.5<0.8<1.0	-90<-49<-33	0.5<1.2<2.1	poor	no
2000.312	SKS	192.56	99.40	6.75	68<89<-86	0.8<1.9<3.7	42<53<66	0.3<0.7<1.1	5<83<-86	0.4<1.5<3.9	fair	no
2002.090	SKS	45.24	99.12	7.09	60<87<-64	0.4<0.9<1.6	81<-89<-79	0.5<0.8<1.2	56<83<-62	0.5<1.0<1.6	poor	no
2002.169	SKS	230.40	93.33	6.43	-90<-64<-52	0.7<1.4<2.3	74<87<-79	0.4<0.8<1.1	54<-74<-52	0.5<1.1<2.2	poor	no
2002.179	SKS	28.84	86.47	7.30	68<83<-90	0.6<0.8<0.9	58<65<73	0.7<0.8<0.9	54<61<74	0.7<0.8<0.9	fair	no
2003.084	SKS	68.72	123.53	6.42	-70<-61<-56	1.6<1.9<2.1	-70<-61<-53	1.7<1.9<2.0	-78<-61<-50	1.6<1.9<2.1	poor	no
2003.146	SKS	23.64	94.47	7.00	84<-84<-82	0.6<0.9<1.2	62<70<80	0.4<0.5<0.6	Inf<-88< inf	0.0<0.8< inf	good	no
2003.171	SKS	230.86	93.48	6.77	Inf<-89<inf	0.0<1.3< inf	-89<-79<-72	1.1<1.2<1.3	-92<-83<-78	1.1<1.2<1.4	fair	no
2004.124	SKS	227.10	99.67	6.62	-90<-73<-66	1.1<1.4<1.8	79<-89<-77	0.9<1.2<1.4	76<-85<-72	1.0<1.2<1.6	fair	no
2004.207	SKS	77.07	107.51	7.28	84<-61<-21	0.3<0.8<2.6	-82<-63<-46	0.4<0.8<1.3	Inf<-89< inf	0.0<1.3< inf	poor	no
2004.249	SKS	29.32	98.15	7.38	56<89<-78	0.6<0.9<1.6	62<69<78	0.6<0.8<0.9	37<51<84	0.6<1.0<1.6	fair	no
2004.289	SKS	44.71	99.18	6.56	-86<-63<-58	1.1<2.2<3.3	59<85<-68	0.4<1.1<2.1	58<-71<-58	0.7<1.7<3.2	poor	no
2004.341	SKS	19.59	91.69	6.74	74<88<-84	0.6<1.1<1.7	50<59<71	0.4<0.6<0.8	54<84<-82	0.5<1.0<1.8	poor	no
2006.002	SKS	186.93	103.38	7.36	60<75<86	0.9<1.4<2.0	49<60<72	0.6<0.9<	62<79<88	0.9<1.5<2.1	fair	no
2006.055	SKKS	341.98	155.02	6.08	-23<-14<-11	3.4<4.0<4.0	-73<-65<-58	0.0<0.1<	-27<-18<-15	3.6<4.0<4.0	poor	no
2006.136	SKS	80.11	100.72	6.80	-92<-40<-15	0.2<0.9<2.9	-77<-67<-58	0.4<0.8<	72<-82<-27	0.2<0.9<2.0	poor	no
2006.173	SKKS	16.00	90.22	5.94	88<-88<-82	1.5<2.3<3.1	38<49<61	0.0<0.2<	84<-86<-78	1.3<2.3<3.1	poor	no
2006.197	SKS	232.66	92.47	6.18	80<-75<-62	0.7<0.9<1.3	86<-82<-69	0.6<0.9<	70<-67<-52	0.7<1.0<1.6	good	no
2006.209	SKS	45.05	99.43	5.86	70<-87<-68	0.3<0.6<0.9	83<89<-85	0.4<0.6<	Inf<-89< inf	0.0<0.6< inf	poor	no
2006.218	SKS	26.55	107.11	5.85	56<-73<-70	0.3<1.7<3.2	58<65<73	0.3<0.5<	19<-69<-64	0.1<2.1<3.2	poor	no
1997.288	SKS	230.38	93.48	7.06	-	-	-	-	-	-	fair	yes
1998.030	SKS	234.37	87.63	7.03	-	-	-	-	-	-	poor	yes
1998.301	SKS	57.00	120.15	6.49	-	-	-	-	-	-	poor	yes
1998.313	SKS	60.15	128.10	6.70	-	-	-	-	-	-	poor	yes
1999.079	SKS	353.87	86.08	6.89	-	-	-	-	-	-	poor	yes
1999.098	SKS	29.11	86.48	7.07	-	-	-	-	-	-	good	yes
1999.345	SKS	52.30	104.59	7.24	-	-	-	-	-	-	good	yes

Date	phase	baz°	Δ°	Mw	ϕ ° ME	δt ME(s)	ϕ° RC	δt RC (s)	ϕ°EV	δt EV(s)	quality	null
2000.028	SKS	18.43	91.94	6.80	-	-	-	-	-	-	fair	yes
2002.010	SKS	42.99	132.88	6.71	-	-	-	-	-	-	fair	yes
2002.116	SKS	31.44	119.29	7.03	-	-	-	-	-	-	fair	yes
2003.268	SKS	20.89	92.38	8.26	-	-	-	-	-	-	poor	yes
2004.250	SKS	192.14	99.00	6.75	-	-	-	-	-	-	good	yes
2004.282	SKKS	19.19	147.72	6.74	-	-	-	-	-	-	fair	yes
2004.333	SKS	19.63	91.56	6.98	-	-	-	-	-	-	fair	yes
2006.232	SKS	193.10	105.25	6.98	-	-	-	-	-	-	fair	yes

Table 5.2 – MTE results. We present the data events in Julian format, the analized phase, the backazimuth of the event, its epicentral distance and the Magnitud. Then, the results for ϕ and δt and their error obtained with the three methodologies and the quality factor assigned. In the grey column are null measurements data.

Tabla 5.2 – Resultados de MTE. Presentamos la fecha de los eventos en formato Juliano, el tipo de fase analizado, el backazimuth del evento, su distancia epicentral y la magnitud. Además de los resultados por ϕ y δt y sus errores obtenidos con las tres metodologías y el parámetro de calidad asignado. Las columnas en gris son los valores null.

5.3 PAB

The PAB station is located in San Pablo, near Toledo town, is in the central Spain, within the Iberian Zone domain and has been operating since Oct 29, 1992.

Digital seismograms from 1996 to the present can be downloaded from the IRIS/IGN network. Of the earthquakes with Mw≥5.5, that occured between January 1996 and December of 2005, the seismograms of 47 earthquakes could be retrieved from the data center. These resulted in 47 usable SKS splitting events, which we classified 7 good, 19 fair, 10 poor, 3 goodNull, 4 fair Null and 4 poor Null. We show all the results obtained in table 5.3. We utilize a filter of 0.01-1.0 Hz for the majority of events, where poor quality is present we elect to use a filter of 0.02-0.3 Hz.

Upper mantle anisotropy beneath PAB has been previously studied by Schmid et al. (2004) who report a mean ϕ of 74.50° and a delay time of 1.25 sec. Silver and Chan (1988, 1991), Vinnik et al. (1989) presented results from the TOL station, which was the old IGN station that was moved a few kilometers and is now the PAB station, and they inferred an anisotropy direction of E89°W. Diaz et al. (1998) inferred seismic anisotropy for a temporary station near the PAB station and they estimated two fast polarization directions of 80° and 105°. Our results are consistent with these previous studies. Since we notice (Figure 5.4) homogeneous distributions of measurement, we propose a one layer model with splitting parameters of ϕ =N86°E and δt = 1.1 sec for PAB station.

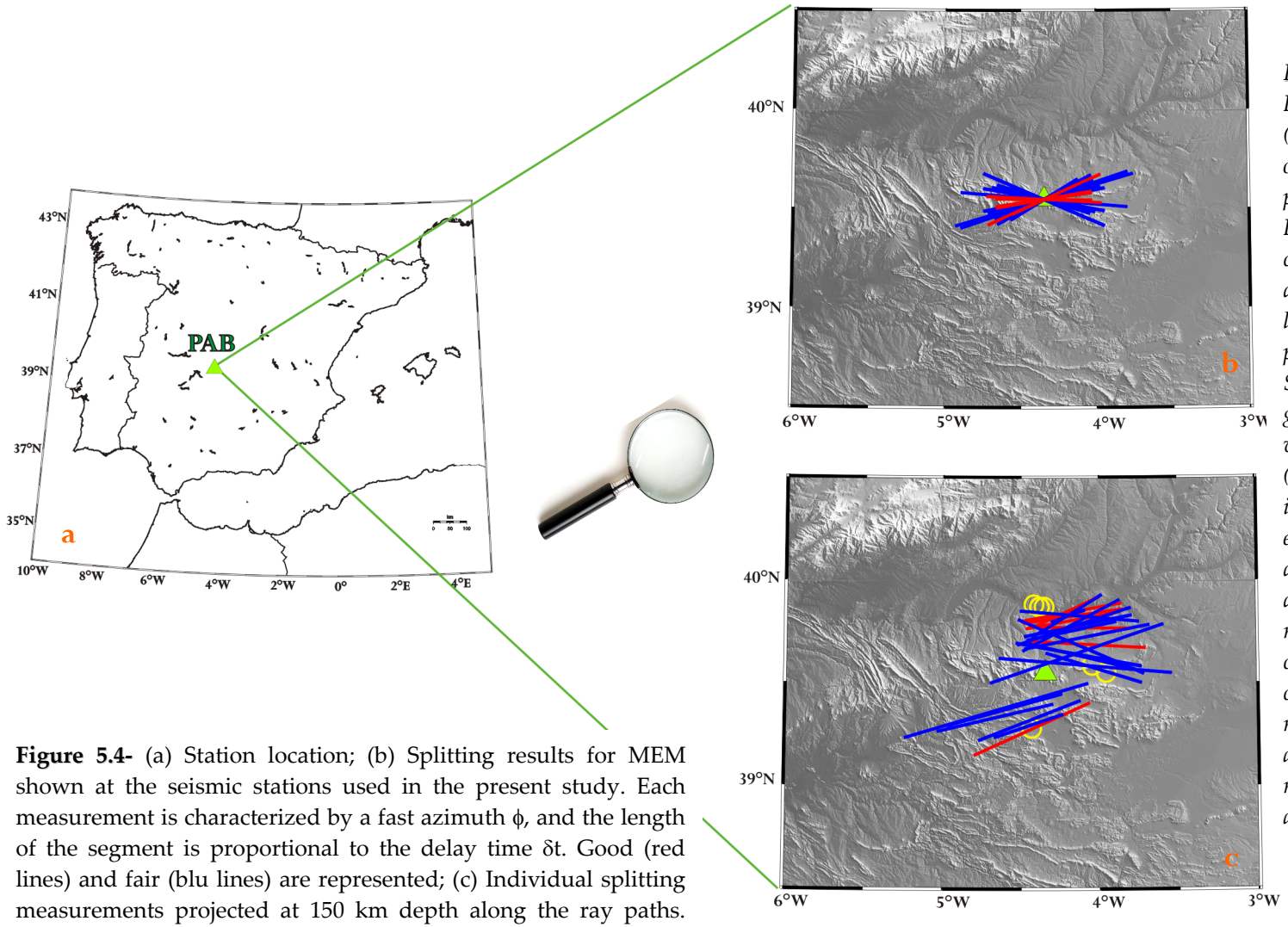

Figure 5.4- (a) Station location; (b) Splitting results for MEM shown at the seismic stations used in the present study. Each measurement is characterized by a fast azimuth ϕ, and the length of the segment is proportional to the delay time δt. Good (red lines) and fair (blu lines) are represented; (c) Individual splitting measurements projected at 150 km depth along the ray paths. Good measurements are shown by red lines, fair measurements by blu lines. Null measurements (events with no apparent splitting) are shown by yellow circles.

Figura 5.4 - (a) Localizacíon de la estación; (b) Resultados del splitting obtenidos con el MEM projectados a la estación. Las medidas están caraterizadas por la direccíon rápida ϕ, y la longitud del segmento es proporcional al retraso δt. Se representan los valores good (líneas rojas) y los valores fair (líneas azules); (c) Las mediciones individuales del splitting estàn proyectadas a 150 km de profundidad a lo largo del recorrido del rayo. Las medidas good se muestran con líneas rojas y las fair con líneas azules. Las medidas Null (eventos con apparente no splitting) se muestran con círculos amarillos.

Date	phase	baz°	Δ°	Mw	ϕ ° ME	δt ME(s)	ϕ° RC	δt RC (s)	ϕ°EV	δt EV(s)	quality	null
1996.163	SKS	53.19	109.86	7.06	-88<-67<-58	1.0<1.4<1.9	88<-83<-73	1.0<1,2<1,5	60<-83<-60	0,9<1,2<2,1	fair	no
1996.198	SKS	65.49	115.24	6.55	-90<-77<-68	0.8<1.1<1.3	-79<-68<-60	0.8<1,0<1,2	-82<-69<-60	0,8<1,0<1,2	fair	no
1996.204	SKS	65.35	115.40	6.98	-92<-81<-72	1.1<1.6<2.0	-83<-72<-62	1.0<1,4<1,7	-92<-79<-68	1,1<1,5<2,0	poor	no
1996.249	SKS	49.89	100.46	6.79	76<86<-88	1.0<1.3<1.7	78<84<-88	1.1<1,4<1,5	64<74<86	1,2<1,5<1,8	poor	no
1996.293	SKS	36,66	97,65	6,71	-inf<-89<inf	0.0<1.0<1.1	71<84<-83	0.7<0.9<1.2	-inf<-89<inf	0.0<1.0<1.1	good	no
1996.357	SKS	25.85	90.83	6.49	78<82<86	0,9<1,0<1,1	84<88<-90	1,0<1,1<1,1	84<90<-90	1,0<1,1<1,1	good	no
1997.288	SKS	232.25	93.87	7.06	74<-88<-68	0,6<0,9<1,3	-87<-78<-70	0,8<1,1<1,3	84<-78<-60	0,7<0,9<1,2	poor	no
1998.232	SKS	32.24	103.64	7.05	70<78<-92	0,8<0,9<1,1	74<82<-90	0,8<1,0<1,1	68<84<-84	0,8<1,0<1,2	fair	no
1998.246	SKS	233.60	93.13	6.53	70<74<78	1,6<1,9<2,3	85<-75<-56	0,7<1,0<1,5	72<78<-78	0,9<1,7<2,1	fair	no
1998.271	SKS	78.87	115.74	6.53	-90<-85<-86	1,5<1,7<2,0	-44<-37<-31	0,0<0,2<0,2	88<-87<-84	1,5<1,8<2,0	fair	no
1998.301	SKS	60.96	119.31	6.49	78<87<-86	1,3<1,8<2,5	68<76<86	1,9<2,2<2,4	62<77<-90	1,5<2,1<2,6	poor	no
1999.098	SKS	31.01	87.34	7.07	88<-85<-84	1,0<1,2<1,4	88<-85<-80	1,0<1,2<1,4	-90<-81<-78	1,1<1,3<1,6	fair	no
1999.263	SKS	49.06	98.71	7.62	62<79<-70	0,8<1,3<2,6	89<-80<-70	0,8<1,1<1,4	78<-69<-52	0,8<1,2<2,5	fair	no
1999.345	SKS	55.25	104.06	7.24	82<-87<-76	1,0<1,2<1,5	89<-79<-67	0,9<1,2<1,4	84<-81<-66	1,0<1,2<1,5	good	no
2000.028	SKS	20.66	93.39	6.80	48<59<74	0,7<0,8<1,0	66<74<84	0,7<0,8<0,9	68<81<-90	0,7<0,8<1,0	fair	no
2000.114	SKS	228.83	87.06	6.93	66<77<-90	0,8<1,2<1,8	-88<-77<-68	0,8<1,0<1,1	78<-81<-60	0,7<0,9<1,3	fair	no
2000.125	SKS	64.50	119.09	7.53	80<86<-88	1,4<1,9<2,5	87<-69<-49	0,5<1,0<1,8	72<82<-84	1,3<2,1<2,6	poor	no
2000.156	SKS	83.07	105.66	7.85	-86<-73<-48	0,6<1,0<1,6	-71<-56<-43	0,5<0,8<1,0	-90<-79<-58	0,7<1,2<1,9	fair	no
2001.055	SKS	60.39	119.18	7.04	88<-80<-66	0,9<1,3<1,6	-84<-63<-45	1,0<1,3<1,6	-92<-58<-37	0,9<1,3<1,7	fair	no
2001.083	SKS	34.72	96.28	6.80	72<79<-92	0,9<1,1<1,3	Inf<90<inf	0,0<1,1<inf	Inf<-89<inf	0,0<1,1<inf	fair	no
2002.090	SKS	47.87	99.01	7.09	88<-76<-68	0,8<1,1<1,5	Inf<90<inf	0,0<1,0<inf	86<-78<-68	0,8<1,1<1,5	poor	no
2002.306	SKS	81.14	96.20	7.24	-88<-75<-62	1,1<1,7<2,4	-90<-83<-68	1,3<2,1<2,6	86<-87<-78	1,5<2,2<2,8	poor	no
2002.319	SKS	197.48	99.39	6.62	27<71<-82	0,2<0,7<1,6	50<62<76	0,2<0,6<0,9	25<75<-66	0,2<0,7<3,5	fair	no
2002.321	SKS	19.28	88.80	7.28	56<65<76	0,6<0,7<0,8	71<76<84	0,7<0,8<0,8	70<81<88	0,7<0,8<0,9	good	no
2003.146	SKS	26.01	95.62	7.00	68<80<-90	0,7<0,9<1,1	74<79<87	0,8<0,9<1,0	84<-86<-80	0,8<1,1<1,3	good	no
2003.146	SKS	57.33	120.09	6.93	66<71<84	0,9<1,8<2,6	-80<-67<-56	0,1<0,4<0,7	66<75<-76	0,4<1,5<2,4	fair	no
2003.208	SKS	23.83	87.44	6.71	70<80<88	0,8<1,0<1,1	70<79<88	0,8<1,0<1,1	76<84<-92	0,9<1,0<1,2	good	no
2003.216	SKS	198.73	105.06	7.56	43<69<-92	0,6<1,1<1,6	65<74<86	0,7<1,0<1,3	70<89<-76	0,8<1,2<1,8	fair	no
2003.272	SKS	22.56	93.24	6.44	33<47<80	0,5<1,1<2,0	60<74<-91	0,2<0,6<0,9	31<55<-80	0,4<0,9<2,1	poor	no
2003.322	SKS	53.37	110.48	6.50	-72<-57<-50	1,1<1,9<2,7	-90<-65<-53	0,6<1,6<2,2	-70<-51<-43	1,3<2,1<2,8	poor	no
2004.052	SKS	185.59	98.37	6.59	52<66<76	1,1<1,7<2,3	47<63<78	1,4<1,8<2,1	33<64<86	1,0<1,7<2,3	poor	no
2004.124	SKS	228.60	99.86	6.62	66<75<-90	0,8<1,2<1,8	85<-83<-71	0,6<0,9<1,1	64<79<-76	0,7<1,1<1,8	fair	no

Date	phase	baz°	Δ°	Mw	ϕ ° ME	δt ME(s)	ϕ° RC	δt RC (s)	ϕ°EV	δt EV(s)	quality	null
2004.150	SKS	28.16	99.71	6.27	46<62<84	0,8<1,1<1,8	69<78<88	0,8<1,1<1,2	50<72<-84	0,7<1,0<1,6	fair	no
2004.250	SKS	193.81	97.21	6.75	70<80<88	1,1<1,3<1,5	53<64<76	1,1<1,3<1,5	54<66<80	1,1<1,3<1,6	good	no
2004.250	SKS	31.77	99.02	6.60	56<66<74	0,8<1,2<1,7	64<78<-87	0,8<1,1<1,4	39<80<-74	0,8<1,1<2,2	fair	no
2004.333	SKS	21.84	92.95	6.98	33<70<-74	0,0<0,4<1,1	53<64<76	0,4<0,6<0,7	35<76<-68	0,1<0,4<1,2	fair	no
1996.162	SKS	355.34	88.74	7.22	-	-	-	-	-	-	good	yes
1996.293	SKS	36.66	97.65	6.71	-	-	-	-	-	-	good	yes
1999.028	SKS	350.87	86.63	6.59	-	-	-	-	-	-	good	yes
1999.319	SKS	88.91	93.42	6.95	-	-	-	-	-	-	fair	yes
2000.312	SKS	194.21	97.63	6.75	-	-	-	-	-	-	fair	yes
2003.027	SKS	153.83	92.57	6.41	-	-	-	-	-	-	poor	yes
2003.174	SKS	359.30	89.01	6.88	-	-	-	-	-	-	fair	yes
2004.207	SKS	79.99	105.62	7.28	-	-	-	-	-	-	fair	yes
2004.289	SKS	47.35	99.10	6.56	-	-	-	-	-	-	poor	yes
2004.316	SKS	69.34	124.95	7.49	-	-	-	-	-	-	poor	yes
2005.046	SKS	57.64	116.68	6.50	-	-	-	-	-	-	poor	yes

Table 5.3 – PAB results. We present the data events in Julian format, the analized phase, the backazimuth of the event, its epicentral distance and the Magnitud. Then, the results for ϕ and δt and their error obtained with the three methodologies and the quality factor assigned. In the grey column are null measurements data.

Tabla 5.3 – Resultados de PAB. Presentamos la fecha de los eventos en formato Juliano, el tipo de fase analizado, el backazimuth del evento, su distancia epicentral y la magnitud. Además de los resultados por ϕ y δt y sus errores obtenidos con las tres metodologías y el parámetro de calidad asignado. Las columnas en gris son los valores null.

5.4 ARAC

The station ARAC is located in the *gruta de las maravillas* in the Sierra of Aracena (Huelva), within the Ossa-Morena domain and at the boundary with the South Portuguese Zone (Figure 5.5). Data for this station since 2004 are available in continuous wave form; however in 2003 only some seismogram fragments are available, from which we were able to obtain 2 events. In the end, we analyzed data up 2006 for an amount of 70 events, that resulted in 13 SKS useful events, which we classified as 4 good, 4 fair, 2 are good Null, 1 fair Null and 2 poor Null. We utilize a filter of 0.01-1.0 Hz for the majority of events, where poor quality is present we elect to use a filter of 0.02-0.3 Hz. We show all the results obtained in table 5.4 and in the Figure A-4 in the appendix.

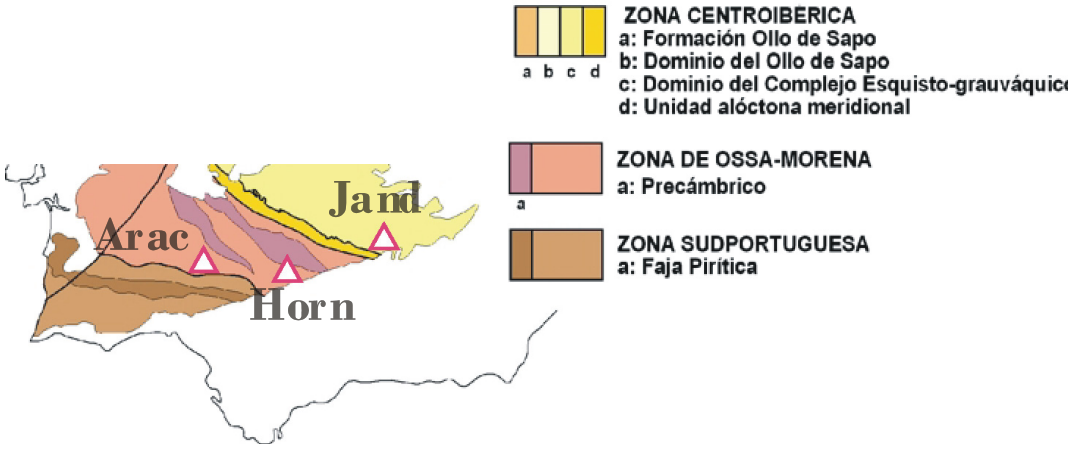

Figure 5.5 - Map of the Southern Iberian Massif showing the main geological units and station location for ARAC, HORN and JAND.

Figura 5.5 – Mapa de la parte sur del Macizo Ibérico, donde se muestran las principales unidades geológicas y la localización de las estaciónes ARAC, HORN y JAND

The majority of events arrived from Northeast, with only three arriving from Southwest (Figure 5.6), and we noted that a backazimuthal dependence of ϕ could be present even without the presence of good azimuthal coverage. Such a backazimuthal dependence of splitting parameters may be explained by either the invoking vertical variation of anisotropy, e.g. by the presence of two (or more) anisotropic layers, or by lateral variations of anisotropy. These possible explications will be further discussed in the Chapter 7.1. Since this ambiguity is in part due to

the backazimuthal distribution of the events being rather limited, we prefer the alternative hypothesis of an anisotropy that varies laterally. Furthermore, we propose a one layer model with splitting parameters of ϕ =N64˚E and δt = 1.0 sec for the ARAC station.

Figure A-5 (appendix) shows the best 2 layer model fit for the upper layer with the fast direction ϕ=N52°E and delay time δt=1.2s, while fast direction in the lower layer ϕ=N136°E and delay time δt=0.2s.

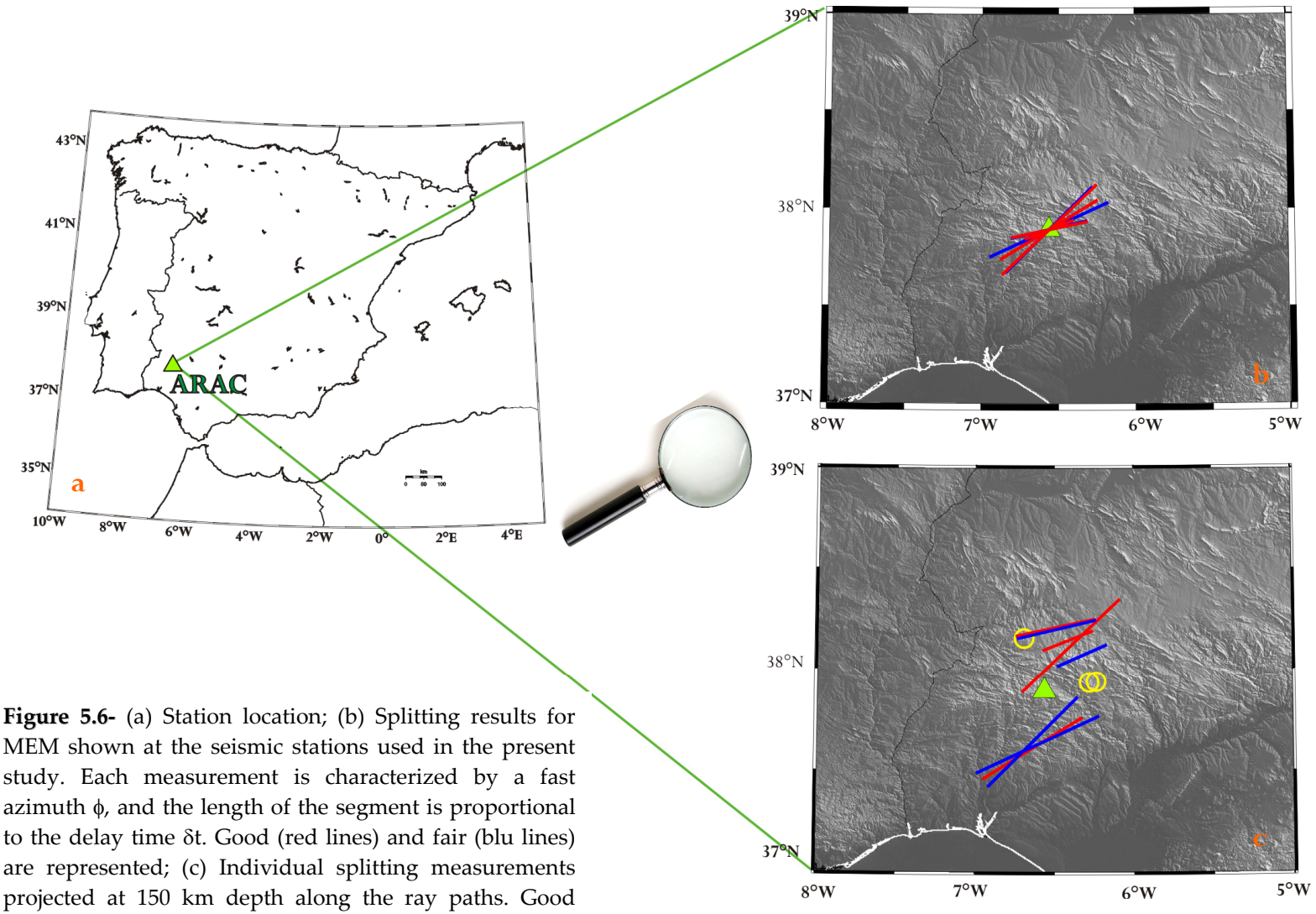

Figure 5.6- (a) Station location; (b) Splitting results for MEM shown at the seismic stations used in the present study. Each measurement is characterized by a fast azimuth ϕ, and the length of the segment is proportional to the delay time δt. Good (red lines) and fair (blu lines) are represented; (c) Individual splitting measurements projected at 150 km depth along the ray paths. Good measurements are shown by red lines, fair measurements bv blu lines. Null measurements (events with no

Figura 5.6 - (a) Localizacíon de la estación; (b) Resultados del splitting obtenidos con el MEM projectados a la estación. Las medidas están caraterizadas por la direccíon rápida ϕ, y la longitud del segmento es proporcional al retraso δt. Se representan los valores good (líneas rojas) y los valores fair (líneas azules); (c) Las mediciones individuales del splitting estàn proyectadas a 150 km de profundidad a lo largo del recorrido del rayo. Las medidas good se muestran con líneas rojas y las fair con líneas azules. Las medidas Null (eventos con apparente no splitting) se muestran con círculos amarillos.

Date	phase	baz°	Δ°	Mw	ϕ ° ME	δt ME(s)	ϕ° RC	δt RC (s)	ϕ°EV	δt EV(s)	quality	null
2003.146	SKS	24.52	97.86	7	50< 69 <-92	0.5<0.6<0.6	75<81<88	0.4< 0.5 <0.7	-92<-79<-74	0.8<1.1<1.1	good	no
2004.249	SKS	30.40	101.29	7.38	39< 46 < 76	0.4<0.6<0.8	73<80<-91	0.6< 1.4 <2.5	41<60<-66	0.4<0.8<2.1	good	no
2004.250	SKS	192.57	95.21	6.75	43< 59 < 74	1.0<1.2<1.3	58<65<73	0.9< 1.2 <1.4	68<81<-92	1.1<1.4<1.9	good	no
2006.002	SKS	187.30	99.45	7.36	39< 65 < 82	0.9<1.1<1.4	49<56<65	0.8< 1.3 <2.1	56<81<-90	1.0<1.8<2.7	fair	no
2006.209	SKS	46.31	101.72	5.86	56< 66 <-86	0.2<0.3<0.4	-91<-85<-79	0.3< 0.6 <1.2	48<72<-62	0.2<0.5<1.8	fair	no
2006.232	SKS	10.87	90.94	5.98	54< 77 < 88	0.4<0.6<0.8	51<59<70	0.5< 0.8 <1.3	72<89<-86	0.7<1.2<1.7	fair	no
2006.232	SKS	193.33	101.48	6.98	27< 45 < 76	0.6<1.1<1.6	46<60<77	0.6< 1.3 <2.3	23<51<-90	0.6<1.2<2.4	fair	no
2006.236	SKS	9.90	89.83	6.46	60< 78 < 86	0.5<0.6<0.7	54<62<72	0.5< 0.8 <1.2	80<90<-86	0.8<1.2<1.6	good	no
2003.146	SKS	57.26	115.74	6.84	-	-	-	-	-	-	poor	yes
2004.207	SKS	79.00	107.62	7.28	-	-	-	-	-	-	good	yes
2005.134	SKS	80.17	101.43	6.72	-	-	-	-	-	-	good	yes
2006.034	SKS	75.08	89.60	6.07	-	-	-	-	-	-	poor	yes
2006.204	SKKS	338.89	158.74	5.76	-	-	-	-	-	-	fair	yes

Table 5.4 – ARAC results. We present the data events in Julian format, the analized phase, the backazimuth of the event, its epicentral distance and the Magnitud. Then, the results for ϕ and δt and their error obtained with the three methodologies and the quality factor assigned. In the grey column are null measurements data.

Tabla 5.4 – Resultados de ARAC. Presentamos la fecha de los eventos en formato Juliano, el tipo de fase analizado, el backazimuth del evento, su distancia epicentral y la magnitud. Además de los resultados por ϕ y δt y sus errores obtenidos con las tres metodologías y el parámetro de calidad asignado. Las columnas en gris son los valores null.

5.5 HORN

The HORN IAG station is located near Hornachuelo town (Cordoba), in the Sierra Morena natural park, within the Ossa Morena geological domain. The data are of relatively good quality. From 2003 to 2006 a total of 195 events were available, of which 22 were processed, 7 are good, 7 are fair, 4 good null and 4 fair null. We show all the results obtained in table 5.5 and in the Figure A-4 in the appendix. For 2003, only same seismogram fragments were available, and continued records are available since 2004. We utilize a filter of 0.01-1.0 Hz for the majority of event, where poor quality is present we elect to use a filter of 0.02-0.3 Hz.

We observe that a backazimuthal dependence of splitting parameters is present. Results for the ARAC station will be further discussed in the Chapter 7.1. Figure A-7 (appendix) presents the best two-layer model fit for fast direction in upper layer ϕ=N52°E and delay time δt=1.2s, while fast direction in the lower layer ϕ=N136°E and delay time δt=0.2s. How we can see we do not obtained a good fit to imagine that two layers are present. Furthermore, we propose a one layer model with splitting parameters of ϕ =N58˚E and δt = 1.1 sec for the HORN station.

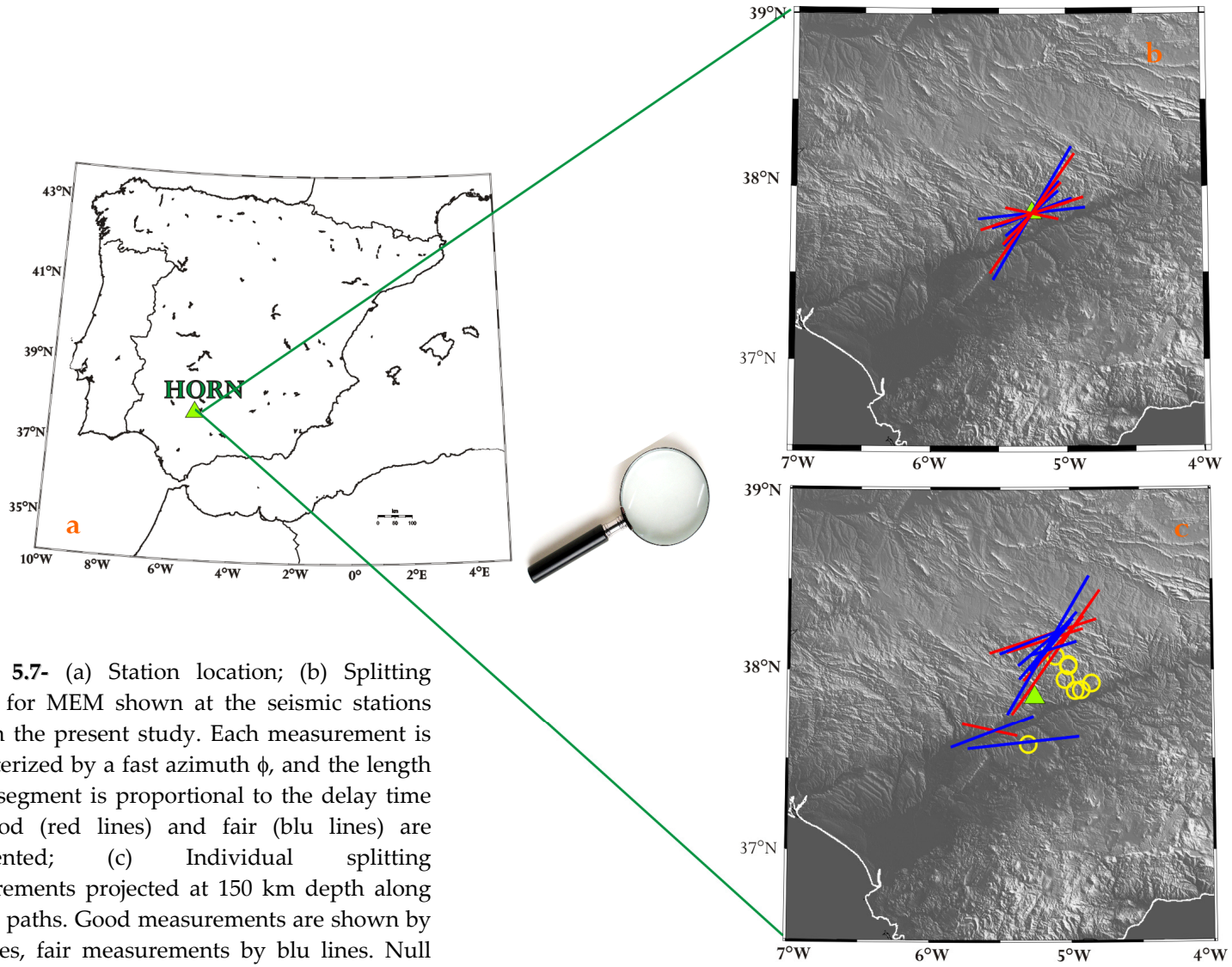

Figure 5.7- (a) Station location; (b) Splitting results for MEM shown at the seismic stations used in the present study. Each measurement is characterized by a fast azimuth ϕ, and the length of the segment is proportional to the delay time δt. Good (red lines) and fair (blu lines) are represented; (c) Individual splitting measurements projected at 150 km depth along the ray paths. Good measurements are shown by red lines, fair measurements by blu lines. Null measurements (events with no apparent splitting) are shown by yellow circles.

Figura 5.7 - (a) Localizacíon de la estación; (b) Resultados del splitting obtenidos con el MEM projectados a la estación. Las medidas están caraterizadas por la direccíon rápida ϕ, y la longitud del segmento es proporcional al retraso δt. Se representan los valores good (líneas rojas) y los valores fair (líneas azules); (c) Las mediciones individuales del splitting están proyectadas a 150 km de profundidad a lo largo del recorrido del rayo. Las medidas good se muestran con líneas rojas y las fair con líneas azules. Las medidas Null (eventos con apparente no splitting) se muestran con círculos amarillos.

Date	phase	baz°	Δ°	Mw	ϕ ° ME	δt ME(s)	ϕ° RC	δt RC (s)	ϕ°EV	δt EV(s)	quality	null
2003.146	SKS	25.45	97,46	7,00	33<35<39	1,4<1,8<2,0	68<75<85	0,3<0,4<0,4	41<43<50	0,8<1,1<1,4	good	no
2003.167	SKS	8.31	85,82	6,86	64<72<82	0,9<1,2<1,7	49<62<-89	0,6<0,9<2,4	76<82<-92	1,2<1,6<2,2	good	no
2003.174	SKS	358.73	90,70	6,88	43<69<80	0,4<0,8<1,5	32<42<54	0,2<0,4<0,6	43<73<84	0,4<1,0<1,6	fair	no
2004.333	SKS	21.27	94,79	6,98	33<73<-78	0,2<0,5<1,5	51<57<65	0,4<0,5<0,7	21<41<-92	0,2<0,6<1,2	fair	no
2004.341	SKS	21.23	94,92	6,74	37<43<56	0,6<1,0<1,3	61<71<82	0,5<0,6<0,7	48<65<-92	0,5<0,6<0,9	fair	no
2005.228	SKS	25.37	98,14	7,19	33<35<43	0,8<1,5<2,0	72<80<-91	0,2<0,3<0,4	39<67<-68	0,3<0,4<1,2	fair	no
2006.173	SKS	17.56	93,64	5,94	29<40<60	0,4<0,7<1,1	60<65<72	0,4<0,5<0,6	31<46<78	0,4<0,6<1,0	good	no
2006.197	SKS	233.98	91,43	6,18	82<-78<-66	0,6<0,7<0,9	-90<-81<-73	0,5<0,6<0,8	70<-84<-60	0,6<0,7<1,1	good	no
2006.232	SKS	11.69	90,79	5,98	29<50<80	0,5<08<1,3	48<61<78	0,6<0,9<1,1	41<-82<-74	0,7<1,8<2,4	good	no
2006.236	SKS	10.69	89,69	6,46	56<73<84	0,6<0,9<1,3	47<56<66	0,6<0,7<0,9	31<61<84	0,6<0,8<1,2	good	no
2006.249	SKS	193.83	101,45	5,75	50<84<-88	0,5<1,2<2,2	52<64<80	0,4<0,8<1,2	80<-84<-78	1,0<1,8<2,6	good	no
2006.274	SKS	14.66	93,41	6,57	23<31<60	0,8<1,8<3,0	47<61<76	0,5<0,9<1,3	17<27<68	0,7<2,2<3,5	fair	no
2006.285	SKS	231.43	92,60	6,36	58<69<-56	0,3<1,0<2,3	-86<-79<-73	0,2<0,4<0,6	62<-57<-37	0,2<0,7<2,6	fair	no
2006.286	SKS	14,68	93,67	5,84	29<41<72	0,6<1,0<1,6	49<62<77	0,6<0,7<0,9	41<83<-82	0,6<0,9<1,8	fair	no
2004.150	SKS	27,62	101,54	6,27	-	-	-	-	-	-	fair	yes
2004.207	SKS	79,87	106,62	7,28	-	-	-	-	-	-	fair	yes
2005.036	SKS	21,27	115,72	7,08	-	-	-	-	-	-	fair	yes
2005.134	SKS	21,23	100,42	6,72	-	-	-	-	-	-	good	yes
2005.288	SKS	59,74	100,55	6.42	-	-	-	-	-	-	good	yes
2006.002	SKS	81,01	99,54	7.36	-	-	-	-	-	-	good	yes
2006.034	SKS	25,37	88,61	6.07	-	-	-	-	-	-	good	yes
2006.209	SKS	45,92	101,00	5.86	-	-	-	-	-	-	fair	yes

Table 5.5 – HORN results. We present the data events in Julian format, the analized phase, the backazimuth of the event, its epicentral distance and the Magnitud. Then, the results for ϕ and δt and their error obtained with the three methodologies and the quality factor assigned. In the grey column are null measurements data.

Tabla 5.5 – Resultados de HORN. Presentamos la fecha de los eventos en formato Juliano, el tipo de fase analizado, el backazimuth del evento, su distancia epicentral y la magnitud. Además de los resultados por ϕ y δt y sus errores obtenidos con las tres metodologías y el parámetro de calidad asignado. Las columnas en gris son los valores null.

5.6 JAND

The JAND station is located in the Sierra Morena, near the *pantano de la Lancia*, within the Central Iberian Zone geological domain (Figure 5.5). This station was installed in July of 2006 and we analyzed data from July of 2006 to December of 2006, therefore we only had available data for the period of a few months. A total of 56 events were checked, but in the end only 4 data are obteined, and we clasified 2 fair, 1 good and 1 fair null. We show all the results obtained in table 5.6 and in the Figure A-6 in the appendix. We utilize a filter of 0.01-1.0 Hz for the majority of events, where poor quality is present we elect to use a filter of 0.02-0.3 Hz.

For Northeastern events, the no-null events gave similar results, while the null events gave a near perpendicular orientation with respect to the no-nulls. Thus, there is that there are two layers of anisotropy mutually perpendicular. On the other hand, the Southeastern event had a WS-NE anisotropy orientation. These results could reflect the presence of two layer anisotropy. Unfortunately, a concrete conclusion cannot be made at this time due to the lack of data, but a growing data set for in the coming years may give us a clearer understanding. Figure A-9 (in the appendix) shows the best fit for two layer model. Furthermore, we propose a one layer model with splitting parameters of ϕ =N6˚E and δt = 1.7 sec for the JAND station.

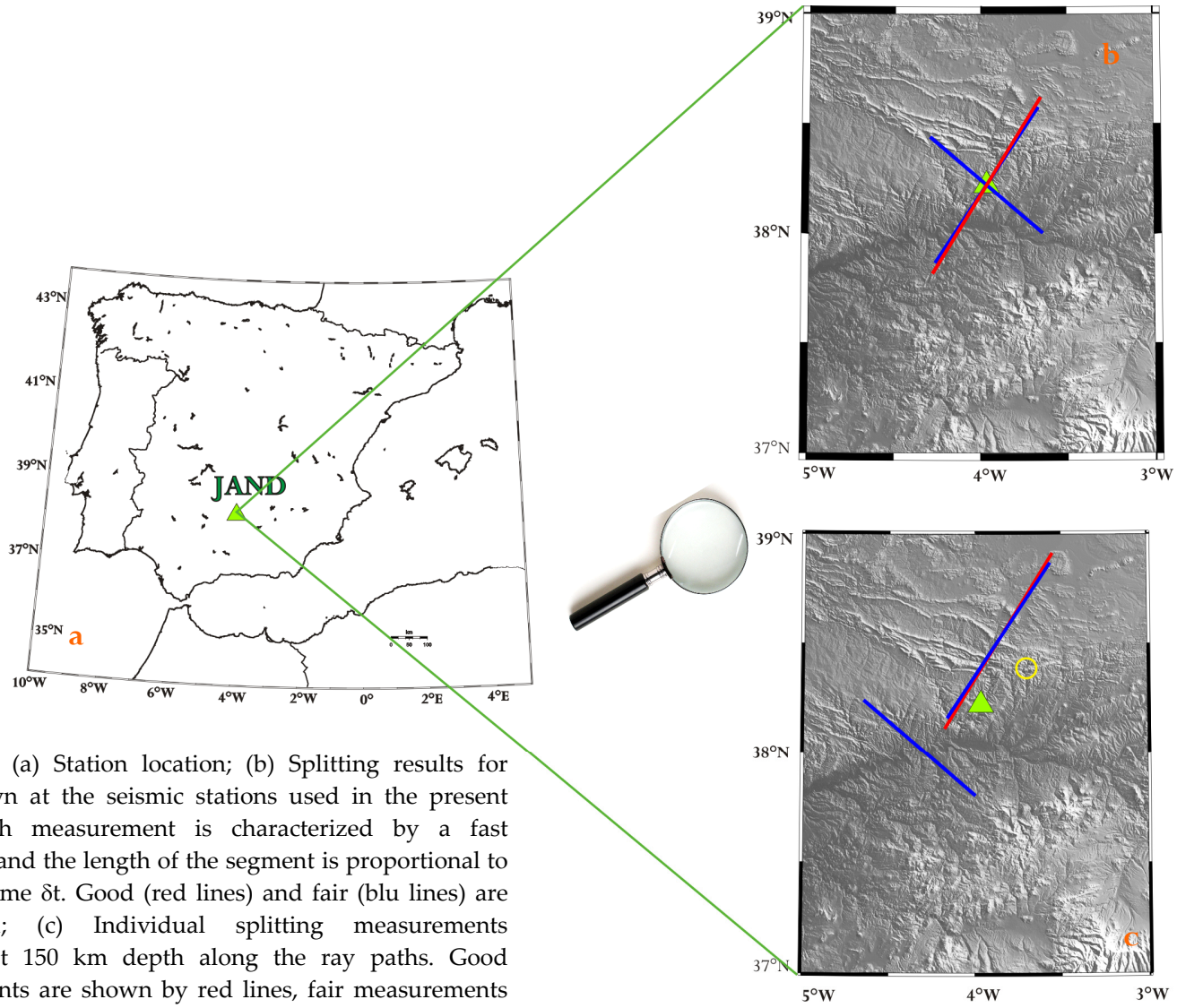

Figure 5.8- (a) Station location; (b) Splitting results for MEM shown at the seismic stations used in the present study. Each measurement is characterized by a fast azimuth ϕ, and the length of the segment is proportional to the delay time δt. Good (red lines) and fair (blu lines) are represented; (c) Individual splitting measurements projected at 150 km depth along the ray paths. Good measurements are shown by red lines, fair measurements by blu lines. Null measurements (events with no apparent splitting) are shown by yellow circles.

Figura 5.8 - (a) Localizacíon de la estación; (b) Resultados del splitting obtenidos con el MEM projectados a la estación. Las medidas están caraterizadas por la direccíon rápida ϕ, y la longitud del segmento es proporcional al retraso δt. Se representan los valores good (líneas rojas) y los valores fair (líneas azules); (c) Las mediciones individuales del splitting estàn proyectadas a 150 km de profundidad a lo largo del recorrido del rayo. Las medidas good se muestran con líneas rojas y las fair con líneas azules. Las medidas Null (eventos con apparente no splitting) se muestran con círculos amarillos.

Date	phase	baz°	Δ°	Mw	ϕ ° ME	δt ME(s)	ϕ° RC	δt RC (s)	ϕ°EV	δt EV(s)	quality	null
2006.237	SKS	234,43	85,92	6,58	-60<-50<-48	1.0<1.4<1.9	84<-88<-80	0.3<0.5<0.7	-62<-50<-46	0.9<1.4<1.8	fair	no
2006.274	SKS	15,50	92,78	6,57	27<34<41	1.2<1.7<2.3	59<65<73	0.6<0.8<0.9	33<44<72	0.7<1.2<1.9	fair	no
2006.286	SKS	15,52	93,04	5,84	27<32<39	1.3<1.9<4.0	59<70<84	0.6<0.8<1.0	33<48<-92	0.6<1.1<1.8	good	no
2006.360	SKS	51,35	100,43	6,85	-	-	-	-	-	-	fair	yes

Table 5.6 – JAND results. We present the data events in Julian format, the analized phase, the backazimuth of the event, its epicentral distance and the Magnitud. Then, the results for ϕ and δt and their error obtained with the three methodologies and the quality factor assigned. In the grey column are null measurements data.

Tabla 5.6 – Resultados de JAND. Presentamos la fecha de los eventos en formato Juliano, el tipo de fase analizado, el backazimuth del evento, su distancia epicentral y la magnitud. Además de los resultados por ϕ y δt y sus errores obtenidos con las tres metodologías y el parámetro de calidad asignado. Las columnas en gris son los valores null.

5.7 SESP

The SESP station is located in Northern Santiago de la Espada (Jaén), near the *paraje de Mirabueno*, within the Prebbetic domain (External Zone of Betics) (Figure 4.4).

We analyzed data from 2002 to 2006 for a total of 212 events, from which 31 anisotropy measurements were obtained 5 good, 6 fair, 1 poor, 8 are good null, 8 are fair null and 3 are poor null. We show all the results obtained in table 5.7 and in the Figure A-7 in the appendix. We utilize a filter of 0.01-1.0 Hz for the majority of events, where poor quality is present we elect to use a filter of 0.02-0.3 Hz.

The average for the fast direction is more or less the same for the three methodologies. The scattering of the data, visible in Figure 5.9a, implies the possible presence of two layers anisotropic. The relation of the results with the back azimuth, as in the projection of 150km depth, shows that this scattering is preserved, both for good and fair data (Figure 5.9b). The Null values are consistent as their back azimuth coincide with fast directions.

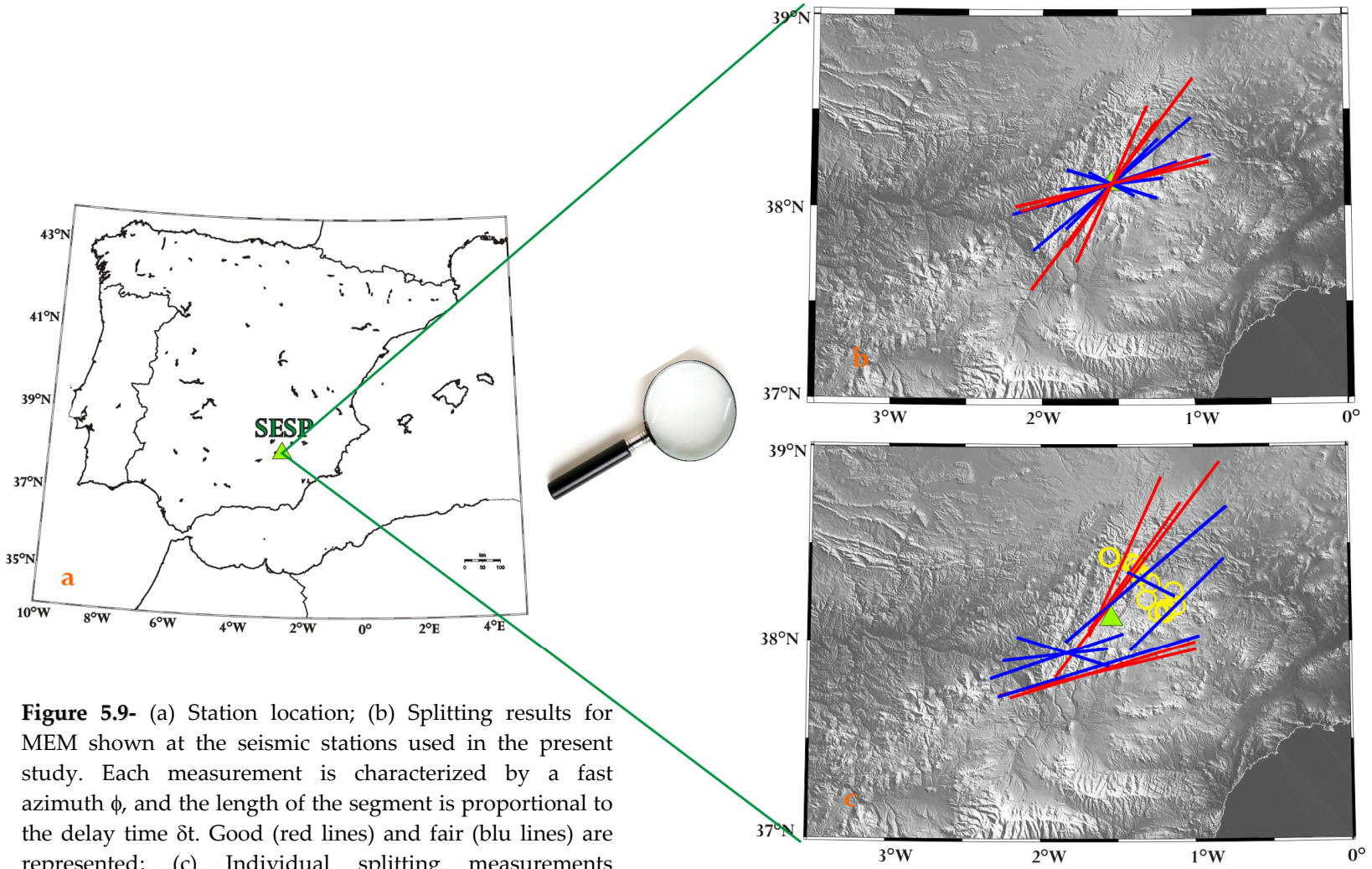

Figure 5.9- (a) Station location; (b) Splitting results for MEM shown at the seismic stations used in the present study. Each measurement is characterized by a fast azimuth ϕ, and the length of the segment is proportional to the delay time δt. Good (red lines) and fair (blu lines) are represented; (c) Individual splitting measurements projected at 150 km depth along the ray paths. Good measurements are shown by red lines, fair measurements by blu lines. Null measurements (events with no apparent splitting) are shown by yellow circles.

Figura 5.9 - (a) Localizacíon de la estación; (b) Resultados del splitting obtenidos con el MEM projectados a la estación. Las medidas están caraterizadas por la direccíon rápida ϕ, y la longitud del segmento es proporcional al retraso δt. Se representan los valores good (líneas rojas) y los valores fair (líneas azules); (c) Las mediciones individuales del splitting estàn proyectadas a 150 km de profundidad a lo largo del recorrido del rayo. Las medidas good se muestran con líneas rojas y las fair con líneas azules. Las medidas Null (eventos con apparente no splitting) se muestran con círculos amarillos.

Date	phase	baz°	Δ°	Mw	ϕ ° ME	δt ME(s)	ϕ° RC	δt RC (s)	ϕ°EV	δt EV(s)	quality	null
2003.146	SKS	27,34	96,27	7,00	35<37<39	2,4<2,8<3,2	81<87<-87	0,0<0,2<0,3	39<41<46	2,2<2,7<3,1	good	no
2004.250	SKS	194,74	96,18	6,75	72<77<82	1,9<2,1<2,4	68<76<83	1,8<2,1<2,4	72<79<86	1,9<2,2<2,5	good	no
2005.079	SKS	37,87	95,72	6,58	46<50<54	1,4<2,2<2,9	89<-80<-70	0,1<0,3<0,5	-41<-28<-23	1,1<1,9<2,3	fair	no
2005.321	SKS	237,43	86,03	6,79	76<83<-88	0,8<1,1<1,4	82<88<-84	0,8<1,0<1,2	70<75<86	1,0<1,3<1,6	fair	no
2006.002	SKS	189,24	100,13	7,36	70<73<80	1,7<2,0<2,4	57<72<81	1,4<2,0<2,3	62<73<84	1,6<2,0<2,5	good	no
2006.034	SKS	77,53	86,46	6,07	27<46<60	0,8<1,4<1,9	26<41<55	1,0<1,3<1,6	15<48<70	0,8<1,4<2,0	fair	no
2006.197	SKS	235,60	93,34	6,18	82<-72<-56	0,6<1,0<1,5	80<87<-86	0,8<0,9<1,1	52<66<-90	0,8<1,3<2,0	fair	no
2006.209	SKS	49,15	99,22	5,86	58<-63<-46	0,0<0,6<4,0	71<81<-88	0,1<0,3<0,5	64<-63<-46	0,1<0,6<1,2	fair	no
2006.219	SKKS	23,63	156,17	6,81	29<36<41	1,3<1,6<1,9	-24<-11<-1	0,0<0,1<0,2	23<32<39	1,4<1,6<1,8	good	no
2006.232	SKS	195,17	102,48	6,98	66<73<80	1,7<2,2<2,7	29<40<52	1,4<1,6<1,8	29<53<70	1,3<1,8<2,4	fair	no
2006.236	SKS	12,34	89,00	6,46	21<24<31	1,3<1,8<2,2	57<67<79	0,1<0,3<0,5	15<22<29	1,5<1,9<2,3	good	no
2006.237	SKS	235,36	86,78	6,58	68<71<78	1,1<1,4<1,8	-87<-79<-73	0,4<0,5<0,6	64<67<72	1,3<1,6<1,8	fair	no
2004.150	SKS	29,62	100,28	6,27	-	-	-	-	-	-	poor	yes
2004.249	SKS	33,73	99,32	7,20	-	-	-	-	-	-	fair	yes
2004.249	SKS	33,35	99,42	7,38	-	-	-	-	-	-	good	yes
2004.297	SKS	30,06	96,64	6,56	-	-	-	-	-	-	poor	yes
2004.333	SKS	23,08	93,73	6,98	-	-	-	-	-	-	good	yes
2004.341	SKS	23,05	93,86	6,74	-	-	-	-	-	-	good	yes
2005.036	SKS	61,79	113,72	7,08	-	-	-	-	-	-	fair	yes
2005.061	SKKS	66,10	126,73	7,11	-	-	-	-	-	-	good	yes
2005.134	SKS	82,69	98,27	6,72	-	-	-	-	-	-	good	yes
2005.139	SKS	82,48	96,29	6,85	-	-	-	-	-	-	poor	yes
2005.165	SKS	358,78	90,63	6,77	-	-	-	-	-	-	fair	yes

Date	phase	baz°	Δ°	Mw	ϕ ° ME	δt ME(s)	ϕ° RC	δt RC (s)	ϕ°EV	δt EV(s)	quality	null
2005.207	SKS	81,56	104,46	7,28	-	-	-	-	-	-	good	yes
2005.228	SKS	27,27	96,94	7,19	-	-	-	-	-	-	good	yes
2005.288	SKS	47,81	98,80	6,42	-	-	-	-	-	-	good	yes
2006.136	SKS	84,01	97,46	6,80	-	-	-	-	-	-	fair	yes
2006.173	SKS	19,34	92,70	5,94	-	-	-	-	-	-	fair	yes
2006.189	SKS	357,91	90,86	6,60	-	-	-	-	-	-	fair	yes
2006.335	SKS	80,07	96,96	6,30	-	-	-	-	-	-	fair	yes
2006.356	SKS	78,57	87,25	6,29	-	-	-	-	-	-	fair	yes

Table 5.7 – SESP results. We present the data events in Julian format, the analized phase, the backazimuth of the event, its epicentral distance and the Magnitud. Then, the results for ϕ and δt and their error obtained with the three methodologies and the quality factor assigned. In the grey column are null measurements data.

Tabla 5.7 – Resultados de SESP. Presentamos la fecha de los eventos en formato Juliano, el tipo de fase analizado, el backazimuth del evento, su distancia epicentral y la magnitud. Además de los resultados por ϕ y δt y sus errores obtenidos con las tres metodologías y el parámetro de calidad asignado. Las columnas en gris son los valores null.

5.8 ESTP

The ESTP IAG station is located in Estepa town, near Sevilla; within the External Betic domain. Of the earthquakes, with magnitude Mw ≥ 5.5, that occurred between January 2004 and December of 2006, the seismograms of 258 events could be retrieved from the IAG data server. We show all the results obtained in table 5.8 and in the Figure A-8 in the appendix. We utilize a filter of 0.01-1.0 Hz for the majority of events, where poor quality is present we elect to use a filter of 0.02-0.3 Hz.

A concrete conclusion has not been made at this time due to the lack of events for backazimuthal coverage hindering a clear interpretation, but might become clearer with a growing data set within the coming years. Thus, we propose a one layer model with splitting parameters of $\Phi = 81°$, $\delta t = 1.6$ sec for the ESTP station.

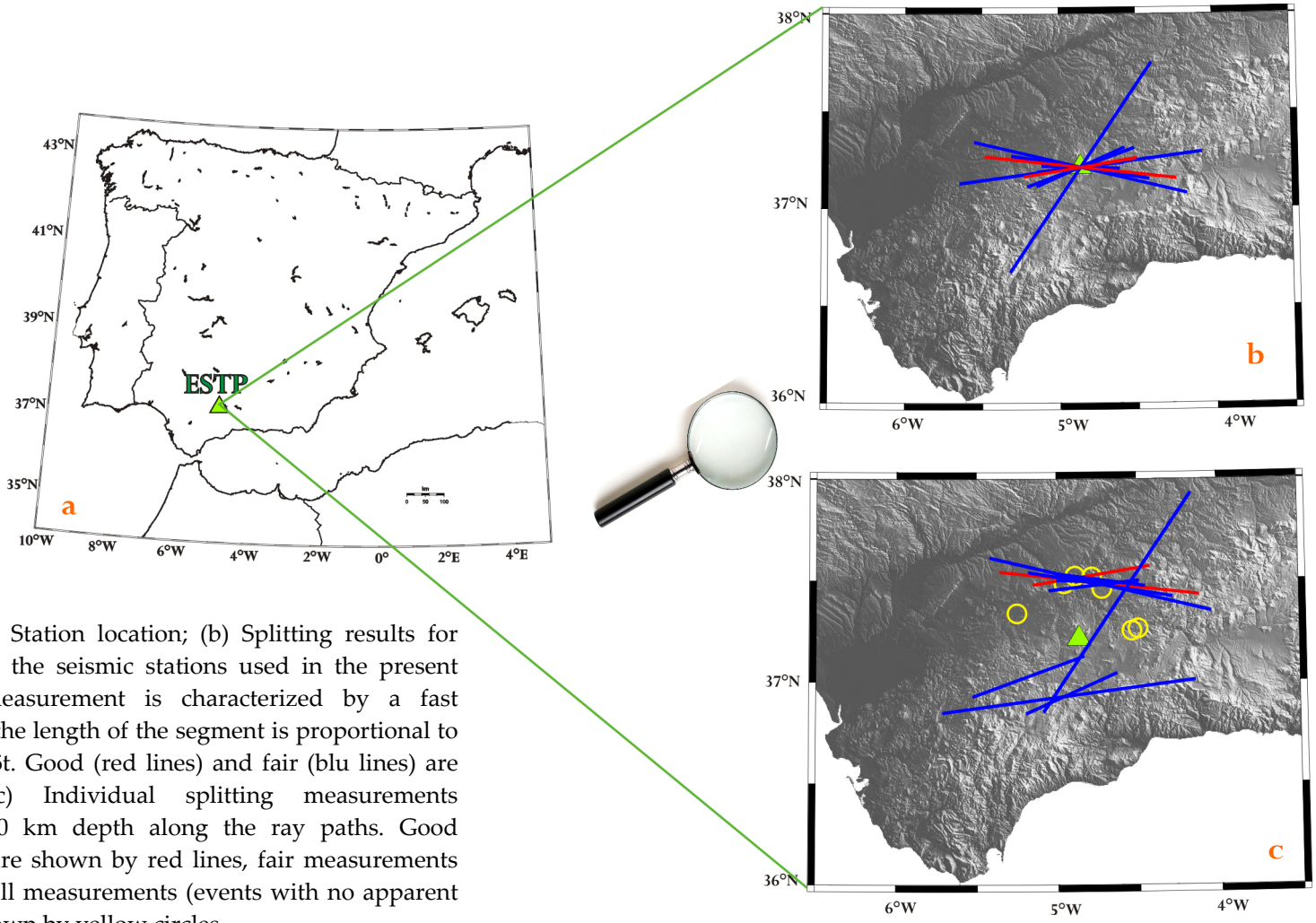

Figure 5.10- (a) Station location; (b) Splitting results for MEM shown at the seismic stations used in the present study. Each measurement is characterized by a fast azimuth ϕ, and the length of the segment is proportional to the delay time δt. Good (red lines) and fair (blu lines) are represented; (c) Individual splitting measurements projected at 150 km depth along the ray paths. Good measurements are shown by red lines, fair measurements by blu lines. Null measurements (events with no apparent splitting) are shown by yellow circles.

Figura 5.10 - (a) Localizacíon de la estación; (b) Resultados del splitting obtenidos con el MEM projectados a la estación. Las medidas están caraterizadas por la direccíon rápida ϕ, y la longitud del segmento es proporcional al retraso δt. Se representan los valores good (líneas rojas) y los valores fair (líneas azules); (c) Las mediciones individuales del splitting estàn proyectadas a 150 km de profundidad a lo largo del recorrido del rayo. Las medidas good se muestran con líneas rojas y las fair con líneas azules. Las medidas Null (eventos con apparente no splitting) se muestran con círculos amarillos.

Date	phase	baz°	Δ°	Mw	ϕ ° ME	δt ME(s)	ϕ° RC	δt RC (s)	ϕ°EV	δt EV(s)	quality	null
2004.312	SKS	19,97	90,56	6,11	48<-82<-78	0.2<0.9<1.8	56<64<74	0.2<0.3<0.4	58<-78<-72	0.2<1.1<2.0	fair	no
2004.333	SKS	21,55	95,26	6,98	-84<-76<-76	1.3<2.3<3.5	54<61<70	0.0<0.2<0.4	-92<-76<-74	0.5<2.3<3.5	fair	no
2004.341	SKS	21,52	95,40	6,74	84<-80<-76	0.5<1.5<3.5	52<61<71	0.1<0.3<0.6	48<-84<-76	0.2<1.2<3.1	fair	no
2005.101	SKS	15,66	164,27	6,72	52<84<-86	0.4<0.9<1.7	53<60<68	0.4<0.6<0.7	39<84<-82	0.3<0.9<1.8	fair	no
2005.228	SKS	25,69	98,58	7,19	52<-86<-76	0.4<1.0<2.0	67<72<80	0.4<0.6<0.8	56<-80<-70	0.4<1.2<2.2	poor	no
2005.264	SKS	20,51	94,75	6,02	-90<-83<-82	0.5<2.0<2.5	45<51<60	0.3<0.4<0.5	78<87<-88	0.8<1.4<2.0	good	no
2005.288	SKS	46,29	100,77	6,42	33<34<39	2.2<2.6<3.0	73<78<86	0.0<0.2<0.4	31<36<43	2.2<2.6<3.0	fair	no
2006.002	SKS	188,11	98,96	7,36	35<66<86	0.6<1.0<1.7	52<82<-88	0.7<0.9<1.0	52<80<-88	0.7<1.4<2.3	fair	no
2006.165	SKS	358,77	90,88	6,45	62<73<82	1.1<1.9<2.5	31<36<44	0.4<0.6<0.9	58<73<84	1.0<1.9<2.5	poor	no
2006.197	SKS	234,20	91,31	6,18	62<70<-82	0.4<1.2<2.2	87<-76<-59	0.1<0.5<0.8	62<72<-41	0.3<1.1<2.2	fair	no
2006.209	SKS	47,63	101,20	5,86	62<80<-78	0.3<0.6<1.0	85<-83<-73	0.4<0.6<0.7	52<80<-56	0.3<0.6<1.1	poor	no
2006.236	SKS	10,93	90,26	6,46	76<81<86	0.9<1.2<1.4	51<58<68	0.6<0.7<0.8	74<83<-92	0.9<1.2<1.6	good	no
2005.134	SKS	81,38	100,21	6,72	-	-	-	-	-	-	fair	yes
2005.178	SKS	292,33	88,15	6,15	-	-	-	-	-	-	fair	yes
2005.211	SKS	80,20	94,26	5,81	-	-	-	-	-	-	fair	yes
2005.242	SKS	24,79	98,78	5,96	-	-	-	-	-	-	fair	yes
2006.055	SKKS	345,24	160,14	6,08	-	-	-	-	-	-	good	yes
2006.173	SKS	17,84	94,15	5,94	-	-	-	-	-	-	fair	yes
2006.189	SKS	356,45	91,68	6,60	-	-	-	-	-	-	fair	yes
2006.232.	SKS	11,93	91,34	5,98	-	-	-	-	-	-	fair	yes

Table 5.8 – ESTP results. We present the data events in Julian format, the analized phase, the backazimuth of the event, its epicentral distance and the Magnitud. Then, the results for ϕ and δt and their error obtained with the three methodologies and the quality factor assigned. In the grey column are null measurements data.

Tabla 5.8 – Resultados de ESTP. Presentamos la fecha de los eventos en formato Juliano, el tipo de fase analizado, el backazimuth del evento, su distancia epicentral y la magnitud. Además de los resultados por ϕ y δt y sus errores obtenidos con las tres metodologías y el parámetro de calidad asignado. Las columnas en gris son los valores null.

5.9 SFS

The SFS station is managed by the ROA of San Fernando, near Cadiz, and is located in the *Complejo del Campo de Gibraltar* formation, which is composed of flysh, thus the data recorded contain a lot of noise and few data recorded at this station is reliablen.

Anisotropy beneath the SFS station has been previously studied by Schimtd et al. (2005) for the old station SFUC who report no anisotropy for this station.

We analyzed events for the years 2004 through 2006 for a total of 163 events which resulted in 10 useful events classified as 1 good, 1 fair, 8 are fair Null. We show all the results obtained in table 5.9 and in the Figure A-9 in the appendix. We utilize a filter of 0.01-1.0 Hz for the majority of events, where poor quality is present we elect to use a filter of 0.02-0.3 Hz.

Consequently, we only have two reliable results that do not constrain well the anisotropy for this station, but give a first indication about the anisotropic direction. A concrete conclusion has not been made at this time due to the lack of events for good backazimuthal coverage hindering a clear interpretation, but might become clearer with a growing data set within the coming years.

Thus, we propose a one layer model with splitting parameters of $\Phi = -1°$, $\delta t = 1.1$ sec for the SFS station.

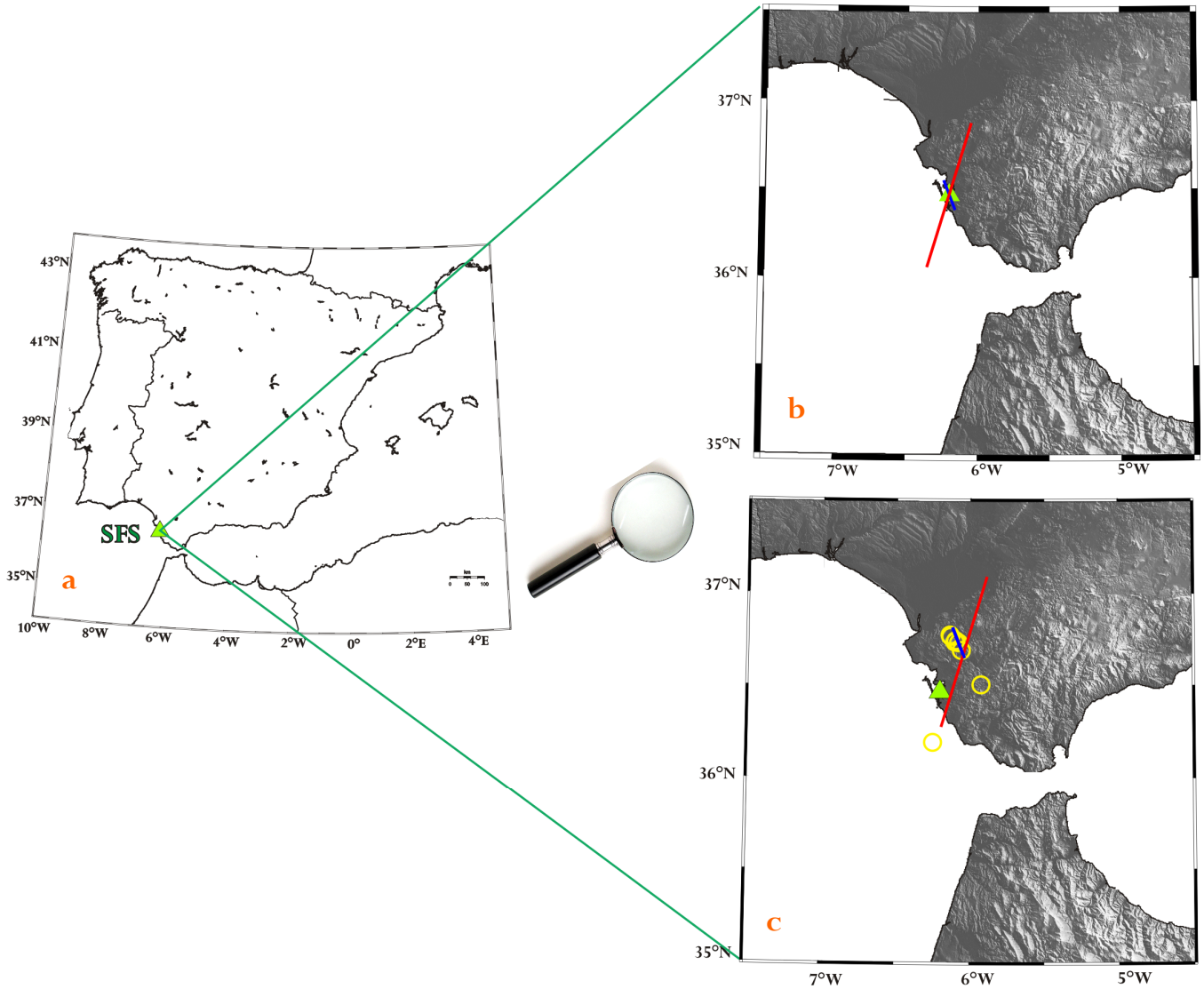

Figura 5.11 - (a) Localizacíon de la estación; (b) Resultados del splitting obtenidos con el MEM projectados a la estación. Las medidas están caraterizadas por la direccíon rápida ϕ, y la longitud del segmento es proporcional al retraso δt. Se representan los valores good (líneas rojas) y los valores fair (líneas azules); (c) Las mediciones individuales del splitting estàn proyectadas a 150 km de profundidad a lo largo del recorrido del rayo. Las medidas good se muestran con líneas rojas y las fair con líneas azules. Las medidas Null (eventos con apparente no splitting) se muestran con círculos amarillos.

Figure 5.11- (a) Station location; (b) Splitting results for MEM shown at the seismic stations used in the present study. Each measurement is characterized by a fast azimuth ϕ, and the length of the segment is proportional to the delay time δt. Good (red lines) and fair (blu lines) are represented; (c) Individual splitting measurements projected at 150 km depth along the ray paths. Good measurements are shown by red lines, fair measurements by blu lines. Null measurements (events with no apparent splitting) are shown by yellow circles.

Date	phase	baz°	Δ°	Mw	ϕ ° ME	δt ME(s)	ϕ° RC	δt RC (s)	ϕ°EV	δt EV(s)	quality	null
2004.249	SKS	30,82	102,37	7,38	7<17<23	0,9<1,7<2,3	-28<-16<-7	0,4<0,6<0,9	3<19<25	0,8<1,8<2,4	good	no
2004.341	SKS	20,64	96,48	6,74	-64<-21<11	0,2<0,4<1,2	-23<-16<-10	0,3<0,4<0,5	19<25<31	1,2<1,7<2,1	fair	no
2004.150	SKS	27,04	103,11	6,27	-	-	-	-	-	-	fair	yes
2004.207	SKS	79,68	107,60	7,28	-	-	-	-	-	-	fair	yes
2004.333	SKS	20,67	96,35	6,98	-	-	-	-	-	-	fair	yes
2006.002	SKS	187,45	98,07	7,36	-	-	-	-	-	-	fair	yes
2006.173	SKS	16,97	95,18	5,94	-	-	-	-	-	-	fair	yes
2006.219	SKKS	16,18	158,72	6,81	-	-	-	-	-	-	fair	yes
2006.232	SKS	11,10	92,29	5,98	-	-	-	-	-	-	fair	yes
2006.236	SKS	10,12	91,19	6,46	-	-	-	-	-	-	fair	yes

Table 5.9 – SFS results. We present the data events in Julian format, the analized phase, the backazimuth of the event, its epicentral distance and the Magnitud. Then, the results for ϕ and δt and their error obtained with the three methodologies and the quality factor assigned. In the grey column are null measurements data.

Tabla 5.9 – Resultados de SFS. Presentamos la fecha de los eventos en formato Juliano, el tipo de fase analizado, el backazimuth del evento, su distancia epicentral y la magnitud. Además de los resultados por ϕ y δt y sus errores obtenidos con las tres metodologías y el parámetro de calidad asignado. Las columnas en gris son los valores null.

5.10 MELI

The MELI Geofon station is located in Melilla town, in the Northern Africa, within the Internal domain. This station has been operating since December of 1999. We analyzed data from 2004 to 2006, for a total of 155 events, of which 10 are available, and we classified as 3 good, 1 poor and 5 are fair null. We show all the results obtained in table 5.10 and in the Figure A-10 in the appendix. We utilize a filter of 0.01-1.0 Hz for the majority of events, where poor quality is present we elect to use a filter of 0.02-0.3 Hz.

For this station, Schmid et al. (2005) found a mean average for $\phi°$=55.68 and δt=1.39 sec. The trend of this station is parallel to the trend of mountain belts, and thus they explain the anisotropy in the context of vertically coherent deformation. We obtain similar fast direction.

In Figure 5.12 we show in the panel ***a*** the station location; in ***b*** the individual splitting measurements are plotted at the various stations to evaluate the coherence of the results. Lines show the fast anisotropy directions ϕ, obtained from the minimum energy method, and their lengths are proportional to the splitting delay time δt. Good data are shown by red lines, and fair data by blu lines; poor data are not plotted. In panel ***c***, in order to better visualize the lateral sampling of the anisotropy measurements and the regional-scale stability of the anisotropy parameters beneath the stations, we choose to project the individual splitting measurements of good and fair quality along their incoming rays to a depth of 150 km. Although the splitting of the SKS waves is not well-located vertically, this representation is helpful since it plots the splitting parameters closer to the location where they were acquired. The measurements with well-constrained anisotropy, good, are presented as red lines while measurements of lower quality, fair, are shown blu lines. In addition, Figure 5.12***c*** presents the Null measurements by open circles. Such a pattern was less clear in Figure 5.12 ***a***. It suggests that the variation is not caused by noise in the observations. It is apparently due to real anisotropic variations at depth. This suggests that the upper mantle beneath the MELI station is dominated by a single anisotropic layer, with smoothly varying fast directions. Thus, we propose a one layer model with splitting parameters of Φ = 68°, δt =1.0 sec for the MELI station.

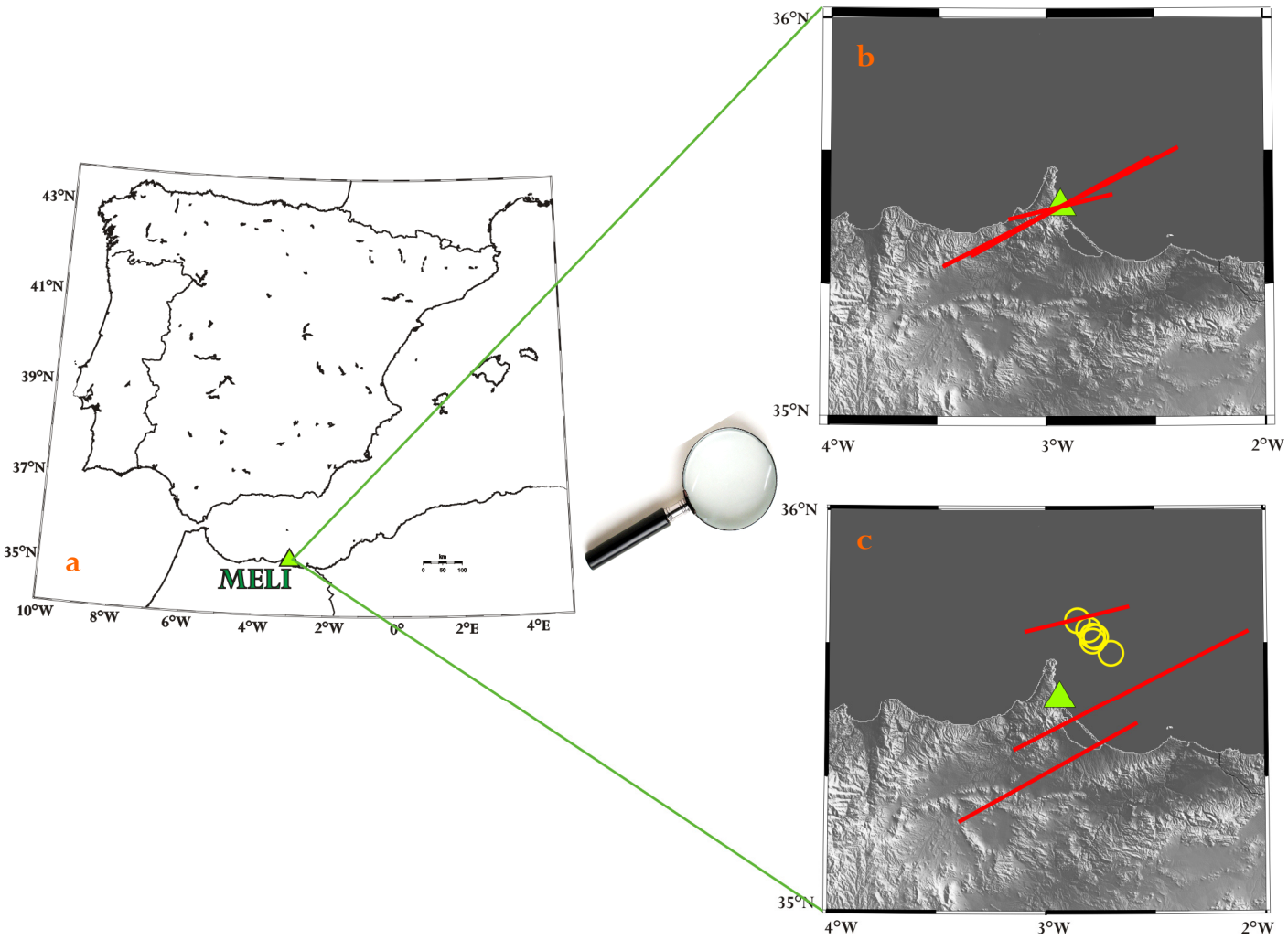

Figura 5.9 - (a) Localizacíon de la estación; (b) Resultados del splitting obtenidos con el MEM projectados a la estación. Las medidas están caraterizadas por la direccíon rápida ϕ, y la longitud del segmento es proporcional al retraso δt. Se representan los valores good con líneas rojas; (c) Las mediciones individuales del splitting estàn proyectadas a 150 km de profundidad a lo largo del recorrido del rayo. Las medidas good se muestran con líneas rojas. Las medidas Null (eventos con apparente no splitting) se muestran con círculos amarillos.

Figure 5.12- (a) Station location; (b) Splitting results for MEM shown at the seismic stations used in the present study. Each measurement is characterized by a fast azimuth ϕ, and the length of the segment is proportional to the delay time δt. Good (red lines) values are represented; (c) Individual splitting measurements projected at 150 km depth along the ray paths. Good measurements are shown by red lines. Null measurements (events with no apparent splitting) are shown by yellow circles.

Date	phase	baz°	Δ°	Mw	ϕ ° ME	δt ME(s)	ϕ° RC	δt RC (s)	ϕ°EV	δt EV(s)	quality	null
2005.050	SKS	73,20	121,26	6,44	31<59<70	0,4<1,4<2,4	-5<8<23	0,2<0,4<0,6	-46<29<62	0,1<0,5<2,2	poor	No
2005.134	SKS	83,11	98,65	6,72	60<63<68	1,7<2,0<2,4	11<18<28	0,3<0,5<0,7	52<57<66	1,3<1,8<2,3	good	No
2006.002	SKS	189,16	97,22	7,36	52<61<70	1,2<1,5<1,8	42<51<61	1,2<1,4<1,6	41<51<64	1,2<1,4<1,6	good	No
2006.236	SKS	12,33	91,88	6,46	72<76<82	0,7<0,8<0,9	56<68<77	0,6<0,7<0,8	66<74<84	0,6<0,8<0,9	good	No
2004.150	SKS	29,91	102,84	6,27	-	-	-	-	-	-	fair	Yes
2004.297	SKS	30,25	99,19	6,56	-	-	-	-	-	-	fair	Yes
2004.333	SKS	23,17	96,44	6,98	-	-	-	-	-	-	good	Yes
2005.228	SKS	27,46	99,57	7,19	-	-	-	-	-	-	fair	Yes
2005.288	SKS	48,17	100,79	6,42	-	-	-	-	-	-	fair	Yes
2006.232	SKS	13,38	92,92	5,98	-	-	-	-	-	-	fair	Yes

Table 5.10 – MELI results. We present the data events in Julian format, the analized phase, the backazimuth of the event, its epicentral distance and the Magnitud. Then, the results for ϕ and δt and their error obtained with the three methodologies and the quality factor assigned. In the grey column are null measurements data.

Tabla 5.10 – Resultados de MELI. Presentamos la fecha de los eventos en formato Juliano, el tipo de fase analizado, el backazimuth del evento, su distancia epicentral y la magnitud. Además de los resultados por ϕ y δt y sus errores obtenidos con las tres metodologías y el parámetro de calidad asignado. Las columnas en gris son los valores null.

5.11 CART

The CART station is located near Cartagena (Murcia), within the Internal Zone of the Betic Cordilleras, and has been operating since December of 1997. We analyzed data from 2004 to 2006 for a total of 155 events which we classified as 8 good, 3 fair, 2 poor, 4 good Null, 3 fair Null and 2 poor Null. We show all the results obtained in table 5.11 and in the Figure A-11 in the appendix. We utilize a filter of 0.01-1.0 Hz for the majority of events, where poor quality is present we elect to use a filter of 0.02-0.3 Hz.

Schmid et al. (2005) found a mean average of ϕ=69.81° and δt=1.72 sec for this station and they explain the anisotropy in the context of vertically coherent deformation. We obtain similar direction to that and thus propose a one layer model with splitting parameters of Φ = 73°, δt =1.5 sec for CART.

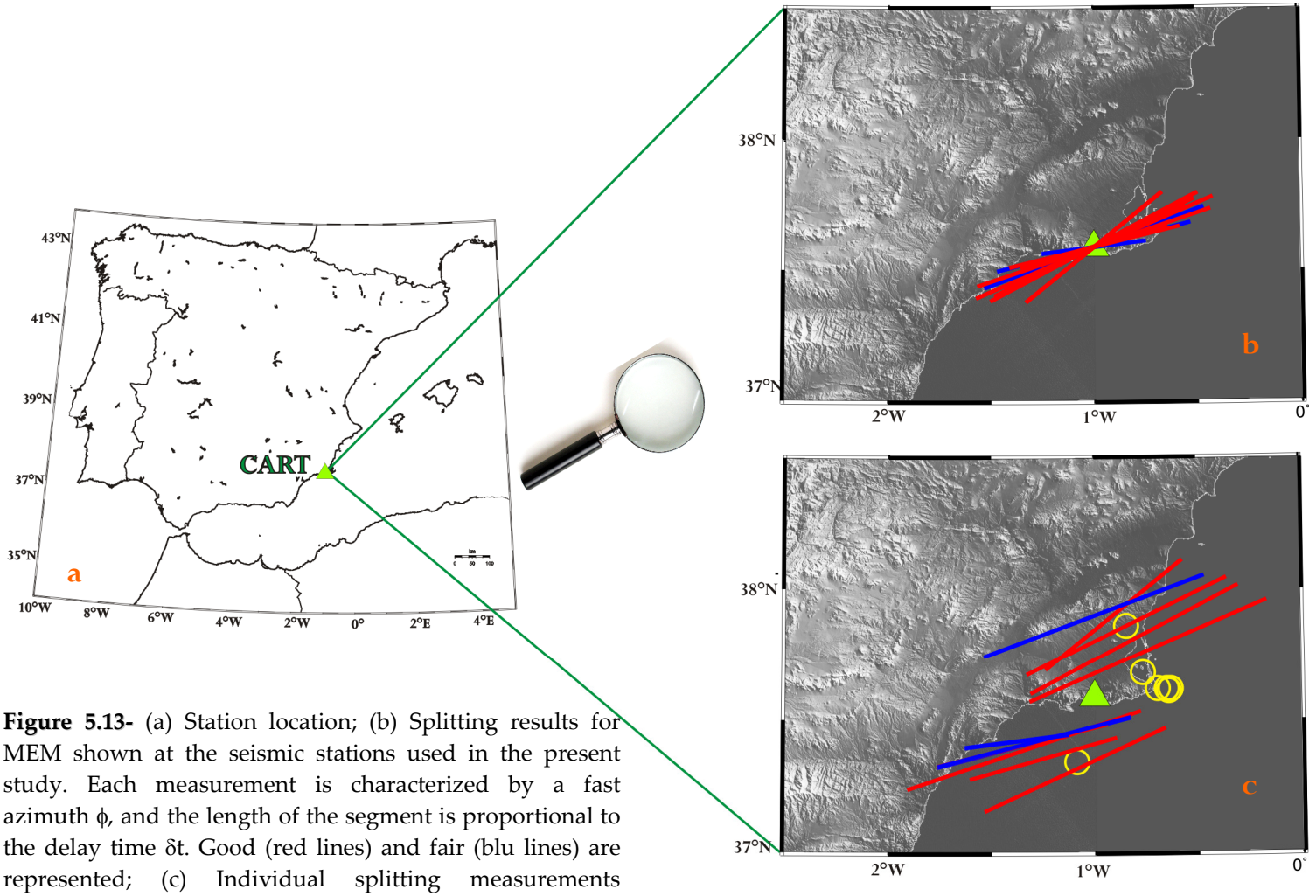

Figure 5.13- (a) Station location; (b) Splitting results for MEM shown at the seismic stations used in the present study. Each measurement is characterized by a fast azimuth ϕ, and the length of the segment is proportional to the delay time δt. Good (red lines) and fair (blu lines) are represented; (c) Individual splitting measurements projected at 150 km depth along the ray paths. Good measurements are shown by red lines, fair measurements by blu lines. Null measurements (events with no apparent splitting) are shown by yellow circles.

Figura 5.13 - (a) Localizacíon de la estación; (b) Resultados del splitting obtenidos con el MEM projectados a la estación. Las medidas están caraterizadas por la direccíon rápida ϕ, y la longitud del segmento es proporcional al retraso δt. Se representan los valores good (líneas rojas) y los valores fair (líneas azules); (c) Las mediciones individuales del splitting estàn proyectadas a 150 km de profundidad a lo largo del recorrido del rayo. Las medidas good se muestran con líneas rojas y las fair con líneas azules. Las medidas Null (eventos con apparente no splitting) se muestran con círculos amarillos.

Date	phase	baz°	Δ°	Mw	ϕ ° ME	δt ME(s)	ϕ° RC	δt RC (s)	ϕ°EV	δt EV(s)	quality	null
2004.150	SKS	30,81	100,12	6,27	70<-87<-76	0,8<1,4<2,2	70<79<88	0,9<1,2<1,5	66<-85<-72	0,8<1,5<2,3	poor	no
2004.249	SKS	34,51	99,18	7,38	52<63<84	1,2<1,8<2,8	60<79<-84	1,1<1,5<2,1	37<49<74	1,5<2,6<3,7	good	no
2004.250	SKS	195,55	95,98	6,75	48<66<80	1,2<1,5<1,9	42<54<69	1,2<1,5<1,8	23<38<74	1,2<1,8<2,7	good	no
2004.297	SKS	31,16	96,47	6,56	56<65<78	1,5<1,9<2,4	68<77<89	1,4<1,8<2,0	56<71<-92	1,4<1,8<2,4	poor	no
2004.333	SKS	24,11	93,73	6,98	58<64<76	1,4<1,7<2,0	72<83<-87	1,4<1,7<1,9	58<70<88	1,4<1,6<1,9	good	no
2005.080	SKS	233,71	85,73	6,84	70<72<74	1,7<1,9<2,1	71<74<80	1,5<1,8<2,0	68<72<76	1,6<1,9<2,1	good	no
2005.132	SKKS	220,38	146,34	6,46	68<74<82	1,0<1,2<1,4	60<68<78	1,1<1,3<1,4	58<70<82	1,0<1,2<1,5	good	no
2005.164	SKS	240,99	86,10	7,75	76<79<88	0,7<1,0<1,3	87<-88<-79	0,4<0,6<0,7	74<73<76	1,1<1,3<1,4	fair	no
2005.165	SKS	359,74	91,18	6,77	50<70<78	1,0<1,8<2,7	37<46<58	0,4<0,7<1,0	43<70<82	0,9<1,7<3,0	fair	no
2005.288	SKS	48,94	98,25	6,42	62<67<74	1,5<2,0<2,6	-89<-74<-62	0,4<0,7<1,0	60<65<72	1,7<2,1<2,5	good	no
2006.236	SKS	13,27	89,25	6,46	43<51<58	1,2<1,4<1,6	38<45<56	1,3<1,5<1,6	37<45<54	1,3<1,4<1,6	good	no
2006.237	SKS	236,36	87,49	6,58	76<76<80	1,3<1,4<1,5	75<77<81	1,3<1,4<1,5	74<76<82	1,3<1,4<1,6	good	no
2006.285	SKS	233,88	95,12	6,36	68<76<84	1,1<1,5<2,0	-90<-82<-76	0,8<1,0<1,2	64<74<88	1,0<1,6<2,2	fair	no
2004.207	SKS	82,68	103,33	7,28	-	-	-	-	-	-	good	yes
2004.341	sSKS	24,09	93,86	6,74	-	-	-	-	-	-	good	yes
2005.036	SKS	63,18	112,89	7,08	-	-	-	-	-	-	fair	yes
2005.134	SKS	83,73	97,12	6,72	-	-	-	-	-	-	good	yes
2006.136	SKS	85,04	96,30	6,80	-	-	-	-	-	-	good	yes
2006.189	SKS	358,88	91,43	6,60	-	-	-	-	-	-	poor	yes
2006.209	SKS	50,29	98,64	5,86	-	-	-	-	-	-	poor	yes
2006.223	SKS	83,64	94,34	6,23	-	-	-	-	-	-	fair	yes
2006.232	SKS	195,83	102,30	6,98	-	-	-	-	-	-	fair	yes

Table 5.11 – CART results. We present the data events in Julian format, the analized phase, the backazimuth of the event, its epicentral distance and the Magnitud. Then, the results for ϕ and δt and their error obtained with the three methodologies and the quality factor assigned. In the grey column are null measurements data.

Tabla 5.11 – Resultados de CART. Presentamos la fecha de los eventos en formato Juliano, el tipo de fase analizado, el backazimuth del evento, su distancia epicentral y la magnitud. Además de los resultados por ϕ y δt y sus errores obtenidos con las tres metodologías y el parámetro de calidad asignado. Las columnas en gris son los valores null.

5.12 VELZ

The VELZ station is managed by IAG and located in Velez Rubio (Almeria), within the Internal Zone. We analyze data from 2004 to 2006 for a total of 178, of wich 12 were reliable observations, which we classified as 5 good, 3 fair, 1 poor, 1 good null, 1 fair null and 1 poor null. We show all the results obtained in table 5.12 and in the Figure A-12 in the appendix. We utilize a filter of 0.01-1.0 Hz for the majority of events, where poor quality is present we elect to use a filter of 0.02-0.3 Hz.

The data shows roughly the same trend, and the poor data are in agreement with the other. Null good and null fair values had back azimuth that coincided with the mean fast direction inferred. We propose a one layer model with splitting parameters of $\Phi = 65°$, $\delta t = 1.4$ sec for VELZ.

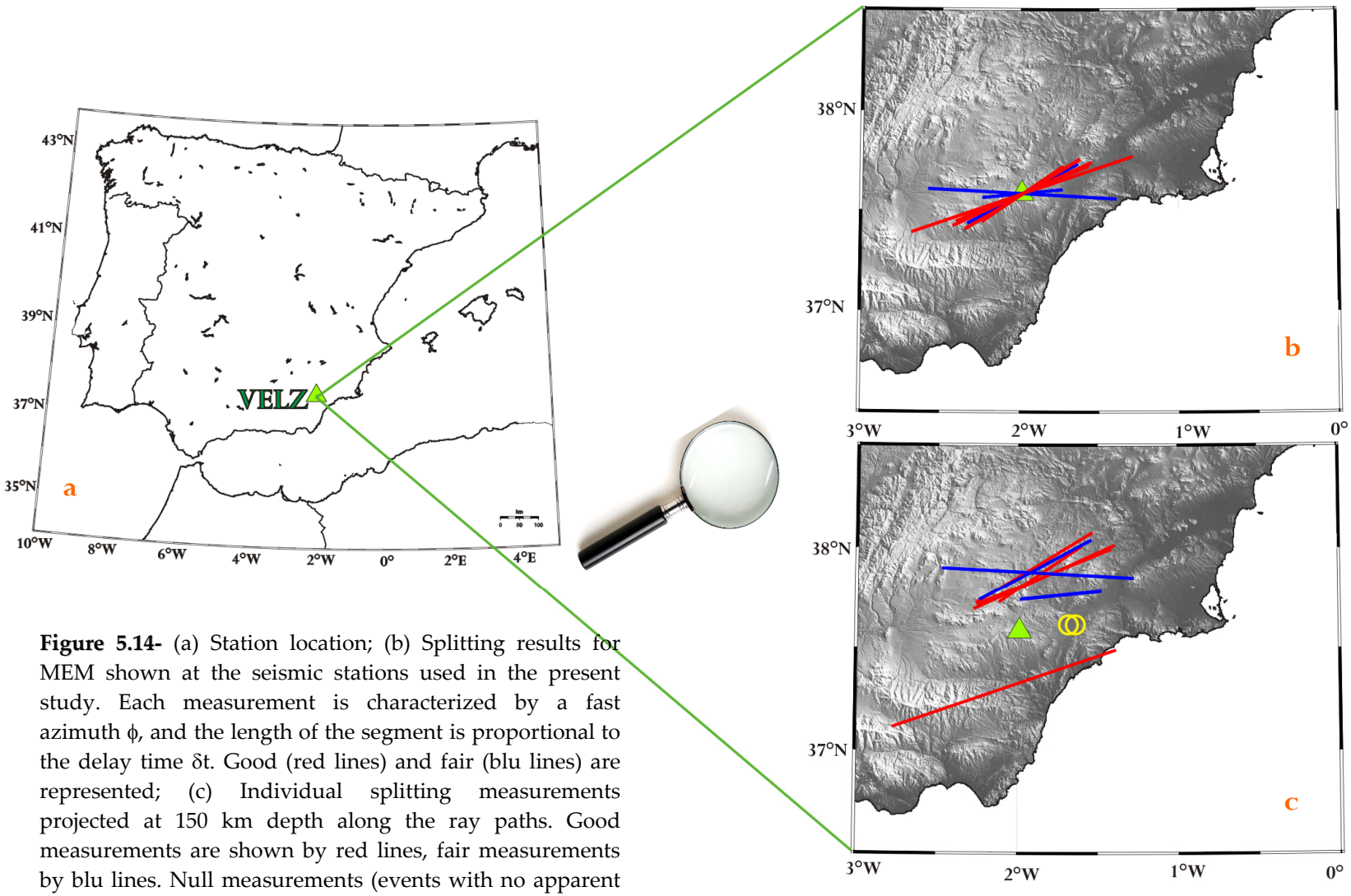

Figure 5.14- (a) Station location; (b) Splitting results for MEM shown at the seismic stations used in the present study. Each measurement is characterized by a fast azimuth ϕ, and the length of the segment is proportional to the delay time δt. Good (red lines) and fair (blu lines) are represented; (c) Individual splitting measurements projected at 150 km depth along the ray paths. Good measurements are shown by red lines, fair measurements by blu lines. Null measurements (events with no apparent splitting) are shown by yellow circles.

Figura 5.14 –
(a) Localizacíon de la estación; (b) Resultados del splitting obtenidos con el MEM projectados a la estación. Las medidas están caracterizadas por la dirección rápida ϕ, y la longitud del segmento es proporcional al retraso δt. Se representan los valores good (líneas rojas) y los valores fair (líneas azules); (c) Las mediciones individuales del splitting están proyectadas a 150 km de profundidad a lo largo del recorrido del rayo. Las medidas good se muestran con líneas rojas y las fair con líneas azules. Las medidas Null (eventos con apparente no splitting) se muestran con círculos amarillos.

Date	phase	baz°	Δ°	Mw	ϕ ° ME	δt ME(s)	ϕ° RC	δt RC (s)	ϕ°EV	δt EV(s)	quality	null
2004.250	SKS	195,02	95,77	6,75	58<71<84	1,7<2,3<3,0	41<51<64	1,6<1,9<2,4	46<65<80	1,6<2,2<2,8	good	no
2004.250	SKS	33,67	99,67	6,60	66<80<-88	1,3<1,8<2,4	62<81<-81	1,3<1,9<2,4	56<80<-82	1,3<1,9<2,4	poor	no
2004.333	SKS	23,46	94,05	6,98	64<67<72	1,4<1,5<1,6	61<67<75	1,3<1,5<1,6	62<67<76	1,4<1,5<1,6	good	no
2004.341	SKS	23,43	94,18	6,74	62<65<72	1,4<1,5<1,6	67<71<77	1,4<1,5<1,6	66<71<78	1,4<1,5<1,6	good	no
2005.288	SKS	48,26	98,83	6,42	68<84<-74	0,5<0,8<1,2	84<-89<-81	0,6<0,8<1,0	62<82<-68	0,5<0,8<1,4	fair	no
2006.173	SKS	19,71	93,06	5,94	46<56<70	0,7<1,0<1,2	52<61<73	0,7<0,9<1,1	35<56<78	0,7<1,0<1,4	good	no
2006232	SKS	13,71	90,47	5,98	52<62<72	1,0<1,3<1,6	47<59<72	1,1<1,3<1,4	37<60<80	1,0<1,3<1,6	fair	no
2006.236	SKS	12,67	89,43	6,46	54<59<68	1,2<1,3<1,5	44<51<59	1,2<1,3<1,4	56<59<66	1,2<1,3<1,4	good	no
2006.273	SKS	16,97	93,05	6,58	52<-87<-80	0,5<1,9<3,9	53<62<73	0,4<0,8<1,2	74<-77<-70	0,8<3,2<4,0	fair	no
2004.207	SKS	82,06	104,10	7,28	-	-	-	-	-	-	fair	yes
2004.249	SKS	33,80	99,63	7,38	-	-	-	-	-	-	poor	yes
2005.134	SKS	83,11	97,90	6,72	-	-	-	-	-	-	good	yes

Table 5.12 – VELZ results. We present the data events in Julian format, the analized phase, the backazimuth of the event, its epicentral distance and the Magnitud. Then, the results for ϕ and δt and their error obtained with the three methodologies and the quality factor assigned. In the grey column are null measurements data.

Tabla 5.12 – Resultados de VELZ. Presentamos la fecha de los eventos en formato Juliano, el tipo de fase analizado, el backazimuth del evento, su distancia epicentral y la magnitud. Además de los resultados por ϕ y δt y sus errores obtenidos con las tres metodologías y el parámetro de calidad asignado. Las columnas en gris son los valores null.

5.13 ASCB

The ASCB station is located in the Sierra Cabrera (Almeria), in the eastern part of Betic Cordillera, within the unit of the Internal Zones. This station has been operating since finally of November of 2003. We analyze data from 2004 to 2006, but the records were not of good quality and contained a lot of noise and some seismograms were not recorded correctly, so although we checked 91 events, only 8 data were available, classified as 5 good, 2 fair, 1 fair null. We show all the results obtained in table 5.13 and in the Figure A-13 in the appendix. We utilize a filter of 0.01-1.0 Hz for the majority of events, where poor quality is present we elect to use a filter of 0.02-0.3 Hz.

We propose a one layer model with splitting parameters of Φ =66° and δt =1.6 sec for ASCB.

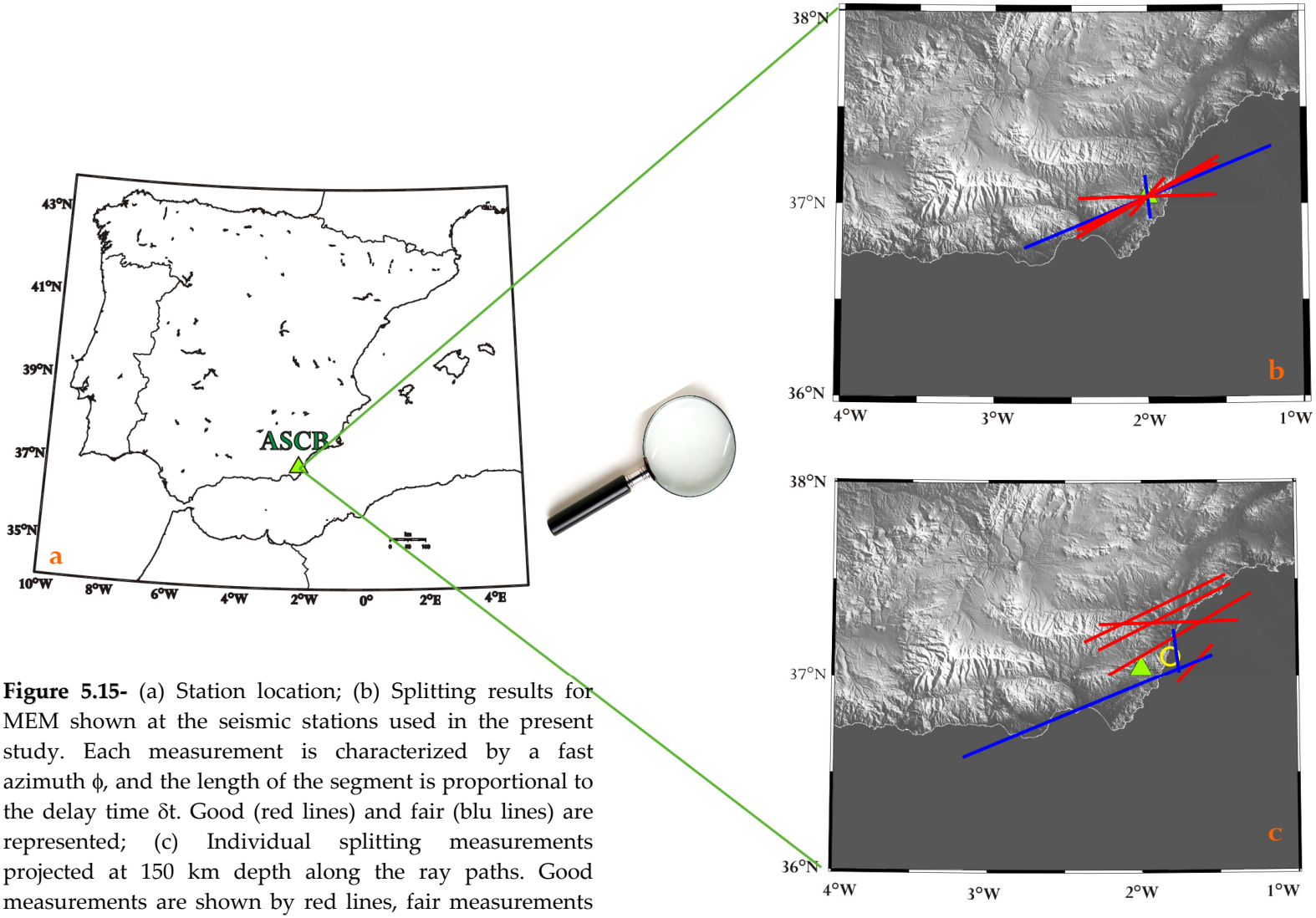

Figure 5.15- (a) Station location; (b) Splitting results for MEM shown at the seismic stations used in the present study. Each measurement is characterized by a fast azimuth ϕ, and the length of the segment is proportional to the delay time δt. Good (red lines) and fair (blu lines) are represented; (c) Individual splitting measurements projected at 150 km depth along the ray paths. Good measurements are shown by red lines, fair measurements by blu lines. Null measurements (events with no apparent splitting) are shown by yellow circles.

Figura 5.15 – (a) Localizacíon de la estación; (b) Resultados del splitting obtenidos con el MEM projectados a la estación. Las medidas están caraterizadas por la direccíon rápida ϕ, y la longitud del segmento es proporcional al retraso δt. Se representan los valores good (líneas rojas) y los valores fair (líneas azules); (c) Las mediciones individuales del splitting estàn proyectadas a 150 km de profundidad a lo largo del recorrido del rayo. Las medidas good se muestran con líneas rojas y las fair con líneas azules. Las medidas Null (eventos con apparente no splitting) se muestran con círculos amarillos.

Date	phase	baz°	Δ°	Mw	ϕ ° ME	δt ME(s)	ϕ° RC	δt RC (s)	ϕ°EV	δt EV(s)	quality	null
2004.297	SKS	30,50	97,35	6,56	72<87<-81	1,0<1,4<1,8	74<89<-84	1,0<1,04<1,9	74<-87<-74	1,0<1,5<2,0	good	No
2004.333	SKS	23,46	94,55	6,98	80<88<-84	1,2<1,4<1,6	54<63<74	1,2<1,5<1,9	68<83<-84	1,1<1,4<1,6	good	No
2005.036	SKS	62,62	113,85	7,08	22<29<39	0,1<0,2<0,4	-27<7<50	0,1<0,5<1,6	-15<23<64	0,1<0,2<0,8	fair	No
2005.288	SKS	48,31	99,21	6,42	-84<-74<-66	0,2<0,4<0,5	56<60<70	1,0<1,8<4,0	56<68<-37	0,2<1,2<2,8	good	No
2006.136	SKS	84,48	97,14	6,80	26<39<55	0,2<0,5<0,7	7<42<76	0,3<0,6<1,4	11<78<-92	0,4<1,5<2,3	good	No
2006.236	SKS	12,66	89,96	6,46	72<80<-91	1,5<1,6<1,8	58<65<72	1,4<1,6<1,8	68<75<86	1,4<1,6<1,8	good	No
2006.237	SKS	235,75	86,52	6,58	66<68<73	2,5<2,7<2,9	64<68<70	2,4<2,8<3,2	64<66<68	2,6<2,9<3,2	fair	No
2005.061	SKS	67,30	126,76	7,11	-	-	-	-	-	-	fair	Yes

Table 5.13 – ASCB results. We present the data events in Julian format, the analized phase, the backazimuth of the event, its epicentral distance and the Magnitud. Then, the results for ϕ and δt and their error obtained with the three methodologies and the quality factor assigned. In the grey column are null measurements data.

Tabla 5.13 – Resultados de ASCB. Presentamos la fecha de los eventos en formato Juliano, el tipo de fase analizado, el backazimuth del evento, su distancia epicentral y la magnitud. Además de los resultados por ϕ y δt y sus errores obtenidos con las tres metodologías y el parámetro de calidad asignado. Las columnas en gris son los valores null.

5.14 ACLR

The ACLR station is located close Calar Alto in the Sierra de Filabres (Almeria), within the Internal Zones unit. We analyzed data in the period 2004-2006, for a total of 125 data. We utilized different filters because the records contained a lot of noise. In the end, 12 data were available, of which 2 are good, 5 are fair, 2 are poor, 2 good null and 1 poor null. We show all the results obtained in table 5.14 and in the Figure A-14 in the appendix. We utilize a filter of 0.01-1.0 Hz for the majority of events, where poor quality is present we elect to use a filter of 0.02-0.3 Hz.

The data show the same trend, only one event gave a fast direction with a difference of few degrees when compared to other results. Thus, we propose a one layer model with splitting parameters of $\Phi = 83°$, $\delta t = 1.7$ sec for ACLR.

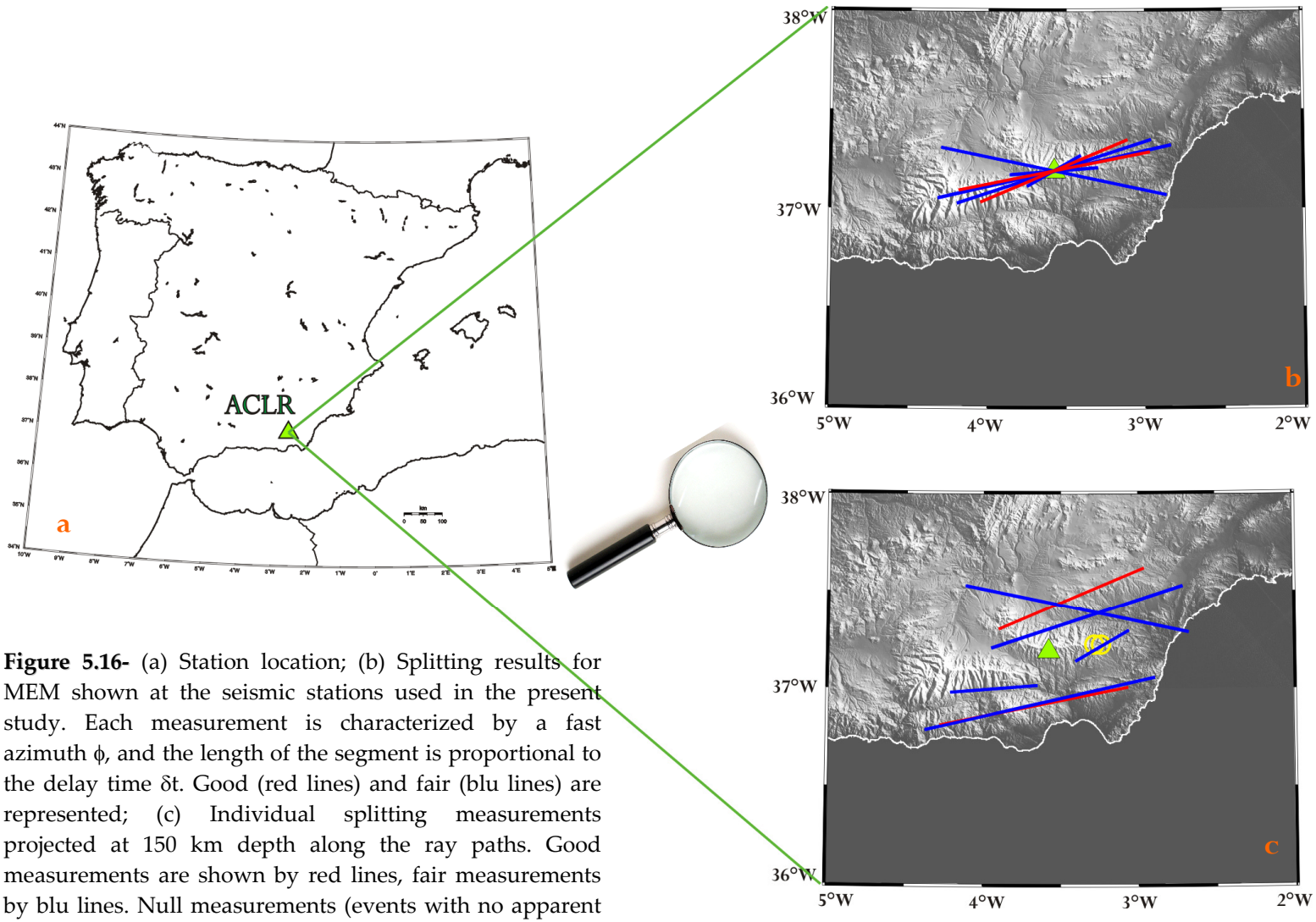

Figure 5.16- (a) Station location; (b) Splitting results for MEM shown at the seismic stations used in the present study. Each measurement is characterized by a fast azimuth ϕ, and the length of the segment is proportional to the delay time δt. Good (red lines) and fair (blu lines) are represented; (c) Individual splitting measurements projected at 150 km depth along the ray paths. Good measurements are shown by red lines, fair measurements by blu lines. Null measurements (events with no apparent splitting) are shown by yellow circles.

Figura 5.9 - (a) Localizacíon de la estación; (b) Resultados del splitting obtenidos con el MEM projectados a la estación. Las medidas están caraterizadas por la direccíon rápida ϕ, y la longitud del segmento es proporcional al retraso δt. Se representan los valores good (líneas rojas) y los valores fair (líneas azules); (c) Las mediciones individuales del splitting estàn proyectadas a 150 km de profundidad a lo largo del recorrido del rayo. Las medidas good se muestran con líneas rojas y las fair con líneas azules. Las medidas Null (eventos con apparente no splitting) se muestran con círculos amarillos.

Date	phase	baz°	Δ°	Mw	ϕ ° ME	δt ME(s)	ϕ° RC	δt RC (s)	ϕ°EV	δt EV(s)	quality	null
2004.297	SKS	30,50	97,35	6,56	72<87<-81	1,0<1,4<1,8	74<89<-84	1,0<1,04<1,9	74<-87<-74	1,0<1,5<2,0	good	No
2004.333	SKS	23,46	94,55	6,98	80<88<-84	1,2<1,4<1,6	54<63<74	1,2<1,5<1,9	68<83<-84	1,1<1,4<1,6	good	No
2005.036	SKS	62,62	113,85	7,08	22<29<39	0,1<0,2<0,4	-27<7<50	0,1<0,5<1,6	-15<23<64	0,1<0,2<0,8	fair	No
2005.288	SKS	48,31	99,21	6,42	-84<-74<-66	0,2<0,4<0,5	56<60<70	1,0<1,8<4,0	56<68<-37	0,2<1,2<2,8	good	No
2006.136	SKS	84,48	97,14	6,80	26<39<55	0,2<0,5<0,7	7<42<76	0,3<0,6<1,4	11<78<-92	0,4<1,5<2,3	good	No
2006.236	SKS	12,66	89,96	6,46	72<80<-91	1,5<1,6<1,8	58<65<72	1,4<1,6<1,8	68<75<86	1,4<1,6<1,8	good	No
2006.237	SKS	235,75	86,52	6,58	66<68<73	2,5<2,7<2,9	64<68<70	2,4<2,8<3,2	64<66<68	2,6<2,9<3,2	fair	No
2005.061	SKS	67,30	126,76	7,11	-	-	-	-	-	-	fair	Yes

Table 5.14 – ACLR results. We present the data events in Julian format, the analized phase, the backazimuth of the event, its epicentral distance and the Magnitud. Then, the results for ϕ and δt obtain with the three methodologies and the quality factor assigned. In the grey column are null measurements data.

Tabla 5.14 – Resultados de ACLR. Presentamos la fecha de los eventos en formato Juliano, el tipo de fase analizado, el backazimuth del evento, su distancia epicentral y la magnitud. Además de los resultados por ϕ y δt y sus errores obtenidos con las tres metodologías y el parámetro de calidad asignado. Las columnas en gris son los valores null.

5.15 ACBG

The ACBG station is located in Cabo de Gata (Almeria), on the Neogene volcanic field, and has been operating since January of 2006. We analyzed data from 2006 for a total of 91 processed events selected with magnitude Mw≥5.5 and distance 85<Δ°<165. The data contained a lot of noise and the utilization of different filters did not change the quality. We utilize a filter of 0.01-1.0 Hz for the majority of events, where poor quality is present we elect to use a filter of 0.02-0.3 Hz. In the end, 6 results were available, of which 3 are good, 2 are fair, 1 is poor. We show all the results obtained in table 5.15 and in the Figure A-15 in the appendix.

All values show a homogenous pattern ranging between 50° and 72°, and thus do not show back azimuth dependence. We propose a one layer model with splitting parameters of $\Phi = 59°$, $\delta t = 1.7$ sec for ACBG.

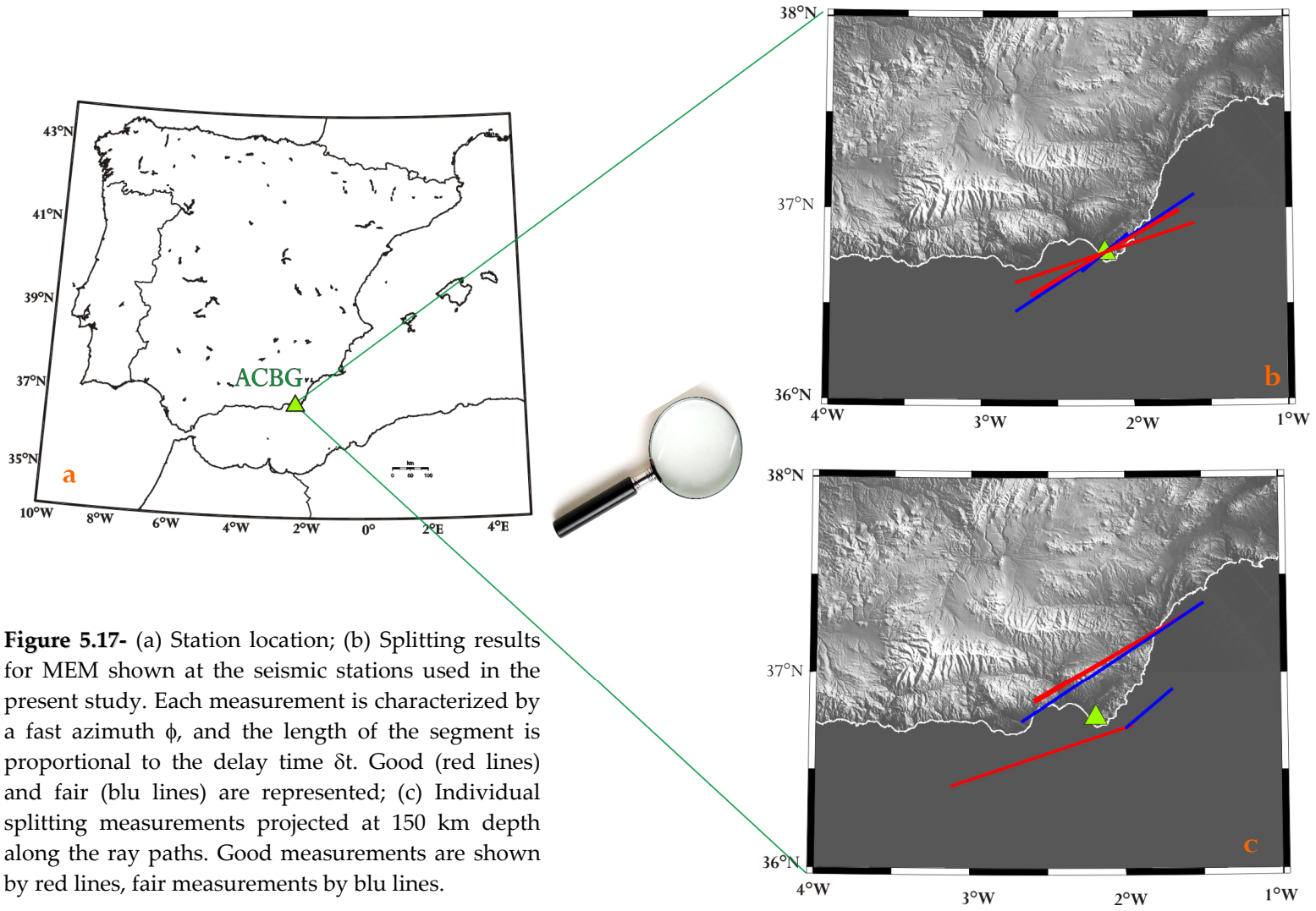

Figure 5.17- (a) Station location; (b) Splitting results for MEM shown at the seismic stations used in the present study. Each measurement is characterized by a fast azimuth ϕ, and the length of the segment is proportional to the delay time δt. Good (red lines) and fair (blu lines) are represented; (c) Individual splitting measurements projected at 150 km depth along the ray paths. Good measurements are shown by red lines, fair measurements by blu lines.

Figura 5.17 –

(a) Localizacíon de la estación; (b) Resultados del splitting obtenidos con el MEM projectados a la estación. Las medidas están caraterizadas por la direccíon rápida ϕ, y la longitud del segmento es proporcional al retraso δt. Se representan los valores good (líneas rojas) y los valores fair (líneas azules); (c) Las mediciones individuales del splitting estàn proyectadas a 150 km de profundidad a lo largo del recorrido del rayo. Las medidas good se muestran con líneas rojas y las fair con líneas azules.

Date	phase	baz°	Δ°	Mw	ϕ ° ME	δt ME(s)	ϕ° RC	δt RC (s)	ϕ°EV	δt EV(s)	quality	null
2006.232	SKS	13,59	91,30	5,98	52<60<66	1,6<1,8<2,1	42<50<59	1,6<1,8<2,0	37<50<62	1,6<1,8<2,1	good	No
2006.232	SKS	195,25	101,25	6,98	52<67<82	1,5<2,2<3,0	56<73<-91	1,7<2,2<2,8	56<81<-82	1,7<2,4<3,2	poor	No
2006.236	SKS	12,55	90,26	6,46	58<61<64	1,7<1,8<1,9	57<61<67	1,7<1,8<1,9	56<61<66	1,7<1,8<1,9	good	No
2006.237	SKS	235,65	86,25	6,58	70<72<74	1,8<2,0<2,2	-70<-62<-56	0,1<0,2<0,3	74<76<78	1,6<1,8<2,0	good	No
2006.273	SKS	16,85	93,88	6,58	50<57<64	1,9<2,2<2,6	60<69<81	1,8<2,1<2,3	54<67<82	1,9<2,1<2,4	fair	No
2006.335	SKS	80,45	96,91	6,30	-1<50<78	0,2<0,6<1,9	32<38<47	0,3<0,5<0,7	17<72<84	0,3<1,2<2,2	fair	No

Table 5.15 – ACBG results. We present the data events in Julian format, the analized phase, the backazimuth of the event, its epicentral distance and the Magnitud. Then, the results for ϕ and δt and their error obtained with the three methodologies and the quality factor assigned. In the grey column are null measurements data.

Tabla 5.15 – Resultados de ACBG. Presentamos la fecha de los eventos en formato Juliano, el tipo de fase analizado, el backazimuth del evento, su distancia epicentral y la magnitud. Además de los resultados por ϕ y δt y sus errores obtenidos con las tres metodologías y el parámetro de calidad asignado. Las columnas en gris son los valores null.

5.16 GORA

The GORA station is located in Gorafe (Granada) on sedimentary units of the Guadix-Baza Basin, within the Betic domain, and is managed by IAG. We analyzed data from 2001 to 2006, for a total of 182 processed events selected with magnitude Mw≥5.5 and distance 85<Δ°<165. The data have a lot of noise and the utilization of different filters did not change the quality. From 182 events analyzed, finally are only 5 results available, of them 4 are good and 1 is fair. We show all the results obtained in table 5.16 and in the Figure A-16 in the appendix. We utilize a filter of 0.01-1.0 Hz for the majority of events, where poor quality is present we elect to use a filter of 0.02-0.3 Hz.

The average fast direction, for the good results obtained with the minimum energy method is ϕ=73°.The only data that come from Southeast show the same direction of the other data so we can conclude that for this station there is a single layer model with splitting parameters of Φ = 73° and δt =1.3 sec.

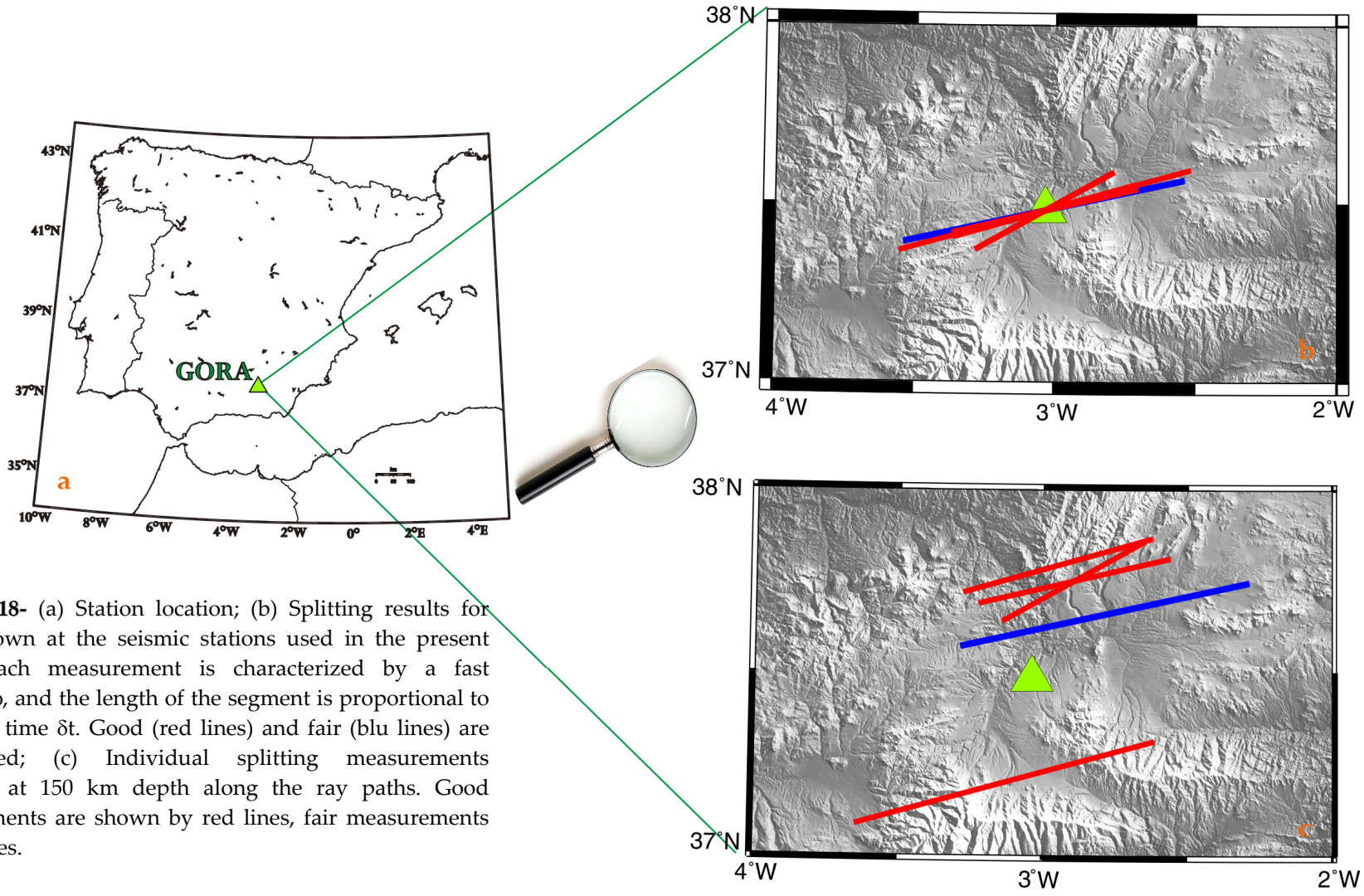

Figure 5.18- (a) Station location; (b) Splitting results for MEM shown at the seismic stations used in the present study. Each measurement is characterized by a fast azimuth ϕ, and the length of the segment is proportional to the delay time δt. Good (red lines) and fair (blu lines) are represented; (c) Individual splitting measurements projected at 150 km depth along the ray paths. Good measurements are shown by red lines, fair measurements by blu lines.

Figura 5.18 - (a) Localizacíon de la estación; (b) Resultados del splitting obtenidos con el MEM projectados a la estación. Las medidas están caraterizadas por la direccíon rápida ϕ, y la longitud del segmento es proporcional al retraso δt. Se representan los valores good (líneas rojas) y los valores fair (líneas azules); (c) Las mediciones individuales del splitting estàn proyectadas a 150 km de profundidad a lo largo del recorrido del rayo. Las medidas good se muestran con líneas rojas y las fair con líneas azules.

Date	phase	baz°	Δ°	Mw	ϕ ° ME	δt ME(s)	ϕ° RC	δt RC (s)	ϕ° EV	δt EV(s)	quality	null
2004.250	SKS	194.46	95.46	6.75	66<74<84	1,4<1,7<2,1	45<55<67	1,1<1,3<1,6	46<64<80	1,2<1,5<1,9	Good	no
2004.333	SKS	22.76	94.47	6.98	58<77<-90	0,8<1,1<1,5	59<67<76	0,8<1,0<1,2	58<83<-80	0,8<1,2<1,6	Good	no
2004.341	SKS	22.74	94.60	6.74	43<61<84	0,6<0,9<1,3	59<68<78	0,7<0,8<1,0	33<61<-86	0,6<0,9<1,5	Good	no
2005.288	SKS	47.54	99.52	6.42	68<78<-92	1,3<1,7<2,4	-67<-56<-46	0,8<0,9<1,1	88<-66<-33	0,6<1,0<1,6	Fair	no
2006.236	SKS	12.04	89.70	6.46	68<74<82	0,9<1,1<1,3	47<57<67	0,7<0,8<1,0	54<66<80	0,7<1,0<1,2	good	no

Table 5.16 – GORA results. We present the data events in Julian format, the analized phase, the backazimuth of the event, its epicentral distance and the Magnitud. Then, the results for ϕ and δt and their error obtained with the three methodologies and the quality factor assigned. In the grey column are null measurements data.

Tabla 5.16 – Resultados de GORA. Presentamos la fecha de los eventos en formato Juliano, el tipo de fase analizado, el backazimuth del evento, su distancia epicentral y la magnitud. Además de los resultados por ϕ y δt y sus errores obtenidos con las tres metodologías y el parámetro de calidad asignado. Las columnas en gris son los valores null.

5.17 SELV

The SELV station is located in Sierra Elvira, near Granada, within the External Zone and is managed by IAG. We analyzed data from 2001 to 2006 for a total of 181. In the end, we obtained 11 reliable observations, of which 6 are good, 1 fair, 3 poor and 1 poor null. We show all the results obtained in table 5.17 and in the Figure A-17 in the appendix. We utilize a filter of 0.01-1.0 Hz for the majority of events, where poor quality is present we elect to use a filter of 0.02-0.3 Hz.

The data show roughly the same trend and the poor data are in agreement with the other. Null good and null fair values have backazimuth that coincided with the mean fast direction inferred. We propose a one layer model with splitting parameters of $\Phi = 59°$, $\delta t = 1.0$ sec for SELV.

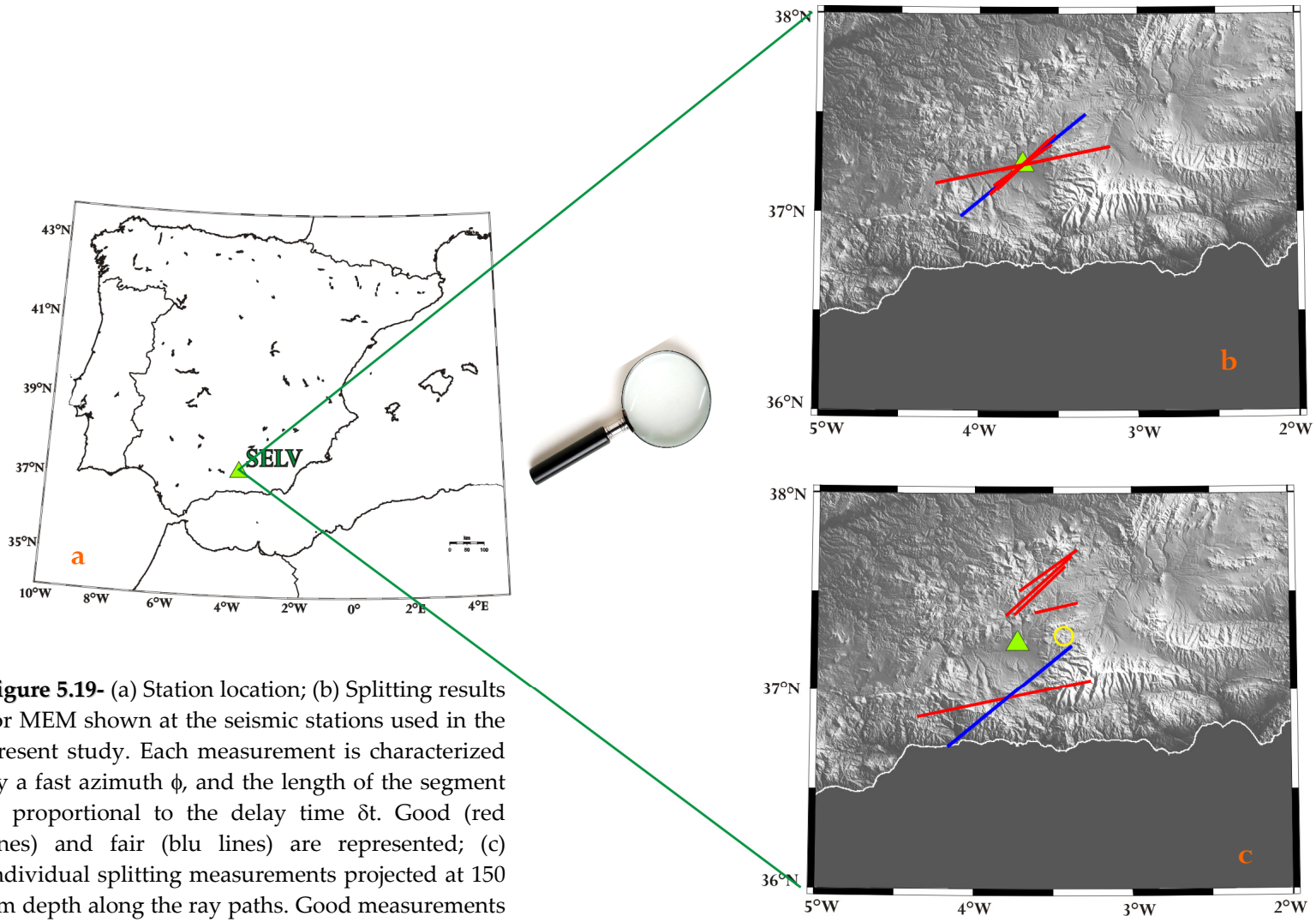

Figure 5.19- (a) Station location; (b) Splitting results for MEM shown at the seismic stations used in the present study. Each measurement is characterized by a fast azimuth ϕ, and the length of the segment is proportional to the delay time δt. Good (red lines) and fair (blu lines) are represented; (c) Individual splitting measurements projected at 150 km depth along the ray paths. Good measurements are shown by red lines, fair measurements by blu lines. Null measurements (events with no apparent splitting) are shown by yellow circles.

Figura 5.19 - (a) Localizacíon de la estación; (b) Resultados del splitting obtenidos con el MEM projectados a la estación. Las medidas están caraterizadas por la direccíon rápida ϕ, y la longitud del segmento es proporcional al retraso δt. Se representan los valores good (líneas rojas) y los valores fair (líneas azules); (c) Las mediciones individuales del splitting estàn proyectadas a 150 km de profundidad a lo largo del recorrido del rayo. Las medidas good se muestran con líneas rojas y las fair con líneas azules. Las medidas Null (eventos con apparente no splitting) se muestran con círculos amarillos.

Date	phase	baz°	Δ°	Mw	ϕ ° ME	δt ME(s)	ϕ° RC	δt RC (s)	ϕ°EV	δt EV(s)	quality	null
2002.321	SKS	19,66	90,82	7,28	41<48<52	0,8<0,9<1,1	54<57<66	0,7<0,8<0,9	43<50<58	0,7<0,8<1,1	good	no
2004.210	SKS	57,55	125,81	6,47	-78<-50<-41	0,6<1,9<4,0	65<76<88	0,2<0,5<0,8	25<64<-58	0,1<0,6<2,2	poor	no
2004.250	SKS	194,09	95,09	6,75	64<78<-92	1,2<1,8<2,7	44<53<64	1,0<1,3<1,6	39<58<80	1,0<1,3<1,9	good	no
2004.333	SKKS	22,31	94,90	6,98	39<54<82	0,4<0,7<1,1	60<75<-90	0,4<0,6<0,8	48<68<-84	0,4<0,6<0,9	good	no
2004.341	sSKS	22,28	95,03	6,74	35<46<70	0,4<0,7<1,2	61<69<80	0,3<0,4<0,6	35<48<82	0,4<0,7<1,3	good	no
2005.252	SKS	38,08	141,22	7,65	15<22<33	2,9<4,0<4,0	58<66<77	0,0<0,3<0,6	11<28<52	3,0<4,0<4,0	poor	no
2005.272	SKS	41,04	141,16	6,61	-31<17<37	0,3<1,0<2,3	-27<-12<2	0,3<0,7<1,0	-58<11<41	0,2<0,9<2,2	poor	no
2005.288	SKS	47,09	100,09	6,42	58<77<-64	0,2<0,4<1,0	86<-86<-79	0,2<0,4<0,5	56<85<-52	0,2<0,4<1,0	good	no
2006.002	SKS	188,65	99,12	7,36	33<51<70	1,0<1,7<2,4	29<36<46	1,4<1,7<2,0	15<35<54	1,1<1,7<2,3	fair	no
2004.207	SKS	81,04	105,52	7.28	-	-	-	-	-	-	good	yes
2004.073	SKS	65,38	123,95	6.69	-	-	-	-	-	-	poor	-yes

Table 5.17 – SELV results. We present the data events in Julian format, the analized phase, the backazimuth of the event, its epicentral distance and the Magnitud. Then, the results for ϕ and δt and their error obtained with the three methodologies and the quality factor assigned. In the grey column are null measurements data.

Tabla 5.17 – Resultados de SELV. Presentamos la fecha de los eventos en formato Juliano, el tipo de fase analizado, el backazimuth del evento, su distancia epicentral y la magnitud. Además de los resultados por ϕ y δt y sus errores obtenidos con las tres metodologías y el parámetro de calidad asignado. Las columnas en gris son los valores null.

5.18 ANER

The ANER station is located in the Nerja's cave in the Maro Village (Malaga), within the Internal Zone of the Betic Range.

We analyzed data from 2001 to 2006 for a total of 194 processed events selected with magnitude Mw≥5.5 and distance 85<Δ°<165. The data have a lot of noise and utilizing different filters did not change the quality. We utilize a filter of 0.01-1.0 Hz for the majority of events, where poor quality is present we elect to use a filter of 0.02-0.3 Hz. Thus, 21 results were availabled, of them 8 are good, 8 are fair, 2 are poor, 2 good null and 1 poor null. We show all the results obtained in table 5.18 and in the Figure A-18 in the appendix.

The data show like two trends, but for the same back azimuth direction. For the MEM, we can notice the first trend for ϕ= 47° and δt= 2,26 sec, the second trend is about 0° and δt is 0,95 sec. If we considered the good and fair date together the average do not change significantly. Infact the ϕ = 45° and ϕ =9°average fast direction for the results obtained with the minimum energy method is 72°.

The majority of events arrived from Northeast, only three from south-west, and we note that a backazimuthal dependence of ϕ could be present. Such a backazimuthal dependence of splitting parameters may be explained either by invoking vertical variation of anisotropy, e.g. by the presence of two (or more) anisotropic layers, or by lateral variations of anisotropy. We discuss about this point in the Chapter 7.1. So for this ambiguity is in part due to the backazimuthal distribution of the events being rather limited, we prefer the alternative hypothesis of an anisotropy that varies laterally. So finally we propose for ANER station a one layer model with splitting parameters of ϕ =N31°E and δt = 1.5 sec

Anyway we present in Figure A-18a-b (appendix) the best 2 layer model fit for fast direction in upper layer ϕ=N28°E and delay time δt=1.0s, while fast direction in the lower layer ϕ=N68°E and delay time δt=0.6s.

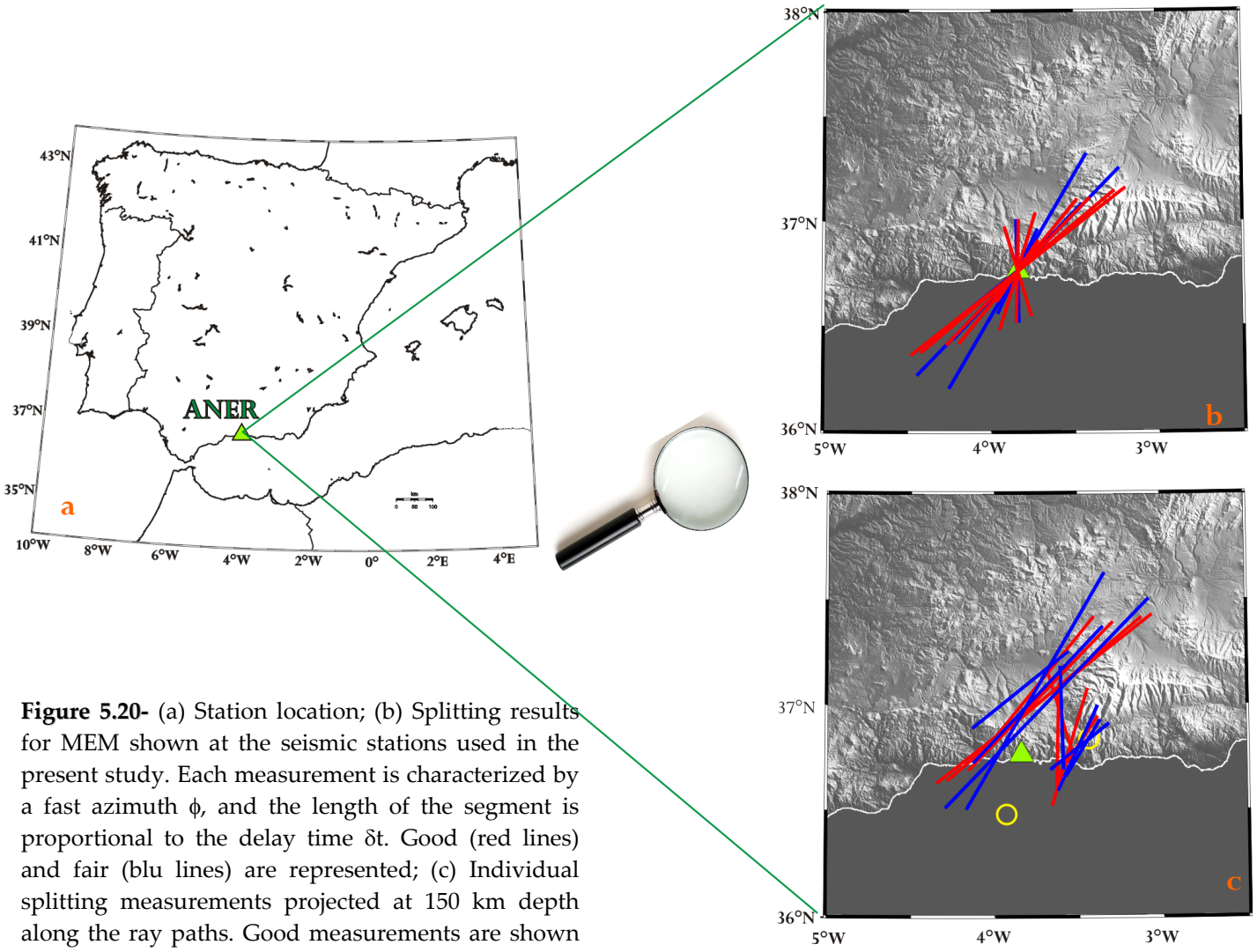

Figure 5.20- (a) Station location; (b) Splitting results for MEM shown at the seismic stations used in the present study. Each measurement is characterized by a fast azimuth ϕ, and the length of the segment is proportional to the delay time δt. Good (red lines) and fair (blu lines) are represented; (c) Individual splitting measurements projected at 150 km depth along the ray paths. Good measurements are shown by red lines, fair measurements by blu lines. Null measurements (events with no apparent splitting) are shown by yellow circles.

Figura 5.20 - (a) Localizacíon de la estación; (b) Resultados del splitting obtenidos con el MEM projectados a la estación. Las medidas están caraterizadas por la direccíon rápida ϕ, y la longitud del segmento es proporcional al retraso δt. Se representan los valores good (líneas rojas) y los valores fair (líneas azules); (c) Las mediciones individuales del splitting estàn proyectadas a 150 km de profundidad a lo largo del recorrido del rayo. Las medidas good se muestran con líneas rojas y las fair con líneas azules. Las medidas Null (eventos con apparente no splitting) se muestran con círculos amarillos.

Date	phase	baz°	Δ°	Mw	ϕ ° ME	δt ME(s)	ϕ° RC	δt RC (s)	ϕ°EV	δt EV(s)	quality	null
2003.146	SKS	26,51	97,95	7,00	41<45<52	2,4<2,8<3,4	-4<4<12	0,0<0,0<0,2	46<51<58	2,2<2,7<3,3	fair	no
2003.174	SKS	359,61	91,80	6,88	43<52<58	1,0<1,2<1,4	43<50<59	1,0<1,2<1,3	39<48<58	1,0<1,2<1,4	fair	no
2004.207	SKS	81,09	105,69	7,28	7<17<29	0,8<1,2<1,6	43<53<64	0,6<0,7<0,8	21<43<76	0,5<0,8<1,2	good	no
2004.333	sSKS	22,25	95,38	6,98	46<50<56	2,2<2,5<2,8	51<55<62	2,1<2,3<2,6	48<52<60	2,2<2,4<2,7	good	no
2004.341	SKS	22,22	95,51	6,74	48<52<60	2,2<2,7<3,1	53<57<63	2,4<2,7<2,9	50<56<66	2,2<2,6<3,1	good	no
2005.036	SKS	61,31	115,27	7,08	-11<1<17	0,6<1,0<1,4	14<20<27	0,7<0,9<1,0	-11<7<31	0,6<0,9<1,4	good	no
2005.079	SKS	37,08	97,42	6,58	56<63<72	2,3<2,7<3,2	24<31<40	0,3<0,5<0,6	54<61<70	2,4<2,6<2,9	poor	no
2005.134	SKS	82,09	99,47	6,72	23<34<48	0,6<0,7<0,8	27<34<43	0,6<0,7<0,8	17<30<50	0,6<0,7<0,9	good	no
2005.288	SKS	47,07	100,48	6,42	-29<-17<-7	0,6<0,9<1,3	9<15<24	0,4<0,6<0,7	-17<-1<19	0,4<0,7<1,0	good	no
2006.109	SKS	83,63	93,94	6,17	9<32<62	0,4<0,6<1,0	38<44<52	0,5<0,6<0,7	11<58<86	0,4<0,6<1,2	fair	no
2006.136	SKS	83,40	98,64	6,80	3<25<62	0,4<0,9<1,6	30<45<62	0,4<0,7<1,0	68<81<-90	3,7<4,0<4,0	fair	no
2006.173	SKS	18,52	94,32	5,94	39<45<50	1,8<2,0<2,2	31<36<42	2,0<2,1<2,2	31<41<50	1,8<2,0<2,2	good	no
2006.209	SKS	48,42	100,90	5,86	-9<-2<5	0,8<1,0<1,2	3<10<18	0,9<0,9<1,0	11<58<86	0,8<1,0<1,1	fair	no
2006.223	SKS	81,97	96,69	6,23	37<52<62	0,6<0,8<1,0	30<37<45	0,5<0,6<0,7	68<81<-90	0,5<0,8<1,0	fair	no
2006.232	SKS	12,57	91,61	5,98	29<31<33	2,4<2,7<2,9	31<34<39	2,2<2,5<2,8	31<41<50	2,3<2,6<2,8	fair	no
2006.236	SKS	11,55	90,54	6,46	37<40<43	1,7<1,8<2,0	36<39<44	1,8<1,8<1,9	-1<10<25	1,7<1,8<2,0	good	no
2006.273	SKS	15,77	94,26	6,58	31<44<60	1,2<1,8<2,6	57<68<82	1,0<1,3<1,7	31<52<64	0,9<1,6<2,3	fair	no
2006.282	SKS	52,55	101,93	6,26	60<69<-88	0,7<1,8<2,8	-85<-76<-70	0,5<0,8<1,0	31<-33<37	1,2<2,4<3,2	poor	no
2004.250	SKS	194,01	94,61	6,75	-	-	-	-	-	-	good	yes
2006.002	SKS	188,59	98,63	7,36	-	-	-	-	-	-	poor	Yes
2006.034	SKS	76,69	87,77	6,07	-	-	-	-	-	-	good	yes

Table 5.18 – ANER results. We present the data events in Julian format, the analized phase, the backazimuth of the event, its epicentral distance and the Magnitud. Then, the results for ϕ and δt and their error obtained with the three methodologies and the quality factor assigned. In the grey column are null measurements data.

Tabla 5.18 – Resultados de ANER. Presentamos la fecha de los eventos en formato Juliano, el tipo de fase analizado, el backazimuth del evento, su distancia epicentral y la magnitud. Además de los resultados por ϕ y δt y sus errores obtenidos con las tres metodologías y el parámetro de calidad asignado. Las columnas en gris son los valores null.

5.19 CEUT

The CEUT station is near Ceuta city, in the Northern of Africa, within the Internal domain. This station has been operating since 15th June of 2004. We analyzed data from 2004 to 2006, for a total of 139 events, which gave 7 available SKS measurements, which we classified as 2 fair, 1 poor, 1 is good Null, 2 are fair Null and 1 poor Null. We show all the results obtained in table 5.19 and in the Figure A-19 in the appendix. We utilize a filter of 0.01-1.0 Hz for the majority of events, where poor quality is present we elect to use a filter of 0.02-0.3 Hz.

So we have only two reliable results that do not constrain the anisotropy well for this station, but give a first indication about the anisotropic direction. The lack of events for good backazimuthal coverage hinders a clear interpretation at this moment, but might become clearer with a growing data set over the next years. The mean of the fast direction is nearly N-S, is $\phi = -4^{\circ}$ and $\delta t = 2.1$ sec.

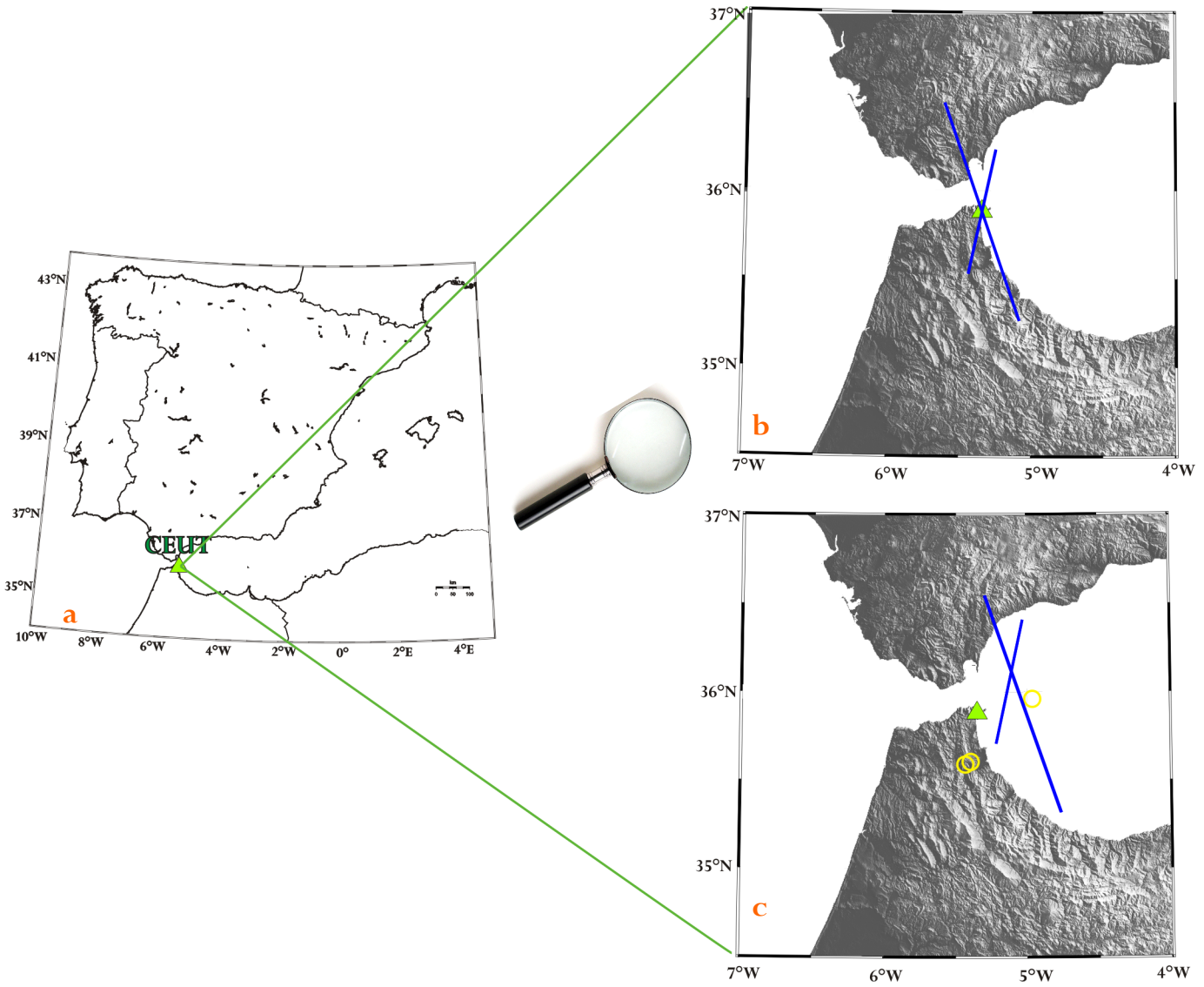

Figura 5.21 - (a) Localizacíon de la estación; (b) Resultados del splitting obtenidos con el MEM projectados a la estación. Las medidas están caraterizadas por la direccíon rápida ϕ, y la longitud del segmento es proporcional al retraso δt. Se representan los valores fair (líneas azules); (c) Las mediciones individuales del splitting estàn proyectadas a 150 km de profundidad a lo largo del recorrido del rayo. Las medidas good se muestran con líneas rojas y las fair con líneas azules. Las medidas Null (eventos con apparente no splitting) se muestran con círculos amarillos.

Figure 5.21- (a) Station location; (b) Splitting results for MEM shown at the seismic stations used in the present study. Each measurement is characterized by a fast azimuth ϕ, and the length of the segment is proportional to the delay time δt. Fair (blu lines) values are represented; (c) Individual splitting measurements projected at 150 km depth along the ray paths. Fair measurements are shown by blu lines. Null measurements (events with no apparent splitting) are shown by yellow circles.

Date	phase	baz°	Δ°	Mw	ϕ ° ME	δt ME(s)	ϕ° RC	δt RC (s)	ϕ°EV	δt EV(s)	quality	null
2005.288	SKS	46,14	101,97	6,42	3<12<23	1,0<1,4<2,0	-20<-7<4	0,8<1,1<1,3	-21<0<17	0,7<1,2<1,8	No	fair
2006.219	SKKS	18,84	159,07	6,81	-70<-63<-41	0,2<1,0<1,6	-24<-15<-7	0,1<0,2<0,2	-80<-65<19	0,0<1,0<1,6	No	poor
2006.335	SKS	78,64	99,58	6,30	-27<-19<-19	1,7<2,7<3,6	-74<-63<-54	0,0<0,3<0,5	-25<-17<-13	2,0<2,8<3,6	No	fair
2004.250	SKS	193,19	93,46	6,75	-	-	-	-	-	-	Yes	good
2004.341	SKS	21,25	96,78	6,74	-	-	-	-	-	-	Yes	poor
2006.002	SKS	187,85	97,59	7,36	-	-	-	-	-	-	Yes	fair
2006.034	SKS	75,78	89,16	6,07	-	-	-	-	-	-	Yes	fair

Table 5.19 – CEUT results. We present the data events in Julian format, the analized phase, the backazimuth of the event, its epicentral distance and the Magnitud. Then, the results for ϕ and δt and their error obtained with the three methodologies and the quality factor assigned. In the grey column are null measurements data.

Tabla 5.19 – Resultados de CEUT. Presentamos la fecha de los eventos en formato Juliano, el tipo de fase analizado, el backazimuth del evento, su distancia epicentral y la magnitud. Además de los resultados por ϕ y δt y sus errores obtenidos con las tres metodologías y el parámetro de calidad asignado. Las columnas en gris son los valores null.

5.20 Summary

In the table 5.20 we summarized the results for each station, showing the station coordinates, the number and quality of the observation, and the mean values obtained for the good and fair observations with the MEM. We present the mean splitting parameters, given as mean values (m), median values (md) and weighted-mean values (w) with 2σ errors. For (m) errors give two times the standard deviation of individual values; for (w) they give the error of the weighted mean.

Station Name	Lat°	Long°	Net	Num. Events	Events quality	ϕ_m (°)	$\sigma\phi_m$ (°)	δt_m (sec)	$\sigma\delta t_m$ (sec)	ϕ_{md} (°)	δt_{md} (sec)	ϕ_w (°)	$\sigma\phi_w$ (°)	δt_w (sec)	$\sigma\delta t_w$ (sec)
ECAL	41.9413	-6.7371	ES	8	1g+1p+3gN+1fN+2pN	-72	11.00	0.80	0.15	-72.00	11.00	-72.00	11.00	0.8	0.35
MTE	40.3997	-7.5442	GE	40	4g+6f+15p+3gN+7fN+5pN	93	12.41	1.30	0.23	90.52	1.21	91.64	7.02	1.16	0.09
PAB	39.5458	-4.3483	IU	47	7g+19f+10p+3gN+4fN+4pN	86	16.21	1.13	0.79	79.28	1.10	81.25	2.35	0.71	0.09
HORN	37.8200	-5.2800	IG	22	7g+7f+4gN+4fN	58	21.19	1.07	0.40	57.56	0.94	40.15	2.28	0.92	0.1
ARAC	37.8800	-6.5800	IG	13	4g+4f+2gN+1fN+2pN	64	12.51	0.99	0.35	67.81	1.00	65.00	6.95	0.79	0.12
JAND	38.22	-3.97	IG	4	1g+2f+1fN	6	6.49	48.64	1.72	0.33	31.52	1.80	1.03	3.75	1.61
SESP	38.1208	-2.5452	IG	31	5g+7f+8gN+8fN+3pN	66	28.69	1.68	0.63	72.26	1.70	47.35	1.38	1.77	0.11
ESTP	37.2713	-4.8662	IG	20	2g+7f+3p+1gN+7fN	81	13.05	1.56	0.59	83.16	1.34	63.44	3.12	1.45	0.18
SFS	36.4656	-6.2055	WM/GE	10	1g+1f+8fN	-1	28.41	1.10	0.99	-1.27	1.10	17.03	7.91	0.87	0.41
MELI	35.2899	-2.9392	WM/GE	10	3g+1p+1gN+5fN	67	8.24	1.43	0.60	63.11	1.50	67.51	3.27	0.95	0.09
CART	37.5868	1.0012	WM/GE	22	8g+3f+2p+4gN+3fN+2pN	69	7.97	1.56	0.31	69.74	1.50	72.93	1.27	1.46	0.07
VELZ	37.5838	-1.9880	IG	12	5g+3f+1p+1gN+1fN+1pN	70	12.87	1.45	0.48	66.45	1.40	64.94	2.64	1.39	0.08
ASCB	37.0394	-2.0056	IG	8	5g+2f+1fN	54	14.76	1.46	0.73	63.46	1.52	65.73	2.51	1.62	0.16
ACLR	37.1897	-2.5822	IG	12	2g+5f+2p+2gN+1pN	77	8.49	1.74	0.69	77.20	2.00	82.60	4.26	1.72	0.18
ACBG	36.7686	-2.1939	IG	6	3g+2f+1p	59	7.94	1.70	0.64	59.59	1.88	67.09	1.59	1.86	0.08
GORA	37.4805	-3.0398	IG	5	4g+1f	73	6.85	1.30	0.38	74.46	1.12	73.28	5.36	1.18	0.14

SELV	37.2383	-3.7277	IG	11	5g+1gN+1f+3p+1pN	59	1.04	0.56	52.48	0.81	48.33	4.56	0.86	0.12	1.04
ANER	36.7623	-3.8453	IG	21	8g+8f+2p+2gN+1pN	31	21.11	1.54	0.80	36.82	1.18	35.91	1.29	1.29	0.06
CEUT	35.8831	-5.3263	IG	7	2f+1p+1gN+2fN+1pN	-4	22.27	2.06	0.88	-3.61	2.06	-15.01	3.76	1.71	0.44

Table 5.20 – Station locations and mean values of splitting parameters measured (mean values (m), median values (md) and weighted-mean values (w) with 2σ errors. For (m) errors give two times the standard deviation of individual values; for (w) they give the error of the weighted mean).

Tabla 5.20– Localización de las estaciones utilizadas y los valores medios de los parámetros de anisotropía medidos (valores medios (m), de la mediana (md) y de la media ponderada (w) con error de 2σ. Para (m) los errores equivalent a dos veces la desviación estandar de las medidas individuales; para (w) los errores equivalen a la media ponderada).

In Figure 5.22 we present the mean fast direction inferred and presented in table 5.20.

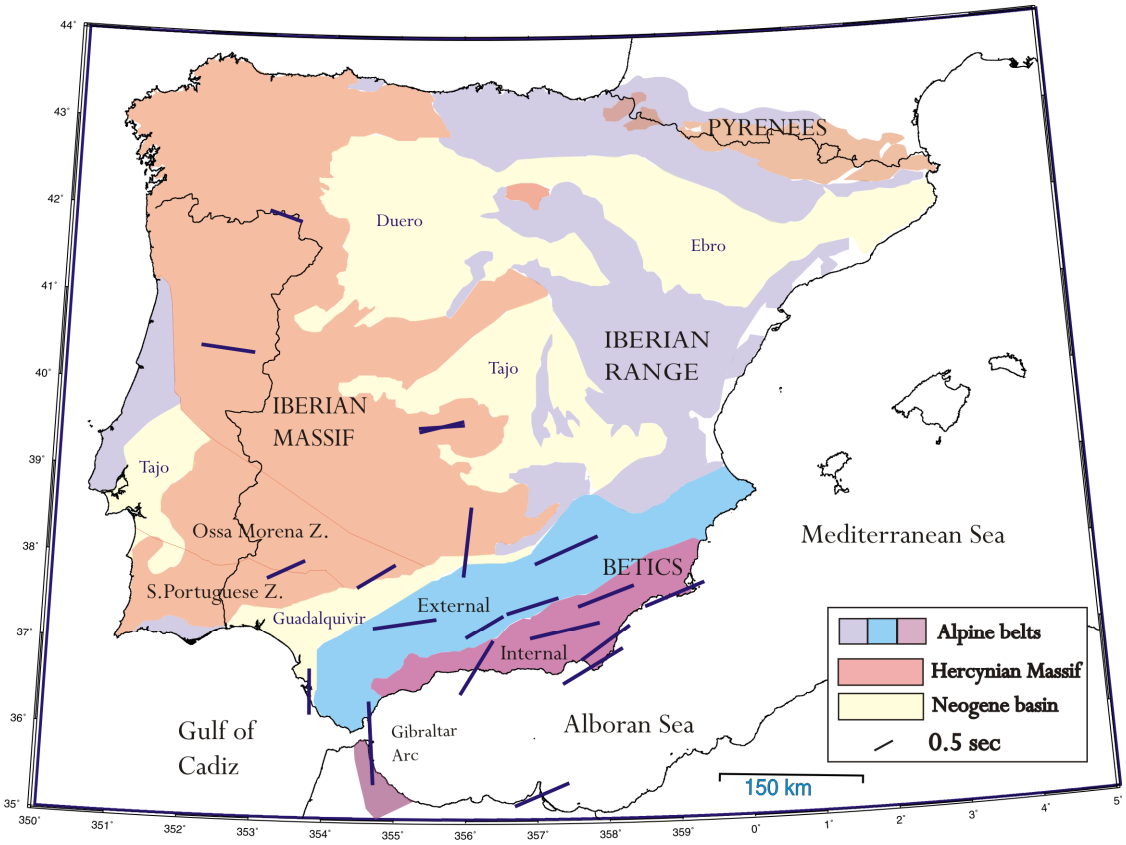

Figure 5.22 – Geologic map for the Iberian Peninsula. Blu lines are the mean fast direction inferred in this work. Each measurement is characterized by a fast azimuth ϕ, and the length of the segment is proportional to the delay time δt.

Figura 5.22 – Mapa geologico de la Peninsula Iberica. Las líneas azules son los valores medio de las direciones rapidas calculadas en este trabajo. Cada medida está caraterizada por la direction rápida ϕ, y la longitud del segmento es proporcional al retraso δt.

6. Geological and geophysical observations

The location of the Iberian Peninsula at close proximity to the active African-European plate boundaries at its southern margins, to the Pyrenean orogen at the north, as well as to active Neogene extensional basin formation at its eastern margin, makes it an almost ideal natural laboratory for the analysis of the underlying lithosphere and the deformational process that have acted and are actually acting in it. This region gives also the possibility to address questions of geodynamics, some of which can be how the lithosphere developed and deformed, if there is evidence for multi-layer (asthenospheric plus lithospheric) anisotropy, if the whole lithosphere is affected, or only part of the keel (in the case of lithospheric anisotropy).

The Iberian Peninsula is a complex zone comprising different structures. Almost the whole zone is affected by shallow and intermediate depth seismicity (Figure 6.1), although some very deep seismicity (660 km) has occurred near Granada (Buforn et al., 1991). Being part of a (diffuse) plate boundary, the southern margin of Iberia is characterized by high level of seismicity, hence amount of large earthquakes mostly occurred in the Gulf of Cadiz and north of Africa. The largest recent earthquakes were in Algeria on October 1980 with Mw of 7.1 (Deschamps et al., 1982) and in the Gulf of Cadiz was of Mw 6.1 on 15th March 1964 (Buforn et al., 1988). Also Morocco was affected on 2004 by an earthquake with Mw of 6.4 (Stich et al., 2005).

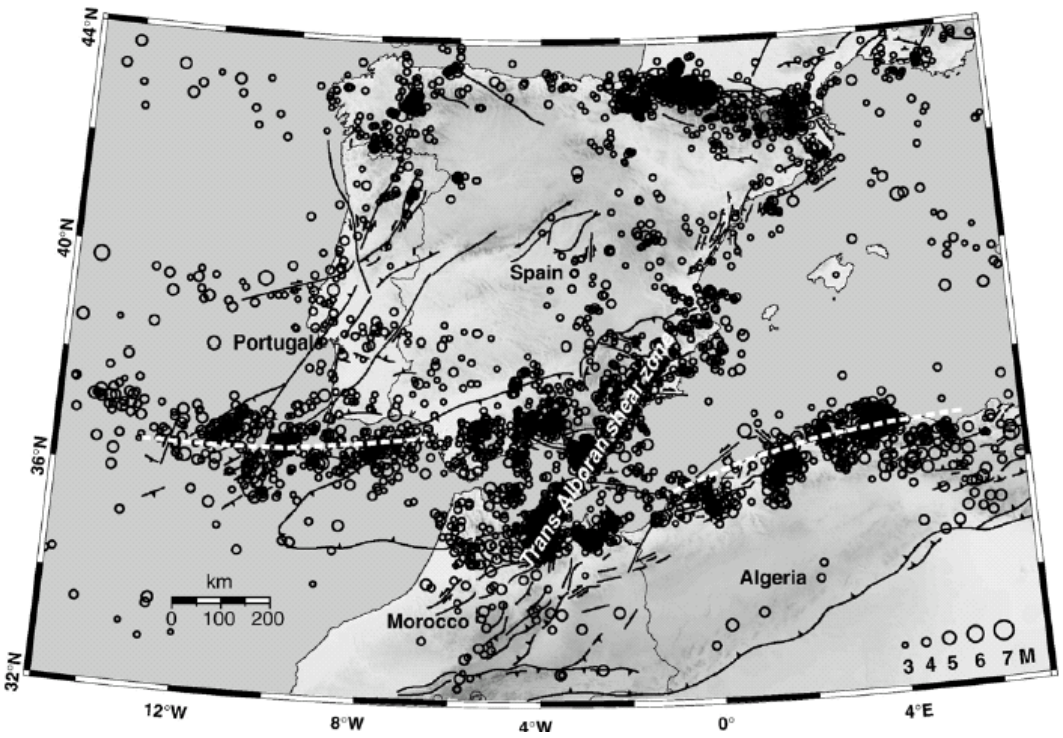

Figure 6.1 - Seismicity of the Ibero–Maghrebian region projected on the map of active and potentially active faults. Epicenters of earthquake with local magnitude ≥3 (scale on lower right) are taken from the NEIC catalogue (http://neic.usgs.gov) (Stich et al., 2006).

Figura 6.1 – Mapa de sismicidad de la región Ibero-Maghrebi proyectado en un mapa de fallas activas y potencialmente activas. El epicentro de los terremotos con magnitudo local ≥3 (escala bajo a la derecha) ha sido tomado desde el catalogo NEIC (http://neic.usgs.gov) (Stich et al., 2006).

Crustal geometry of the Iberian Peninsula is well known in many areas due to seismic, geological, topographic, magnetic, tomographic and gravimetric studies, while subcrustal images rely almost solely in seismic tomography works. Some anisotropic studies have been carried out by Diaz et al. (1998), Calvert et al. (2000a, 2000b), Schmid et al. (2004), Serrano et al. (2005), which have improved the knowledge on lithosphere behaviour.

One of the major questions remains in geodynamics of the Alboran domain is to know which depth the measured anisotropy occurs. In contrast to surface wave studies, shear wave splitting data have excellent lateral resolution, but no (direct) vertical resolution, since the splitting parameters reflect the integrated anisotropy along the travel path. An argumentative approach includes correlation with other observables: a large-scale uniform distribution of anisotropy orientations which correlate with plate motion direction strongly support asthenospheric origins. In

contrast, regionalized orientations of anisotropy, which correlate with surface-geologic features, indicate lithospheric origins, if vertically coherent deformation throughout the lithosphere and crust is assumed (Silver, 1996). So to correlate possible source for the observed anisotropy, we will successively considere crustal and lithospheric structures, both geological and geophysical features, in the light of the geodynamic evolution of the Iberian Peninsula. Anyway we start introducing the geological and geodynamic evolution for the Iberian Peninsula.

6.1 Geological and geodynamic setting

Shear wave splitting data of the Iberian Peninsula are analyzed in this work. Now we want introduce the geological framework of this area, discussing separately the two main domains of the Peninsula: the Hercynian or Iberian Massif and the Betic Cordillera. Subsequently, in the light of geodynamic evolution we will explain the inferred anisotropy.

6.1.1 Iberian Massif

The Variscan orogeny started in the middle Devonian and ended in the Carboniferous (Ribeiro et al., 1979), as results of oblique collision between two big continents, the Laurentia-Baltica in the NW part and the Gondwana to SE (Figure 6.2).

The Iberian Massif is the westernmost outcrop of the Variscan Orogen, therefore it is the main Hercynian Massif of the Iberian Peninsula, taking up its half western part. The Massif consists mainly of folded, thrusted and metamorphosed rocks, which during the Palaeozoic were under sea level and were constituted by very variable deposits in lithology and thickness depending on the zone and the age. Hercynian orogeny deformed these materials during upper Carboniferous and the entire unit is outcropped from the Palaeozoic at the present. The erosion processes have left unscovered very deep crustal zones that have allowed to deduce characteristics of the Variscan Massif. The Iberian Massif is delimited on its eastern

and southern parts by sedimentary basins and Alpine orogens and has escaped significant Alpine rejuvenation except along its margin (Matte, 1986).

The Massif has been divided into five main zones, each characterized by distinct paleogeography, structural style, metamorphism and magmatism (Julivert et al., 1980; Ribeiro et al., 1979) and which trend is roughly NW-SE. These are: Cantabrian Zone (CZ), the West Asturian-Leonese Zone (WAIZ), the Galicia-Tras-Os-Montes Zone (GTMZ), the Central Iberian Zone (CIZ), the Ossa Morena Zone (OMZ) and South Portuguese Zone (SPZ).

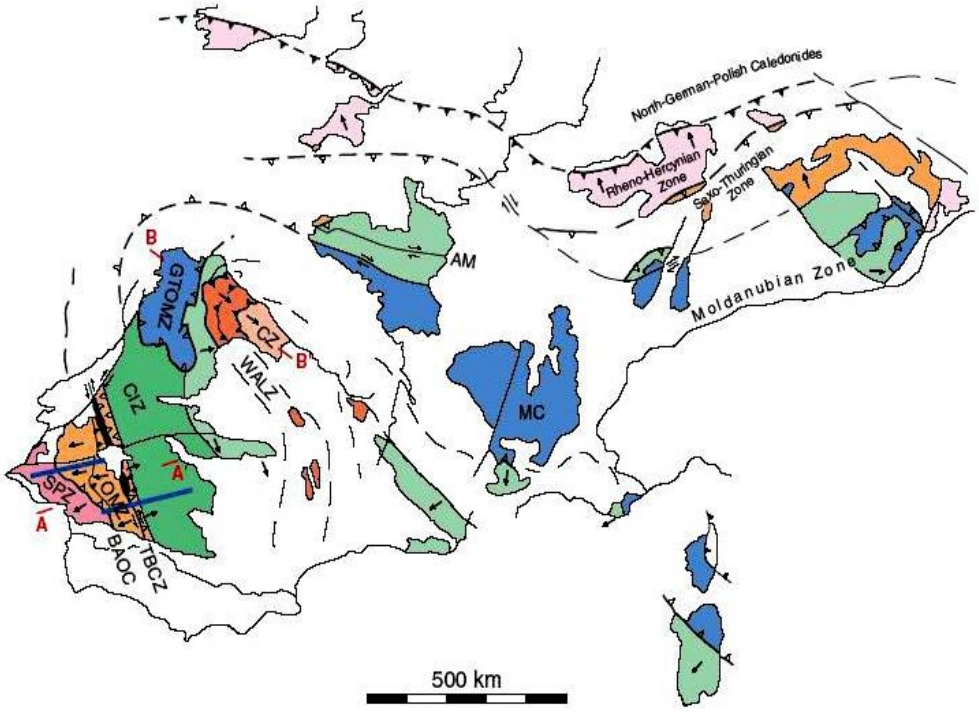

Figure 6.2 – Generalized geologic map of the Variscan Orogen in Iberian Peninsula and part of Europe (after Franke, 1989).

Figura 6.2 – Mapa geológico general de la orogenia Varisca en la Península Ibérica y en parte de Europa (según Franke, 1989).

The Iberian Massif displays certain symmetry or bilaterality. The most external zones, the CZ to the north and the SPZ to the south, occupy the extremity (Figure 6.3). The deformations that take place in CZ affect at cortical level with absence of metamorphism and magmatism. The WALZ, CIZ and GTMZ are constituted by rocks of the Precambric and lower Palaeozoic, and have more cortical deformation

that the CZ more deeply deformed and metamorphosed, and the deformation involve the lithospheric mantle. These three latter zones are part of one terrane.

The OMZ and SPZ underlie the southern Iberian Margin, they are two different terranes that have become attached. In the Mesozoic they were mostly covered with other sediments, which have since eroded.

In summary, the Iberian Massif is the result of the amalgamation of three continental blocks: the SPZ, the OMZ, and the ensemble of the CIZ, WALZ and CZ. The three latter ones belonged to the Gondwana continental margin while the SPZ seems to be the Avalonian border of the opposite continent; in between, the OMZ would be a terrane whose degree of separation from Gondwana is still controversial (Simancas et al., 2003).

The boundary between the SPZ and the OMZ and that between OMZ and CIZ has been recognized as suture contacts (Simancas et al., 2001). The first boundary, the SPZ/OMZ contact, can be considered as a suture based on existence of a strip of oceanic amphibolites (Andrade, 1983; Munhá et al., 1986; Quesada et al., 1994). It is commonly interpretate like a Variscan orogenic suture, and probably it is the main suture of the Variscan orogeny. The second boundary, the OMZ/CIZ contact, has a complex geometry and kinematics and it is of controversial interpretation. Some studies made on rocks of this limits, favor the interpretation that the contact is another Variscan suture (Azor et al., 1994; Simancas et al., 2001). An added difficulty to study this zone is the lack of units as consequence of the transpressional tectonic episode. Anyway three main stages in its tectonic evolution can be distinguished: continental underthrusting (first transpressional stage), an oblique extension (transtensional stage) and a high shortening episode ending with left-lateral faulting.

In the OMZ, the crustal stretching associated with transtension, as well as important thermal processes (astenosphere upwelling), have occurred since the Lower Paleozoic or even since the end of the Proterozoic (Silva, 1999).

Studies of seismic reflection perfiles revel the discontinuous character of the Moho reflection beneath the OMZ, as well as the relatively transparent OMZ lower crust is probably the results of the intrusion magmas (Simancas et al., 2003). This intrusion reworked the old lower crust destroying its internal structure. The Moho reflection beneath the SPZ is sharp and high amplitude, with an almost constant

thickness. At surface, the erosion level of most of the SPZ is shallow and approximately constant. This suggest that in the SPZ there was not significant crustal thickening during collision and that the Moho imaged in this part is mainly an old pre-Variscan Moho, scarcely modified during the Variscan collision time. Under the OMZ the Moho is discontinuous and with increases of thickness. The boundary zone SPZ/OMZ and OMZ/CIZ display dipping reflectors with fan-like geometry, interpreted as faults with variable strike-slip component of displacement. The thrust separating the CIZ from OMZ is inclined to the southwest, whereas the thrust that marks the northern boundary of the SPZ dips north or northeast (Simancas et al., 2003).

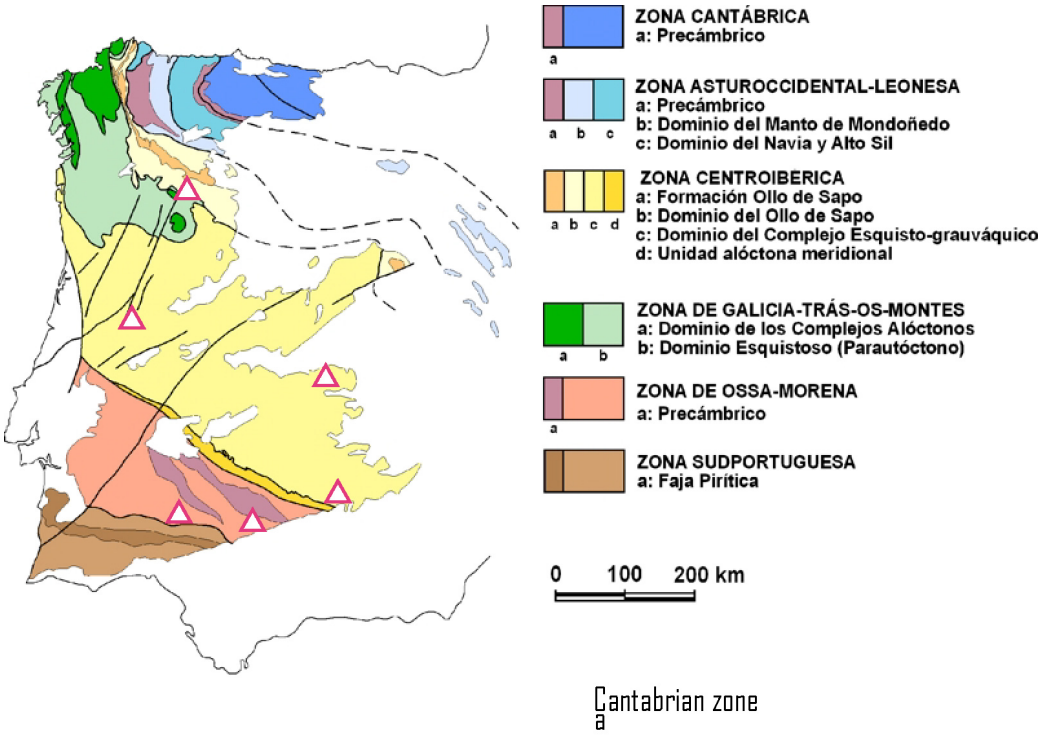

Figure 6.3 - Main tectonic subdivisions of Iberian Massif with approximate station locations (white triangles with magenta border) deployed in that area (modified after Simancas, 2003).

Figura 6.3 – Principal subdivisión tectónica del Macizo Ibérico y con la localización de las estaciónes (triángulos blancos con borde en magenta) desplegadas en esta área (modificado según Simancas, 2003).

6.1.2 Geodynamic setting of Betics Cordillera and Gibraltar Arc

The Betic and Rif belts, connected through the Gibraltar Arc, represent the most westerly Alpine range in southern Europe (Figure 6.4). Together with the Alboran basin, these belts constitute one of most complex and most debated geological regions in the western Mediterranean. A major challenge is to explain how the Alboran basin, in extensional regime (Comas et al.,1999), can coexist within a continent-continent collision regime, here by the convergence of Africa and Eurasia from the Cretaceous to Paleogene (Dewey, 1989). The geological records and geophysical observations shed some light on the evolution of the region. Formally the Gibraltar arc is divided in three pre-Neogene crustal domains: the first consists of Mesozoic and Tertiary sedimentary rocks deformed during the Neogene as a thrust-and-fold belt mainly directed to the NW and WNW (e.g. Garcia-Dueñas, 1969; Garcia-Hernandez et al., 1980), which covered the South-Iberian and Maghrebian continental paleomargens and constitute the External Zones of the Betics and Rif.

The second corresponds to the sediments deposited on oceanic troughs or thin continental crust (Luján et al., 2006) and belongs to the so-called Flysch Trough that is well-represented in the Rif and Tell regions. The last one, the Alboran crustal domain, represents the Internal Zones of the orogeny, composed mainly of Paleozoic to Mesozoic rocks affected by low to very high-grade metamorphism that were deformed mainly during the late Cretaceous to Paleogene and thrust onto the south Iberian and North African margins during the Early Miocene (Balanya et al., 1988). Three tectono-metamorphic complexes are recognized in this zone, the Nevado-Filabride, the Alpujarride and the Malaguide in the Betics. The Alboran domain shows N-S continuity below the sea and constitutes the metamorphic basement of the Alboran basin (Platt et al., 1998). That basin represents a post-orogenic back arc basin (Lonergan and White, 1997), similar to the Calabrian arc (Faccenna et al., 2004; Rosenbaum et al., 2002), formed during the westward migration of the orogenic wedge.

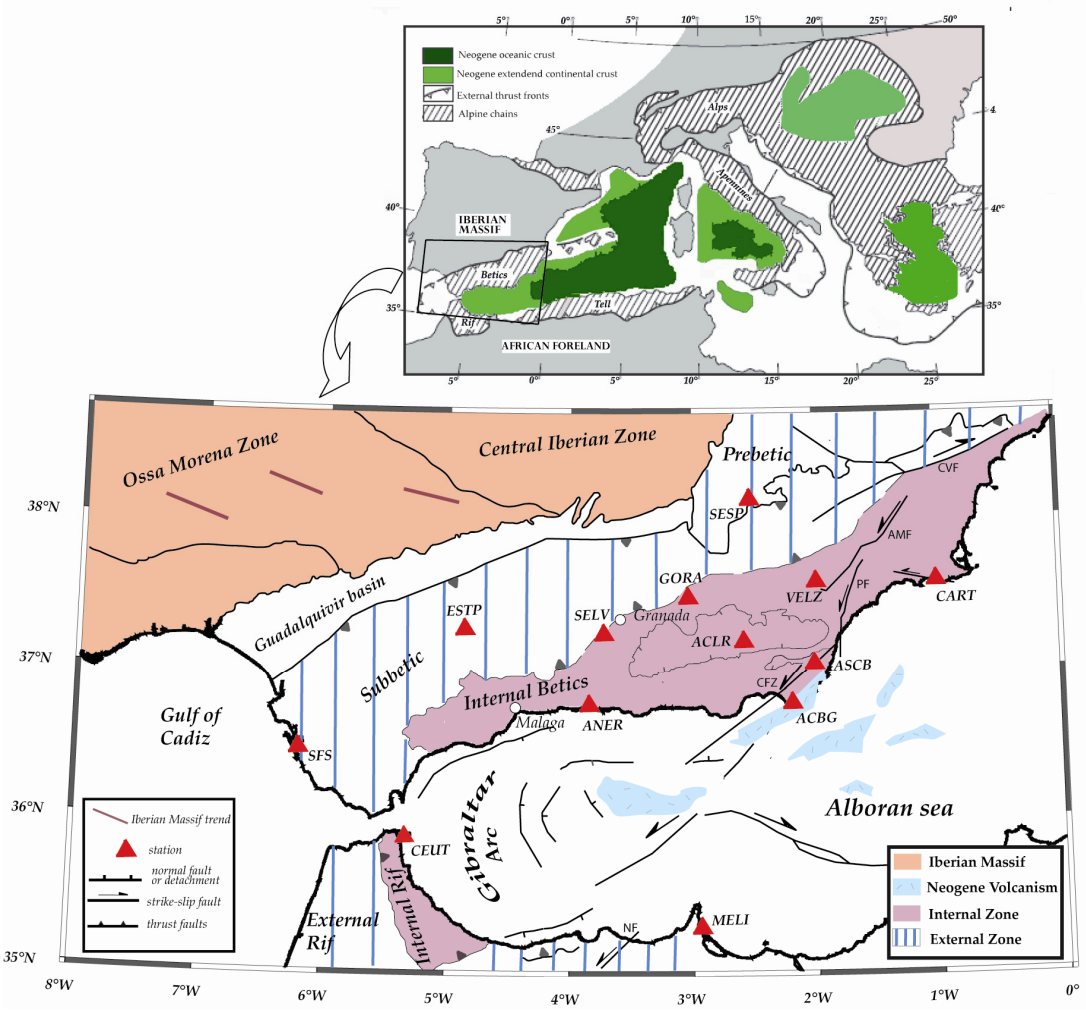

Figure 6.4 - Tectonic sketch of the Mediterranean area showing the Neogene basins and Alpine chains (top, redrawn from Comas et al., 1999) and geological setting of South of Iberia and North of Africa (bottom, redrawn from Lonergan and White, 1997; Platt el al., 2003). Main faults are shown in the External and Internal Zones (CVF: Crevillente fault, AMF: Alhama de Murcia faul, PF: Palomares fault, CFZ: Carboneras fault, NF: Nekor fault). Locations of seismological stations used in this study are also shown.

Figura 6.4 – Esquema tectónico del área del Mediteraneo representando las cuencas Neogencias y las cadenas alpines (arriba, tomado de Comas et al., 1999) y escenario geológico del sur de Iberia y Norte de Africa (abajo, tomado de Lonergan and White, 1997; Platt el al., 2003). Están señaladas las principales fallas en la zona Externas e Internas (CVF: Falla de Crevillente, AMF: Falla de Alhama de Murcia, PF: Falla de Palomares, CFZ: Falla de Carboneras, NF: Falla de Nekor). Se muestra la localización de las estacines sísmicas utilizadas en este trabajo.

The main extension occurred during the early Miocene (Comas et al., 1999), coeval with shortening in the orogen. The extension was associated with subsidence during the Miocene and accompanied by toleitic and calcoalkaline magmatism (Turner et al., 1999; Duggen et al., 2005). Since the upper Miocene-Pliocene until present, a contractive episode with a roughly NW-SE direction, although varying

from the Upper Miocene to the Pliocene (Ott D'Estevou and Montenat, 1985; Larouziére et al., 1988; Galindo-Zaldívar et al., 1997) manifests itself by strike-slip tectonics, mainly in the eastern Betics and Alboran basin. This contractive episode was accompanied by magmatism of mainly shoshonitic, lamproitic and alkaline basalts (Lonergan and White, 1997; Zeck et al., 1998; Duggen et al., 2005).

At present, the kinematics of the Gibraltar arc as defined by GPS and seismic moment tensor observations shows different deformation styles that are characterized by NNW-directed thrust faulting near the Algerian coast and the SW of Iberia and an E-W extensional regime in the Alboran sea (Stich et al., 2003, 2006). A crucial role is played by the so-called Trans-Alboran shear zone, a major structure formed by NE-SW sinistral strike slip faults, and NW-SE conjugates in the partitioning of the strain in the region (Fernandez-Ibanez et al., 2007) that allow the coexistence of shortening and extensional structures in a oblique convergent plate margin between Africa and Europe.

6.1.2.1 Geodynamic models

Different geodynamical models have been proposed to explain the formation of the Alboran region and Gibraltar Arc: convective removal and orogenic collapse (e.g. Dewey, 1988; Platt and Vissers, 1989; Platt et al., 2003), mantle delamination (e.g. Seber et al., 1996a; Mezcua and Rueda, 1997; Calvert et al., 2000a), slab roll back (Frizon de Lamotte et al., 1991; Lonergan and White, 1997), active subduction (Gutscher et al., 2002), slab break-off (Zeck, 1996; Wortel and Spakman, 2000), or slab roll-back and lithospheric tearing (Spakman and Wortel, 2004).

Platt and Vissers (1989), in their **convective removal model,** proposed that a lithospheric thickening as a result of convergence created a collisional ridge of thick crust underlain by a thick root of cold lithospheric mantle, during late Eocene to Oligocene time.

Such a gravitationally unstable root could have been removed by convection and replaced by an asthenospheric mantle during the late Oligocene, resulting in the uplift and extension of the region and in the exhumation of metamorphic rocks and high-temperature peridotites from the base of the crust. The continuous

convergence between Africa and Eurasia is then proposed to be accommodated by shortening in the external zones of the belts (Subbetic and External Rif).

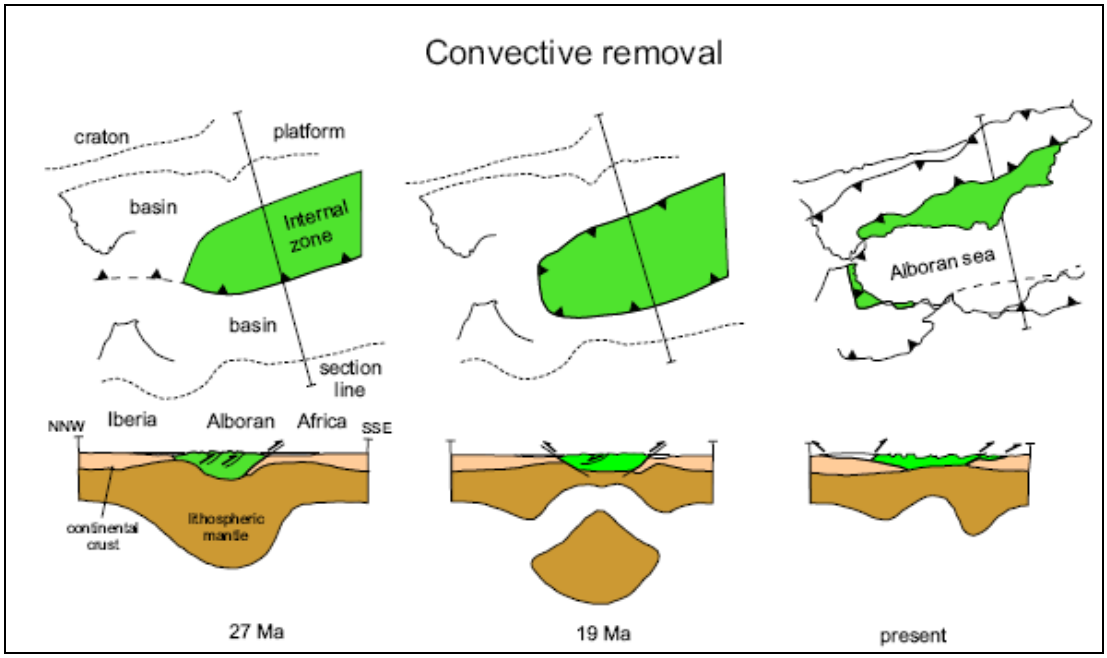

Figure 6.5 - Tectonic evolution of Alboran region for Platt and Visser (1989). In their model there was in Mid-Oligocene a thickened lithospheric root, formed by Late Cretaceous-Paleogene convergence, which was removed by convective removal in the Burdigalian. This removal provocated extension which was accommodated by crustal shortening. Extending Alboran domain was emplaced onto surrounding continental margins and the center subsides as lithosphere thickens by cooling and continued slow convergence.

Figura 6.5 – Evolución tectónica de la región de Alborán presentada por Platt and Visser (1989). En el modelo que presentan consideran la presencia de una raíz litosferica gruesa durante el Oligoceno medio, formada como consecuencia de la convergencia en el Cretacico Supeior-Paleogeno, la cual fue eliminada por convective removal en el Burdigaliense. Esta eliminación provoca la extencion que fue seguida de acortamiento cortical. El dominio de Alborán se emplazó en los márgenes continentales adyacentes y la zona central sufrió subsidencia.

The delamination model initially proposed by Garcia-Duenas et al. (1992) and **Seber et al. (1996a)** shares many similarities with the convective removal hypothesis of Platt and Vissers (1989). The main difference between the two models centers on how the lithospheric root was removed from the crust. Lithospheric thickening during the Late Cretaceous through Paleogene resulted in a large, gravitationally unstable lithospheric root beneath a NE striking zone of thickened crust. Possibly induced by some convective removal, this root mechanically detached from the

crust and was replaced by hot asthenosphere (Figure 6.6). The lithosphere peeled back to the west and northwest where it may still be attached beneath portions of Spain (Calvert et al. 2000a/b; see below). The loss of the lithospheric root, along with the inflow of hot asthenospheric material, resulted in heating of the crust, uplift and extension in the Alboran area. The horizontal forces caused by extension, combined with those forces resulting from the convergence of Africa and Eurasia, were accommodated by shortening within the Betic and Rif orogenic systems.

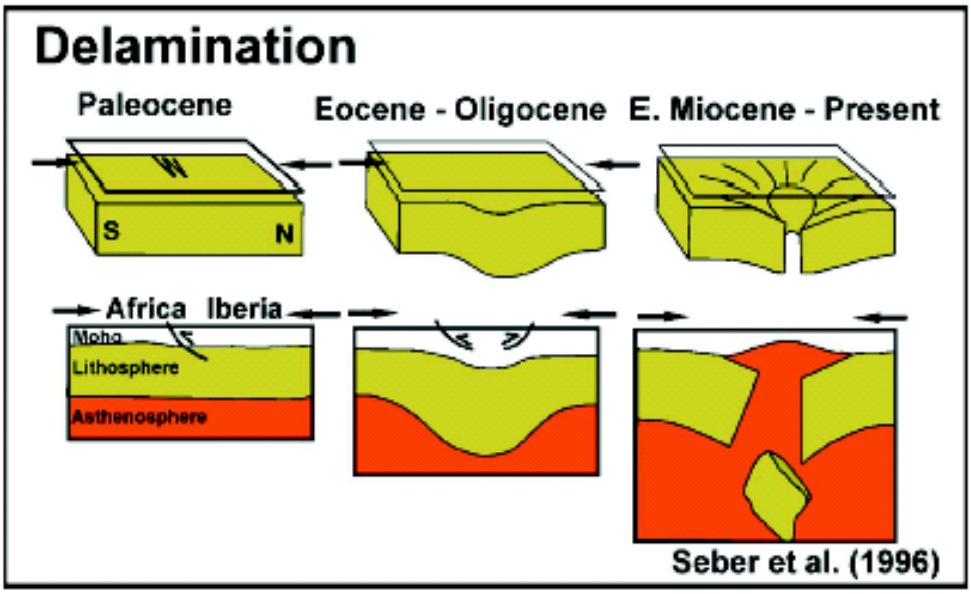

Figure 6.6 - Delamination model proposed for Seber et al. (1996).

Figura 6.6 – Modelo de delaminación presentado por Seber et al. (1996).

The apparent inability of a convective removal model to explain the predominant westward migration of deformation lead García-Dueñas et al. (1992) to hypothesize that a delamination model (Bird, 1979) might be applicable to the Alboran. Docherty and Banda, 1995) and Tandon et al. (1998) proposed a SE migrating delamination model based on marine seismic reflection profiles and wells. Observations of the 3-D pattern of earthquake hypocenters, gravity modeling and regional wave propagation characteristics also lead Seber et al. (1996a) to propose a delamination model. The N-S line of intermediate-depth seismicity apparently overlain by an aseismic, attenuating, low velocity mantle and underlain by a region of high velocity mantle (Seber et al., 1996b) was considered evidence that Iberian and African lithosphere peeled back from the east to west (Seber et al., 1996a) perhaps

initiated by detachment of a gravitationally unstable thickened lithospheric root beneath the Internal zones. Mezcua and Rueda (1997) supported this hypothesis based on their earthquake relocations. Seber et al. (1996a) further suggested that the delamination process is still active today in the western Alboran.

The **slab rollback** model of **Royden (1993) and Lonergan and White (1997)** is very different from the above models, since it focalizes primarily on subduction of oceanic lithosphere under the Alboran Sea. As the rate of subduction exceeds the rate of convergence, the subduction zone began migrating to the west while the crust of the former collision ridge (Internal Zone) was broken up and dispersed, and the crust behind this region was thinned by extension. In the northern and southern portions of the subduction zone, the westward movement slowed down as Iberian and African lithosphere was encountered and the emplacement of the Internal Zone was accommodated by shortening in the continental margins. The central portion of the subducting trench continued its westward migration and the continued subduction-zone rollback induced extension beneath the Alboran Sea (Figure 6.7).

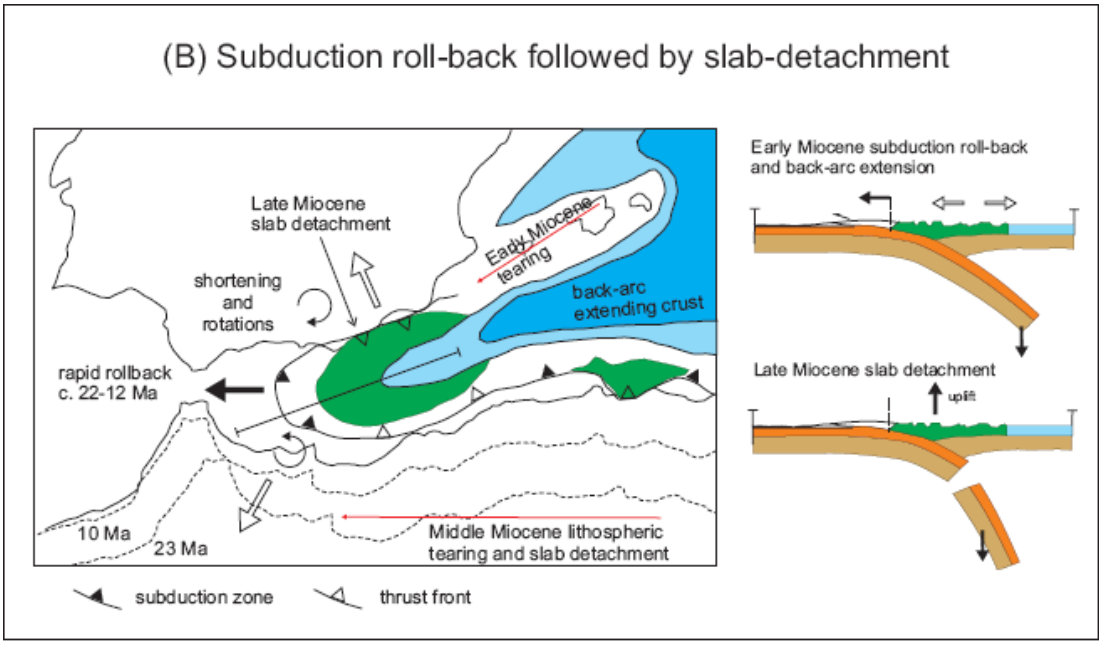

Figure 6.7 – Subduction rolled back model after Lonergan and White, 1997)

Figura 6.7 – Modelo de subducion tipo roll-back según Lonergan and White, 1997).

An alternative subduction related model was initially proposed by Blanco and Spakman (1993) based tomography results and further modified by Zeck (1996). **Zeck (1996),** in his **slab break off model,** suggested that a NW dipping slab was

subducted beneath SE Iberia during the eastward movement of Africa and Iberia relative to Eurasia during the Cretaceous and Paleogene. This subducted slab was proposed to have broken off during the earliest Miocene initiating uplift, extension, and peripheral thrusting, and now is oriented vertically beneath southern Spain (Figure 6.8). This hypothesis is attractive as it provides a mechanism for considerable lithospheric thickening and/or subduction of significant quantities of lithosphere beneath Spain, as the significant length of the imaged high velocity anomaly (~450-500 km) is hard to explain given the limited convergence between Africa and Iberia. However, it should be noted that most of the eastward motion of Africa and Iberia probably occurred before the Mid Cretaceous (Srivastava et al., 1990), requiring any subducted lithosphere to remain hanging in the mantle for 60 million years before finally detaching and descending into the mantle.

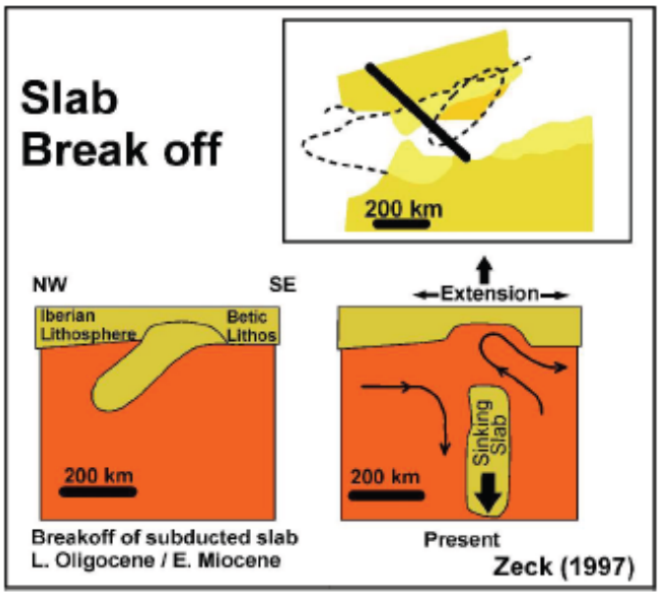

Figure 6.8 – Cartoon for slab break off model for Zeck (1996).

Figura 6.8 – Modelo de slab break off presentado por Zeck (1996).

On the other hand, several other models consider different geometries and dip direction for the subducting slab: the above models invoke eastward subduction of oceanic lithosphere rolling back to the west (Lonergan and White, 1997; Gutscher et al., 2002); others consider an extinct subduction oriented northwards (e.g., Zeck, 1996). Recent analyses of body-wave dispersion at Ceuta (Bokelmann and Maufroy,

2007) indicate a very different character of events arriving from the West from those arriving from the East. The authors interpret this signature as induced by an eastward dipping oceanic slab beneath the Alboran Sea.

6.2 Geophysical features in the Iberian Peninsula

The long and complex geologic history of the Iberian Peninsula has built his lithospheric structure. The analysis of the lithosphere can be realized through the indirect information of geophysics data, so, for example, seismic perfils, gravimetric models, magnetic data, can be help to making some light on the internal structure of the lithosphere. In this Chapter we will show a synthesis about the mean information about cortical and lithospheric characteristics.

Several models have been proposed to explain the anomalous structure of lithosphere in southern Iberia. The characteristic lithospheric thickening and thinning features, suggests that the Iberian-African margin was possibly formed by more than one mechanism that are not necessary coeval.

Recently Fullea et al. (2007) have modeled the lithosphere-asthenosphere boundary beneath southern Iberia and NW Africa (Figure 6.9), where they show that in the south-western Iberian Peninsula lithosphere-asthenosphere boundary has a NE-SW trend that affects the western Betics and the NW Atlantic margin of Morocco, and is located at about 130-140 km depth. Moreover they record significant thickness variation around Gibraltar Arc, founding a maximum thickness beneath the Gulf of Cadiz and Gibraltar Arc, about 160 km, and then lithosphere thins from 140 km in the Gibraltar Strait, to minus 45 km in the Betics and Rift (Figure 6.9). Anyway these data show discrepancies when compared to global tomography anomalies, which show a lithospheric slab beneath the Gibraltar Arc region down to 500-600 km (Spakman and Wortel, 2004).

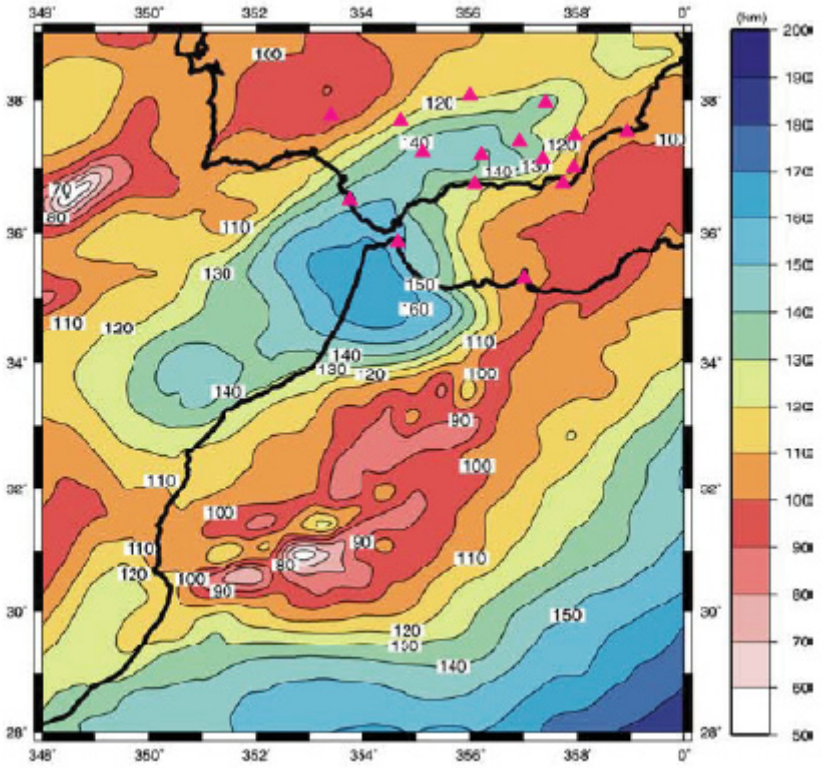

Figure 6.9 - Map by Fullea et al. (2007) with lithospheric thickness where the approximate seismic station locations (magenta triangles) in southern Iberia are shown.

Figura 6.9 – Mapa de Fullea et al. (2007) de espesor litoférico donde se indica también la localización aproximada de las estacióness sísmicas (con triángulos magenta) en el sur de la Península Ibérica.

Other information about subcrustal structures are presented by Villaseñor et al. (2007) in a tomography with ambient noise. With this tomography they obtain an average of shear velocities at depth between 15 and 30 km (Figure 6.10). They observe a high velocity region in correspondent of Iberian Massif and clearly define its southern boundary. In the Betic Cordillera they observe low velocities associated probably to the presence of widespread intramontane Neogene-Quaternary basin, formed by extensional phase of orogeny.

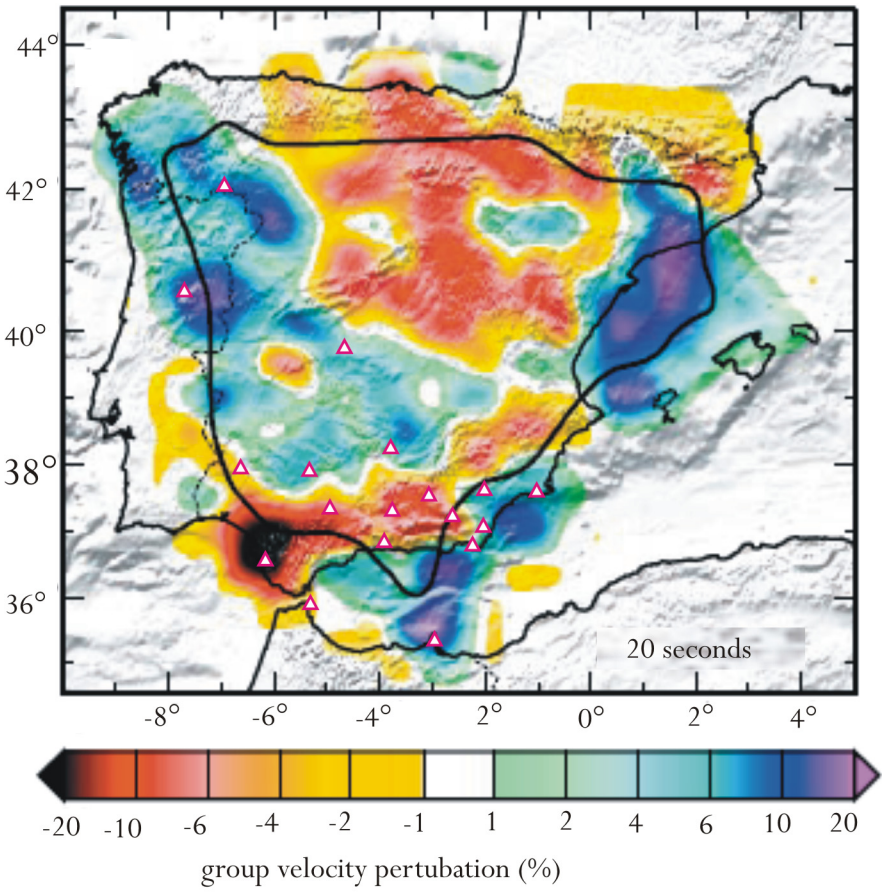

Figure 6.10 - Rayleigh wave velocity perturbation map at 20 seconds (Villaseñor et al., 2007) and with approximate station locations (magenta triangles with white border) utilized in this work.

Figura 6.10 – Mapa de perturbación de velocidad de las ondas de Rayleigh calculadas a 20 segundos (Villaseñor et al., 2007) y localizacion de las estaciónes sismicas analizads en este trabajo (triangulos magenta con bordes blancos).

The map of Bouguer anomalies (Figure 6.11) present large variation of values, maximum values are recorded in the abyssal zone and minimum values in the Betic Cordillera. Negative values are almost in all Iberian Peninsula except for the south part of Variscan Massif, where are Ossa Morena and South Portuguese zones, where high density rocks are present. Interesting is notice how the negative anomaly continue around the Gibraltar Arc.

Moreover in the map are overlap informations of crustal and lithospheric thickness.

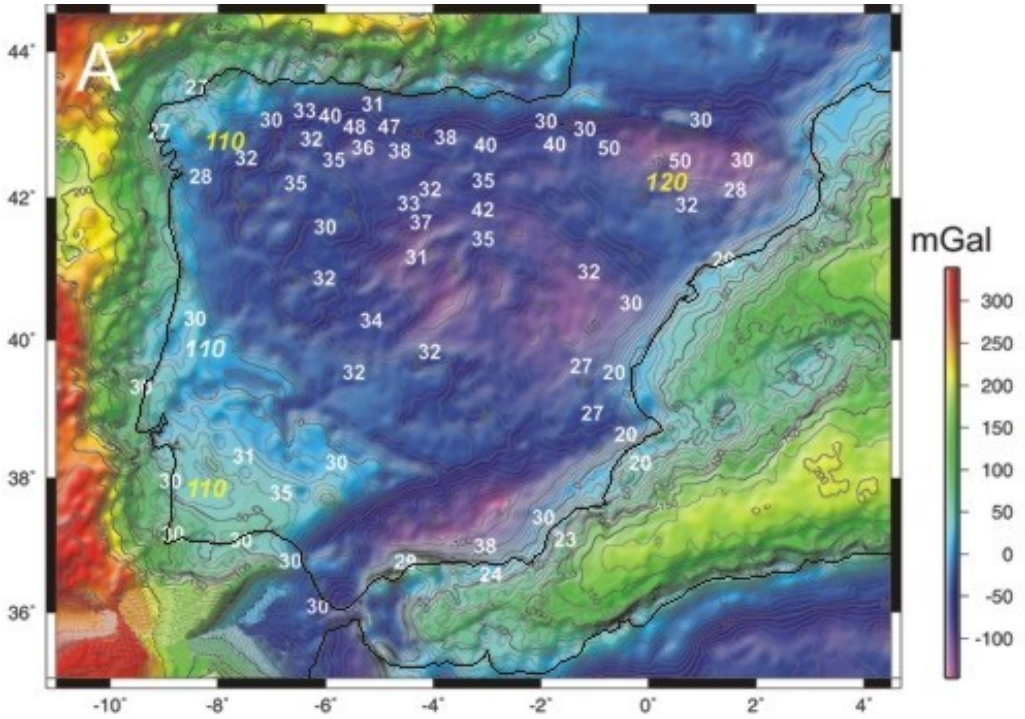

Figure 6.11 – Map of Bouguer anomalies with overlap data of crustal and lithospheric thickness fill out from the works of Córdoba et al., 1987; Banda, 1988; Suriñach and Vegas, 1988, ILIHA DSS Group (1993); Whitmarsh et al., 1993; Whitmarsh and Miles, 1995; Paulssen et al., 1993; Banda et al., 1993; Pinheiro et al., 1992; ESCI (1995); Marzán, 2000; Simancas, et al.,2003; Pedreira et al., 2003).

Figura 6.11 – Mapa de las anomalías de Bouguer con datos sobreimpuestos de espesor cortical y litosférico tomada de los trabajos de Córdoba et al., (1987); Banda (1988); Suriñach and Vegas (1988), ILIHA DSS Group (1993); Whitmarsh et al.(1993); Whitmarsh and Miles (1995); Paulssen and Visser (1993); Banda et al., (1993); Pinheiro et al., (1992); ESCI (1995); Marzán (2000); Simancas et al., (2003); Pedreira et al., (2003).

6.2.1 Seismic Tomography

Seismic tomography on regional and global scale provides useful information to answer questions of geodynamics and tectonics. It c yield estimates for example the amount of subducted lithosphere, can image roots of orogens and may permit to argue about the style of deformation. The Iberian Peninsula and more specifically the Gibraltar Arc is a wide and complex geophysical laboratory where many questions are still open. Numerous studies, from global to regional scales, are available in literatures that imagine the velocity mantle structure in this area. A common feature in many tomographic studies is a pronounced upper mantle high velocity anomalies located beneath the Alboran Sea and southern Spain (Blanco and

Spakman, 1993; Seber et al., 1996b; Piromallo et al., 1997, Piromallo and Morelli, 2003).

Global seismic tomography shows a lithospheric slab extending down to 500-600 km depth with a P-wave velocity anomaly of 1-1.5% (Spakman and Wortel, 2004).

Tomographic studies of the lithosphere-mantle structure of smaller areas utilizing data from local network, are studied for example by Seber el al. (1996a) which imagine a high velocity body beneath the Alboran Sea extending to the eastern Rif area as well, from subcrustal depths down to 350 km. Other study realized by Calvert et al. (2000a), shows in the upper crustal layer a pronounced low-velocity region in vicinity of the Strait of Gibraltar both in Spain and Morocco. Low velocities in this region are imaged by other tomography studies (Blanco and Spakman, 1993; Piromallo and Morelli, 2003; Piromallo, 1997). A deeper depth Calvert et al. (2000a) and Birjwaard et al. (1997) find fast anomalies in the mantle suggesting the hypothesis about the presence of two smaller pieces of delaminated lithospheric material. Blanco and Spakman (1993) find a positive anomaly below Betic-Alboran area at 200-700 km depth range, that for the shape and amplitude they explain as a subducted lithosphere slab.

Indeed Facenna et al. (2004), at depth of 100 and 150 km, found a high velocity anomaly located beneath northern Algeria and the Gibraltar Arc. In a cross section runs from northwest Morocco to south Spain they show the presence of a rather continuous high-velocity anomaly dipping 40°ENE down to 400 km (Figure 6.12).

Moreover, P wave velocity structures have been studied for example by Piromallo and Morelli (2003) beneath the Alboran region. They found a slow material at shallow depth (50-150 Km) which is underlain by a single coherent fast body, SW-NE oriented, apparently continuous from 250 down to 700 km depth. Also their model reveals significant anomalies in northern Africa, in correspondence of the Rif region, in the 50-150 km depth range.

A more local seismic tomography studies is by Serrano et al. (1998) in the Betics and northern half part of the Alboran Sea basin. Their study images low velocity in the upper mantle from 50 to 90 km depth under the northern margin of the Alboran Sea basin, and they interpret this structure as continental crust belonging to

collisional/subduction beneath the northern part of the Alboran Sea and the southern part of the Central Betics (Morales et al.,1999).

Gurria and Mezcua (2000) present a 1D and 3D inversion model. In the 3D model, they provide structural information of the Alboran basin over the depth range 24-60 km. In the depth range between 40-60 km they observe low velocities which they explain with a lithospheric delamination process that have occurred within the lithospheric mantle at an approximate depth of 40 km or that delamination has not occurred and the lower velocities can be correlated with a low velocity layer within the lithospheric mantle.

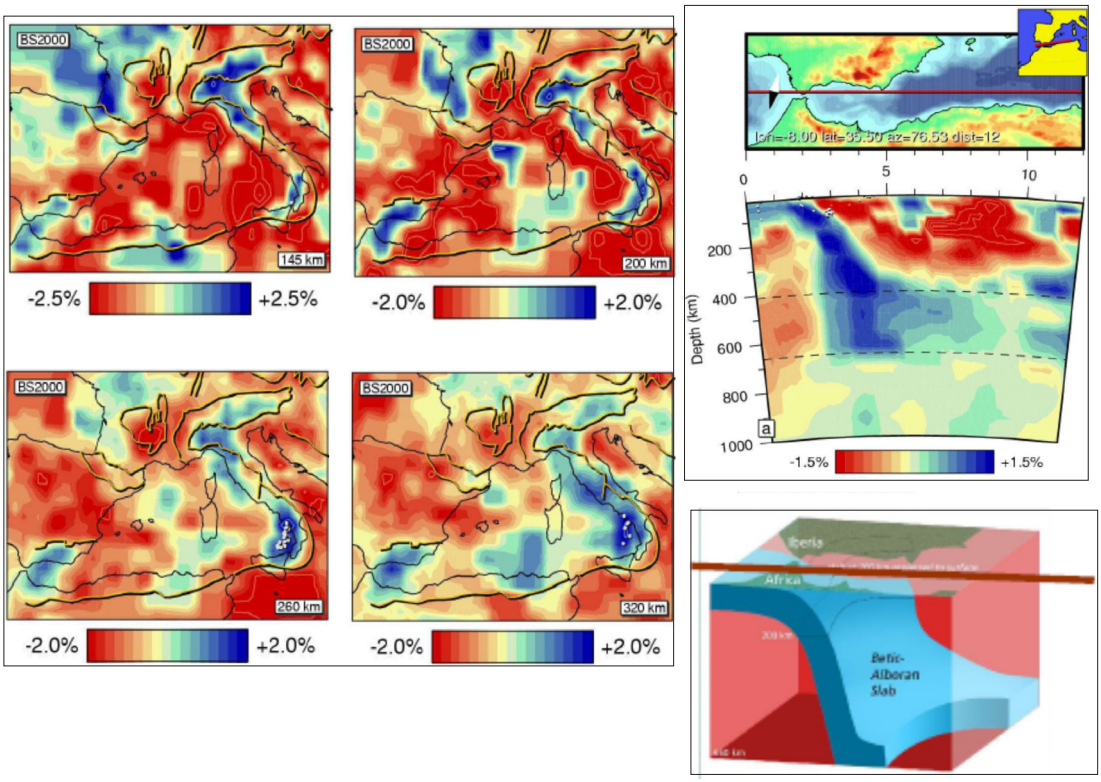

Figure 6.12 – (a and b) BS200 model proposed by Bijwaard and Spakman (2000) and (c) geodynamic model proposed by Faccenna et al. (2004).

Figura 6.12 – (a y b) Modelo BS200 propuesto por Bijwaard and Spakman (2000) y (c) modelo geodinámico propuesto por Faccenna et al. (2004).

6.2.2 Absolute Plate Motion

Absolute plate motion (APM) should align olivine a-axes in the asthenosphere and hence fast split directions, parallel to the direction of motion (Nicolas and Christensen, 1987). The current APM velocity of Iberian Peninsula is relatively slow and it is 20mm/yr in the hotspot reference frame model HS3-Nuvel1A (Gripp et al., 2002). The HS3 plate motion vectors in the Iberian Peninsula are showed in Figure 6.13, where also are shown our fast anisotropy directions. In general there is no correlation of fast direction with plate motion vectors. In contrast for the station in the southern Iberian Massif we note similarity in the direction. We discuss this point better in Chapter 7.

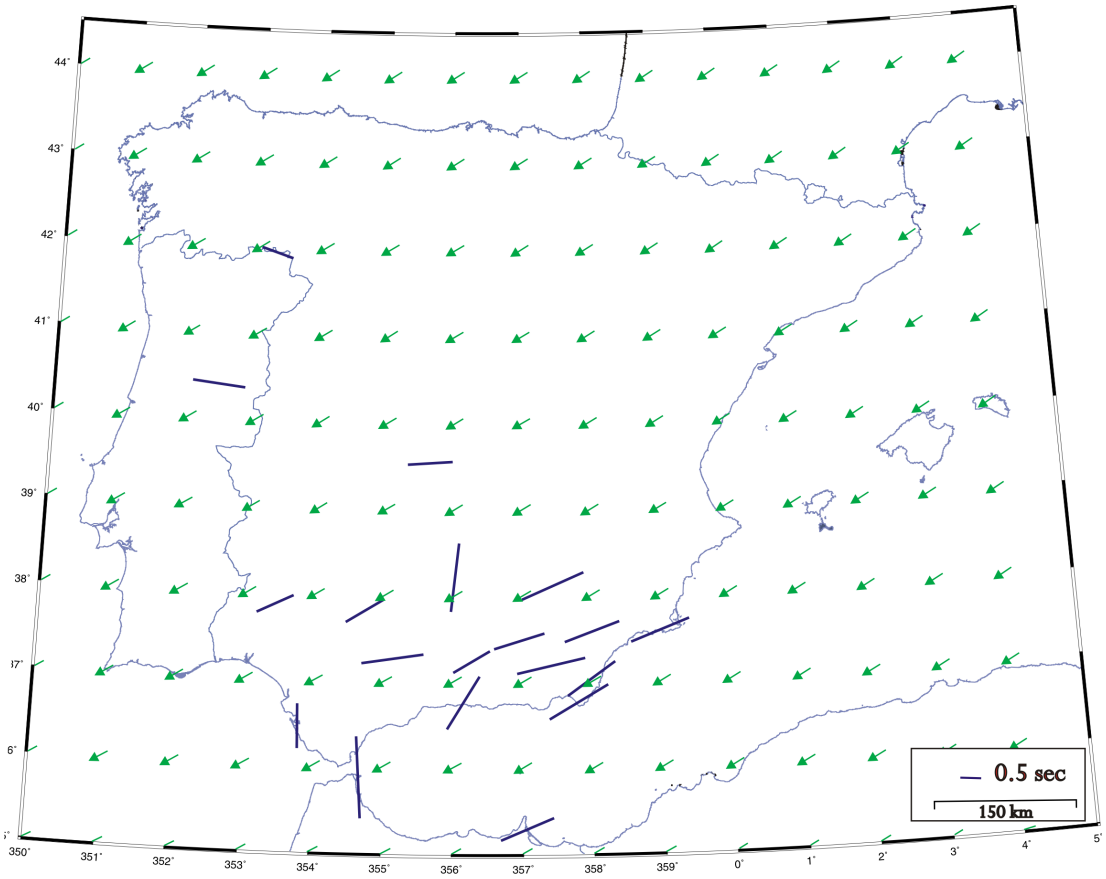

Figure 6.13 - Absolute plate motion vectors (black lines) in the Iberian Peninsula relative a hotspot reference system HS3-Nuvel1A (Gripp and Gordon, 2002). Also are represented the mean splitting fast directions (blue bars) calculated in our work.

Figura 6.13 -Vectores absolutos de movimiento de placa (líneas negras) en la Península Ibérica relativo al sistema de referencia de los hotspot HS3-Nuvel1A (Gripp and Gordon, 2002). También se representan las direcciones rápidas medias (líneas azules) calculadas en nuestro trabajo.

6.2.3 Magnetic anomalies

The magnetic map of Iberian Peninsula shows different magnetic lineations and thus different magnetic propriety zones; a lot of these magnetic lineations generally correspond to important faults or to structures (Figure 6.14). It is evident the structural Variscan direction with NW-SE to E-W orientation. Also are recognizable discontinuity connected to alpine structures, with main orientation NE-SW. The Ossa Morena Zone shows a great number of local anomalies, most of them related to outcropping mafic rocks, and a large-scale positive magnetic anomaly that can be explained by the presence at depth of a relatively planar mafic intrusion of large dimension (Simancas et al., 2003).

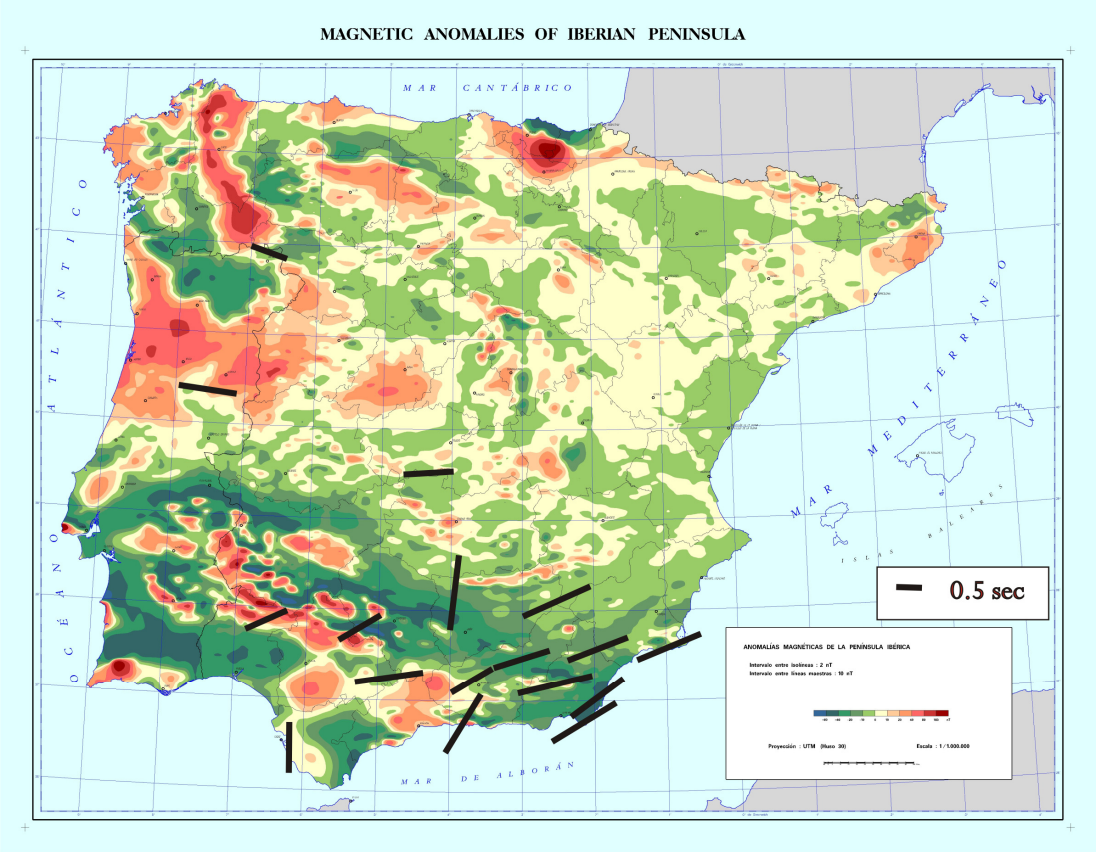

Figure 6.14 - Magnetic map of Iberian Peninsula. We also show the mean splitting fast directions (black lines) calculated in our work.

Figura 6.14 – Mapa de anomalías magnéticas en la Península Ibérica con sobrepuestas las direcciones medias de anisotropía (líneas negras) calculadas en este trabajo.

The comparison of magnetic lineaments with anisotropic directions can yield valuable information of crust-mantle interaction. In fact if there is parallelism between these two dataset, in crust and lithosphere vertical coherent deformation is present. In our case we note a poor parallelism with ECAL station and in general for the station in the Iberian Massif, where the fast orientations are roughly NE-SW in contrast with the WNW-ESE magnetic directions. In the south of Betic there is poor correlation, only in the most eastern part a parallelism can be present. In the eastern Betic there is not clear orientation of the magnetic anomalies, thus we conclude that poor correlation is present.

6.3 Previous studies of anisotropic structures in the Iberian Peninsula

6.3.1 SKS anisotropy

Few studies were led in the Iberian Peninsula to detecte anisotropy. The first study was in 1988 for Silver and Chan, in their global study of seismic anisotropy they analyzed the station TOL, near Toledo. In this work they calculated the anisotropy with the methodology developed by themselves, founding an E-W fast direction which they explicated as frozen anisotropy in the lithosphere related to the last geologic event occurred in the area (Figure 6.15, red lines).

Diaz et al. (1998) used data from temporary stations to calculate the parameters of anisotropy with the cross-correlation method. They found fast direction oriented N80°E at the station in the southern part of the Iberian Massif. In the Betic they found a trend that is NNE-SSW in the eastern part, which changes to E-W in the central part, near Granada, and again NNE-SSW near the coast of Malaga. They explain the fast direction as related to the particular lithospheric geodynamics (Figure 6.15, magenta lines).

More recent is the study in the Mediterranean area presented by Schmid et al. (2004). They analyze data for the stations of PAB, MTE, CART, SFUC, MELI and MAHO. For CART, in the eastern part of Betic, and MELI in the north of Africa,

founding a fast direction oriented N70°E and N56°E respectively, which explain in the context of vertical coherent deformation. For the other stations they found these results: for PAB ϕ°= 74.50; for MTE ϕ°= 89.63 and for SFUC ϕ°= 0 (Figure 6.15, yellow lines).

Shear-wave splitting measurements in the north of the Iberina Peninsula are calculates for the western part for Diaz et al. (2002) (Figure 6.15, magenta lines) and in east part for Barruol et al (1999) (Figure 6.15, green lines).

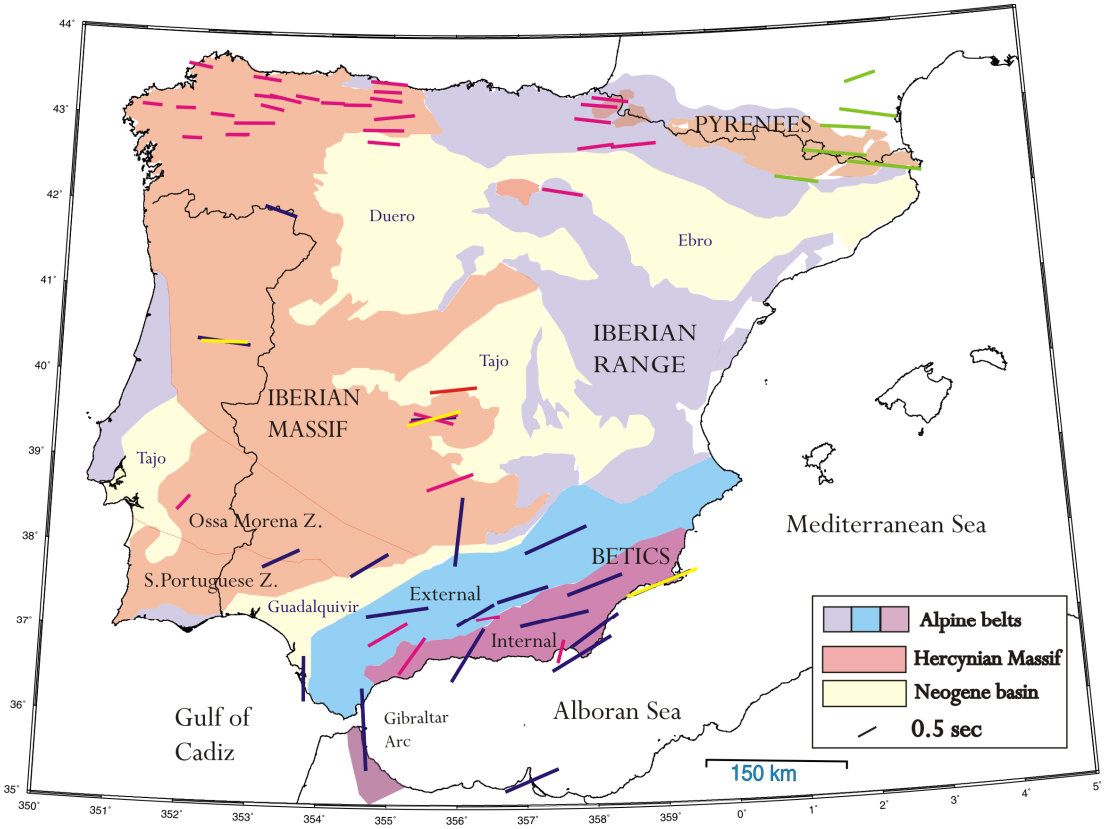

Figure 6.15 – Previous results for anisotropy in the Iberian Peninsula (magenta lines by Diaz et al., 1998, 2002; yellow lines by Schmid et al., 2004; green lines by Barruol et al, 1999; red lines by Silver and Chan, 1988), and our results (blu lines).

Figura 6.15 – Resultados previos de anisotropia en la Peninsula Iberica (líneas magenta según Diaz et al., 1998, 2002; líneas amarillas según Schmid et al., 2004; líneas verdes según Barruol et al, 1999; líneas rojas según Silver and Chan, 1988), y nuestros resultados (líneas azules).

In this study, we present new shear-wave splitting measurements obtained at permanent stations located in the Betic and Rif Cordillera and in the Variscan Iberian Massif (Figure 6.15, blu lines). A continuation we discuss separately the inferred anisotropy and its implications for the two domains. Then we compare

these new results with previous ones from Iberia, as well as from other geophysics observations.

Splitting pattern for most of northern Iberian Peninsula show E-W direction (Diaz et al., 2002) and the primary cause of their splitting results can be related with geodynamic evolution of this zone.

6.3.2 Pn anisotropy

Since Pn waves travel within the uppermost part of the lithospheric mantle this technique is unable to provide information on the deeper structure of the lithosphere and on the asthenospheric flow that could corresponds to the present-day plate motion. Anyway they help to better understand if for example the style of deformation is the same for the crust and mantle and thus to establish if coherent vertical deformation is in it.

The anisotropy inferred from the Pn waves in the Iberian Peninsula are carried out by Calvert et al. (2000b) (Figure 6.16) and Serrano et al. (2005). A large positive delay localized in the strait of Gibraltar is imaged in both studies. Calvert et al. (2000b) revel a low Pn velocity (7.6-7.8 km/sec) anomaly beneath the Internal Betics and may extend beneath the External Betics, this observation represents the evidence for the existence of partial melt at the base of Betics crust. Also low velocity is imaged beneath the Rif region. While the strait of Gibraltar and the Iberian Meseta are imaged as region with average Pn velocities of 8.1-8.3 km/s for Calvert et al. (2000b) and with a Pn velocity of 8.0 km/sec for Serrano et al. (2005).

The Pn fast directions of Calvert et al. (2000b) have a good fit with the SKS direction, especially for the Betics and Rif domain, perhaps related to the best coverage of rays.

It is remarkable the same rotation for the Pn and SKS direction have the same pattern in the Betics and Gibraltar Arc. These let to presuppose that a vertical coherent deformation model can be assumed. In contrast for the SKS direction in the Iberian Massif, we do not observe correlation with Pn, so the two techniques are sampling different depth of anisotropy.

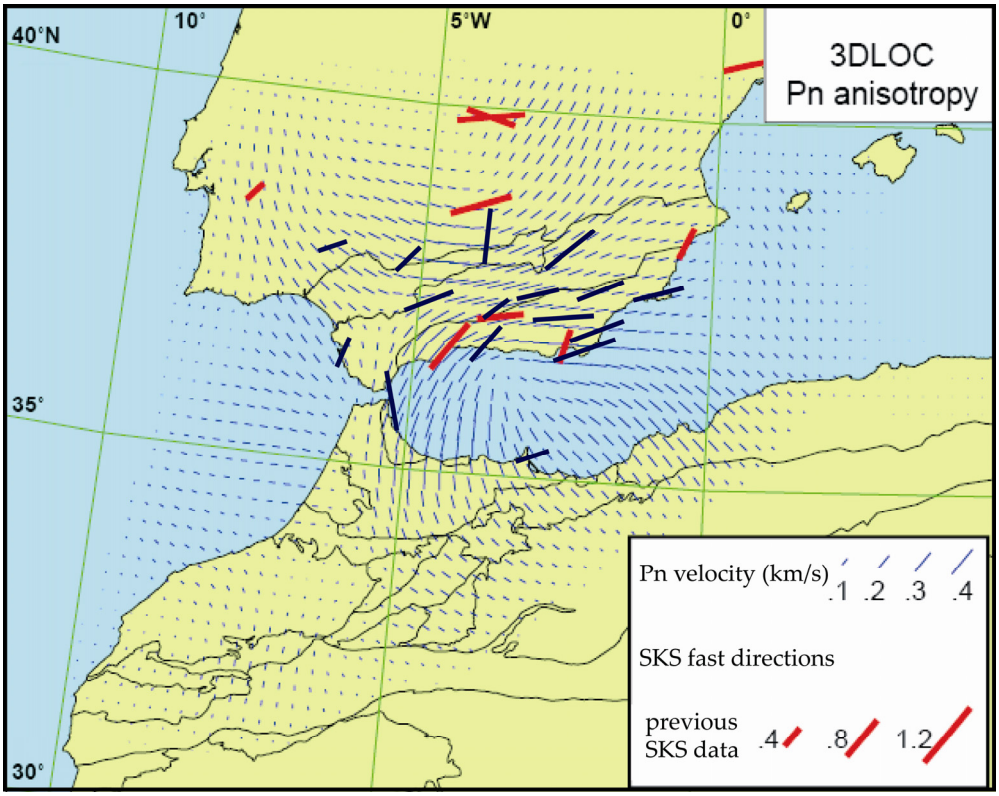

Figure 6.16 - Comparison of SKS fast directions (mean values from this study in blue lines and previous works (Diaz et al., 1998) in red lines) with Pn-fast directions (Calvert et al., 2002b).

Figura 6.16 – Comparación de las direcciones de anisotropía obtenidas con las fases SKS (valores medios de este estudio mostrado en líneas azules y de resultados previos (Diaz et al., 1998) en líneas rojas) con las direcciones rápidas de Pn (Calvert et al., 2002b).

7. Discussion of anisotropy in the Iberian Peninsula

7.1 Anisotropic structure in the Iberian Massif

The observed shear-wave fast directions for the Iberian Hercynian Massif show roughly E-W direction in the north-center part (ECAL, MTE and PAB) and NNE-SSW directions in the southern part (ARAC, HORN and JAND). This discrepancy between the north and south might perhaps be interpreted as different origin of anisotropy (Figure 7.1).

The stations PAB and MTE that are in the Central Iberian zone, and ECAL station that is in the Galicia-Tras-Os-Montes Zone, show approximately E-W trend. These two areas are considered as part of one geologically stable block of continental lithosphere. For the stations PAB and MTE the results performed are similar at those presented for previous works (Silver et al., 1988; Scmid et al., 2004; Diaz et al., 1998), we found an average fast direction of ϕ=83° and ϕ=89° respectively. For ECAL we record a ϕ=-72°.

If the anisotropy was controlled by the large scale asthenospheric flow related to the present day absolute plate motion (Chapter 6.2.2) we would expect approximately the same directions of the anisotropy. But our observations suggest that it is not the case (Figure 6.13). Magnetic anomalies reflect compositional and/or

structural contrasts in the crust. A parallelism between fast direction and crustal magnetic lineaments thus suggests vertically coherent deformation. In our case, the stations have fast axes close-perpendicular to the trend of the magnetic anomalies (Figure 6.14). The fast direction inferred for the stations PAB, MTE and ECAL are roughly corresponded to E-W trend of deformation intraplate Iberia, a relitic of N-S compressive in the past (Banda et al., 1981). These observations imply that the anisotropy should be frozen in the lithosphere, as it has been defined by Silver and Chan (1991), so the last significant orogenic episode in the area induced the lattice preferred orientation.

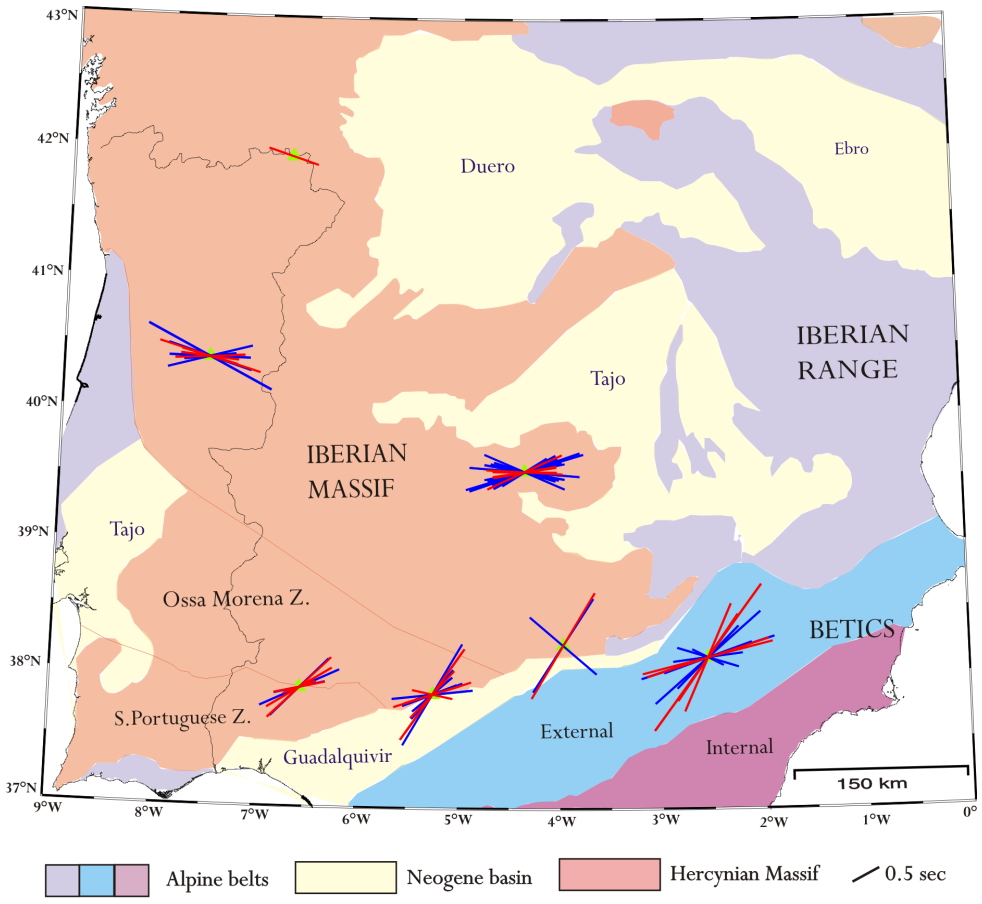

Figure 7.1 - Splitting results shown at the respective stations. Each measurement is characterized by a fast azimuth ϕ, and the length of the segment is proportional to the delay time δt. Good (red lines) and fair (blu lines) are represented.

Figura 7.1 – Resultados del splitting mostrado para cada estación. Cada medida está caraterizada por el azimuth rápido ϕ, y la longitude del segmento es proporcional al tiempo de retraso δt. Good (líneas rojas) y fair (líneas azules) están representadas.

On the other hand at the stations in the southern part, ARAC, HORN and JAND, there is a clear backazimuthal dependence of the splitting parameters. Such a backazimuthal dependence of splitting parameters may be explained either by invoking vertical variation of anisotropy, e.g. by the presence of two (or more) anisotropic layers, or by lateral variations of anisotropy. First, we address the case of lateral heterogeneity. In order to better visualize the lateral sampling of the anisotropy measurements and the regional-scale stability of the anisotropy parameters beneath the stations, we choose to project the individual splitting measurements of good and fair quality along their incoming rays to a depth of 150 km (Figure 7.2).

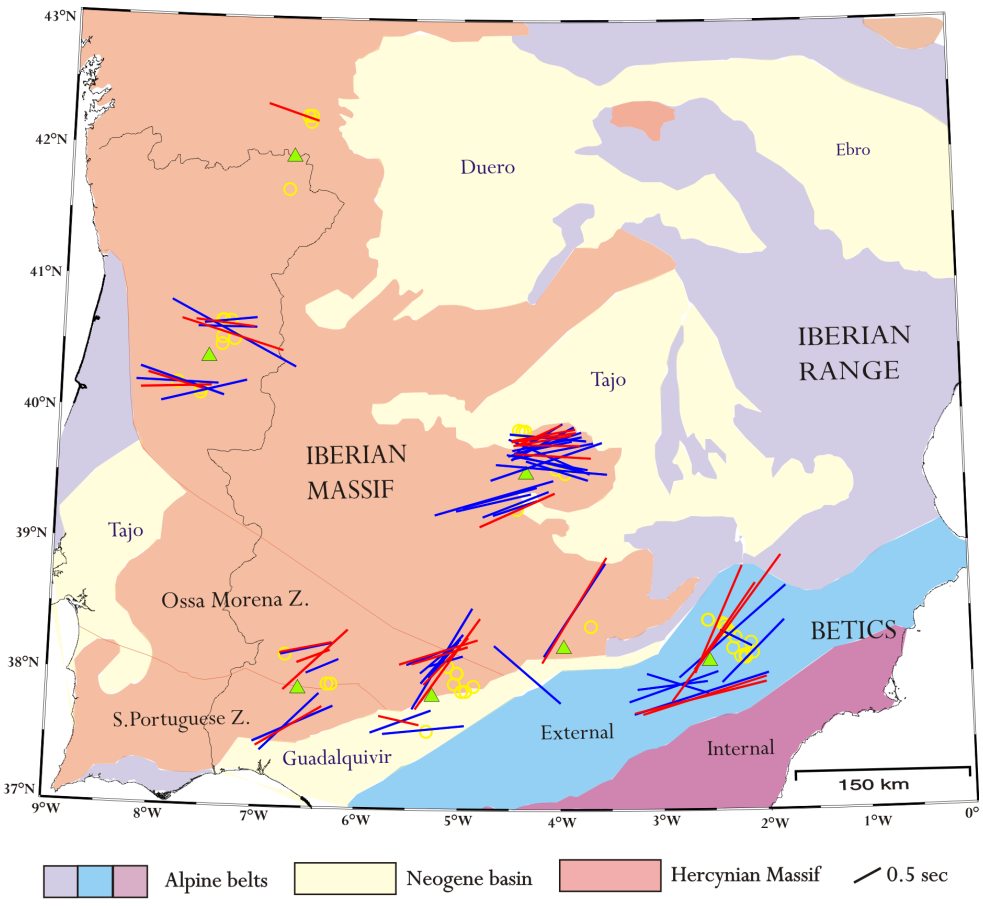

Figure 7.2 - Individual splitting measurements projected at 150 km depth along the ray paths. Good measurements are shown by red lines, fair measurements by blu lines. Null measurements (events with no apparent splitting) are shown by yellow circles.

Figura 7.2 – Medidas individuales projectadas a 150 km de profundidad a lo largo del trayecto del rayo. Las medidas good estan representadas con líneas rojas, las fair con líneas azul y medidas Null (eventos con aparentemente no splitting) están representadas con círculos amarillos.

Although the splitting of the SKS waves is not well-located vertically, this representation is helpful since it plots the splitting parameters closer to the location where they were acquired. The measurements with well-constrained anisotropy ("good") are presented as thick dark lines while measurements of lower quality ("fair") are shown by thin lines. In addition, Figure 7.2 presents the Null measurements by open circles. In the eastern and internal Betics, this Figure 7.2 clearly indicates smooth spatial variation of the anisotropic structures beneath most stations. Such a pattern was less clear in Figure 7.1. It suggests that the variation is not caused by noise in the observations. It is apparently due to real anisotropy variations at depth.

In this part we included SESP station in the discussion. Even if this station is in the Prebetic units, it shows similar trend in the fast directions than the other stations in the south of Iberian Massif and moreover the basement of this unit is of Hercynian orogeny. The splitting parameters observed at stations ARAC, HORN and JAND near the transition to the Iberian Massif, and SESP are not fully explained by lateral variation of splitting. These 4 stations are characterized by an apparent backazimuthal variation of the splitting parameters as shown in Figure 7.3. The projection at depth of the individual splitting measurements (Figure 7.2) suggests strong lateral variations at small scale-length. Such a rapid variation is not easily explained by lateral variation since the Fresnel zone of SKS phases in the upper mantle that quantifies the width of the zone over which the SKS 'average' the structure, is 100 to 200 km wide for SKS waves with 10 seconds period. For these 4 stations, we show the detailed ϕ and δt backazimuthal variation in Figure 7.3. A single anisotropic layer would produce a constant fast direction ϕ, independent of backazimuth, as well as a constant splitting delay δt. With the possible exception of station ARAC, such a simple single layer does not explain the observations at these stations. However, the stations are characterized by varying amounts of data, partly due to the different running periods of the stations. Data at station JAND were available only from July 2006 and therefore provide only few SKS measurements. Nevertheless, the station exhibits a general NE trend except for the event on day 237 (year 2006, see Table 5.6) with backazimuth of 234 degrees that shows a different ϕ. The small number of data cannot constrain the results for that station.

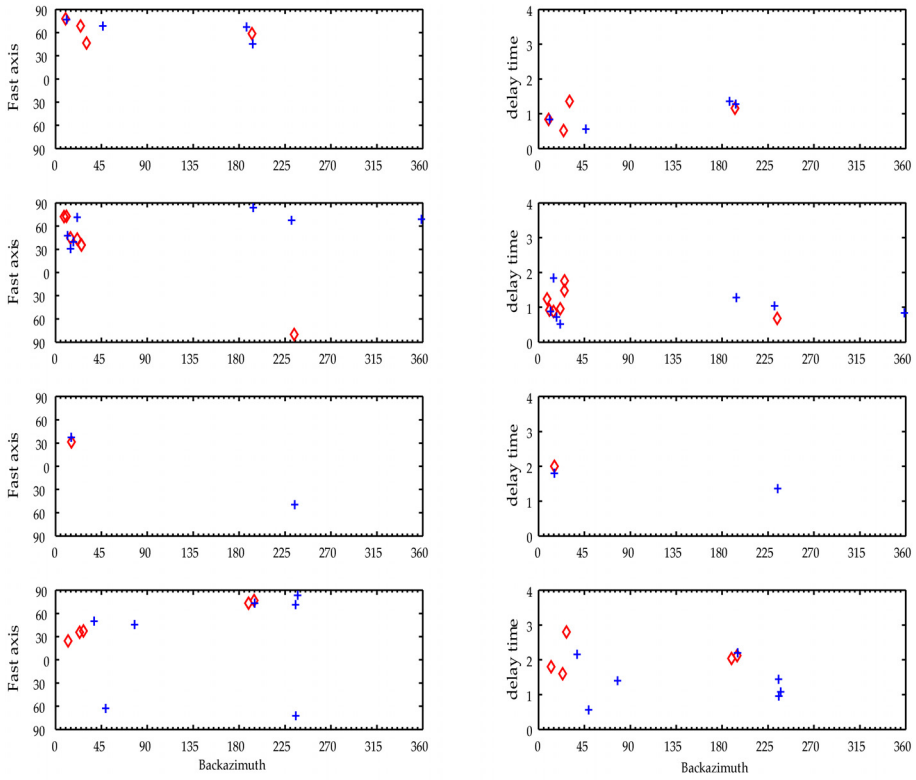

Figure 7.3 - Backazimuthal distribution of SKS splitting for stations SESP, JAND, HORN and ARAC that are not easily explained by a single anisotropic layer.

Figura 7.3 – Distribución según el backazimuth del splitting con SKS para las estaciónes SESP, JAND, HORN y ARAC que no son facilmente explicadas con modelo de una sola capa anisotropa.

Stations in the southern part of the Hercynian Iberia show homogeneous fast directions however trending NS to NE-SW, different from those ones recorded in the northern that trend more E-W.

These directions do not appear to correspond to orientations of geological structures in the Hercynian basement, since the latter trend more or less NW-SE in the Northwest portion of Iberia and East-West in eastern Spain. While we do not obtain those "Hercynian" directions for our southernmost stations of the Hercynian belt, they are in fact observed further North, in the center of Variscan Iberia, where they are roughly E-W. Three of our northernmost stations show a wide range of fast orientations (Figure 7.1 and 7.2). Different anisotropy parameters are obtained for measurements arriving from North and South. This is not easily explained by lateral

heterogeneity, unless all these stations are located above a geological suture zone so that events arriving from the North and the South could experience a different medium. Since these stations are indeed near the Betics deformation front, we wish to further test both hypotheses for the northernmost stations, namely the 'lateral heterogeneity hypothesis' and the 'two-layer anisotropy hypothesis'. Figure 7.3 illustrated the 'lateral variation hypothesis', where splitting results were projected along the incoming rays to 150 km depth. In this view, fast directions that show up to the North of the stations, within the Hercynian, are generally associated with NE-SW fast direction, while results generally show more East-West trending fast directions, for southern backazimuth i.e., close to the general Betics trend. This is particularly clear at station SESP, and it may indicate that the events arriving from the south are experiencing the same anisotropic structure as the stations located further south in the Internal Betics. This would suggest that SESP may lie close to an important boundary between lithospheric blocks. Among the northern stations of our study area, ARAC shows little backazimuthal dependence of the anisotropy parameters: NE-SW fast directions are visible both to the North and to the South of the station.

On the other hand, we may assume a two-layer model for each of these four northern stations, to try to explain the observed variation of the splitting parameters apparent in Figure 7.3. Constraining the four parameters of a two-layer model requires a relatively good backazimuthal coverage, which we do not have. We therefore decided to apply a similar approach as Fontaine et al. (2007) for the SKS splitting obtained at oceanic island stations, by considering the area as homogeneous enough to group the individual splitting measurements together into a single "virtual" station. We processed measurements obtained from the four stations together, since they have similar backazimuthal coverages.

If there were several anisotropic layers present at depth, mantle deformation would not necessarily mimic crustal deformation. A tectonic decoupling somewhere within the lithosphere might explain why anisotropy directions in the area are different from the trend of the mountain belt. Seismic reflection profiles in the south-western portion of the Hercynian massif show that the Moho is discontinuous

(Simancas et al. 2001), particularly under the Central Iberian Zone. In fact, the Moho is probably a decoupling zone between the mantle and the crust in the area.

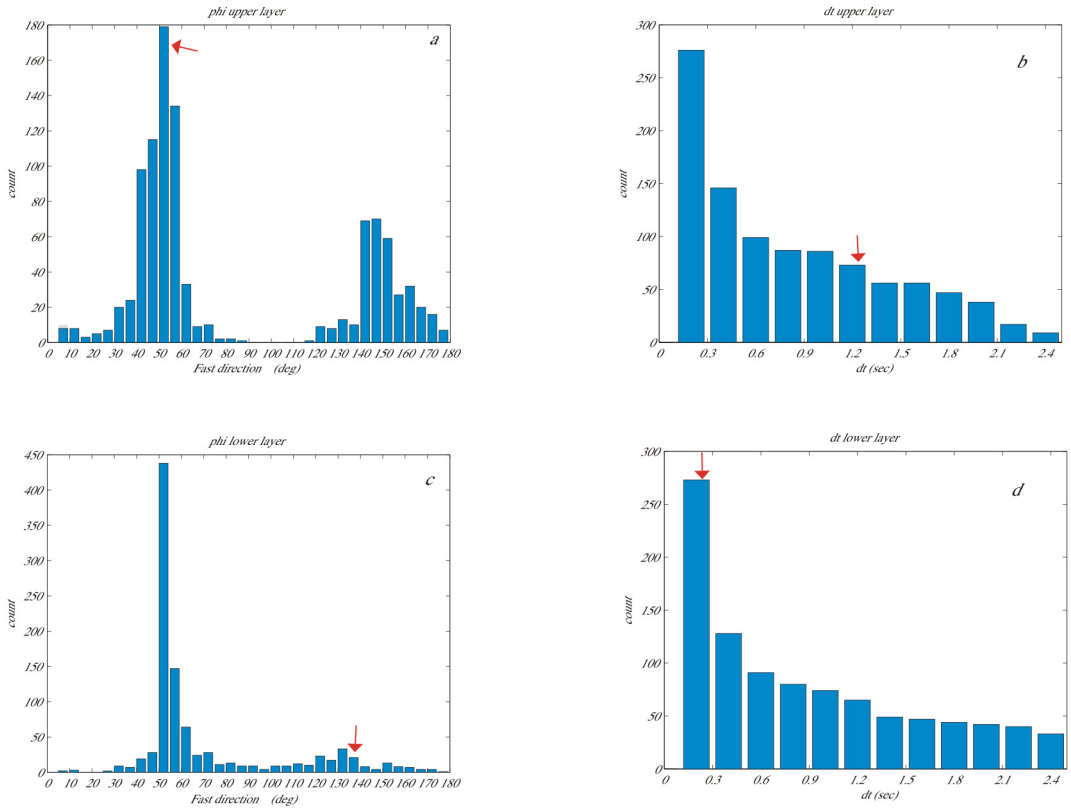

Figure. 7.4 - Statistical analysis of two-layer modelling for the joint data set of 4 stations (ARAC+HORN+JAND+SESP): parameters for the 1000 best-fitting models are shown as histograms for a) fast direction in upper layer; b) delay time in the upper layer c) fast direction in the lower layer, d) delay time in the lower layer. The arrows show the optimum values for each model, ϕ=N52°E and ϕ=N136°E for a) and c) respectively, and δt=1.2s and δt=0.2s for b) and d) respectively.

Figura. 7.4 – Análisis estadísticos del modelo de dos capas anisótropas para el conjunto de datos de cuatros estaciónes (ARAC+HORN+JAND+SESP): los parámetros para los 1000 mejores ajustes están representados como histogramas por a) direccion rápida en la capa superior; b) tiempo de retraso en la capa superior c) dirección rápida en la capa inferior, d) tiempo de retraso en la capa inferior. La flechas rojas indican el valor óptimo para cada modelo ϕ=N52°E y ϕ=N136°E para a) y c) respectivamente, y δt=1.2s y δt=0.2s para b) y d) respectivamente.

Following the approach defined by Silver and Savage (1994), we therefore tested two-layer models by varying ϕ and δt in the upper and lower layer by increments of 2° and 0.2 s, respectively and compared the expected backazimuthal variations with our observations. Testing all possible two-layer models (Figure 7.4), we find that the best-fitting models belong to three groups of models, 1) those having NE-SW fast directions in both layers, 2) those having NE-SW for the upper layer and NW-SE for

the lower layer, and 3) vice-versa. While the best model formally falls into the second category, we cannot rule out the other two cases, including the one of a shallower layer with NW-SE fast azimuths, that would indeed correspond to the trend of the Hercynian basement in its southern portion. This ambiguity is in part due to the backazimuthal distribution of the events being rather limited, but more likely this represents a complexity that is not well-characterized by the presence of two anisotropic layers. In this light, we prefer the alternative hypothesis of an anisotropy that varies laterally.

An alternative explication for the anisotropy fast direction is if subcontinental mantle anisotropy is dominated by asthenospheric flow. In that case there exists a decoupling zone between the motion of the continental plate and (presumed stationary) mantle below (Silver 1996), and it is assumed that the memory of asthenospheric flow direction is short, only a few million years, since strains of order unity, enough to completely reorient olivine aggregates (Nicolas, 1993; Mainprice et al., 1993). Seismic reflection profiles in the south-western portion of the Hercynian Massif, near the Sierra of Aracena, show that the Moho is discontinuous (Simancas et al., 2001), particularly under the Central Iberian Zone. In fact, the Moho is probably a decoupling zone between the mantle and the crust in the area. Furthmore the presence of thin lithosphere beneath the Iberian Massif and the absence of strong crustal anisotropy imply that observed SKS split occur dominantly beneath the lithosphere. A shallow asthenosphere exists beneath the Iberian Massif and that the deformation within this asthenosphere creates a coherent and uniform anisotropy with the expected strain field (Figure 7.6). We test the parallelism between fast directions and AMP directions (Figure 7.6).

Thus the anisotropy measured could reflect both a post Hercynian deformation of Ossa Morena zone, related to the main stages in the tectonic evolution of this part like transpressional stage, transtensional stage and shortening episode, and a deformation related at the latter Alpine orogeny. Little evidence for Alpine deformation has been found in SW Iberia, furthermore some studies indicate minor Alpine reworking of some exiting faults and moderate regional uplift.

7.2 Anisotropic Structure in the Betic Cordillera

The individual splitting measurements are plotted in Figure 7.5 at the various stations to evaluate the coherence of the results. Lines show the fast anisotropy directions ϕ, obtained from the minimum energy method, and their lengths are proportional to the splitting delay time δt. "Good" data are shown by thick dark lines, and "fair" data by thin lines; "poor'' data are not plotted. Most stations in the Eastern Betics, CART, VELZ, ACBG, GORA, ACLR and ASCB show a homogeneous ϕ trending roughly N70°E and high delay times of around 1.5 seconds. Given the weak spreading of fast direction measurements ϕ at stations in that region, and the spatial coherence, the splitting observed at those stations is likely originating within a single anisotropic layer that is well constrained by a suitable number of measurements. We record a similar trend for the station MELI in Northern Africa, where the fast direction is N68°E with a delay time of roughly 0.95 sec. Interestingly, ϕ is nearly North-South at stations SFS and CEUT, i.e., parallel to the trend of the Gibraltar arc. At each of these two stations unfortunately, measurement conditions were relatively difficult, and there are only two measurements available at CEUT from 3 years of data analyzed, (N12°E, δt=1.44 s and N19°W δt=2.68 s), and two non-Null measurements at SFS (N19°E, δt=1.80 s and N21°W δt=0.4 s).

Diaz et al. (1998) used data from temporary stations and found a fast direction oriented N80°E at the station in the southern part of the Iberian Massif. In the Betics, they observed a NNE-SSW trend in the eastern part that changes to E-W in the central part, near Granada, and again NNE-SSW near the coast of Malaga interpreted in terms of their particular lithospheric geodynamic settings. Schmidt et al., (2004) studied the station CART, in the eastern part of Betic, and MELI in the north of Africa, finding fast directions in the Betic trend, oriented N70°E and N56°E respectively.

At ANER station, there is a clear backazimuthal dependence of the splitting parameters. For this station we follow the same criteria that for the stations in the southern Massif. So first to better visualize the lateral sampling of the anisotropy measurements and the regional-scale stability of the anisotropy parameters beneath

the stations, we choose to project the individual splitting measurements of good and fair quality along their incoming rays to a depth of 150 km (Figure 7.6).

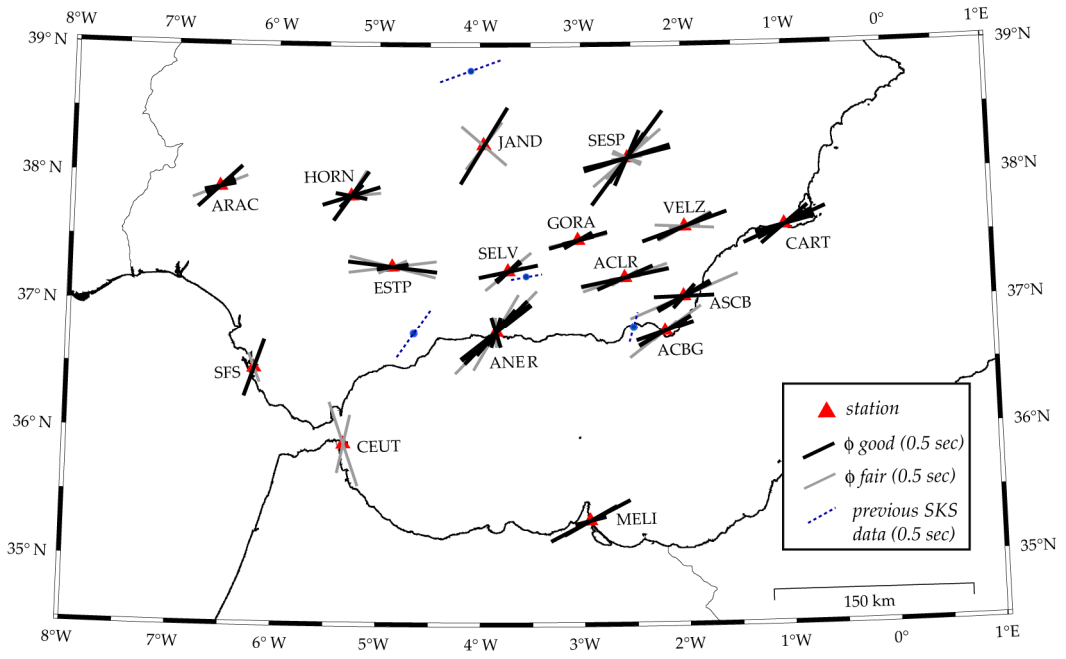

Figure 7.5 - Splitting results shown at the respective stations. Each measurement is characterized by a fast azimuth ϕ, and the length of the segment is proportional to the delay time δt. Good (thick dark lines) and fair (thin lines) are represented.

Figura 7.5 - Resultados del splitting mostrado para cada estación. Cada medida está caracterizada por la dirección rápida ϕ, y la longitud del segmento es proporcional al tiempo de retraso δt. Good (linea negra guesa) y fair (linea gris fina).

The measurements with well-constrained anisotropy ("good") are presented as thick dark lines while measurements of lower quality ("fair") are shown by thin lines. In addition, Figure 7.6 presents the Null measurements by open circles. In the eastern and internal Betics, this Figure 7.6 clearly indicates smooth spatial variation of the anisotropic structures beneath most stations (with the exception of ANER, see discussion below). Such a pattern was less clear in Figure 7.5. It suggests that the variation is not caused by noise in the observations. It is apparently due to real anisotropic variations in the subsurface.

This strongly suggests that the upper mantle beneath the Internal Betics is dominated by a single anisotropic layer, with smoothly varying fast directions.

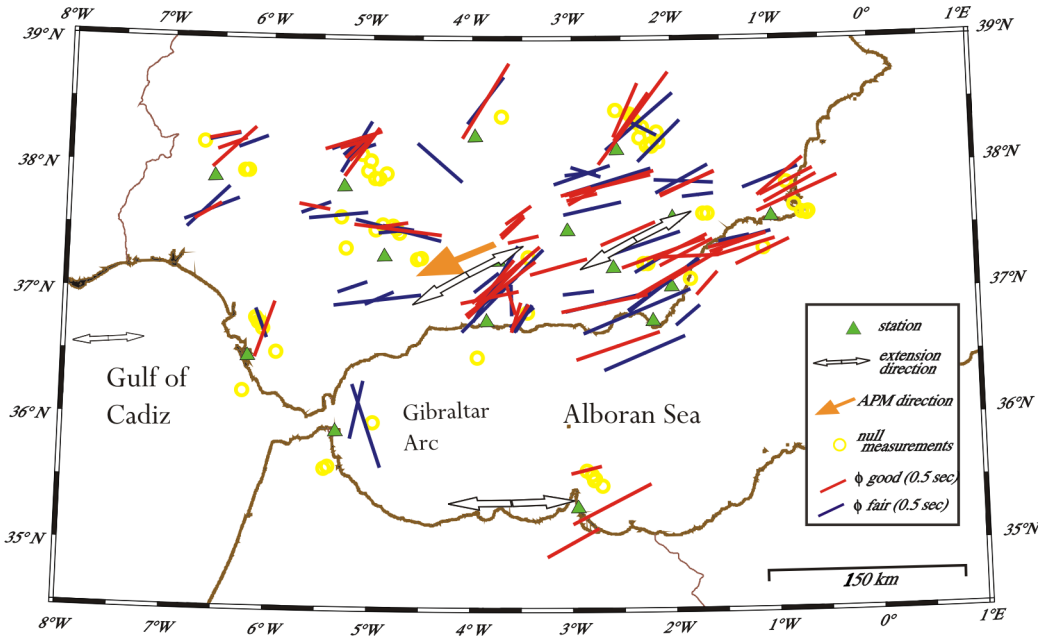

Figure 7.6- Individual splitting measurements projected at 150 km depth along the ray paths. Good measurements are shown by thick lines, fair measurements by thin lines. Null measurements (events with no apparent splitting) are shown by circles. White arrows are average stress extension directions calculated by Stich el al., 2006, the orange arrow shows absolute plate motion direction for the model HS3-Nuvel-lA (Gripp and Gordon, 2002).

Figura 7.6- Medidas individuales projectadas a 150 km de profundidad a lo largo del trayecto del rayo. Las medidas good están representada con líneas rojas, las fair con líneas azules y medidas Null (eventos con aparentemente no splitting) están representados con círculos amarillos Las felchas blancas son la direcciónes medias de la direccion del eje σ_3 del tensor de esfuerzos calculado por Stich et al. (2006), la flecha naranja muestra la direccion absoluta del movimiento de placa según el modelo HS3-Nuvel-lA (Gripp and Gordon, 2002).

On the other hand, the splitting parameters observed at station ANER in the Internal Betics, are apparently not well explained by lateral variation of splitting. This station is characterized by an apparent back azimuthal variation of the splitting parameters as shown in Figure 7.5. The projection at depth of the individual splitting measurements (Figure 7.6) suggests strong lateral variations at small scale-length. Such a rapid variation is not easily explained by lateral variation since the Fresnel zone of SKS phases in the upper mantle that quantifies the width of the zone over which the SKS 'average' the structure, is 100 to 200 km wide for SKS waves with 10 seconds period. A single anisotropic layer would produce a constant fast direction ϕ, independent of back azimuth, as well as a constant splitting delay δt. Such a simple single layer does not explain the observations at these stations.

However, the stations are characterized by varying amounts of data, partly due to the different running periods of the stations. For ANER, there is a nearly North-South trend for such events that arrive for E-NE, but data with N-NE backazimuth show NE-SW fast directions.

A striking feature in the anisotropy pattern observed in this study is that the Eastern Betics seem to be well-described by a single and rather homogeneous anisotropic layer, whereas a more complex anisotropic model seems to be present in the upper mantle beneath stations in the North, and perhaps the West and the South. The Eastern Betics show indeed a smooth lateral variation of anisotropy, whereas stations in the Western and Southern part of this region indicate much stronger lateral variations in the splitting parameters. There are also strong lateral variations associated with the transition from the Betic to Variscan Iberia, in addition to two-layer anisotropy, as is required at some of the stations at least.

Eastern Betics

Fast directions are oriented ENE-WSW in the Eastern Betics, and there is a smooth spatial variation clearly visible in Figure 7.5 that is more or less parallel to the mountain belt. The anisotropy in that region is easily explained by a single anisotropic layer. The average splitting delay time in that region is about 1.5 seconds, which is consistent with a layer that is 150 km thick assuming the typically used value of 4% anisotropy in the upper mantle (Mainprice and Silver, 1993, Mainprice et al., 2000). Tomographic models for the region, (e.g. Blanco and Spakman,1993), show a pronounced low velocity anomaly in the upper mantle under the Betics between 30 and 100 km depth that is also apparent and even more pronounced in the Pn tomographic model of Calvert et al. (2000a). This area is also the locus of a pronounced high attenuation anomaly of Sn waves (Calvert et al., 2000b). This may suggest, that continental mantle material under the Betics has been replaced by asthenospheric material. Geochemical studies favor such a hypothesis by suggesting an edge delamination that could have occurred under the Betics (Duggen et al., 2005). If the lithosphere has indeed been removed, this should suggest that the deformation recorded by the seismic anisotropy under the Betics is associated rather with hot and thus relatively low-viscosity material. At deeper

depths, however, velocities are again relatively high in tomographic models (e.g., Blanco and Spakman, 1993) results down to the transition zone, including the zone of very deep seismicity around 600 km depth (Buforn et al., 1997).

The ENE-WSW fast directions observed in the Eastern Betics are nearly parallel to the absolute plate motion direction, which is 239 degrees and 2 cm/yr for the motion model Nuvel1A relative to the hotspot reference system HS3 (Gripp and Gordon, 2002). A simple deformation model related to plate motion of the Iberian/Eurasian plate over the deeper mantle might thus explain the anisotropy. In this context, the gradual rotation of fast direction along the coast might be explained reasonably by invoking a deviation of mantle flow around the Iberian lithosphere, following similar suggestions of Bormann et al. (1996) for central Europe and of Barruol et al. (1997) and Fouch et al. (2000) for North America. This might also explain the minor difference of 10 degrees between the average fast direction in the Eastern Betics and the absolute plate motion direction.

On the other hand, the observed fast directions in the Eastern Betics also show an interesting correlation with crustal features. The convergence direction between the African and the Iberian/Eurasian plate is NNW-SSE, and the current style of deformation in the crust is predominately by left-lateral strike-slip faults run with a NE-SW trend (e.g. Alhama de Murcia, Palomares and Carboneras faults). Vauchez and Nicolas (1991) suggested that in many collisional belts the dominant motion is strike-slip parallel to the main trend of the belt. In this case both crustal and mantle fabrics may reflect these movements, hence the entire lithosphere develops a fabric and becomes anisotropic. They attribute this anisotropy to a dominant mantle flow parallel to the mountain belt during orogenies. The present-day extension direction inferred by Stich et al. (2006), using moment tensors of crustal earthquakes, is N240°E, which is indeed parallel to the inferred fast polarization directions. The anisotropy is thus also consistent with a notion of vertically coherent deformation of crust and mantle as initially proposed by Silver and Chan (1988, 1991), except that we are dealing with hot deformed mantle in this region, and thus probably with current deformation, rather than fossil deformation remaining from the creation of continental lithosphere. For the close-by Gulf of Cadiz region, Stich et al (2005) have shown that the stresses imposed by the Africa-Iberia plate convergence have the

same geometry in the crust and the mantle. The convergence thus imposes a similar lateral boundary condition over a considerable depth range. Crust and mantle in the Betics may thus both be constrained to deform in a similar fashion. The observed anisotropy under the Eastern Betics could be thus caused by a combination of this kind of vertically coherent deformation, and absolute-motion-related deformation, both producing a seismic anisotropy such as the observed one. The relative importance of each is not constrained.

Gibraltar arc: Constraints on geodynamic models

Fast directions in Southernmost Spain, close to Gibraltar show rather distinct orientations from those in the Internal or External Betics: ϕ trends more or less North-South at the two stations CEUT and SFS but this likely results from a westward gradual rotation around the Gibraltar arc, from the ENE trend in the Internal Betics to NE at station ANER and to NS at CEUT.

Station ANER near Malaga provides evidence for higher complexity and perhaps multi-layer anisotropy. We have therefore performed a two-layer modeling as detailed above but consider only the results obtained at this station. The thousand best two-layer models obtained for ANER give a best-fitting model with fast direction ϕ for the upper layer of N28°E and for the lower layer of N68°E (Figure 7.7), and splitting delays 1.0 and 0.6 seconds. These results strongly suggest that this station lies in a region of transition between the eastern Betics where ϕ trend ENE (i.e., close to the ANER lower layer ϕ) and the Gibraltar arc where ϕ trend close to NS (i.e., close to the ANER upper layer ϕ). Interestingly, the close NS trend of the upper layer seems also to coincide with the N-S line of intermediate-depth earthquakes (Morales et al., 1999; Calvert et al., 2000b).

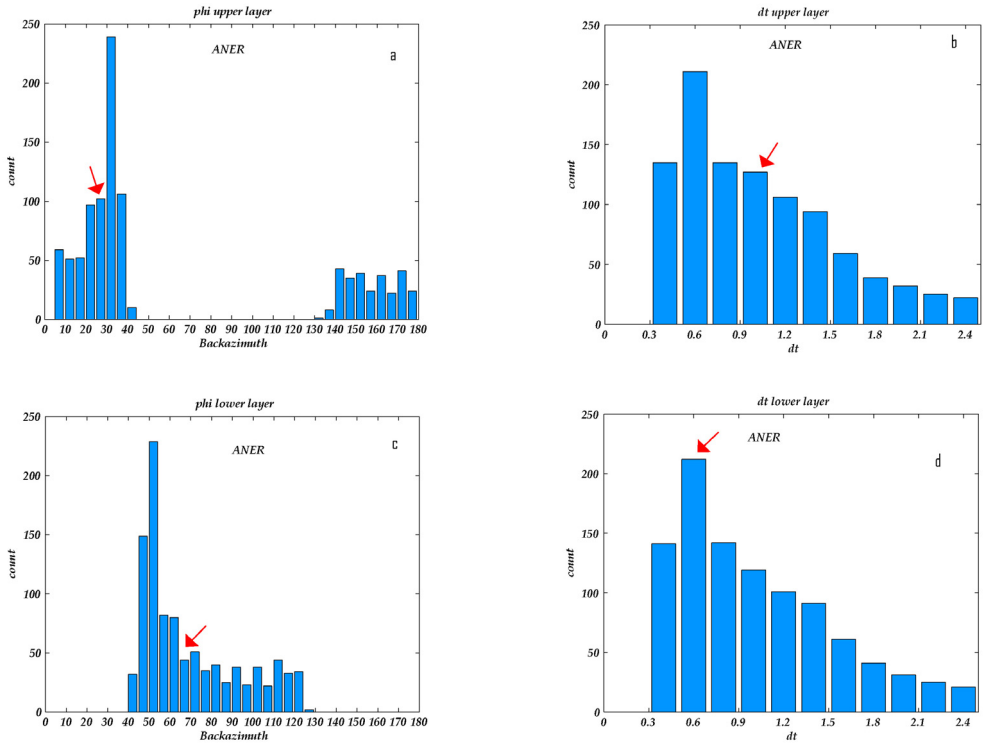

Figure 7.7 - Statistical analysis of two-layer modelling for station ANER: parameters for the 1000 best-fitting models are shown as histograms for a) fast direction in upper layer; b) delay time in the upper layer; c) fast direction in the lower layer; d) delay time in the lower layer. The arrows show the optimum values for each model, ϕ=N28°E and ϕ=N68°E for a) and c) respectively, and δt=1.0s and δt=0.6s for b) and d) respectively.

Figura 7.7 - Análisis estadístico del modelo de dos capas anisótropas por la estación ANER: los parametros para los 1000 mejores ajustes están representados como histogramas para a) dirección rápida en la capa superior; b) tiempo de retraso en la capa superior c) direccion rápida en la capa inferior, d) tiempo de retraso en la capa inferior. La flechas rojas indican el valor óptimo para cada modelo ϕ=N28°E and ϕ=N68°E for a) and c) respectivamente, y δt=1.0s y δt=0.6s para b) y d) respectivamente.

We dispose of both Pn and SKS anisotropy measurements, which provide different and complementary depth sampling (e.g., Pera et al., 2003). While Pn travels horizontally just below the Moho, and thus constrains anisotropy at that depth level, SKS waves travel almost vertically and is not able to localize the depth of the anisotropy, except that a layer of more than 100 km thickness is required to explain the observed splitting delay times (Mainprice and Silver, 1993; Ismail et al., 1998a). The agreement of Pn and SKS fast directions on the Spanish side of the Alboran arc is remarkable (Figure 6.16), since these fast directions are not only parallel in the eastern Betics, but they seem to rotate together with the large-scale

geological structures of the Alboran arc, and parallel with the coast, in a similar fashion for the shallowest and somewhat deeper mantle. Interestingly, this parallelism is not present on the African side of the Gibraltar arc where fast Pn trend NS to NNW-SSW and fast split SKS trend NE-SW, suggesting a complete decoupling between the sub-Moho and the deeper anisotropy.

However, the similarity between Pn and SKS fast directions may reflect different tectonic processes at depth, particularly in the vicinity of a subduction zone. Indeed, if there is a subduction in the area, as has often been argued (Gutscher et al., 2002), Pn may be affected by the anisotropy above the slab, whereas SKS might be sensitive to the anisotropy below (and above) the slab. Fast split directions parallel to the slab is a rather common feature in subduction zones, both above and below the slab. This has been found for instance in New Zealand (Marson-Pidgeon and Savage, 2004) and in Northern Italy (Mele, 1998). Trench-parallel fast directions, may be explained either by invoking trench-parallel flow (e.g., Russo and Silver, 1994), or by invoking a hydrated mantle wedge above the slab (Jung and Karato, 2001). The degree of hydration of the mantle wedge and of magnitude of the applied stress above a subduction zone appears to have a strong influence on the style of seismic anisotropy (e.g., Jung and Karato, 2001; Kaminski, 2002): Slab-parallel seismic fast axes from SKS can in principle be explained either by slab-parallel flow in an anhydrous mantle wedge or by slab-normal compression in a hydrous mantle wedge. Such a pattern of anisotropy may show apparently erratic behaviour in some places, this may perhaps help to explain the complexity that we find at station ANER.

Deep structure and dynamics beneath the Alboran area has been widely debated throughout the last decades and a wide variety of geodynamic models has been proposed for the area. These models can be categorized by the way material is recycled into the mantle. If mantle lithosphere has been removed as has been proposed in the convection-removal hypothesis (Platt and Vissers, 1989) and the delamination model (e.g., Seber et al., 1996a), this would require that the removed material be replaced by asthenospheric material. This replacement would correspond to a flow that is directed radially inwards. An idealized convective-removal model would in fact imply that such a flow would be acting radially

inwards from all directions. One should not expect to observe a flow of this kind though, since any asymmetry or heterogeneity would easily lead to an asymmetric flow, more like that to be expected in a delamination model. However, a radial flow would necessarily exist somewhere, to replace the material that has been recycled into the mantle. This flow would produce anisotropic fast directions that are oriented radially. E.g., Figure 7.6 shows however, that the flow is oriented more or less tangentially to the Alboran Sea region. The required radial flow is thus not observed. This suggests that convective-removal and delamination models are unlikely to explain the anisotropy observations. On the other hand, subduction to the Northwest, as proposed by Zeck (1996), would require a rollback to the South to produce trench-parallel flow. Focal mechanisms of intermediate-depth seismicity are not inconsistent with this, but hypocenters do not show a dip toward the North. In fact, they do not show a clear Benioff zone at all, but a line of seismicity dipping steeply to the South. For that same area, teleseismic and regional tomographic studies indicate a pronounced high-velocity anomaly located beneath the Alboran Sea (e.g. Blanco and Spakman, 1993; Calvert et al., 2000b; Seber et al., 1996a). Calvert et al. (2000b) produced a tomographic model that showed a robust high-velocity anomaly beneath the west Alboran Sea and west and central Betics between 100 and 150 km. Assuming that these positive velocity anomalies indicate a region of cooler mantle, the most likely interpretation is that it indicates the presence of lithospheric mantle in view of the coherent continuation of the anomaly at depth. The positive anomaly extends from lithospheric depths beneath the Strait of Gibraltar and southern Spain to depths of about 350-400 km beneath the Alboran Sea, and it is interpreted as a lithospheric body that has descended into the upper mantle. More recently, waveform studies (Bokelmann and Maufroy, 2007) indicated dispersed body-wave arrivals propagating through the mantle under the Alboran Sea, that favor the presence of a subducted slab under the Alboran Sea, still containing a continuous low-velocity crustal layer. Wortel and Spakman (2000) also proposed a slab structure isolated in the mantle below the Betic-Alboran region at 200 km depth and that seems to be connected with deep seismicity at depths of about 640 km. Lonergan and White (1997) proposed that the now extinct subduction zone beneath the Alboran Sea was originally contiguous with the Calabrian Arc. They suggest

that the ancient subducting slab was split into two fragments, the eastern one of which has continued to roll back toward the south-east, generating the Tyrrhenian Sea and forming the present-day Calabrian Arc. The other slab fragment rolled back to the west, generating the Alboran Sea and the Betic-Rif orocline. Our SKS splitting observations, together with the previously published Pn results, show a spectacular rotation following the curvature of the roll back and of the mountain chain. There is an interesting similarity with the Calabrian arc in Southern Italy, for which shear-wave splitting results have been presented by Civello et al. (2004) and more recently by Baccheschi et al. (2007). If the SKS fast directions are to be explained by rotation similar as Pn, this would be explained most easily by a toroidal mantle flow under the subducting lithosphere that shows rollback toward the west. Such toroidal flow is apparent beneath Calabria and likely induced by the Tyrrhenean slab roll back (Civello and Margheriti, 2004; Baccheschi et al., 2007). Since that toroidal flow would occur under the slab characterized itself as a high-velocity anomaly in tomographic models (e.g. that of Calvert et al., 2000b), it would be located at depths of at least 200 km.

8. Conclusions

We have studied seismic anisotropy in the Iberian Peninsula, specifically in Central-Northern and Southern Spain, and around the Gibraltar arc. Previous studies in this area were conducted mainly in the Northern region of the Peninsula, and only few data were available in the other areas. Thus, this Thesis has contributed information that will be used to map the anisotropy of the entire Peninsula, giving additional information in the geophysics contest and related to the geodynamic evolution of the Peninsula.

The main observations are a) Eastwest direction for Central-North Spain station is consistent with fast directions in Northern region, b) more Northerly directions toward the transition Variscan Iberia with Betic, c) consistent splitting directions parallel to the Betics, and d) an apparent rotation of fast directions toward NS azimuths around the Gibraltar arc.

The Pn distribution of Calvert et al. (2000b) has a good fit with the SKS direction, especially for the Betics and Rif domain, and is perhaps related to the best coverage of rays.

Observations made from tomographic images and from Pn anisotropy allow us to determine that a uniform deformation of crust and mantle in the Eastern part of Betic exists, and remarkably the Pn and SKS direction rotations have the same pattern in the Betics and Gibraltar arc. These observations allow us to presuppose that a vertical coherent deformation model can be assumed, in which case the last penetrative episode of lithosphere deformation prevails and therefore, the anisotropy from the last significant tectonic episode might be preserved in the upper mantle.

In contrast, for the SKS direction in the Iberian Massif, we did not observe any correlation with Pn, so it is probably that there is a decoupled area between mantle

and crust in the areas of transition Variscan Iberia with Betic. For the Central-North part of the Iberian, no constrain data are available. For the zone of transition Variscan Iberia with Betic, we tested models of two-layer anisotropy and lateral heterogeneous anisotropy and found the presence of two layers, in which the upper layer has fast directions related to the Hercynian orogeny and the lower layer has fast directions parallel related to the Alpine orogeny. Unfortunatley, backazimuthal distribution of the events are rather limited, but more likely represent a complexity that is not well-characterized by the presence of two anisotropic layers. In this light, we prefer the alternative hypothesis of an anisotropy that varies laterally. Indeed, an explanation in term of simple astenospheric flow is also possible for the transition Variscan Iberia with Betic. The fast directions are nearly parallel to the absolute plate motion direction, 238.8 degrees and 2 cm/yr for Nuvel1A relative to HS3, taken at latitude 37 deg and longitude 05 degrees (Gripp and Gordon, 2002). Plate motion of the Iberian/Eurasian plate may explain part of the anisotropy.

For the Betic, where we observe a consistent and rather simple (single-layer) anisotropy, the correlation with Pn fast direction is less well-defined with a deviation of about 10 degrees. This difference is probably not significant however, especially since the Pn anisotropy appears weaker there than around the Gibraltar arc.

The Eastern Betics anisotropy observations are explained well by a single layer of anisotropy with a fast anisotropic direction trending ENE, with smooth and small variations in space. In the transition region between the Variscan and the Betics, the anisotropy shows clear backazimuthal variations of splitting parameters. Models of two-layer anisotropy and lateral heterogeneous anisotropy have been tested, and a strong lateral change in anisotropy is likely for the transition region toward the Hercynian. Near Gibraltar, fast directions are oriented close to N-S at CEUT and SFS, suggesting a gradual rotation around the arc. Combining Pn and SKS anisotropy, geological features and tomographic images allow us to discuss the various families of geodynamic models. Our SKS measurements are difficult to reconcile with geodynamic models based on delamination or convective removal. Indead, the observations favor models of subduction and rollback of the western Mediterranean slab.

Conclusiones

En esta tesis hemos estudiado la anisotropía sísmica en la Península Ibérica, más específicamente en la parte centro-norte, meridional y alrededor del arco de Gibraltar. Los trabajos de anisotropia previos en la Península se refieren principalmente a las partes septentrionales de la Península, y sólo pocos datos han sido calculados en las partes central y meridional. Por lo tanto, con este trabajo hemos aportado una importante contribución para trazar la anisotropía en la Península, aportando informaciones adicionales en el contexto de la geofísica relacionado con la evolución geodinámica de la Península.

Las principales observaciones que se destacan son a) la dirección de anisotropía Este-Oeste obtenidas para las estaciones en el centro-norte de la Peninsula son consistentes con direcciones rápidas en la parte norte, b) en la zona de transición entre el Macizo Varisco y las Béticas, se registra un cambio de la dirección de ansiotropía, siendo más hacia el norte que las anteriores c) las direcciones en la parte oriental de las Béticas son paralelas a la dirección de la cadena Bética y d) se evidencia una rotación evidente de direcciones rápidas orientas hacia el NS alrededor del arco de Gibraltar.

La distribución del Pn de Calvert y otros (2000b) tiene un buen ajuste con la dirección de SKS, especialmente para el dominio de Beticas y de Rif, quizás relacionado con la mejor cobertura de rayos. Las observaciones de las imágenes tomográficas y de la anisotropía del Pn permiten determinar que existe una deformación uniforme de la corteza en la zona oriental de las Beticas, y es notable la misma rotación alrededor del arco de Gibraltar tanto para la Pn como para la dirección de SKS. Éstas evidencias hacen presuponer que un modelo de deformación coherente vertical se puede asumir, y la ansiotropia registrada se relaciona con el último episodio de deformatcón que ha actuado en la litosfera, por lo tanto el episodio tectónico significativo pasado ha preservado la anisotropía en el

manto superior. En cambio en el macizo Varisco, no observamos correlación entre dirección de SKS y Pn, así que probablemente hay desacoplamiento entre el manto superior y la corteza en las áreas de transición entre el Varisco y las Béticas. Para la parte centro-norte de la Península no hay mucho datos disponibles. Para la zona de la transición entre Varisco y Béticas, hemos probado modelos estadísticos para relacionar la anisotropía con la presencia de más capas anisótropas o con heterogeneidad lateral. Lo resultados obtenidos de estos modelos, indican que hay un ajuste con la presencia de dos capas anisótropas, donde la capa superior tiene dirección rápida relacionada con la orogenia herciniana y la capa inferior presenta una dirección relacionada más bien con la orogenia alpina. Sin embrago, la distribución *backazimuthal* de las medidas es limitada, por lo tanto no se puede relacionar la ansiotropía sísmica con la presencia de mas capas anisótropas. En este sentido, preferimos la hipótesis alternativa de una anisotropía que varíe lateralmente.

En la zona de transición entre Varisco y Béticas es posible explicar la anisotropía en términos del flujo astenosférico. De hecho, las direcciones rápidas son casi paralelas a la dirección absoluta del movimiento de placa, a 238.8 grados y 2 cm/yr para el modelo Nuvel1A HS3, tomados a latitud 37 grados y longitud de 0.5 grados (Gripp y Gordon, 2002). El movimiento de placa de la placa ibérica/eurasiática puede explicar parte de la anisotropía.

Para las Béticas observamos una anisotropía (de una sola capa) constante y algo mas simple que la anterior, aquí la correlación con la dirección de la Pn presenta una diferencia de aproximadamente 10 grados. Esta diferencia probablemente no es significativa, sin embargo observamos que la anisotropía del Pn aparece más débil en esta parte que alrededor del arco de Gibraltar.

Las observaciones de la anisotropía en la parte oriental de las Béticas se explican bien con un modelo de una sola capa anisotrópa, con dirección ENE, presentando pequeñas variaciones espaciales, a diferencia de las direcciones en la zona de transición entre Varisco y Béticas, donde las medidas de anisotropía presentan evidentes variaciones *backazimuthal*.

Cerca de Gibraltar, las direcciones rápidas se orientan segù la direccion N-S en las estaciones de CEUT y SFS, ésta observacion sugiere que hay una rotación gradual alrededor del arco.

Combinando medidas de anisotropía de Pn y de SKS, con las características geológicas y las imágenes topográficas, se pueden discutir los datos en clave de

varios modelos geodinámicos propuesto. Las medidas de SKS que han sido calculadas en este trabajo, son difícil de reconciliar con los modelos geodinámicos basados en la delaminación o en la eliminación convectiva (*convective renoval*). Las observaciones realizadas favorecen más bien un modelo de subducción retroceso (*slab roll-back*) del Mediterraneo occidental.

9. References

Almendros, J., Barclay, A., Wilcock, W.S.D., Purdy and G.M. (2000). Seismic anisotropy of the shallow crust at the Juan de Fuca ridge. *Geophysical Research Letters* **27**: 3109-3112.

Alsina, D., Snieder and R. (1995). Small-scale sublithospheric continental mantle deformation: Constraints from SKS splitting informations. *Geophysical Journal International* **123**: 431-448.

Anderson, M. L. Zandt, G. Triep, E. Fouch, M. a. Beck and S (2004). Anisotropy and mantle flow in the Chile-Argentina subduction zone from shear wave splitting analysis. *Geophys. Res.Let* **31**(23608).

Ando, M., Ishikawa, Y., Yamazaki and F. (1983). Shear wave polarization anisotropy in the upper mantle beneath Honshu, Japan. *Journal of Geophysical Research* **88**(B7): 5850-5864.

Andrade, A. S. (1983). Contribution á l'analyse de la suture hercynième de Beja (Portugal), perspectives métallogéniques. *Ph.D. thesis, 137 pp., Inst. Nat. Polytech.de Lorraine, Nancy.*

Ansel, V., Nataf and H.C. (1989). Anisotropy beneath 9 stations of the Geoscope broadband network as deduced from shear-wave splitting. *Geophysical Research Letters* **16**: 409-412.

Azor, A., F. G. Lodeiro and J. F. Simancas (1994). Tectonic Evolution of the Boundary between the Central Iberian and Ossa-Morena Zones (Variscan Belt, Southwest Spain). *Tectonics* **13**(1): 45-61.

Babuska, V., Plomerova, J., Sileny and J. (1993). Models of seismic anisotropy in the deep continental lithosphere. *Physics of the Earth and Planetary Interiors* **78**: 167-191.

Babuska, V. and M. Cara (1992). Seismic anisotropy in the Earth. Dordrecht, Kluwer academic publ.

Babuska, V. and Z. Pros (1984). Velocity Anisotropy in Granodiorite and Quartzite Due to the Distribution of Microcracks. *Geophysical Journal of the Royal Astronomical Society* **76**(1): 121-&.

Baccheschi, P., L. Margheriti and M. S. Steckler (2007). Seismic anisotropy reveals focused mantle flow around the Calabrian slab (Southern Italy). *Geophys. Res. Lett.* **34, L05302, doi:10.1029/2006GL028899.**

Backus, G. E. (1962). Long-wave elastic anisotropy produced by horizontal layering. *Journal of Geophysical Research* **67**: 4427-4440.

Balanya, J. C., Campos, I., G. Duenas, V., Simancas, J. E., Munoz, J. A., S. d. Galdeano, C., Santanach and P. (1988). La estructuracion de los mantos alpujarrides (beticas). 22.

Banda, E., Gallart, J., G. Duenas, V., Danobeitia, J. J., Makris and J. (1993). Lateral variation of the crust in the Iberian Peninsula; new evidence from the Betic Cordillera.; Seismic studies of the Iberian Peninsula. *Tectonophysics* **221**(1): 53-66.

Banda, E. (1988). Crustal Parameters in the Iberian Peninsula. *Physics of the Earth and Planetary Interiors* **51**(1-3): 222-225.

Banda, E., E. Surinach, A. Aparicio, J. Sierra and E. R. de la Parte (1981). Crust and upper mantle structure of the central Iberian Meseta (Spain). **67:** 779-789.

Barruol, G., Helffrich, G., Vauchez and A. (1997a). Shear wave splitting around the northern Atlantic: Frozen Pangean lithospheric anisotropy? *Tectonophysics* **279**(1-4): 135-148, doi:10.1016/S0040-1951(97)00126-1.

Barruol, G., Mainprice and D. (1993). A quantitative evaluation of the contribution of crustal rocks to the shear wave splitting of teleseismic SKS waves. *Physics of the Earth and Planetary Interiors* **78**(3-4): 281-300, doi:10.1016/0031-9201(93)90161-2.

Barruol, G., Souriau, A., Vauchez, A., Diaz, J., Gallart, J., Tubia, J., Cuevas and J. (1997b). Mantle structure beneath the Pyrenees from SKS splitting. AGU fall meeting, San Francisco, Ca, American Geophysical Union.

Barruol, G., Souriau, A., Vauchez, A., Diaz, J., Gallart, J., Tubia, J., Cuevas and J. (1998). Lithospheric anisotropy beneath the Pyrenees from shear wave splitting. *Journal of Geophysical Research* **103**: 30039-30054.

Barruol, G., Vauchez, A., Souriau, A., Gallart, J., Diaz and J. (1996). Seismic anisotropy in the eastern Pyrenees. Geodynamics of the lithosphere and Earth's mantle, Trest, Czech Republik, july 8-13.

Bjarnason, I.T., Wolfe, C.J., Solomon, S.C., Gudmundson and G. (1996). Initial results from the ICEMELT experiment: body wave delay times and shear-wave splitting across Iceland. *Geophysical Research Letters* **23**: 459-462.

Blanco, M. J. and W. Spakman (1993). The P-Wave Velocity Structure of the Mantle Below the Iberian Peninsula - Evidence for Subducted Lithosphere Below Southern Spain. *Tectonophysics* **221**(1): 13-34.

Bokelmann, G.H.R., Harjes and H.P. (2000). Evidence for temporal variation of seismic velocity within the upper continental crust. *Journal of Geophysical Research* **105**: 23879-23894.

Bokelmann, G. H. R. and E. Maufroy (2007). Mantle structure under Gibraltar constrained by dispersion of body waves. . *Geophys. Res. Lett.* **34**: L22305, doi:10.1029/2007GL030964.

Bowman, J.R., Ando and M. (1987). Shear-wave splitting in the upper-mantle wedge above the Tonga subduction zone. *Geophysical Journal of the Royal Astronomical Society* **88**: 25-41.

Brechner, S., K. Klinge, F. Kruger and T. Plenefisch (1998). Backazimuthal variations of splitting parameters of teleseismic SKS phases observed at the broadband stations in Germany. International Workshop on Geodynamics of the Lithosphere and the Earths Mantle - Seismic Anisotropy as a Record of the Past and Present Dynamic Processes, Trest, Czech Republic.

Buforn, E., Udías, A., Madariaga and R. (1991). Intermediate and deep earthquakes in Spain. *Pure and Applied Geophysics.* **136**: 375-393.

Buforn, E., P. Coca, A. Udias and C. Lasa (1997). Source mechanism of intermediate and deep earthquakes in southern Spain. *Journal of Seismology* **1**(2): 113-130.

Buforn, E., A. Udias and M. A. Colombas (1988). Seismicity, Source Mechanisms and Tectonics of the Azores-Gibraltar Plate Boundary. *Tectonophysics* **152**(1-2): 89-118.

Buland, R. and C. H. Chapman (1983). The computation of seismic travel times. . *Bull. Seism. Soc. Am.* **73**: 1,271–1,302.

Calvert, A., Sandvol, E., Seber, D., Barazangi, M., Roecker, S., Mourabit, T., Vidal, F., Alguacil, G., Jabour and N. (2000a). Geodynamic evolution of the lithosphere and upper mantle beneath the Alboran region of the western Mediterranean: constraints from travel time tomography. *Journal of Geophysical Research* **105**: 10871-10898.

Calvert, A., Sandvol, E., Seber, D., Barazangi, M., Vidal, F., Alguacil, G., Jabour and N. (2000b). Propagation of regional seismic phases (Lg and Sn) and Pn velocity structure along the Africa-Iberia plate boundary zone: tectonic implications. *Geophysical Journal International* **142**(2): 384-408.

Civello, S. and L. Margheriti (2004). Toroidal mantle flow around the Calabrian slab (Italy) from SKS splitting. *Geophysical Research Letters* **31**: doi:10.1029/2004GL019607.

Comas, M. C., J. P. Platt, J. I. Soto and A. B. Watts (1999). The origin and tectonic history of the Alboran Basin; insights from Leg 161 results.; Proceedings of the Ocean Drilling Program; scientific results; Mediterranean Sea II, the western Mediterranean; covering Leg 161 of the cruises of the Drilling Vessel JOIDES Resolution, Naples, Italy, to Malaga, Spain, sites 974-979, 3 May-2 July 1995. *in Proc. ODP,Sci. Results, edit by R. Zahn, M. C. Comas y A.Klau. Ocean Drilling Program, College Station, TX.* **161**: 555-579.

Conrad, C. P., M. D. Behn and P. G. Silver (2007). Global mantle flow and the development of seismic anisotropy: Differences between the oceanic and continental upper mantle. *J. Geophys. Res.* **112, B07317.**

Córdoba, D., E. Banda and J. Ansorge (1987). The Hercynian crust in Northwestern Spain: A review. . *Tectonophysics* **132**: 321–333.

Crampin, S., Arnaud, Jean, Helbig, Klaus, Rasolofosaon, Patrick, Thomsen and Leon (1999). Shear-wave splitting in a critical crust; the next step.; Eighth international workshop on Seismic anisotropy (8IWSA); abstracts. *Geophysics* **64**(6): 1954-1955.

Crampin, Stuart, Gao and Yuan (2006). A review of techniques for measuring shear-wave splitting above small earthquakes. *Physics of The Earth and Planetary Interiors* **159**(1-2): 1-14.

Crampin, S. (1984). An introduction to wave propagation in anisotropic media. *Geophysical Journal of the Royal Astronomical Society* **76**: 17-28.

Crampin, S. (1991a). An alternative scenario for earthquake prediction experiments. *Geophys. J. Int.* **107**: 185-189.

Crampin, S. (1991b). Seismic Anisotropy Due to Preferred Mineral Orientation Observed in Shallow Crustal Rocks in Southern Alaska - Comment. *Geology* **19**(8): 859-859.

Crampin, S. (1994). Title The fracture criticality of crustal rocks *Geophysical Journal International* **118**((2)): pp.428-438.

Crampin, S. and D. C. Booth (1985). Shear-Wave Polarizations near the North Anatolian Fault .2. Interpretation in Terms of Crack-Induced Anisotropy. *Geophysical Journal of the Royal Astronomical Society* **83**(1): 75-92.

Crampin, S., E. M. Chesnokov and R. G. Hipkin (1984). Seismic Anisotropy - the State of the Art .2. Introduction. *Geophysical Journal of the Royal Astronomical Society* **76**(1): 1-16.

Crampin, S. and Y. Gao (2006). A review of techniques for measuring shear-wave splitting above small earthquakes. *Physics of The Earth and Planetary Interiors* **159**(1-2): 1-14.

Currie, C. A., J. F. Cassidy, R. D. Hyndman and M. G. Bostock (2004). Shear wave anisotropy beneath the Cascadia subduction zone and western North American craton. *Geophysical Journal International* **157**(1): 341-353.

Deschamps, A., Y. Gaudemer and A. Cisternas (1982). The El Asnam, Algeria, Earthquake of 10 October 1980 - Multiple-Source Mechanism Determined from Long-Period Records. *Bulletin of the Seismological Society of America* **72**(4): 1111-1128.

Dewey, J.F., Helman, M.L., Torco, E., Hutton, D.H.W., Knott and S. (1989). Kinematics of the western Mediterranean. Alpine Tectonics. Coward, M.P., Dietrich and D. London, Geol. Soc. Spec. Public. **45:** 265-283.

Dewey, J. F. (1988). Extensional collapse of orogens. *Tectonics* **7**(6): 1123-1139.

Dewey, J. F. (1989). Kinematics and dynamics of basin inversion.; Inversion tectonics meeting. *Geological Society Special Publications* **44**: 352.

Diaz, J., Gallart, J., Hirn, A., Paulssen and H. (1998). Anisotropy beneath the Iberian Peninsula; the contribution of the ILIHA-NARS broad-band experiment.; Geodynamics of lithosphere and Earth's mantle; seismic anisotropy as a record of the past and present dynamic processes. *Pure and Applied Geophysics* **151**(2-4): 395-405.

Diaz, J., Gallart, J., Ruiz, M., Pulgar, J. A., Lopez, C., G. Cortina and J. M. (2002). Anisotropic features of the Alpine lithosphere in northern Spain. *Geophysical Research Letters*.

Docherty, C. and E. Banda (1995). Evidence for the eastward migration of the Alboran Sea based on regional subsidence analysis: A case for basin formation by delamination of the subcrustal lithosphere. *Tectonics* **14**: 804-818.

Duggen, S., K. Hoernle, P. van den Bogaard and C. Harris (2004). Magmatic evolution of the Alboran region: The role of subduction in forming the western Mediterranean and causing the Messinian Salinity Crisis. *Earth and Planetary Science Letters* **218**(1-2): 91-108.

Duggen, S., H. K., P. Van den Bogaard and G.-S. D. (2005). Post-collisional transition from subduction- to intraplate-type magmatism in the westernmost Mediterranean: Evidence for continental-edge delamination of subcontinental lithosphere. *J. Petrology* **46**: 1155-1201.

El Bakkali, S., L. L. Bourdier and A. Gourgaud (1998). Characterisation and stratigraphy of upper Miocene volcaniclastic marker beds in the Melilla lower Kert Basin (eastern Rif, Morocco). *Comptes Rendus De L Academie Des Sciences Serie Ii Fascicule a-Sciences De La Terre Et Des Planetes* **327**(2): 93-100.

Faccenna, C., Piromallo, C., Crespo-Blanc, A., Jolivet, L., Rossetti and F. (2004). Lateral slab deformation and the origin of the western Mediterranean arcs. *Tectonics* **23**(TC1012): doi:10.1029/2002TC001488.

Fernandez-Ibanez, F., Soto, J. I., Zoback, M. D., Morales and J. (2007). Present-day stress field in the Gibraltar Arc (western Mediterranean). Journal of Geophysical Research-Solid Earth. **112**.

Fischer, K.M., Fouchs, M.J., Wiens, D.A., Boettcher and M.S. (1998). Anisotropy and flow in Pacific subduction zone back-arcs. *Pure and Applied Geophysics* **151**: 463-475.

Fischer and Wiens (1995). The depth distribution of mantle anisotropy beneath the Tonga subduction zone. *Earth and Planetary Science Letters* **142**: 253-260.

Fouch and Rondenay (2006). Seismic anisotropy beneath stable continental interiors. *Physics of The Earth and Planetary Interiors* **158**(2-4): 292-320.

Fouch, M. J. and K. M. Fischer (1996). Mantle anisotropy beneath northwest Pacific subduction zones. *Journal of Geophysical Research-Solid Earth* **101**(B7): 15987-16002.

Franke, W. (1989). Tectonostratigraphic units in the Variscan belt of central Europe. . *Geol. Soc. Am., Special Paper* **230**: 67-90.

Galindo-Zaldívar, J., A. Jabaloy, F. González-Lodeiro and F. Aldaya (1997). Crustal structure of the central sector of the Betic Cordillera (SE Spain). . *Tectonics* **16**: 18-37.

Garcia-Dueñas, V. (1969). Les unités allochtones de la zone Subbétique,dans la transversale de Grenade (Cordillères Bétiques, Espagne). *Rev. Geogr. Phys. Geol. Dyn.* **2**: 211-222.

Garcia-Hernandez, M., A. C. Lopez-Garrido, P. Rivas, C. Sanz de Galdeano and J. A. Vera (1980). Mesozoic paleogeographic evolution of the External Zones of the Betic Cordillera. *Geol. Mijnbouw* **59**: 155-168.

Garnero, E.J., Lay and T. (1998). Effect of D" anisotropy on seismic velocity models of the outermost core. *Geophysical Research Letters* **25**: 2341-2344.

Garnero, E. J. (2000). Heterogeneity in the lowermost mantle. *Annu. Rev. Earth Planetary Sci.* **28**: 509-537. doi:10.1146/annurev.earth.28.1.50.

Gill, R. C. O., A. Aparicio, M. El Azzouzi, J. Hernández, M. F. Thirlwall, J. Bourgois and G. F. Marriner (2004). Depleted arc volcanism in the Alboran Sea and shoshonitic volcanism in Morocco : geochemical and isotopic constraints on Neogene tectonic processes. *Lithos.* **78**: 363-388.

Gledhill, K. and G. Stuart (1996). Seismic anisotropy in the fore-arc region of the Hikurangi subduction zone, New Zealand. *Physics of the Earth and Planetary Interiors* **95**: 211-225.

Grésillaud, A., Cara and M. (1996). Anisotropy and P-wave tomography: a new approach for inverting teleseismic data from a dense array of stations. *Geophysical Journal International* **126**: 77-91.

Gripp, A.E., Gordon and R.B. (2002). Young tracks of hotspots and current plate velocities. *Geophysical Journal International* **150**: 321-361.

Gutscher, M. A., J. Malod, J. P. Rehault, I. Contrucci, F. Klingelhoefer, L. Mendes-Victor and W. Spakman (2002). Evidence for active subduction beneath Gibraltar. *Geology* **30**(12): 1071-1074.

Hanka, W., A. Heinloo and K.-H. Jaeckel (2000). Networked Seismographs: GEOFON Real-Time Data Distribution. Orfeus Newsletter. *Orfeus Newsletter* **vol. 2 nº 3**: pag. 24.

Hartog and Schwartz (2000). Subduction-induced strain in the upper mantle east of the Mendocino triple junction, California. *J.Geophys. Res.* **105 (B4)**: 7909-7930.

Hedlin, M. A. H. and P. M. Shearer (2000). An analysis of large-scale variations in small-scale mantle heterogeneity using global seismographic network ecordings of precursors to PKP. *J. Geophys. Res.* **105 (B6)**: 13655–13673.

Heintz, M., Kenneth and B.L.N. (2006). The apparent isotropic Australian upper mantle. *Geophysical Research Letters* **33**(L15319): doi:10.1029/2006GL026401.

Helbig, K. (1993). Simultaneous observation of seismic waves of different polarization indicates subsurface anisotropy and might help to unravel its cause. *J. Appl. Geophys.* **30**: 1–24.

Helffrich, George, Silver, Paul, Given and Holly (1994). Shear-wave splitting variation over short spatial scales on continents. **119:** 561-573.

Holt, W. (1997). Placing constraints on the crust and mantle deformation field in Asia (abstract). *Eos Trans. AGU, 78(46), Fall Meet. Suppl., F699.*

Hudson, J. A. (1991). Crack distribution which account for a given seismic anisotropy. *Geophysical Journal International* **104**: 517-521.

Ismail, B., W., Mainprice and D. (1998). An olivine fabric database: an interpretative frame for upper mantle seismology. 7th kimberlite conference, Cape Town, South Africa.

James, D.E., Assumpçao and M. (1996). Tectonic implications of S-wave anisotropy beneath SE Brazil. *Geophysical Journal International* **126**: 1-10.

Jolivet, L., Faccenna and C. (2000). Mediterranean extension and the Africa-Eurasia collision. *Tectonics* **19**(6): 1095-1106.

Julivert, M., F. J. Martinez and A. Ribeiro (1980). The Iberian segment of the European Hercynian foldbelt. *In: Cogné, J., Slansky, M. (Eds.), Géologie de l'Europe. Mém. B.R.G.M.* **108**: 132–158.

Jung, H. and S. Karato (2001). Water-induced fabric transitions in olivine. *Science* **293**(5534): 1460-1463.

Kaminski, E. (2002). The influence of water on the development of lattice preferred orientation in olivine aggregates. *Geophysical Research Letters* **29**(12).

Kaminski, E. and N. M. Ribe (2002). Timescale for the evolution of seismic anisotropy in mantle flow. *Geochemistry, Geophysics, Geosystems* **3**: 10.1029/2001GC000222.

Kaneshima, S., Ando, M., Kimura and S. (1988). Evidence from shear-wave splitting for the restriction of seismic anisotropy to the upper crust. *Nature* **335**: 627-629.

Karato, S.I., Zhang, S., Wenk and H.R. (1995). Superplasticity in the Earth's lower mantle: Evidence from seismic anisotropy and rock physics. *Science* **270**: 458-461.

Karato, S. (1987). Seismic anisotropy due to lattice preferred orientation of minerals: kinematic or dynamic?In: M.H. Manghnani and S. Syono, Editors, High-Pressure Research in Mineral Physics, Geophysical Monograph Ser. AGU, Washington, DC (1987), pp. 455–471.

Karato, S. (1998). Seismic anisotropy in the deep mantle, boundary layers and the geometry of mantle convection. *Pure and Applied Geophysics* **151**: 565-587.

Karato, S. (2003). Mapping water content in the upper mantle. In: Eiler, J.M. (Ed.), Inside the Subduction Factory. . *Am. Geophys. Union, Geophys. Monogr. Ser.* **138**.

Kendall, J., S. Pilidou, D. Keir, I. Bastow, G. Stuart and A. Ayele (2006). Mantle upwellings,melt migration and magma assisted rifting in Africa: Insights from seismic anisotropy, in G. Yirgu; C. J. Ebinger & P. K. H. Maguire, ed.,Structure and evolution of the rift systems within the Afar volcanic province, Northeast Africa, pp. 57-74.

Kendall, J. M. (1994). Teleseismic arrivals at a mid-ocean ridge: Effect of mantle melt and anisotropy. *Geophysical Research Letters* **21**: 301-304.

Kendall, J. M. (2000). Seismic anisotropy in the boundary layers of the mantle. . *Geophysical monograph* **117(4)**: 133-159.

Kendall, J. M. and P. G. Silver (1996). Constraints from seismic anisotropy on the nature of the lowermost mantle. *Nature* **381**: 409-412.

Kennett, B. L. N. (1995). Seismic traveltime tables. Global Earth Physics. A Handbook of Physical Constants. Ahrens and T.J. Washington, D. C., AGU. **1:** 126-143.

Kennett, B. L. N. and E. R. Engdahl (1991). Traveltimes for global earthquake location and phase identification. *Geophysical Journal International* **105**: 429-465.

Kern, H., Richter and A. (1981). Temperatures derivatives of compressional and shear wave velocities in crustal and mantle rocks at 6 Kbar confining pressure. *Journal of Geophysic* **49**: 47-56.

Kern, H. (1990). Laboratory seismic measurements: an aid in the interpretation of seismic field data. *Terra Nova* **2**: 617-628.

Kern, H. (1993). P- and S-wave anisotropy and shear wave splitting at pressure and temperature in possible mantle rocks and their relations to the rock fabric. *Physics of the Earth and Planetary Interiors* **78**: 245-256.

Kneller, E. A., P. E. v. Keken, S. Karato and J. Park (2005). B-type olivine fabric in the mantle wedge: Insights from high-resolution non-Newtonian subduction zone models. *Earth Planet. Sci. Lett.* **237** 781–797.

Larouziére, F. D. D., J. Bolze, P.Bordet, J. Hernandez, C. Montenat and P. O. d'Estevou (1988). The Betic segment of the lithospheric Trans-Alboran shear zone during the late Miocene. . *Tectonophys.* **152**: 41-52.

Lay, T. and D. V. Helmberger (1983). The shear-wave velocity gradient at the base of the mantle. *J. Geophys. Res.* **88**: 8160–8170.

Lay, T. and T. C. Wallace (1995). Modern Global Seismology. *Academic Press, London*.

Lay, T., Q. Williams and E. J. Garnero (1998). The core-mantle boundary layer and deep Earth dynamics. *Nature* **392**: 461-468. doi:10.1038/33083.

Levin, V., W. Menke and J. Sileny (1996). Seismic anisotropy in the deep continental lithosphere. *Geophysical Journal International* **78**: 593-603.

Lonergan, L. and N. White (1997). Origin of the Betic-Rif mountain belt. *Tectonics* **16**: 504-522.

Luján, M., A. Crespo-Blanc and J. C. Balanyá (2006). The Flysch Trough thrust imbricate (Betic Cordillera):A key element of the Gibraltar Arc orogenic wedge. *Tectonics* **25**(TC6001, doi:10.1029/2005TC001910).

Mainprice, D., Barruol, G., B. Ismail and W. (2000). The seismic anisotropy of the Earth's mantle: from single crystal to polycrystal. Earth's deep interior: Mineral Physics and Tomography from the atomic to the global scale. Karato and S.I. Washington, D.C., AGU. **117:** 237-264.

Mainprice, D., Nicolas and A. (1989). Development of shape and lattice preferred orientations: application to the seismic anisotropy of the lower crust. *Journal of Structural Geology* **11**(1/2): 175-189.

Mainprice, D., Silver and P.G. (1993). Interpretation of *SKS*-waves using samples from the subcontinental lithosphere. *Physics of the Earth and Planetary Interiors* **78**: 257-280.

Mainprice, D., Tommasi, A., Couvy, H., Cordier and P. (2005). Pressure sensitivity of olivine slip systems and seismic anisotropy of earth's upper mantle. *Nature* **433**: 731-733.

Makeyeva, L.I., Vinnik, L.P., Roecker and S.W. (1992). Shear-wave splitting and small-scale convection in the continental upper mantle. *Nature* **358**: 144-147.

Marson-Pidgeon, K., M. K. Savage, K. Gledhill and G. Stuart (1999). Seismic anisotropy beneath the lower half of the North Island, New Zealand. *J. Geophys. Res.* **104(B9)**: 20,277–20,286. .

Marson-Pidgeon, M. and M. Savage (2004). Shear-wave splitting variations across an array in the southern North Island, New Zealand. *Geophysical Research Letters* **31**(L21602): doi:10.1029/2004GL021190.

Marson-Pidgeon, M. and M. K. Savage (1997). Frequency-dependent anisotropy in Wellington, New Zealand. *Geophysical Research Letters* **24**: 3297-3300.

Matte, P. (1986). Tectonics and plate tectonics model for the Variscan belt of Europe. *Tectonophysics* **126**: 329-374.

Maupin, V. (1994). On the possibility of anisotropy in the D'' layer as inferred from the polarization of diffracted S waves. *Phys.Earth Planet. Inter.* **87** 1–32.

Mehl, L., B. R. Hacker, G. Hirth and P. B. Kelemen (2003). Arc-parallel flow within the mantle wedge: evidence from the accreted Talkeetna arc, south central Alaska. . *J. Geophys. Res. Solid Earth* **108.(B8).**

Mele, G. (1998). Pn anisotropyin the northern Apennine chain (Italy). *Pure and Applied Geophysics* **151**: 495-502.

Mezcua, J. and J. Rueda (1997). Seismological evidence for a delamination process in the lithospere under the Alboran Sea. *Geophys. J. Int.* **129**: F1-F8.

Montagner, J. P. (1998). Where can seismic anisotropy be detected in the Earth's mantle? In boundary layers. *Pure and Applied Geophysics* **151**: 223-256.

Moore, M. M., Garnero, E. J., Lay, T., Williams and Q. (2004). Shear wave splitting and waveform complexity for lowermost mantle structures with low-velocity lamellae and transverse isotropy. *J. Geophys. Res.* **109** 2319. doi:10.1029/2003JB002546.

Morales, J., G. Alguacil, M. J.B. and M. A. (2007). The Instituto Andaluz de Geofisica-Universidad de Granada seismic network in Southern Spain. *Orfeus Newsletter* **vol. 7, nº 2. .** pag 1.

Morales, J., I. Serrano, A. Jabajoy, J. Galindo-Zaldívar, D. Zhao, F. Torcal, F. Vidal and F. González Lodeiro (1999). Active continental subduction beneath the Betic Cordillera and the Alborán Sea. . *Geology* **27**: 735-738. .

Munhá, J., J. T. Oliveira, A. Ribeiro, V. Oliveira, C. Quesada and R. Kerrich (1986). Beja-Acebuches ophiolite, characterization and geodynamic significance. *Maleo* **2.** : 31.

Nicolas (1993). Why are fast polarisation directions of *SKS* seismic waves parallel to mountain belts. *Physics of the Earth and Planetary Interiors* **78**: 337-342.

Nicolas, A. and N. I. Christensen (1987). Formation of anisotropy in upper mantle peridotites-A review. Composition, Structure and Dynamics of the Lithosphere-Asthenosphere System. K. Fuchs and C. Froidevaux. Washington, D. C., AGU. **16:** 111-123.

Niu, F., Perez and A. (2004). Seismic anisotropy in the lower mantle: a comparison of waveform splitting of SKS and SKKS. *Geophysical Research Letters* **31**: 10.1029/2004GL021196.

Ott D'Estevou, P. and C. Montenat (1985). Evolution structurale de la zone bétique orientale (Espagne) du Tortonian a l'Holocene. . *Comptes Rendus de l'Académie des Sciences Paris* **300**: 363-368.

Ottemoller, L. and J. Havskov (1999). SeisNet: A General Purpose Virtual Seismic Network. . *Seismological Research Letters* **70**: 5.

Ozalaybey, S., Chen and W.P. (1999). Frequency-dependent analysis of SKS/SKKS waveforms observed in Australia: evidence for null birefringence. *Physics of the Earth and Planetary Interiors* **114**: 197-210.

Ozalaybey, S. and M. K. Savage (1995). Shear wave splitting beneath the western United States in relation to plate tectonics. *Journal of Geophysical Research* **100**: 18135-18149.

Park, J., Levin and V. (2001). Receiver functions from regional P waves. *Geophysical Journal International* **147**: 1-11.

Park, J., Levin, V., Brandon, M., Lees, J., Peyton, V., Gordeev, E., Ozerov and A. (2002). A dangling slab, amplified arc volcanism, mantle flow and seismic anisotropy in the Kamchatka plate corner. Geodynamic series, Plate boundary zones. A. G. Union. **30:** 10/1029/030GD18.

Paulssen, Hanneke, Visser and Jeanette (1993). The crustal structure in Iberia inferred from P-wave coda.; Seismic studies of the Iberian Peninsula. *Tectonophysics* **221**(1): 111-123.

Pedreira, D., Pulgar, J. A., Gallart, J., Diaz and J. (2003). Seismic evidence of Alpine crustal thickening and wedging from the western Pyrenees to the Cantabrian Mountains (north Iberia). *Journal of Geophysical Research, B, Solid Earth and Planets*.

Pera, E., Mainprice, D., Burlini and L. (2003). Petrophysical properties of the upper mantle beneath the Torre Alfina area (Northern Apennines, Central Italy). . *Tectonophysics.* **370.**: 11-30. .

Pérez-Estaún, A., F. Bea, F. Bastida, A. Marcos, J. R. M. Catalán, D. M. Poyatos, R. Arenas, F. D. Garcia, A. Azor, J. F. Simancas and F. G. Lodeiro (2004). Geologia de España. Editor J.A. Vera.

Pinheiro, L. M., R. B. Whitmarsh and P. R. Miles (1992). The ocean-continent boundary off the western continental margin of Iberia - II. Crustal structure in Tagus Abyssal Plain. *Geophys. J. Int.* **109**: 106-124.

Piromallo, C., I. N. d. Geofisica, R. Italy, Morelli, A., I. N. d. Geofisica and R. Italy (1997). Imaging the Mediterranean upper mantle by p- wave travel time tomography.

Platt, J. P., Soto, J. I., Whitehouse, M. J., Hurford, A. J., Kelley and S. P. (1998). Thermal evolution, rate of exhumation, and tectonic significance of metamorphic rocks from the floor of the Alboran extensional basin, western Mediterranean. *Tectonics* **17**(5): 671-689.

Platt, J. P. and R. L. M. Vissers (1989). Extensional collapse of thickened continental lithosphere: A working hypothesis for the Alboran Sea and Gibraltar Arc. *Geology* **17** 540-543.

Platt, J. P., M. J. Whitehouse, S. P. Kelley, A. Carter and L. Hollick (2003). Simultaneous extensional exhumation across the Alboran Basin: Implications for the causes of late orogenic extension. *Geology* **31**(3): 251-254.

Pozgay, S. H., D. A. Wiens, J. A. Conder, H. Shiobara and H. Sugioka (2007). Complex mantle flow in the Mariana subduction system: evidence from shear wave splitting. *Geophysical Journal International* **170**(1): 371-386.

Quesada, C., P. Fonseca, J. Munhá, J. T. Oliveira and A. Ribeiro (1994). The Beja-Acebuches Ophiolite (Southern Iberia Variscan fold belt): Geological characterization and geodynamic significance. *Bol. Geol. Min.* **105.** : 3 – 49.

Ribe, N. M. (1989). Seismic anisotropy and mantle flow. *Journal of Geophysical Research* **94**: 4213-4223.

Ribe, N. M. (1992). On the Relation between Seismic Anisotropy and Finite Strain. *Journal of Geophysical Research-Solid Earth* **97**(B6): 8737-8747.

Ribeiro, A., M. T. Antunes, M. P. Ferreira, R. B. Rocha, A. F. Soares, G. Zbyszewski, F. Moitinho de Almeida, D. Carvalho and J. H. Monteiro (1979). Introduction à la Géologie generale du Portugal. Ed. Serv. Geol. Portugal. **114.**

Rosenbaum, G., Lister, G.S., Duboz and C. (2002). Relative motions of Africa, Iberia and Europe during Alpine orogeny. *Tectonophysics* **359**: 117-129.

Sandvol, E., Ni, J., Ozalaybey, S., Schlue and J. (1992). Shear-wave splitting in the Rio Grande rift. *Geophysical Research Letters* **19**(23): 2337-2340.

Sandvol, E., Seber, D., Barazangi, M., Vernon, F., Mellors, R., Al-Amri and A. (1998). Lithospheric seismic velocity discontinuities beneath the Arabian shield. *Geophysical Research Letters* **25**: 2873-2876.

Sandvol, E. and J. Ni (1997). Deep azimuthal seismic anisotropy in the southern Kurile and Japan subduction zones. *Journal of Geophysical Research-Solid Earth* **102**(B5): 9911-9922.

Savage, M. K. (1998). Lower crustal anisotropy or dipping boundaries? Effect of receiver functions and a case study in New Zealand. *Journal of Geophysical Research* **103**: 15069-15087.

Savage, M. K. (1999). Seismic anisotropy and mantle deformation: What have we learned from shear wave splitting? *Reviews of Geophysics* **37**: 65-106.

Schmid, C., V. d. Lee, S., Giardini and D. (2004). Delay times and shear wave splitting in the Mediterranean region. . *Geophys. J. Int.* **159**: 275-290.

Seber, D., Barazangi, M., Tadili, B. A., Ramdani, M., Ibenbrahim, A., BenSari and D. (1996b). Three-dimensional upper mantle structure beneath the intraplate atlas and interplate Rif mountains of Morocco. *Journal of Geophysical Research-Solid Earth* **101**(B2): 3125-3138.

Seber, Dogan, Barazangi, Muawia, Ibenbrahim, Aomar, Demnati and Ahmed (1996a). Geophysical evidence for lithospheric delamination beneath the Alboran Sea and Rif-Betic mountains. *Nature* **379**(6568): 785-790.

Serrano, I., Hearn, T.M., Morales, J., Torcal and F. (2005). Seismic anisotropy and velocity structure beneath the southern half of the Iberian peninsula. *Physics of the Earth and Planetary Interiors* **150**: doi:10.1016/j.pepi.2004.12.003.

Shearer, M. (1999). Introduction to seismology. *Cambridge Univ. Press*.

Sheehan, A. F., C. H. Jones, M. K. Savage, S. Ozalabey and J. M. Schneider (1997). Contrasting lithospheric structure between the Colorado plateau and great Basin: Initial results from Colorado Plateau-Great Basin PASSCAL experiment. *Geophysical Research Letters* **24**: 2609-2612.

Sieminski, A., Liu, Q. Y., Trampert, J., Tromp and J. (2007). Finite-frequency sensitivity of surface waves to anisotropy based upon adjoint methods. *Geophysical Journal International* **168**(3): 1153-1174.

Silva, J. B. (1999). The pre-Mesozoic cycles in West Iberia: a continuous transpressional regime from the Cadomian to the end of the Variscan times. *J. Conf. Abst. 4 (1)89*.

Silver, P.G., Carlson, R.W., Olson and P. (1988). Deep slabs, geochemical heterogeneity, and the large scale structure of mantyle convection: investigation of an enduring paradox. *Annual Review of the Earth and Planetary Sciences* **16**: 477-541.

Silver, P.G., Chan and W.W. (1991). Shear wave splitting and subcontinental mantle deformation. *Journal of Geophysical Research* **96**: 16429-16454.

Silver, P.G., Savage and M.K. (1994). The interpretation of shear-wave splitting parameters in the presence of two anisotropic layers. *Geophysical Journal International* **119**: 949-963.

Silver, P. G. (1996). Seismic anisotropy beneath the continents: Probing the depths of geology. *Annual Review of the Earth and Planetary Sciences* **24**: 385-432.

Silver, P. G. and W. W. Chan (1988). Implications for continental structure and evolution from seismic anisotropy. *Nature* **335**: 34-39.

Silver, P. G. and W. W. Chan (1991). Shear wave splitting and subcontinental mantle deformation. *Journal of Geophysical Research* **96**: 16429-16454.

Simancas, J. F., D. M. Poyatos, I. Exposito, A. Azor and F. G. Lodeiro (2001). The structure of a major suture zone in the SW Iberian Massif: the Ossa-Morena/Central Iberian contact *Tectonophysics* **332 nº1**: pp. 295-308(14).

Simancas, J. F., C. R., F. Gonzalez Lodeiro, A. Perez Estaun, C. Juhlin, P. Ayarza, A. Kashubin, A. Azor, D. Martınez Poyatos, G. R. Almodovar, E. Pascual, R. Saez and I. Exposito (2003). Crustal structure of the transpressional Variscan orogen of SW Iberia: SW Iberia deep seismic reflection profile (IBERSEIS). *Tectonics* **22, no. 6**: 1062.

Smith, G. P., D. A. Wiens, K. M. Fischer, L. M. Dorman, S. C. Webb and J. A. Hildebrand (2001). A complex pattern of mantle flow in the Lau Backarc. *Science* **292**: 713–716.

Spakman, W., S. Vanderlee and R. Vanderhilst (1993). Travel-Time Tomography of the European Mediterranean Mantle Down to 1400 Km. 7th Conf of the European Union of Geosciences :

Structure and Evolution of the European Lithosphere and Upper Mantle, Strasbourg, France, Elsevier Science Bv.

Spakman, W. and M. J. R. Wortel (2004). A tomographic view on western Mediterranean geodynamics, en The TRANSMED Atlas - The Mediterranean region from crust to mantle, edit by W. Cavazza, F. Roure, W. Spakman, G. M. Stampfli y P. Ziegler. *Springer, Berlin Heidelberg*.: 31-52.

Stapel (1999). The nature of isostasy in West Iberia and its bearing on Mesozoic and Cenozoic regional tectonics. *Ph.D. thesis*: 148 pp., Vrije Univ., Amsterdam,.

Stein, S. and M. Wysession (2003). An Introduction to Seismology, Earthquakes, and Earth Structure. *Blackwell Publishing.*

Stich, D., F. Mancilla and J. Morales (2005). Crust-mantle coupling in the Gulf of Cadiz (SW-Iberia). *Geophys. Res. Lett.* **2**(L13306, doi:10.1029/2005GL023098.).

Stich, D., E. Serpelloni, F. Mancilla and J. Morales (2006). Kinematics of the Iberia-Maghreb plate contact from seismic moment tensors and GPS observations. *Tectonophysics* **426**: 295-317.

Suriñach, E. and R. Vegas (1988). Lateral inhomogeneities of the Hercynian crust in central Spain. *Phys. Earth Planet. Inter.* **51** 226–234.

Teanby, N.A., Kendall, J.M., v. d. Baan and M. (2004). Automation of shear-wave splitting measurements using cluster analysis. *Bulletin of the Seismological Society of America* **94**(2): 453-463.

Tommasi, A. (1998). Forward modeling of the development of seismic anisotropy in the upper mantle. *Earth and Planetary Science Letters* **160**: 1-13.

Turner, S. P., J. P. Platt, R. M. M. George, S. P. Kelley, D. G. Pearson and G. M. Nowell (1999). Magmatism associated with orogenic collapse of the Betic-Alboran Domain. SE Spain. *J. Petrol.* **40**: 1011-1036.

Utheim, T. and J.Havskov (2001). Seislog data acquisition systems. . *Seismological Research Letters.* **72**: 77-79

Vinnik, L., Chevrot, S., Montagner and J.P. (1997). Evidence for a stagnant plume in the transition zone? *Geophysical Research Letters* **24**: 1007-1010.

Vinnik, L.P., Kind, R., Kosarev, G.L., Makeyeva and L.I. (1989). Azimuthal anisotropy in the lithosphere from observations of long-period S-waves. *Geophysical Journal International* **99**: 549-559.

Vinnik, L.P., Makeyeva, L.I., Milev, A., Usenko and A.Y. (1992). Global patterns of azimuthal anisotropy and deformations in the continental mantle. *Geophysical Journal International* **111**: 433-437.

Walker, K.T., Bokelmann, G.H.R., Klemperer and S.L. (2004). Shear-wave splitting beneath the Snake river plain suggests a mantle upwelling beneath eastern Nevada, USA. *Earth and Planetary Science Letters* **222**: 529-542.

Wenk, H.-R., Bennett, K., Canova, G.R., Molinari and A. (1991). Modeling plastic deformation of peridotite with the self-consistent theory. . *J.Geophys. Res.* **96 (B5)**: 8337–8349.

Whitmarsh, R. B. and P. R. Miles (1995). Models of the development of the West Iberia rifted continental margin at 40˚30'N deduced from surface and deep-tow magnetic anomalies. . *J. Geophys. Res.* **100**: 3789-3806.

Whitmarsh, R. B., L. M. Pinheiro, P. R. Miles, M. Recq and J.-C. Sibuet (1993). Thin crust at the western Iberian ocean-continent transition and ophiolites. *Tectonics* **12**: 1230-1239.

Wiens, D. A. and G. P. Smith (2003). Seismological constraints on structure and flow patterns within the mantle wedge. *In: Eiler, J.M. (Ed.), Inside the Subduction Factory. Am. Geophys. Union, Geophys. Monogr. Ser.* **138**.

Wookey, J., Kendall and J.M. (2004). Evidence of midmantle anisotropy from shear wave splitting and the influence of shear-coupled P waves. *Journal of Geophysical Research* **109**(B07309): doi:10.1029/2003JB002871.

Wookey, J., J. M. Kendall and G. Barruol (2002). Mid-mantle deformation inferred from seismic anisotropy. *Nature* **415**(6873): 777-780.

Wortel, M. J. R. and W. Spakman (2000). Subduction and slab detachment in the Mediterranean-Carpathian region. *Science* **290**: 1910-1917.

Wüstefeld, A., Bokelmann, G.H.R., Zaroli, C., Barruol, G. and (2008). SplitLab: A shear-wave splitting environment in Matlab. *Computer & Geosciences.*: doi:10.1016/j.cageo.2007.1008.1002.

Wüstefeld, A. (2007). Methods and applications of shear wave splitting: The East European Craton. *Ph.D. Thesis, 240 pp., Universite Montpellier II. Sciences et Techiques du Languedoc*.

Wysession, M. E., A. Langenhorst, M. J. Fouch, K. M. Fischer, G. I. Al-Eqabi, P. J. Shore and T. J. Clarke (1999). Lateral variations in compressional/shear velocities at the base of the mantle. *Science* **284**(5411): 120-125.

Yang, X., Fischer, K.M., Abers and G.A. (1995). Seismic anisotropy beneath the Shumagin Islands segment of the Aleutian-Alaska subduction zone. *Journal of Geophysical Research* **100**: 18165-18177.

Young, C. J. and T. Lay (1990). Multiple phase analysis of the shear velocity structure in the D'' region beneath Alaska. *J. Geophys. Res.* **95**: 17 385-17 402.

Zeck, H. P. (1996). Betic-Rif orogeny:subduction of Mesozoic Tethys lithosphere under eastward drifting Iberia, slab detachment shortly before 22 Ma, and subsequent uplift and extensional tectonics. . *Tectonophysics* **254**: 1-16.

Zeck, H. P., K. A.B. and I. S. Williams (1998). Post-collisional volcanism in a sinking slab setting-crustal anatectic origin of pyroxene-andesite magma, Caldear Volcanic Group, Neogene Alborán volcanic Province, southeastern Spain. . *Lithos* **45**: 499-522.

GLOSSARY

Alpine orogeny: Mountain-building event that affected a broad segment of southern Europe and the Mediterranean region during the middle Tertiary period. It produced intense metamorphism, crumpling of rock strata, and uplift accompanied by faulting. It was responsible for the elevation of the present Alps, from which the name derives, the uplifting of plateaus in the Balkan Peninsula and in Corsica and Sardinia, and volcanic activity in England, France, Iceland, and parts of Italy.

Anisotropy: a medium is anisotropic if its physical properties depend on the direction. Predictable variation of a property of a material with the direction in which it is measured, which can occur at all scales. For a crystal of a mineral, variation in physical properties observed in different directions is anisotropy. In rocks, variation in seismic velocity measured parallel or perpendicular to bedding surfaces is a form of anisotropy.

Azimuthal anisotropy: The variation of speed for a given wave type as a function of the azimuth of the propagation direction.

Back azimuth: the angle measured between north and the direction to the source.

Heterogeneity: a medium is heterogeneous if its physical properties depend on the space coordinates. A critical point is the scale of heterogeneities as compared with seismic wavelengths. For a large wavelength, an intrinsically isotropic medium with oriented heterogeneities may become equivalent to an overall anisotropic medium.

LPO: Lattice preferred orientation is the alignment of intrinsically anisotropic crystal due to deformation.

Orthorhombic symmetry: there are 9 independent elastic parameters for an orthorhombic material.

Pn, Sn: refracted waves below the crust, se propagan justo por debajo de la discontinuidad de Mohorovicic.

ScS: reflected waves in the core.

Shear wave splitting: behaviour of S wave in an anisotropic medium which are split into two shear waves with mutually perpendicular polarization directions.

SPO: shape preferred orientation is the primary mechanism for crustak anisotropy and can result from fluid-filled cracks due to responses to stress.

SKS, PKS, SKKS: refracted waves in external core.

Transverse isotropy: anisotropy with hexagonal symmetrywhere summetry axis is vertical.

Variscan orogeny: is a geologic mountain-building event caused by Late Paleozoic continental collision between Laurasia and Gondwana to form the supercontinent of Pangea.

APPENDIX I: Backazimuthal plot of splitting parameters

We present in the Figures fromt A-1 to A-19 the backazimutal variations plot obteined for each station with the three methodologies utilized (Rotation-correlation, Minimum Energy and Eigenvalue). In the top and center row are shown for each technique the backazimuthal variation of fast orientation (ϕ) estimate and delay time (δt) estimates. In the bottom row displays a stereoplot of good and fair quality non-Nulls. Markers are plotted at their according backazimuth and incident angle (grid lines each 5°). Marker lengths are according to delay time.

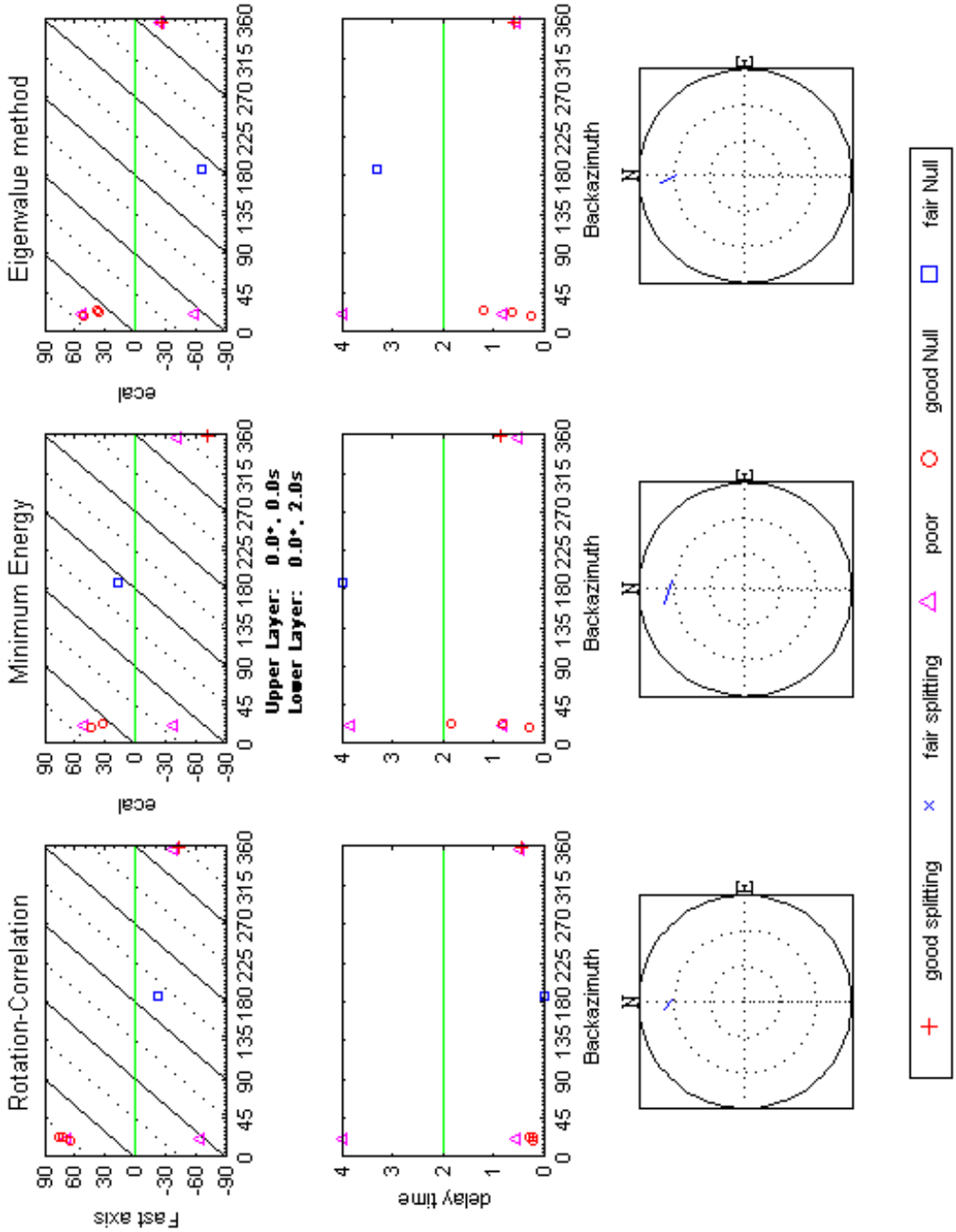

Figure A-1 – Backazimuthal distribution and stereoplot for ECAL station.
Figura A-1 –Distribución por backazimut y estereoplot para la estación de ECAL

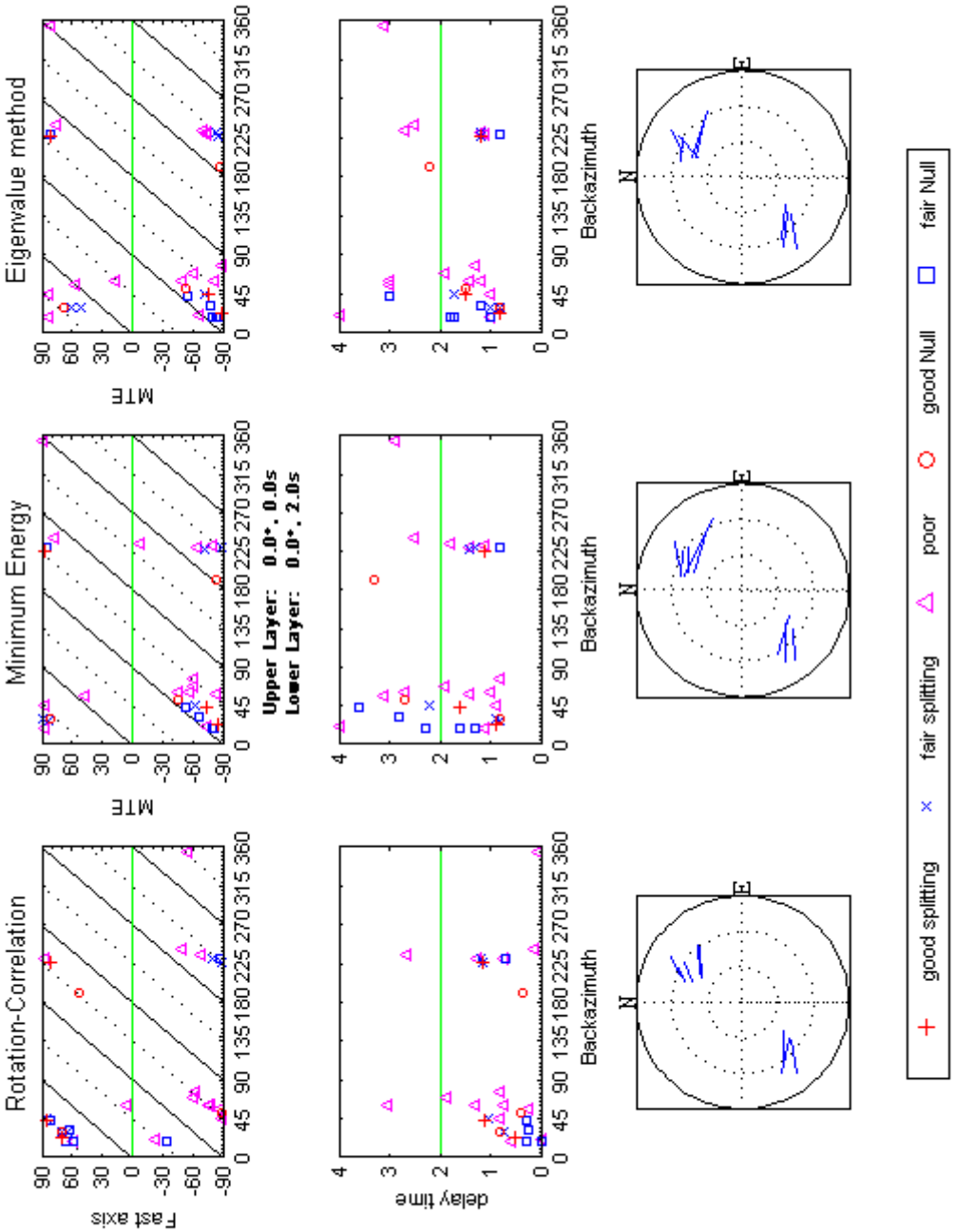

Figure A2 – Backazimuthal distribution and stereoplot for MTE station.
Figura A2 –Distribución por backazimut y estereoplot para la estación de MTE

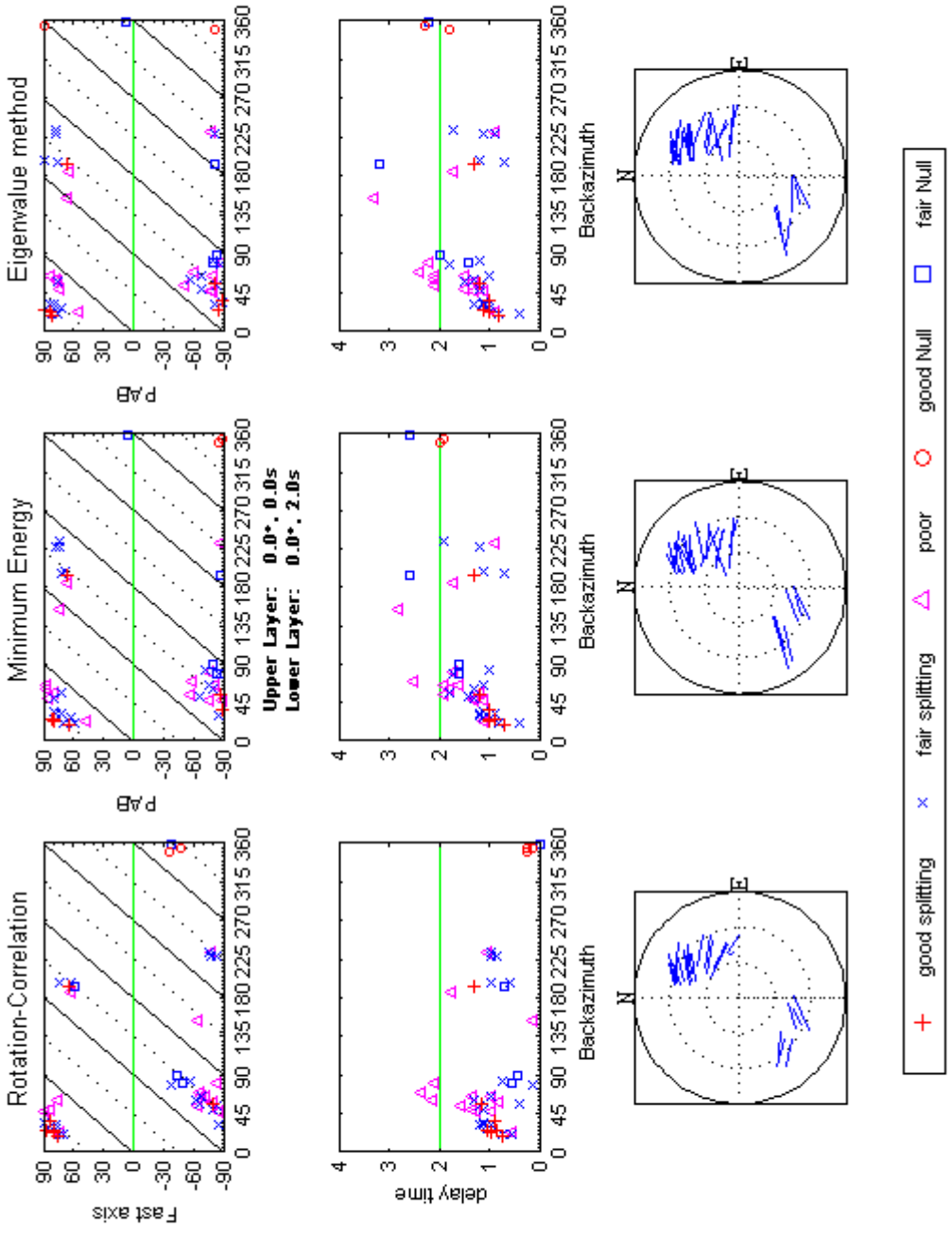

Figure A3 – Backazimuthal distribution and stereoplot for PAB station.
Figura A3 – Distribución por backazimut y estereoplot para la estación de PAB

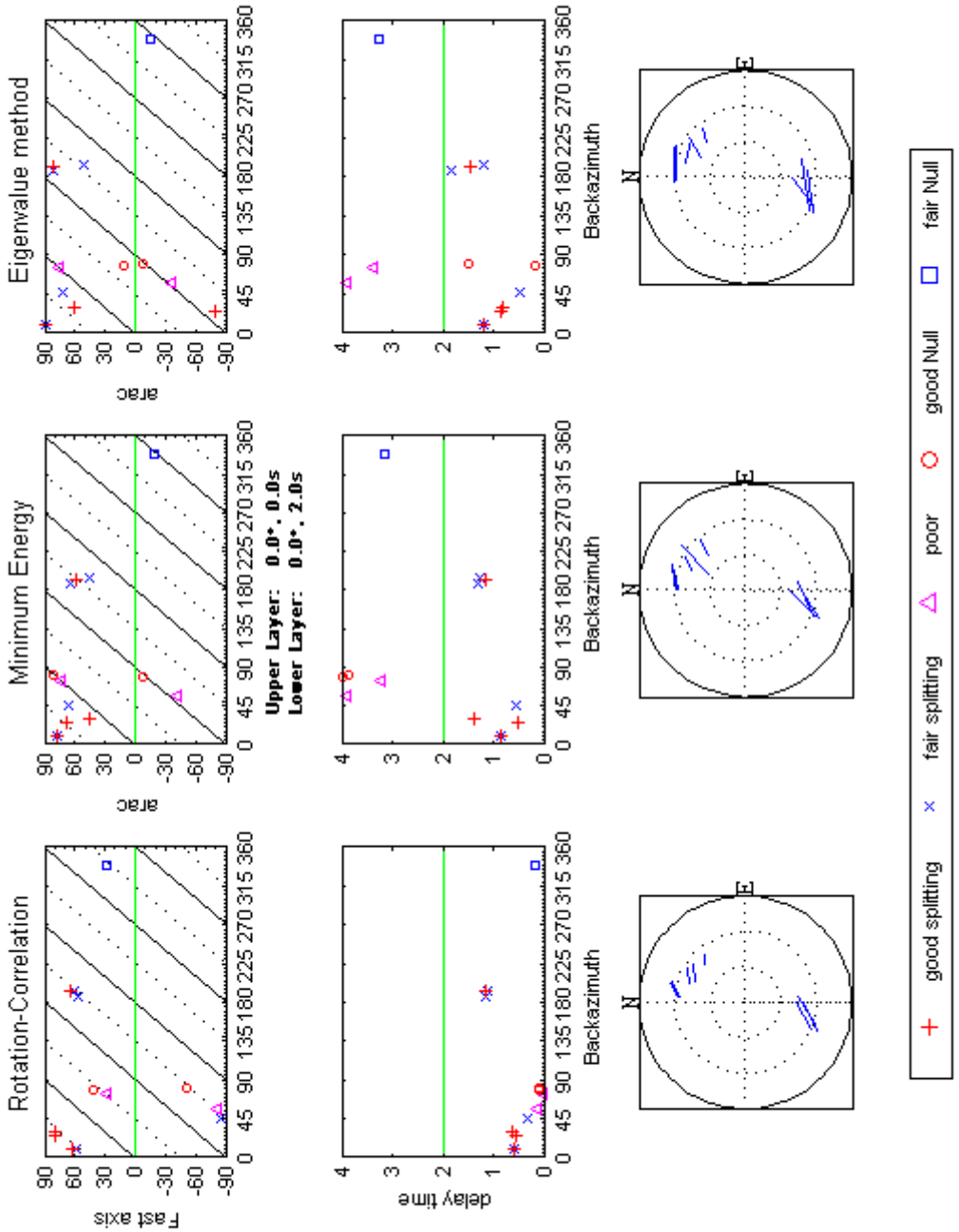

Figure A-4 – Backazimuthal distribution and stereoplot for ARAC station
Figura A-4 – Distribución por backazimut y estereoplot para la estación de ARAC

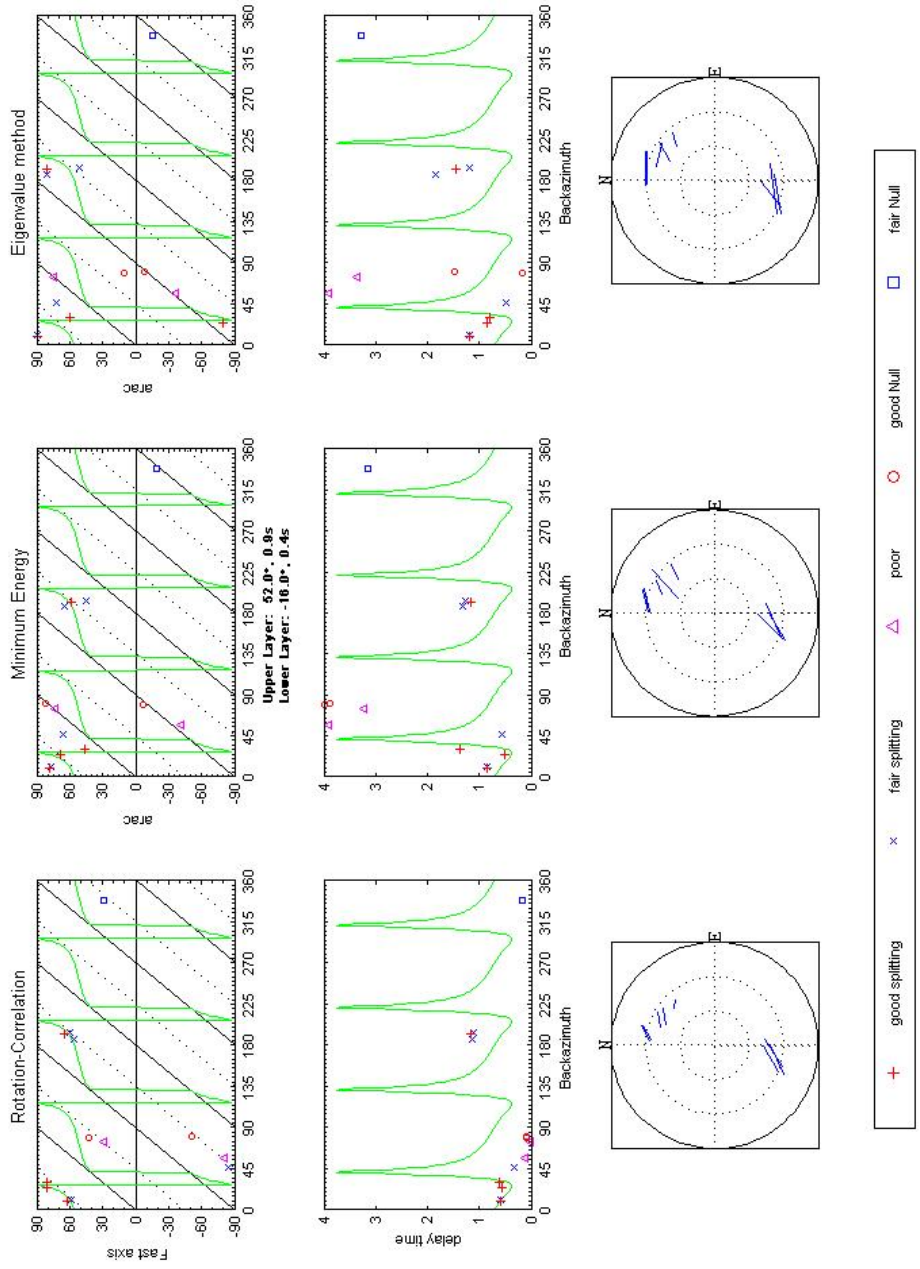

Figure A-4a – Backazimuthal distribution and stereoplot for ARAC station, and the best fit model for the two layer case situation.
Figura A-4a – Distribución por backazimut y estereoplot para la estación de ARAC, y mejor modelo de ajuste en caso de modelo de dos capas anisotropas.

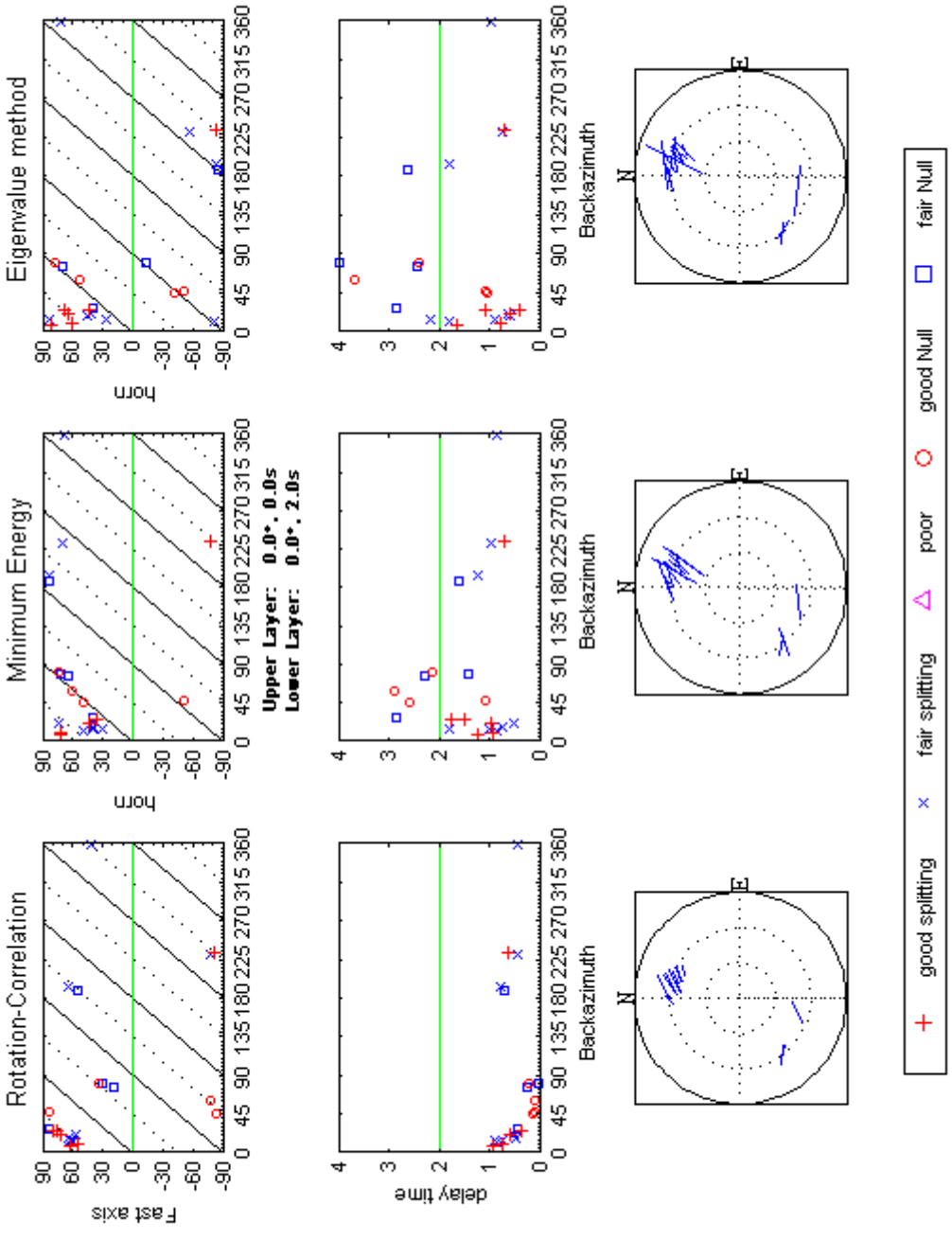

Figure A-5 – Backazimuthal distribution and stereoplot for HORN.
Figura A-5 – Distribución por backazimut y estereoplot para la estación de HORN

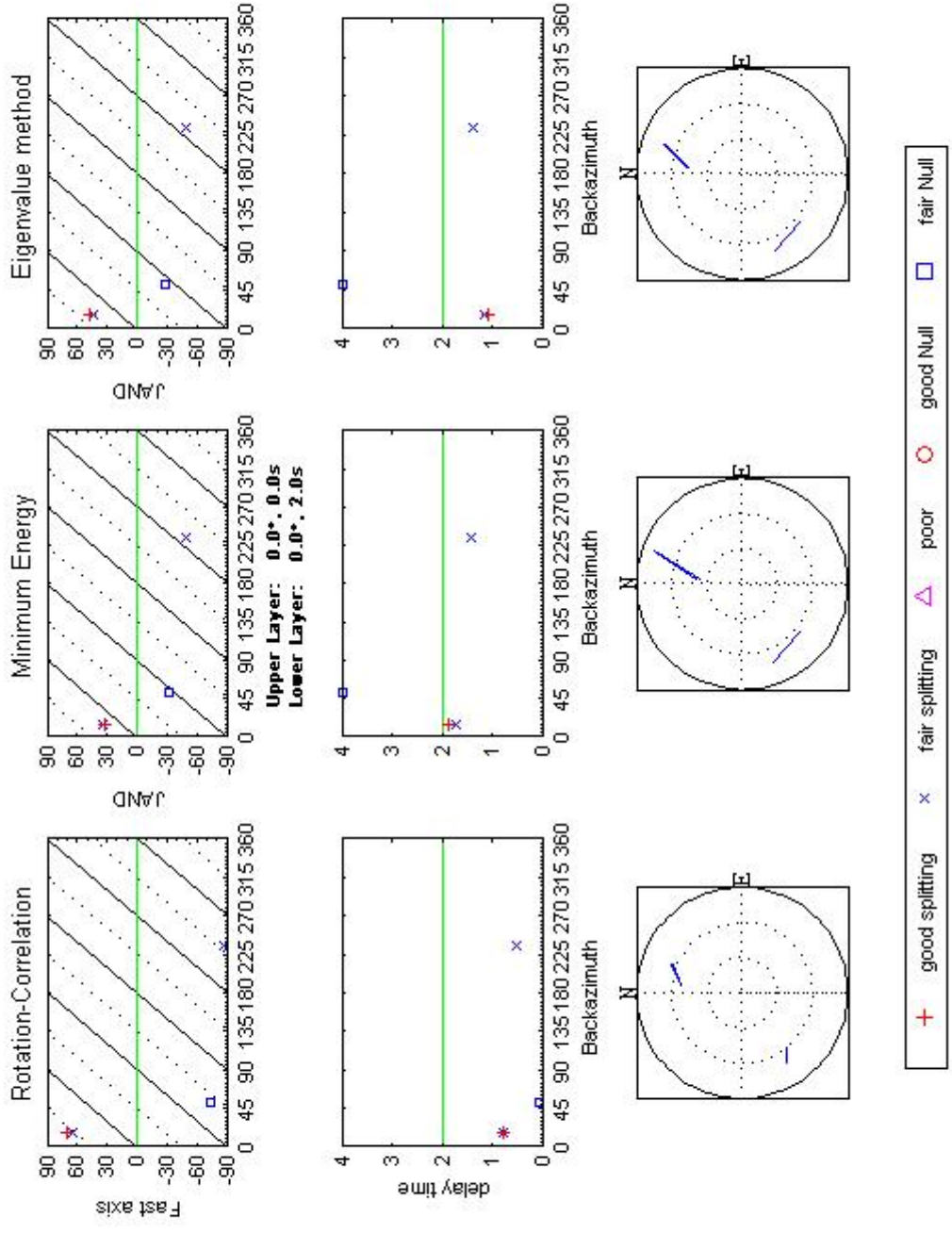

Figure A-6 – Backazimuthal distribution and stereoplot for JAND.
Figura A-6 - Distribución por backazimut y estereoplot para la estación de JAND

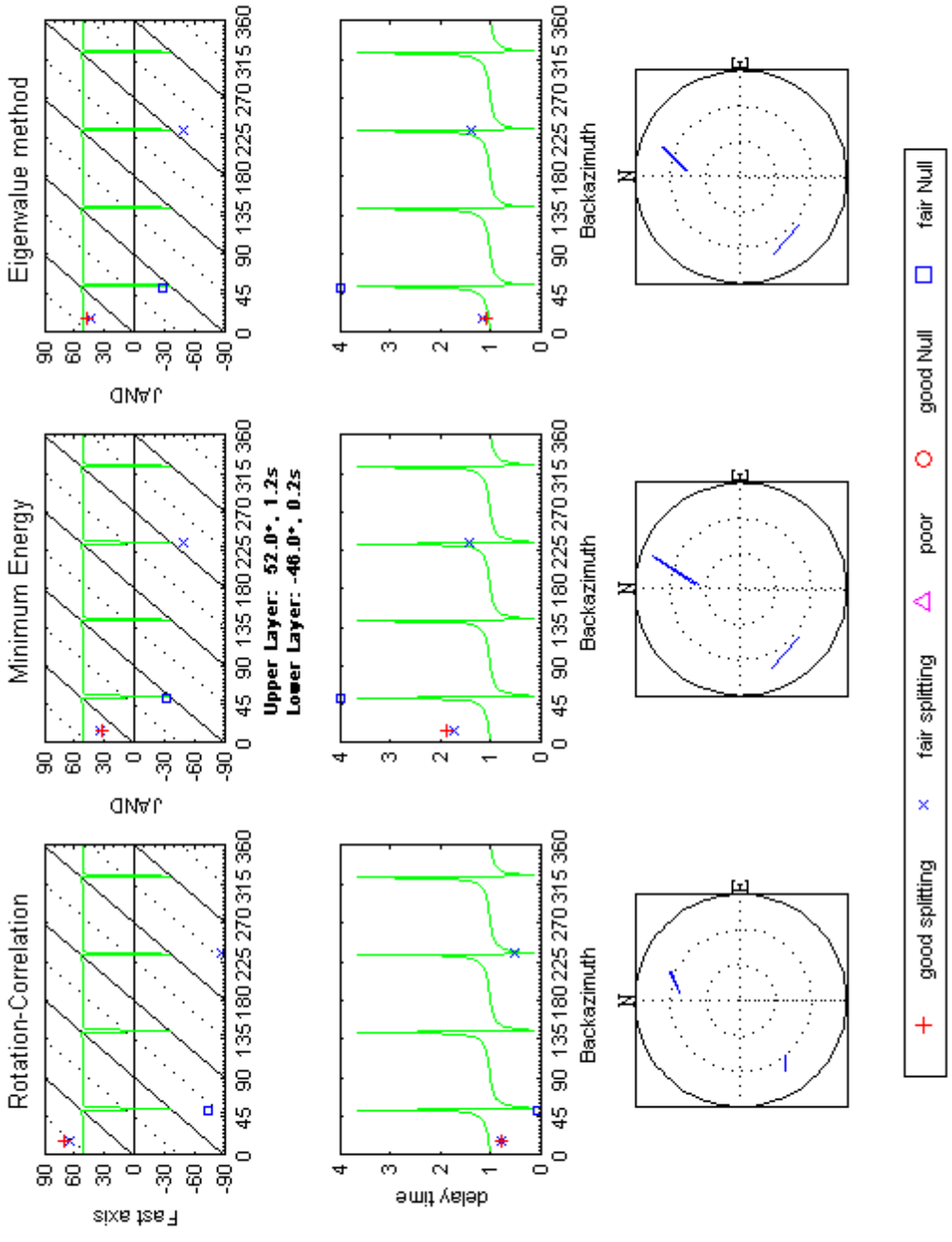

Figure A-6a – Backazimuthal distribution and stereoplot for JAND station, and the best fit model for the two layer case situation.
Figura A-6a – Distribución por backazimut y estereoplot para la estación de JAND y mejor modelo de ajuste en caso de modelo de dos capas anisotropas.

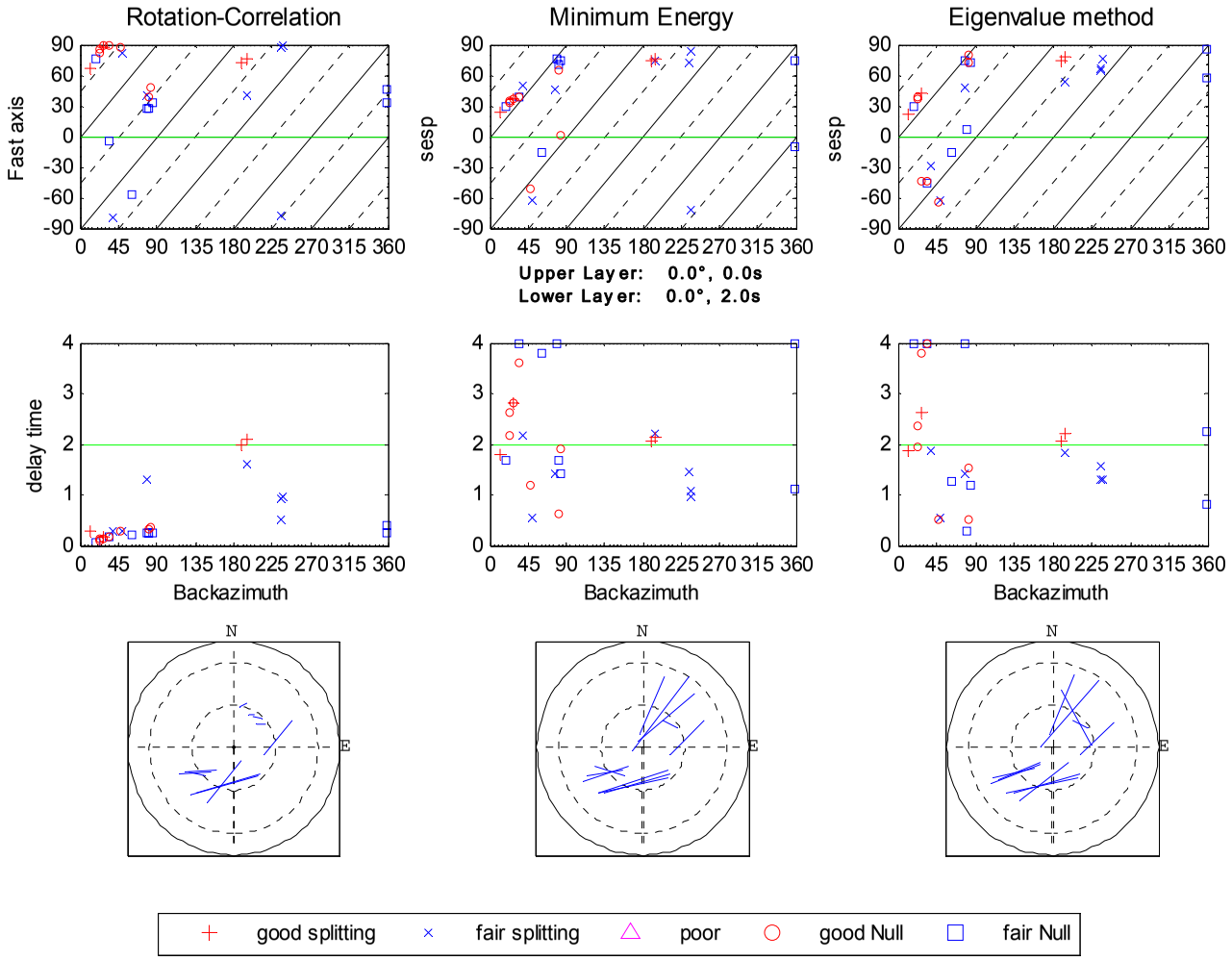

Figure A-7 – Backazimuthal distribution and stereoplot for SESP.
Figura A-7 – Distribución por backazimut y estereoplot para la estación de SESP

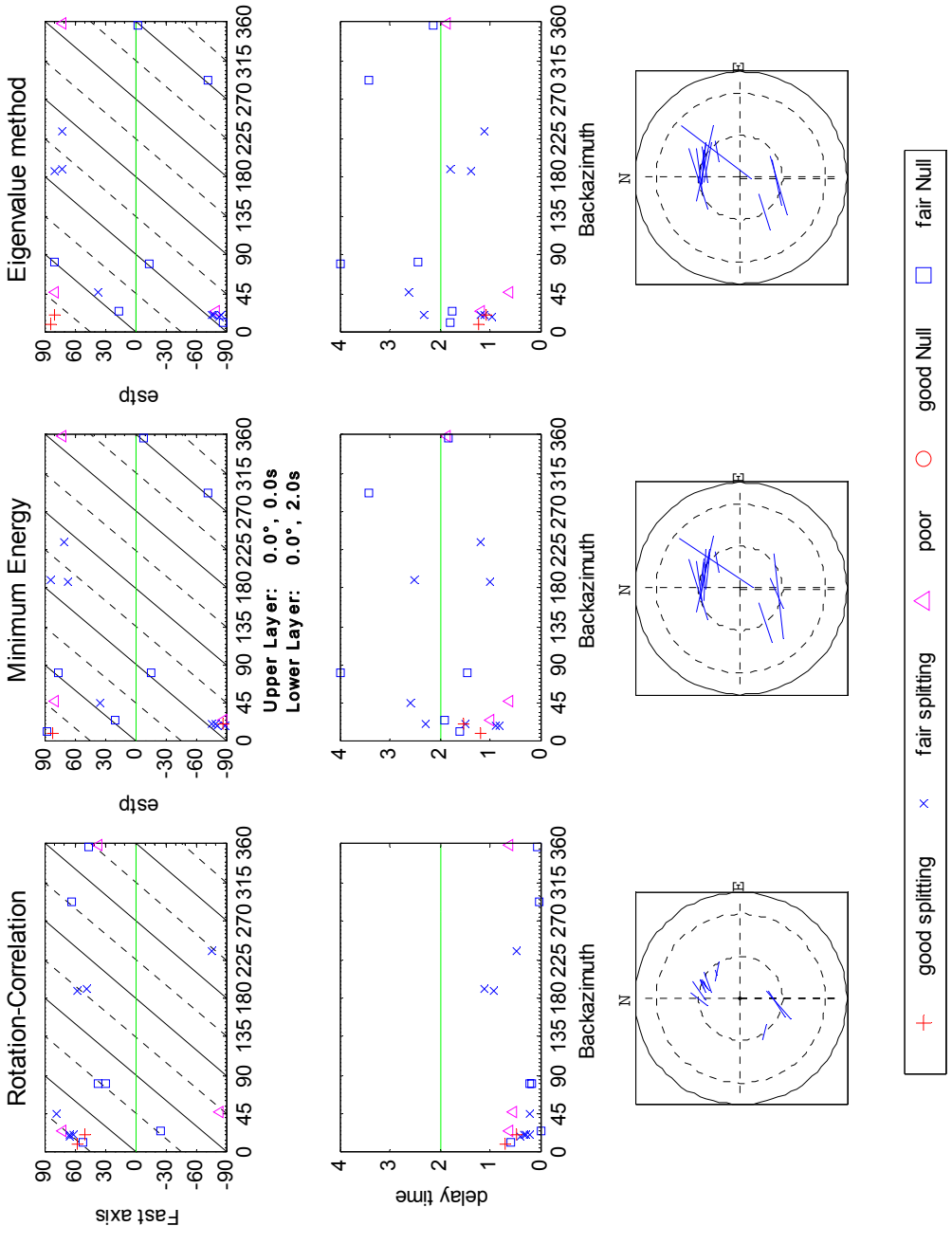

Figure A-8 – Backazimuthal distribution and stereoplot for ESTP.
Figura A-8 – Distribución por backazimut y estereoplot para la estación de ESTP

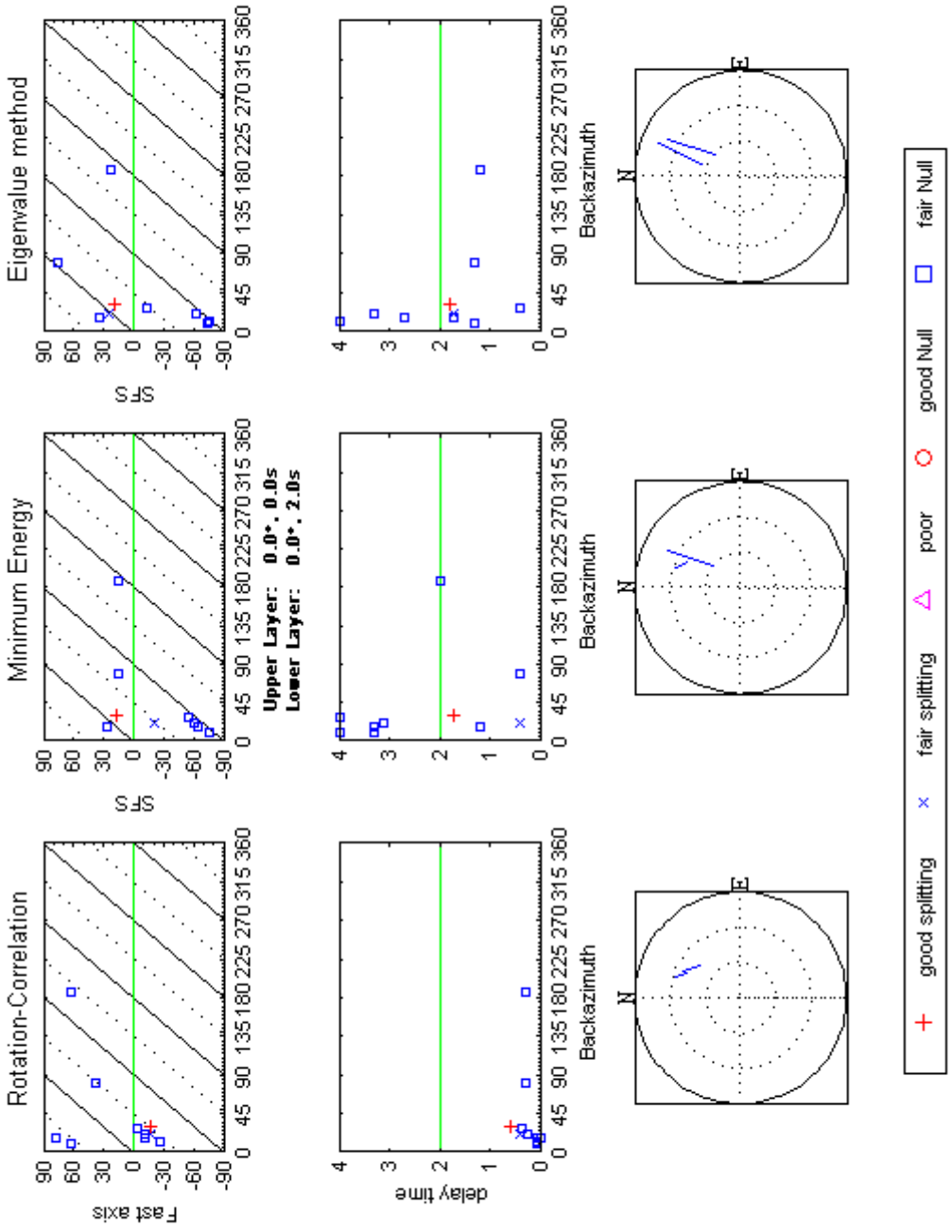

Figure A-9 – Backazimuthal distribution and stereoplot for SFS.
Figura A-9 – Distribución por backazimut y estereoplot para la estación de SFS

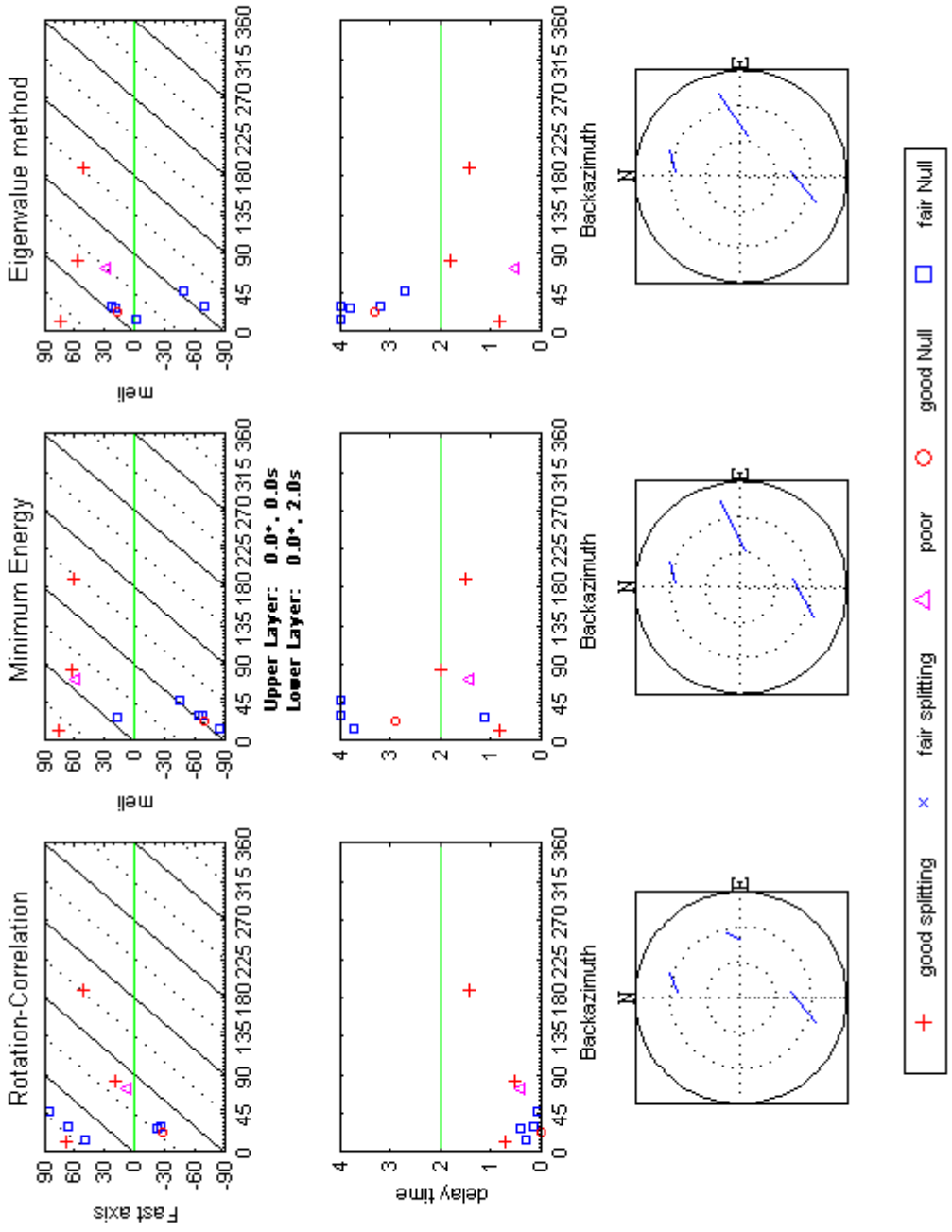

Figure A-10 – Backazimuthal distribution and stereoplot for MELI.
Figura A-10 – Distribución por backazimut y estereoplot para la estación de MELI

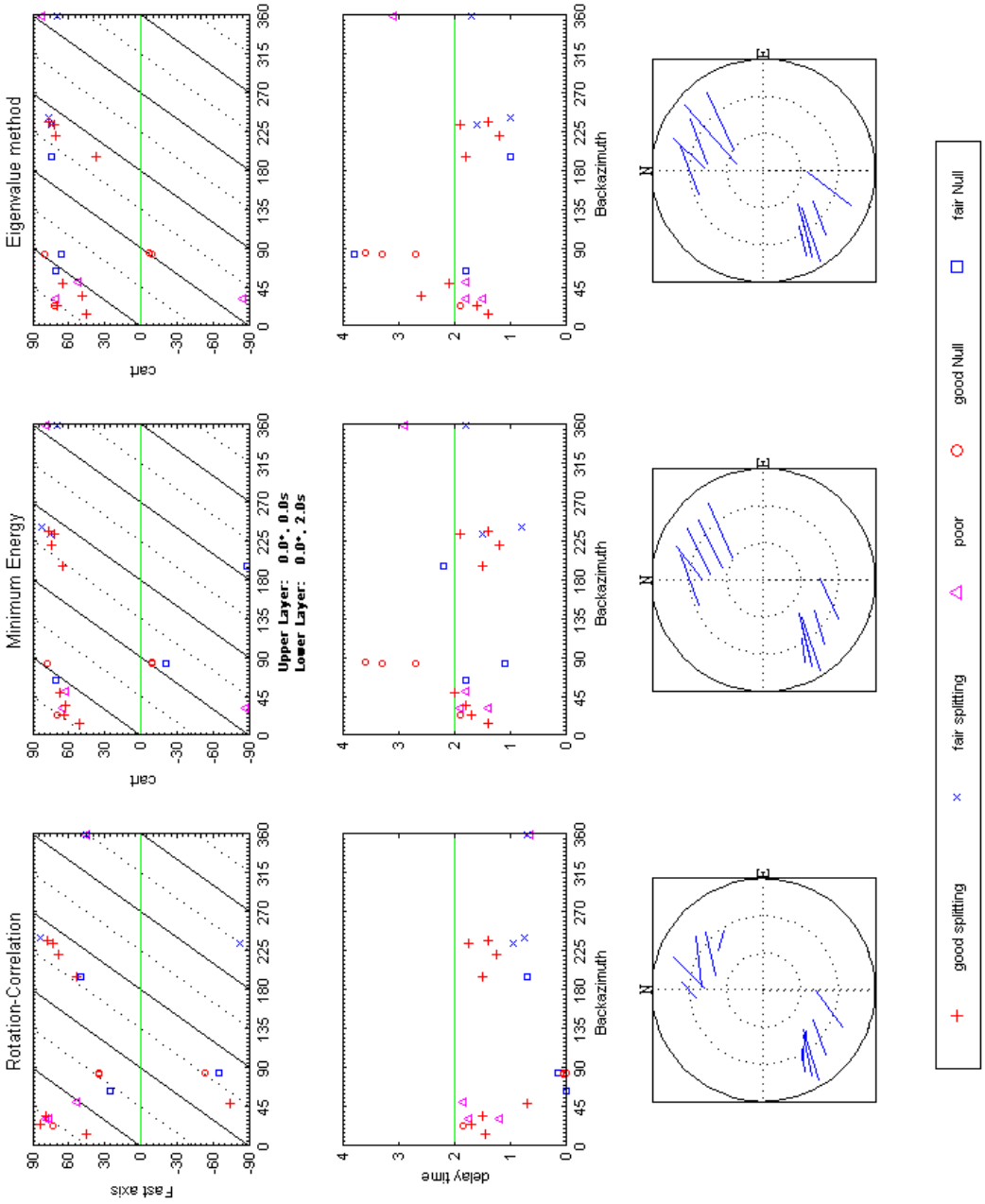

Figure A-11 – Backazimuthal distribution and stereoplot for CART.
Figura A-11 – Distribución por backazimut y estereoplot para la estación de CART

Figure A-12 – Backazimuthal distribution and stereoplot for VELZ.
Figura A-12 –Distribución por backazimut y estereoplot para la estación de VELZ.

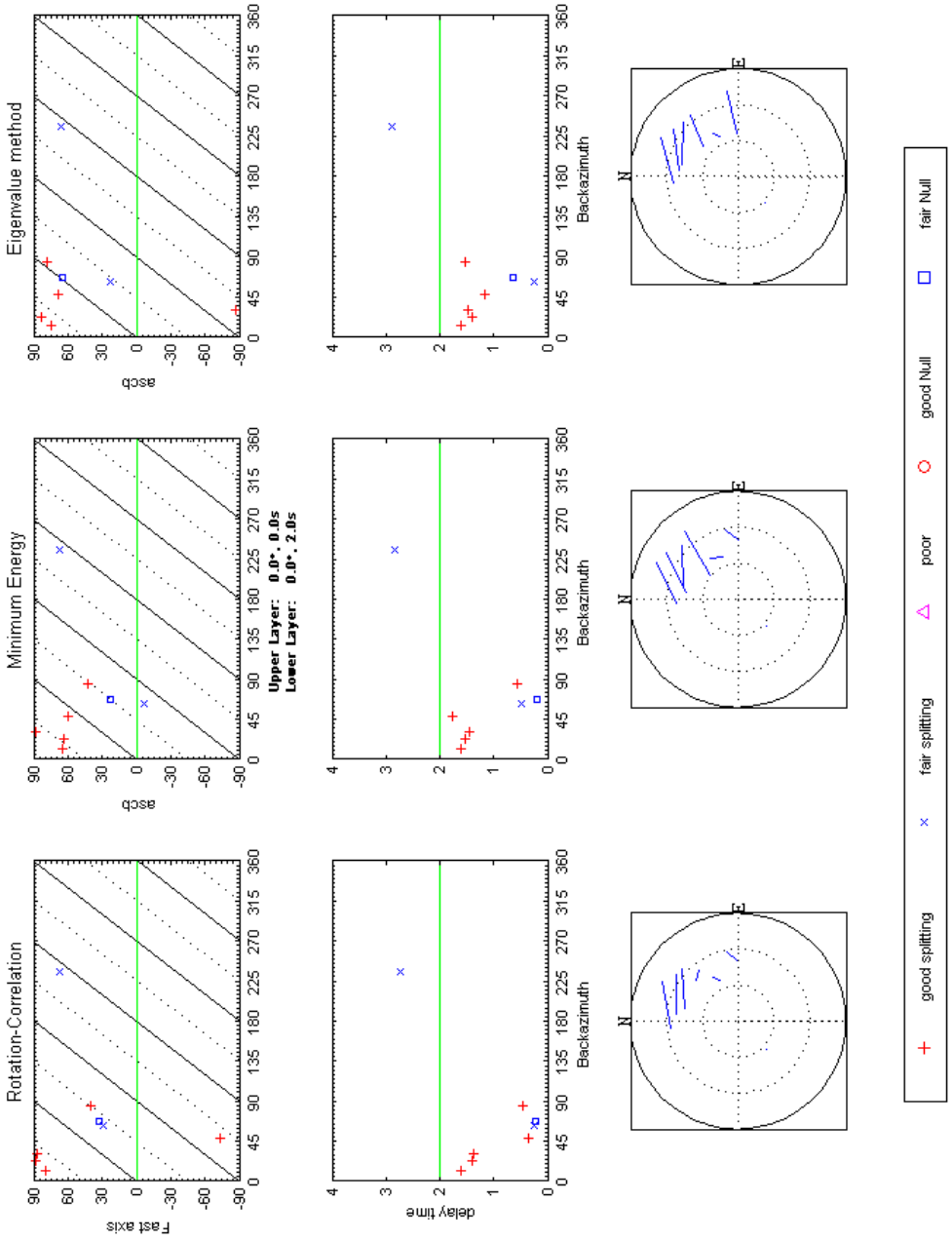

Figure A-13 – Backazimuthal distribution and stereoplot for ASCB.

Figura A-13 – Distribución por backazimut y estereoplot para la estación de ASCB.

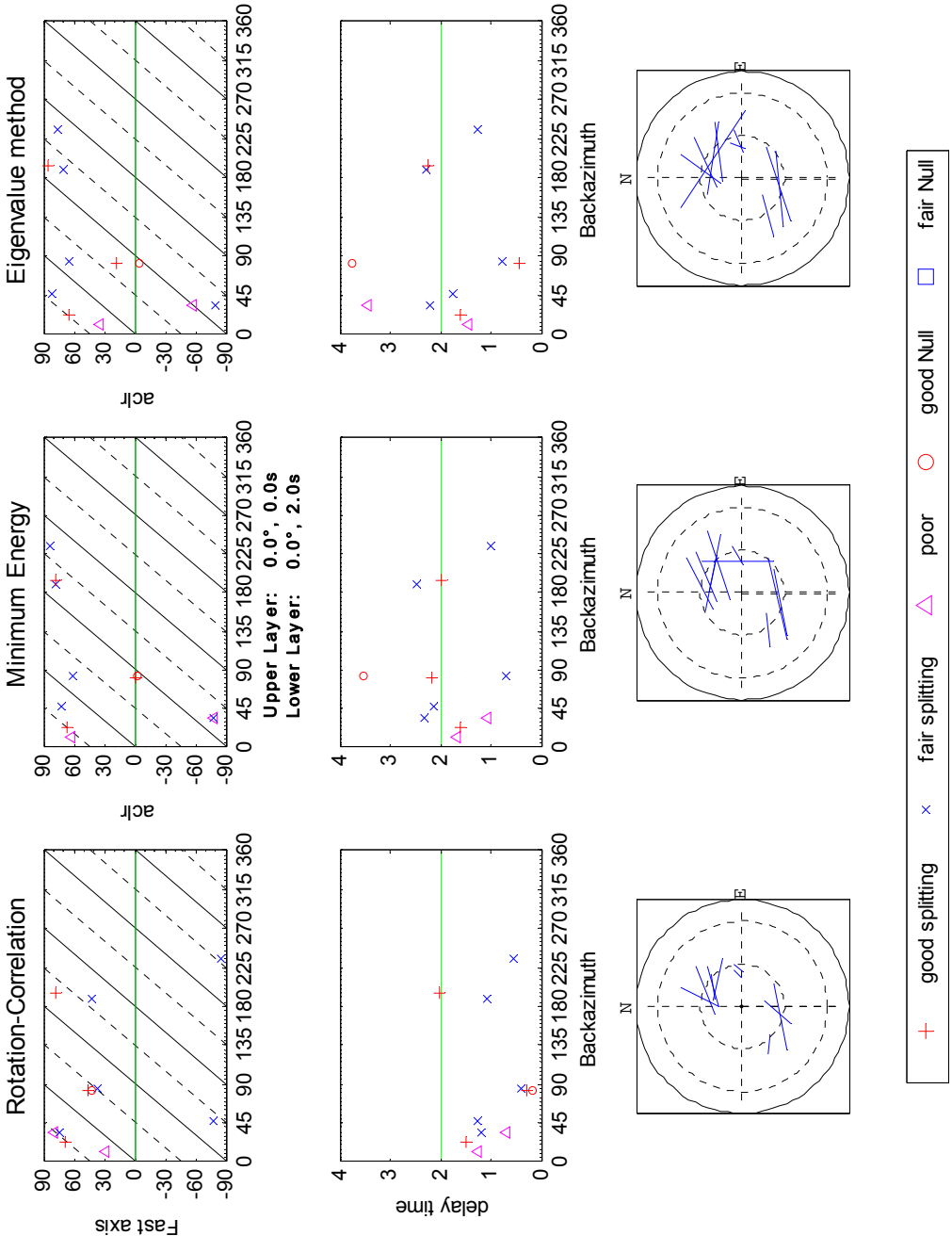

Figure A-14 – Backazimuthal distribution and stereoplot for ACLR.

Figura A-14 – Distribución por backazimut y estereoplot para la estación de ACLR

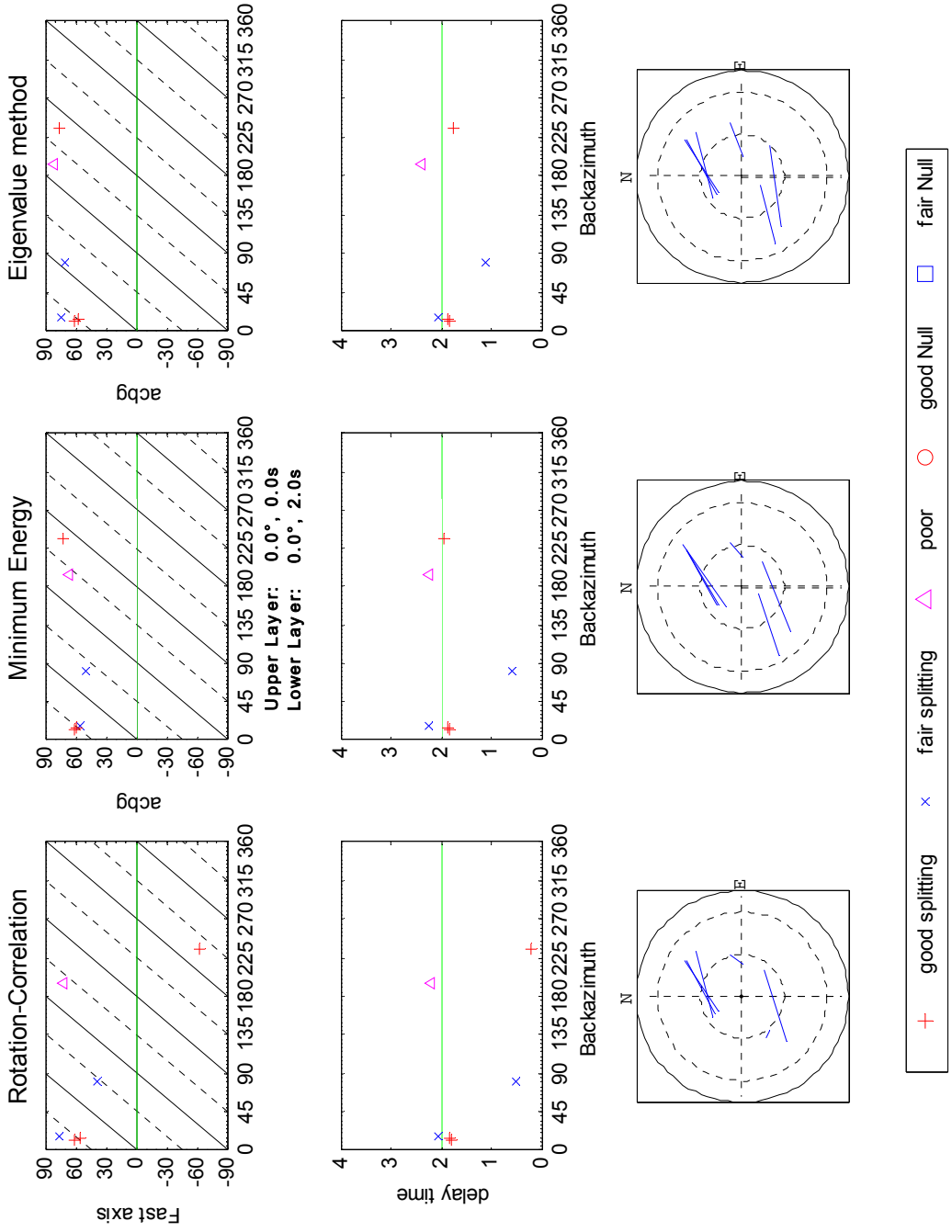

Figure A-15 – Backazimuthal distribution and stereoplot for ACBG.

Figura A-15 – Distribución por backazimut y estereoplot para la estación de ACBG.

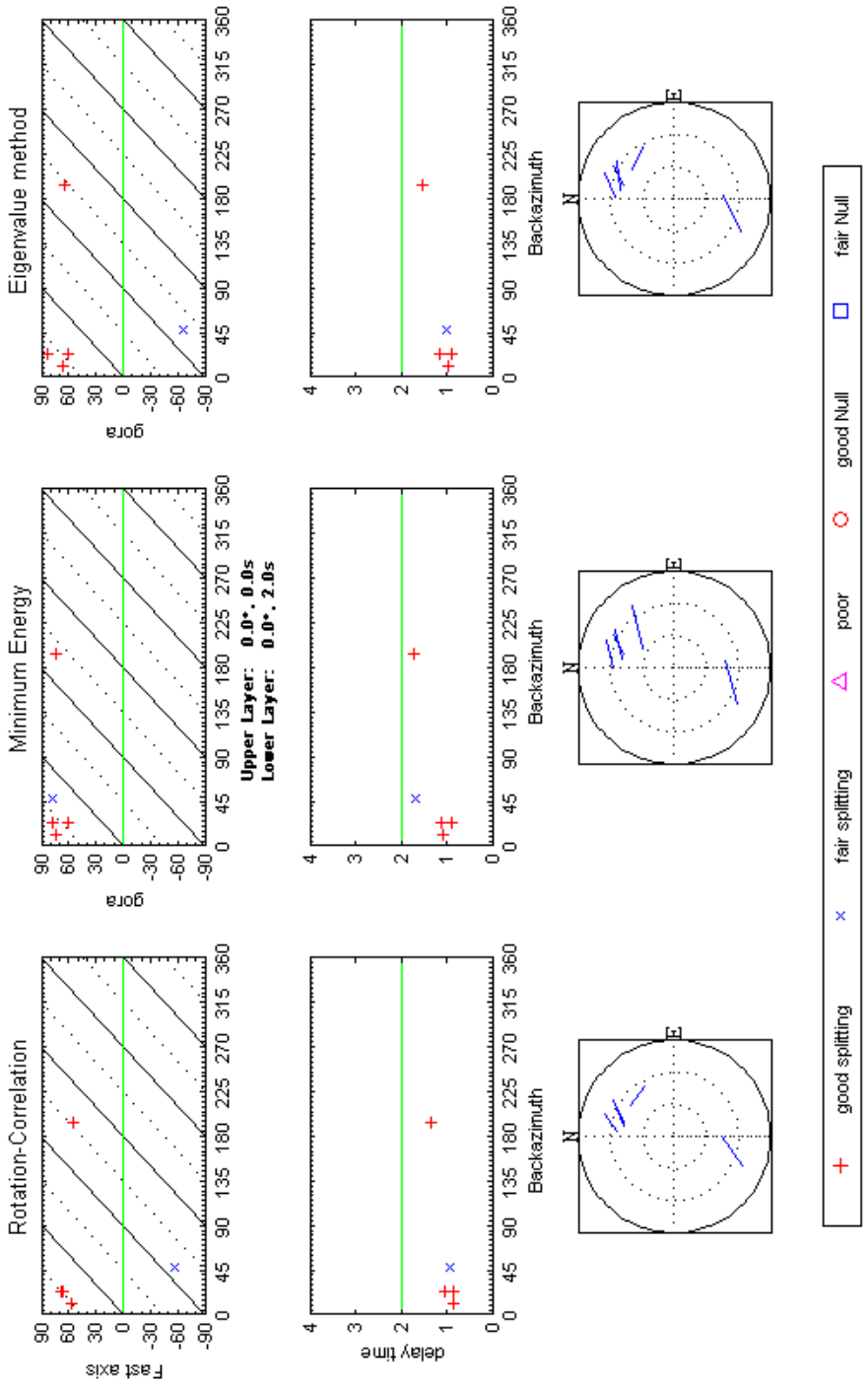

Figure A-16 – Backazimuthal distribution and stereoplot for GORA.

Figura A-16 – Distribución por backazimut y estereoplot para la estación de GORA.

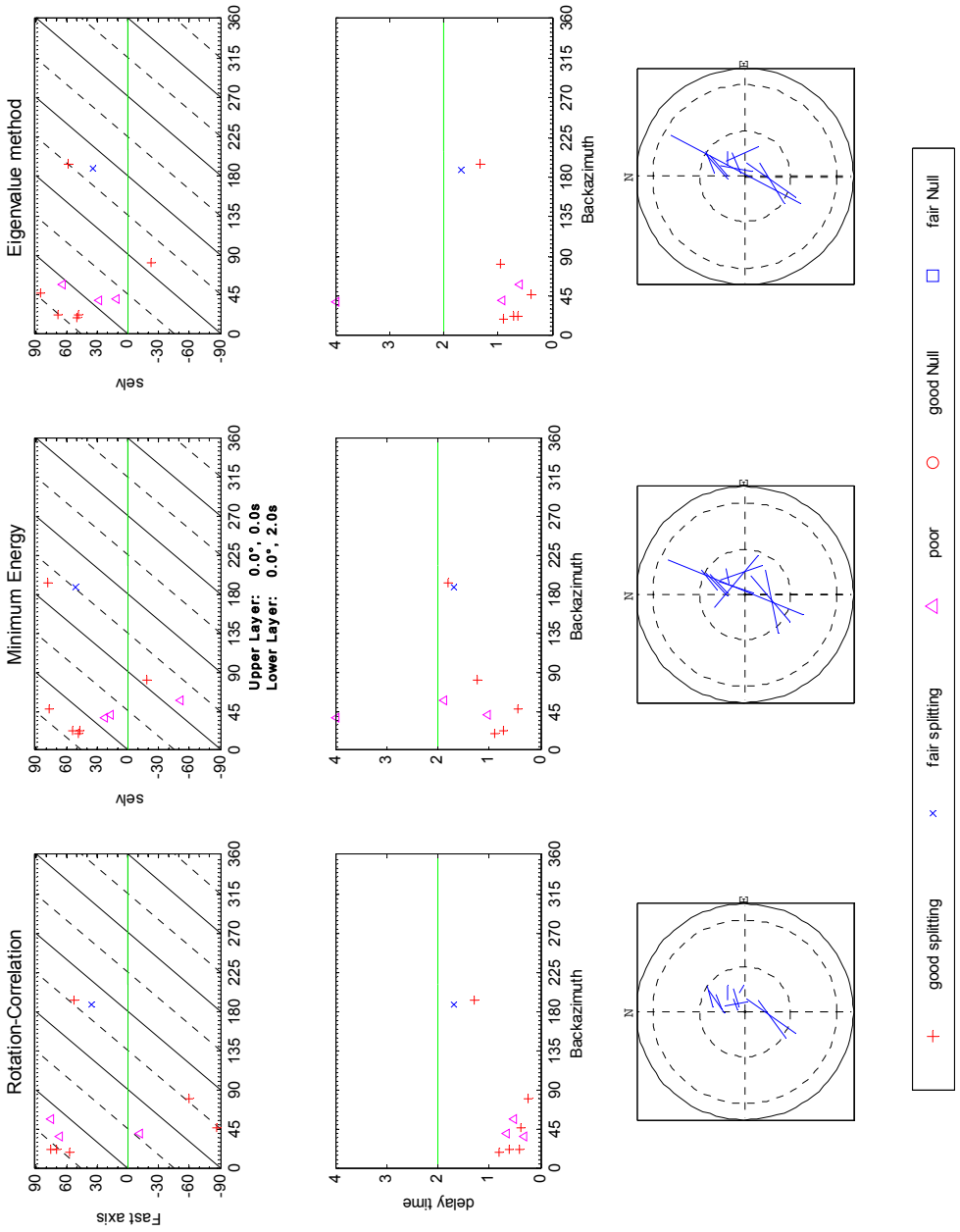

Figure A-17 – Backazimuthal distribution and stereoplot for SELV.
Figura A-17 – Distribución por backazimut y estereoplot para la estación de SELV

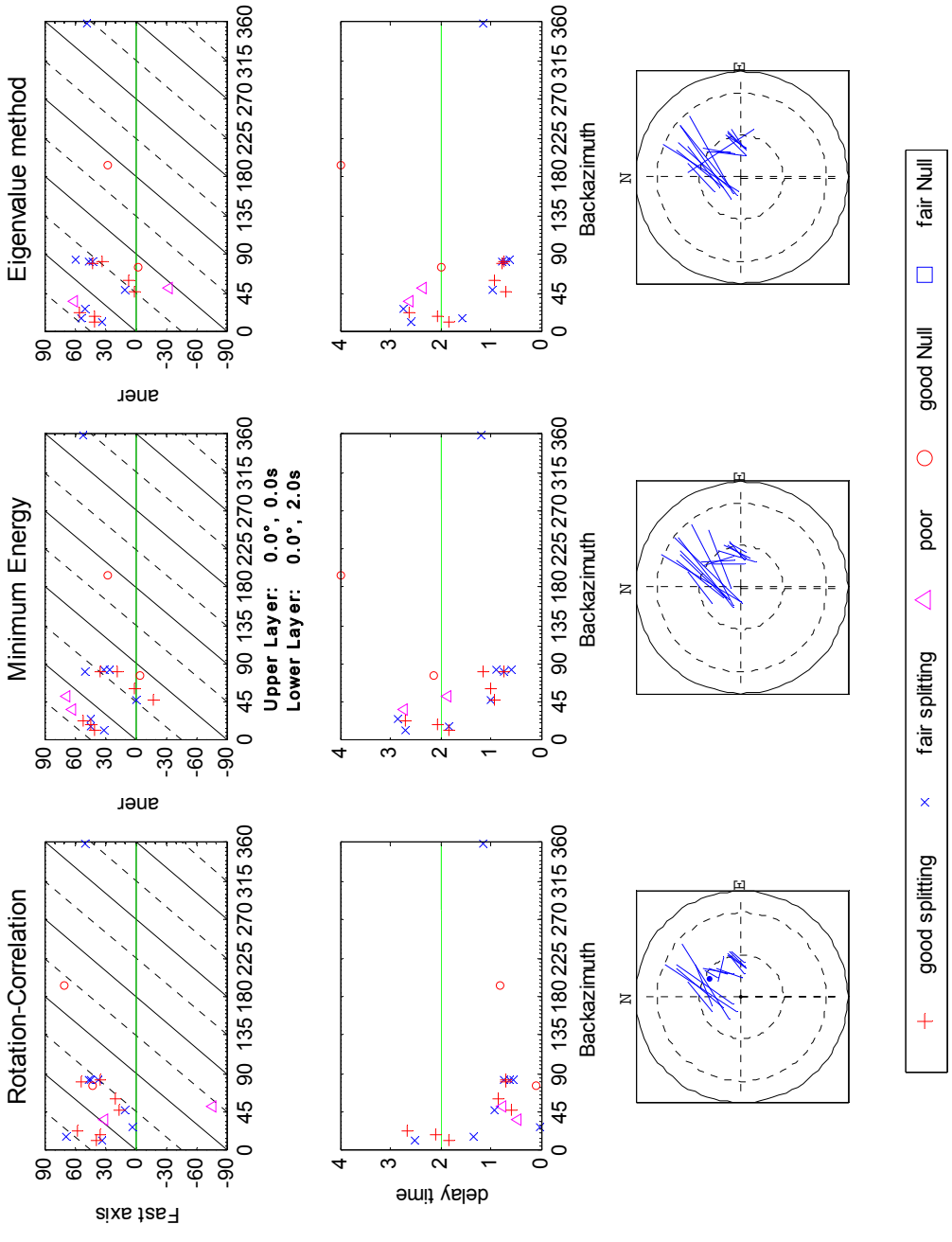

Figure A-18– Backazimuthal distribution and stereoplot for ANER

Figura A-18– Distribución por backazimut y estereoplot para la estación de ANER.

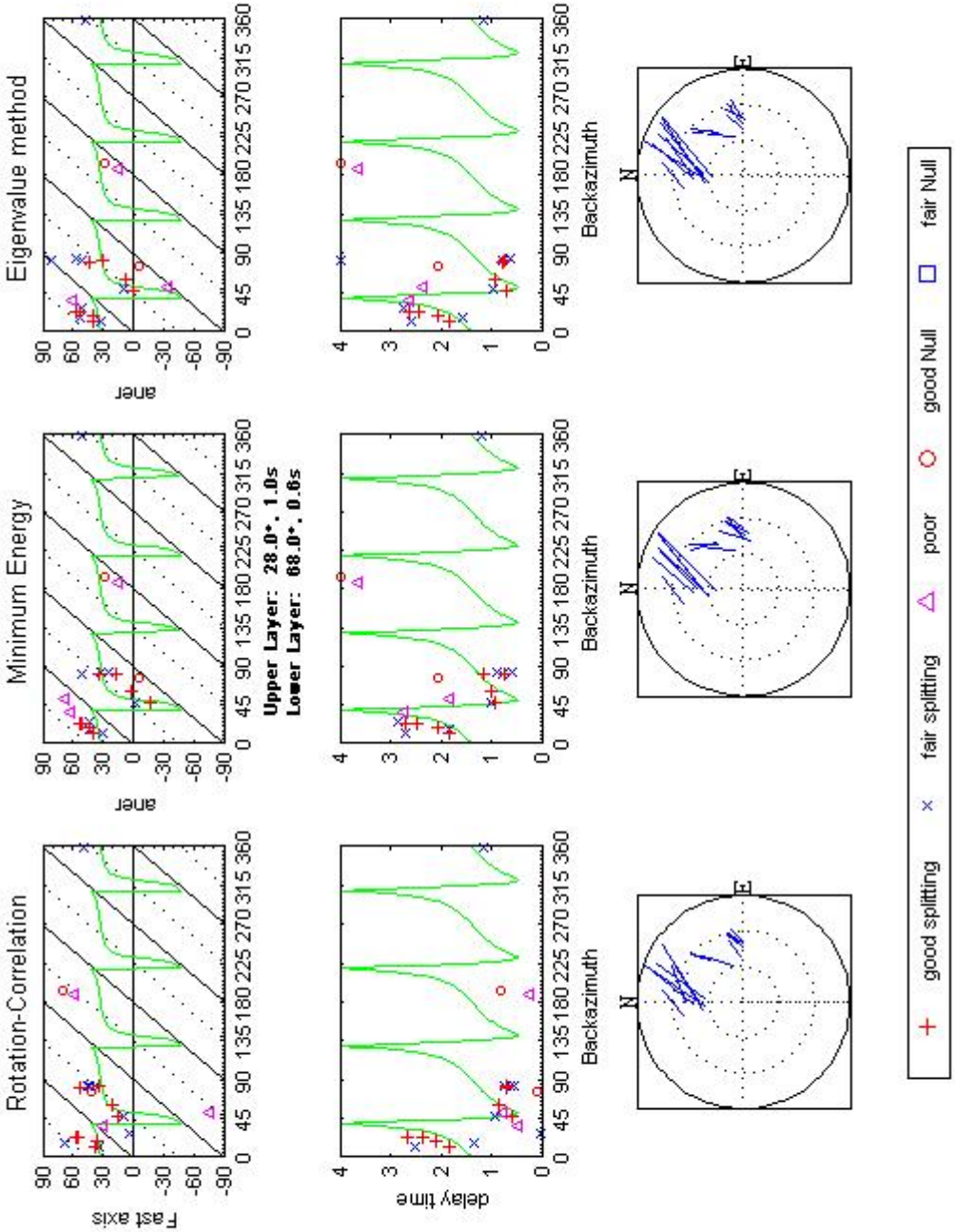

Figure A-18a – Backazimuthal distribution and stereoplot for ANER and the best fit model for the two layer case situation.
Figura A-18a –Distribución por backazimut y estereoplot para la estación de ANER y mejor modelo de ajuste en caso de modelo de dos capas anisotropas.

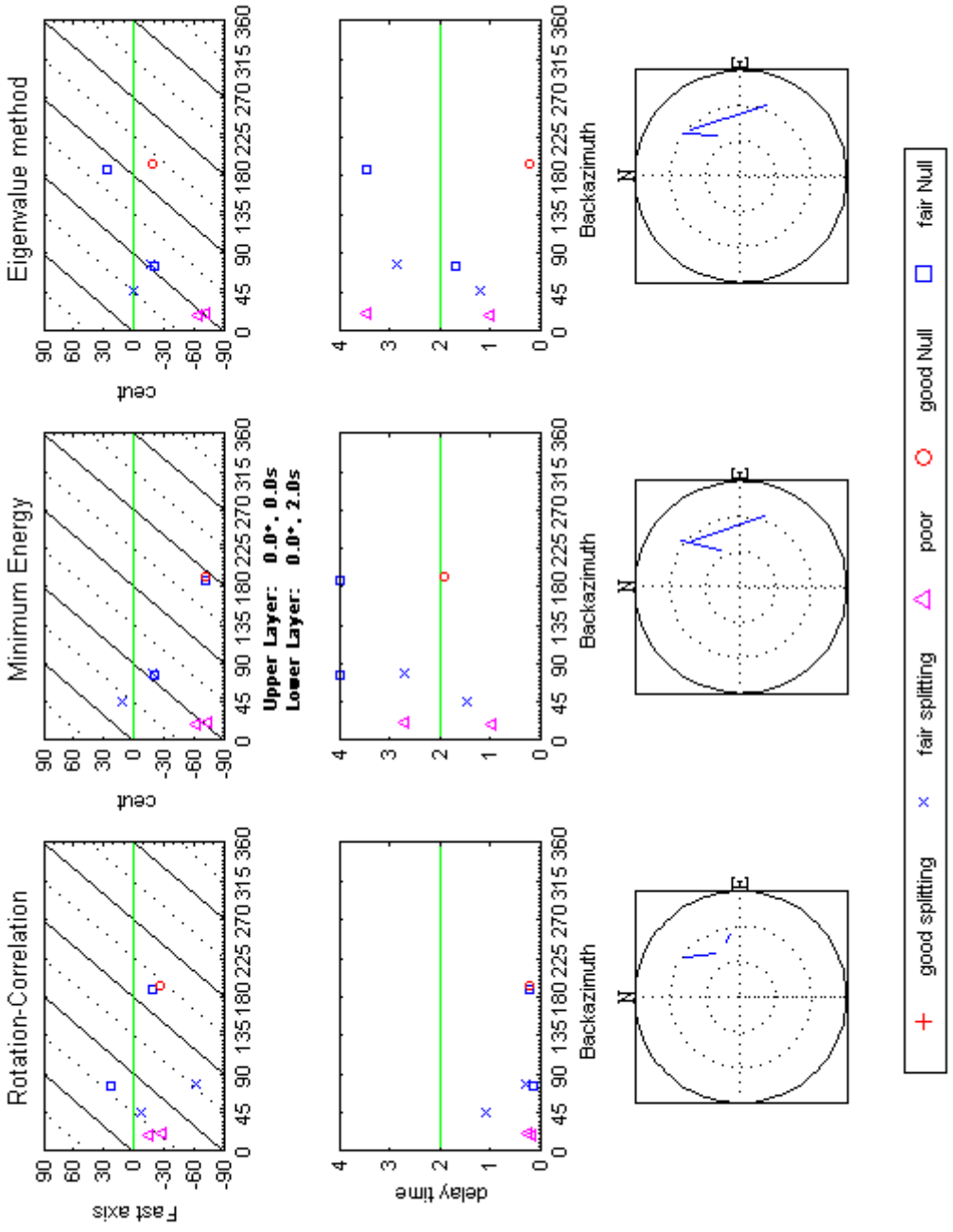

Figure A-19 – Backazimuthal distribution and stereoplot for CEUT.
Figura A-19 – Distribución por backazimut y estereoplot para la estación de CEUT.

APPENDIX II: EPSL publication

Buontempo L., Bokelmann G., Barruol G. and Morales J. Seismic Anisotropy Beneath Southern Iberia From SKS Splitting (2008). Earth and Planetary Science Letters,Volume 273, Issues 3-4, 15, Pages 237-250 doi:10.1016/j.epsl.2008.06.024.

Earth and Planetary Science Letters 273 (2008) 237–250

Contents lists available at ScienceDirect

Earth and Planetary Science Letters

journal homepage: www.elsevier.com/locate/epsl

Seismic anisotropy beneath southern Iberia from SKS splitting

L. Buontempo [a,*], G.H.R. Bokelmann [b], G. Barruol [b], J. Morales [a]

[a] Instituto Andaluz de Geofísica, Universidad de Granada, Campus Cartuja, Spain
[b] Université Montpellier II, CNRS, Géosciences Montpellier, CC060, F-34095 Montpellier cedex 5, France

ARTICLE INFO

Article history:
Received 19 January 2008
Received in revised form 16 May 2008
Accepted 11 June 2008
Available online 26 June 2008

Editor: R.D. van der Hilst

Keywords:
seismic anisotropy
lithosphere
asthenosphere
subduction
delamination
Gibraltar arc

ABSTRACT

Seismic anisotropy of the south Iberian upper mantle is investigated using shear-wave splitting of SKS phases. We analyzed teleseismic events recorded by sixteen permanent broadband stations installed on the southern Iberian Peninsula and in northern Africa, and we determined fast polarization directions ϕ, and delay times δt between fast and slow components. The area of investigation extends across two important geological structures in the Variscan Iberian Peninsula: the Variscan Iberian Massif in its center, and the Gibraltar arc in the Southeast, that represents the most westerly Alpine belt in the western Mediterranean. Shear-wave splitting measurements from stations in the Betic domain show homogeneous ENE–WSW fast directions nearly parallel to the trend of the mountain belt, and smooth spatial variations. Stations in the North, toward the southern part of the Variscan Iberian Massif show homogeneous fast directions however trending NS to NE–SW, different from those recorded in the Betic. These observations may reflect a post-Hercynian (Variscan) deformation of the Ossa-Morena zone, related to the main stages in the tectonic evolution of this part, namely transpressional stage, transtensional stage and shortening episode, or a deformation related to the posterior Alpine orogeny. Along the Gibraltar arc, we observe a smoothly varying ϕ trend changing from ENE–WSW in the Eastern Betics to NS in the area of Gibraltar and Ceuta, following more or less the general trend of the mountain belt around the Alboran Sea, and the coastline. Since a similar rotation is also visible in results from Pn anisotropy, this suggests that the anisotropy is vertically coherent starting from just below the Moho. Comparing the anisotropy pattern expected from various geodynamic models with the observed SKS splitting suggests that the anisotropy is best explained by a model of slab rollback, rather than by delamination models.

1. Introduction

During the last decades, seismological techniques have been developed to analyze the deep deformation of the Earth, and particularly the relation between plate tectonics and mantle flow as well as the internal deformation of the plate (e.g., Silver and Chan, 1988). The most popular technique uses the birefringence in anisotropic media that induces the splitting of shear waves and allows one to obtain quantitative information about seismic anisotropy in the upper mantle below a seismic station. Seismic anisotropy in the upper mantle is dominated by elastic anisotropy of rock-forming minerals which develop lattice-preferred orientations (LPO) or fabrics in response to strain (e.g. Nicolas and Christensen, 1987; Mainprice et al., 2000). The primary constituent of the upper mantle is olivine which is more anisotropic than most other minerals. Olivine deforms by dislocation-creep at upper mantle conditions (Nicolas and Christensen, 1987), and it generally aligns the main crystallographic axes with respect to the structural directions (lineation, pole of the foliation), therefore producing a large-scale anisotropy that is detectable by seismic waves. The anisotropy is thus correlated with the strain in the upper mantle, and it therefore allows constraining deformation at that depth within the Earth remotely from the surface.

The most useful seismological phase for studying shear-wave splitting is the SKS phase. It travels through the mantle as an S wave, through the liquid outer core as a P wave after a S to P conversion at the core–mantle boundary, and is converted back into a radially polarized S wave when passing back in the mantle. On its way to the Earth's surface, this SKS phase is split into two mutually orthogonally polarized shear waves as it propagates through an anisotropic medium. From three-component seismic records, two parameters can be measured to quantify the anisotropy: 1) the difference in arrival time (δt) between the two split waves that depends on thickness and the intrinsic anisotropy of the medium, and 2) the polarization plane azimuth ϕ of the faster split shear wave that is related to the orientation of the anisotropic structure. Shear-wave splitting measurements can therefore characterize the orientation and to a lesser degree the depth extent of the mantle strain field (see review by Savage, 1999).

Determining the vertical location of the anisotropic layer(s) is always challenging since the splitting of SKS phases may occur somewhere between the core–mantle boundary and the station.

* Corresponding author. Tel.: +34 958 249554; fax: +34 958160907.
E-mail addresses: luisa@iag.ugr.es (L. Buontempo), Bokelmann@gm.univ-montp2.fr (G.H.R. Bokelmann), barruol@gm.univ-montp2.fr (G. Barruol), morales@iag.ugr.es (J. Morales).

0012-821X/$ – see front matter © 2008 Elsevier B.V. All rights reserved.
doi:10.1016/j.epsl.2008.06.024

Other phases such as local S (e.g. Bowman and Ando, 1987), may help to constrain the anisotropy distribution beneath a station, but they require the presence of nearby seismogenic zones. Petrophysical analyses of mantle minerals and rocks (Mainprice et al., 2000; Mainprice et al., 2005) suggest that anisotropy lies in the uppermost 400 km of the Earth. Recent theoretical studies using finite-frequency sensitivity kernels provide similar conclusions since SKS splitting are shown to be more sensitive to the upper mantle above the transition zone than to the lower mantle (Sieminski et al., 2007). If one assumes that the crust may contribute only a few tenths of a second to the total SKS splitting (Barruol and Mainprice, 1993; Godfrey et al., 2000), these arguments suggest that the anisotropy lies primarily in the subcrustal upper mantle. It is however not clear whether the anisotropy lies within the lithosphere and is related to a 'frozen' deformation (Silver and Chan, 1988), or within the asthenosphere and is thus related to present-day plate motion (Vinnik et al., 1992). This question can be addressed by SKS splitting only indirectly since these observations constrain only weakly the depth of anisotropy within the upper mantle. On the other hand, this question can in principle be resolved combining SKS observations with surface wave anisotropy and Pn observations. We will in fact use Pn in this study to compare with SKS splitting results.

The area of interest of this paper, in southern Iberia and around the Gibraltar arc, represents a key area of geodynamic interest for the Africa–Eurasia collision and for the various stages of opening and closure of the Mediterranean basins. Various geodynamic models and mechanisms have been proposed to explain the large-scale structures and timing constraints, based on regional-scale recycling of lithosphere into the mantle, such as active continental subduction (Morales et al., 1999), delamination (Seber et al., 1996a) or active oceanic subduction (Lonergan and White, 1997; Gutscher et al., 2002).

In this study, we present new shear-wave splitting measurements obtained at permanent stations located in the Betic and Rif Cordillera and in the southern part of the Variscan Iberian Massif. We compare these new results with previous ones from Iberia (Diaz et al., 1998; Schmid et al., 2004), as well as from Pn phase anisotropy (Calvert et al.,

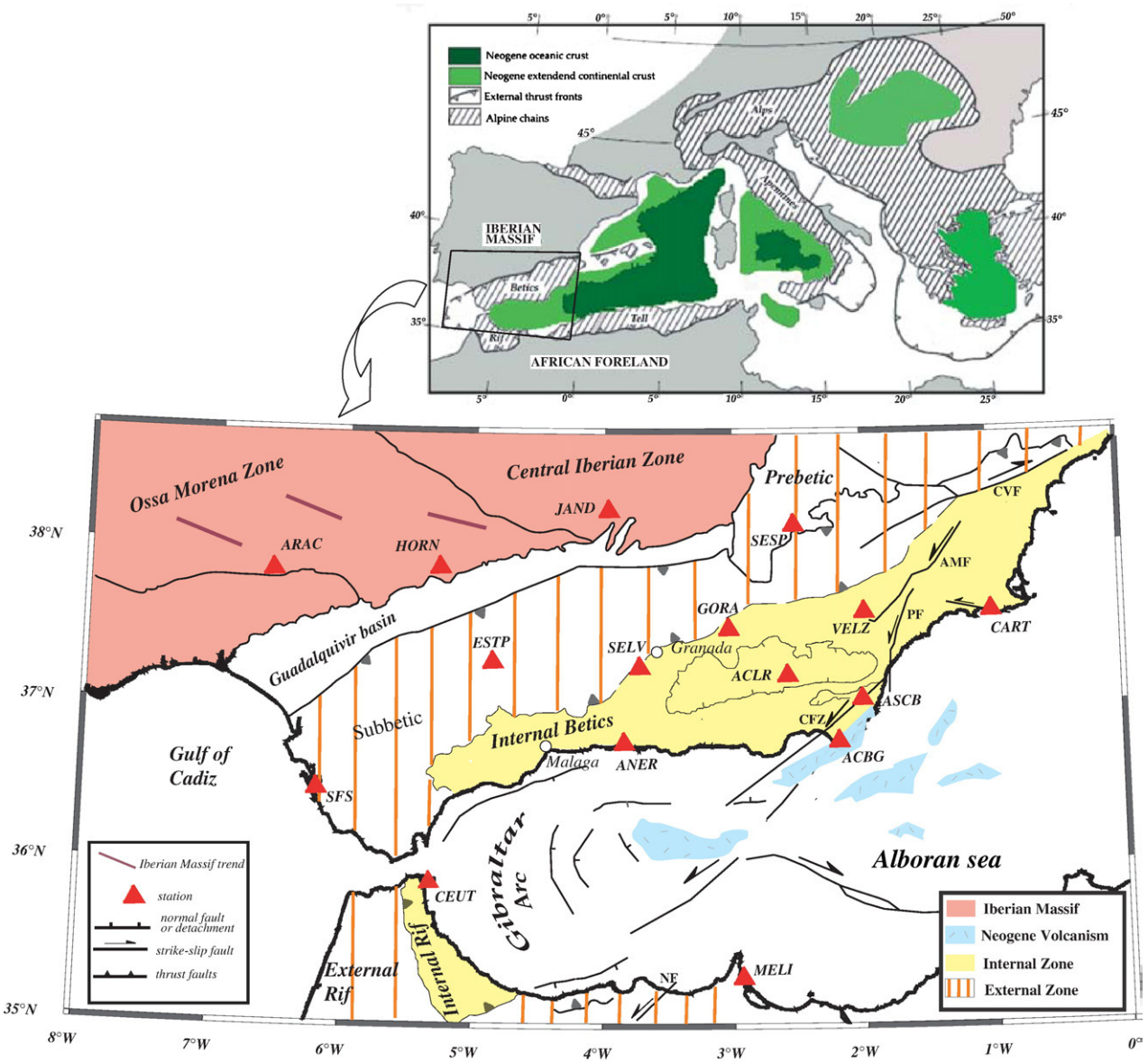

Fig. 1. Tectonic sketch of the Mediterranean area showing the Neogene basins and Alpine chains (top, redrawn from Comas et al., 1999) and geological setting of South of Iberia and North of Africa (bottom, redrawn from Lonergan and White, 1997; Platt el al., 2003). Main faults are shown in the External and Internal Zones and in the Alboran Domain (CVF: Crevillente fault, AMF: Alhama de Murcia fault, PF: Palomares fault, CFZ: Carboneras fault, NF: Nekor fault). Locations of seismological stations used in this study are also shown by triangles.

2000b). In the light of tomographic models for this region we propose that all these anisotropy observations may help to constrain and to better understand the geodynamic setting of this complex area.

2. Geodynamic setting

The Betic and Rif belts, connected through the Gibraltar arc, represent the most westerly Alpine range in southern Europe (Fig. 1). Together with the Alboran basin, these belts constitute one of the most complex and most debated geological regions in the western Mediterranean. A major characteristic of the Alboran basin is that it is an extensional regime (Comas et al., 1999) within a general collision regime, induced by the convergence of Africa and Eurasia from the Cretaceous to Paleogene (Dewey et al., 1989). The geological records and geophysical observations shed some light on the evolution of the region. Formally, the Gibraltar arc is divided into three pre-Neogene crustal domains: the first consists of Mesozoic and Tertiary sedimentary rocks deformed during the Neogene as a thrust-and-fold belt mainly directed to the NW and WNW (e.g., Garcia-Dueñas, 1969; Garcia-Hernandez et al., 1980), which covered the South-Iberian and Maghrebian continental paleomargins and constitute the External Zones of the Betics and Rif. The second corresponds to the sediments deposited on oceanic troughs or thin continental crust (Luján et al., 2006) and belongs to the so-called Flysch Trough that is well-represented in the Rif and Tell regions. The last one, the Alboran crustal domain, represents the internal zones of the orogen, composed mainly of Paleozoic to Mesozoic rocks affected by low to very high-grade metamorphism that were deformed mainly during the late Cretaceous to Paleogene and thrust onto the south Iberian and north African margins during the Early Miocene (Balanyá and García-Dueñas, 1988). Three tectono-metamorphic complexes are recognized in this zone, the Nevado-Filabride, the Alpujarride and the Malaguide in the Betics. The Alboran domain shows N–S continuity below the sea and constitutes the metamorphic basement of the Alboran basin (Platt et al., 1996). That basin represents a post-orogenic back arc basin (Lonergan and White, 1997), similar to the Calabrian arc (Faccenna et al., 2004; Rosenbaum and Lister, 2004), formed during the westward migration of the orogenic wedge. The main extension occurred during the Early Miocene (Comas et al., 1999), coeval with shortening in the orogen. The extension was associated with subsidence during the Miocene and accompanied by tholeitic and calcoalkaline magmatism (Turner et al., 1999; Duggen et al., 2005). Since the Upper Miocene–Pliocene until present, a contractive episode with a roughly NW–SE direction, although varying from the Upper Miocene to the Pliocene (Ott D'Estevou and Montenat, 1985; De Larouzière et al., 1988; Galindo-Zaldívar et al., 1997) manifests itself by strike–slip tectonics, mainly in the eastern Betics and Alboran basin. This contractive episode was accompanied by magmatism of mainly shoshonitic, lamproitic and alkaline basalts (Lonergan and White, 1997; Zeck et al., 1998; Duggen et al., 2005).

At present, the kinematics of the Gibraltar arc as defined by GPS and seismic moment tensor observations shows different deformation styles that are characterized by NNW-directed thrust faulting near the Algerian coast and the SW of Iberia and an E–W extensional regime in the Alboran Sea (Stich et al., 2003, 2006). A crucial role is played by the so-called Trans-Alboran shear zone, a major structure formed by NE–SW sinistral strike–slip faults, and NW–SE conjugates in the partitioning of the strain in the region (Fernández-Ibáñez et al., 2007) that allow coeval shortening and extensional structures in a oblique convergent plate margin between Africa and Europe.

Several models have been proposed to explain the formation of the Gibraltar arc. These models may be compared by considering the style of recycling of lithospheric material back into the mantle that may occur in the form of lithospheric delamination (e.g. Seber et al., 1996a; Platt et al., 1998; Calvert et al., 2000b), convective removal (Platt and Vissers, 1989), or subduction (Lonergan and White, 1997; Gutscher et al., 2002).

Platt and Vissers (1989) proposed that a lithospheric thickening as a result of convergence created a collisional ridge of thick crust underlain by a thick root of cold lithospheric mantle, during late Eocene to Oligocene time. Such a gravitationally unstable root could have been removed by convection and replaced by an asthenospheric mantle during the late Oligocene, resulting in the uplift and extension of the region and in the exhumation of metamorphic rocks and high-temperature peridotites from the base of the crust. The continuous convergence between Africa and Eurasia is then proposed to be accommodated by shortening in the external zones of the belts (Subbetic and External Rif).

The model proposed by Seber et al. (1996a) is also based on delamination, and is somewhat similar to the model of Platt and Vissers (1989). The difference is the style of removal of the thickened lithosphere. Seber et al. (1996a) proposed indeed that, as a consequence of compression, a thickened lithosphere was underlying the (thickened) crust, and that gravitationally unstable lithospheric root was progressively replaced by hot asthenosphere by convective removal from the crust toward W and NW. A consequence of the resulting asthenospheric inflow is the heating of the crust inducing an uplift and the extension in the Alboran area.

The slab rollback model of Royden (1993) and Lonergan and White (1997) is very different from the above models, since it focuses primarily on subduction of oceanic lithosphere under the Alboran Sea. As the rate of subduction exceeds the rate of convergence, the subduction zone began migrating to the west while the crust of the

Table 1
Station locations and mean splitting parameters, given as mean values (m), median values (md) and weighted-mean values (w) with 2σ errors

Station name	Latitude (°)	Longitude (°)	ϕ_m (°)	$\sigma\phi_m$ (°)	δt_m	$\sigma\delta t_m$	ϕ_{md} (°)	δt_{md}	ϕ_w	$\sigma\phi_w$	δt_w	$\sigma\delta t_w$	Number of observations
ACBG	36.7686	−2.1939	59.42	7.94	1.70	0.64	59.59	1.88	67.09	1.59	1.86	0.08	5
ACLR	37.1897	−2.5822	77.16	8.49	1.74	0.69	77.20	2.00	82.60	4.26	1.72	0.18	6
ANER	36.7623	−3.8453	31.12	21.11	1.54	0.8	36.82	1.18	35.91	1.29	1.29	0.06	16
ARAC	37.8800	−6.5800	63.65	12.51	0.99	0.35	67.81	1.00	65.00	6.95	0.79	0.12	8
ASCB	37.0394	−2.0056	54.26	14.76	1.46	0.73	63.46	1.52	65.73	2.51	1.62	0.16	6
CART	37.5868	−1.0012	68.86	7.97	1.56	0.31	69.74	1.50	72.93	1.27	1.46	0.07	11
CEUT	35.8831	−5.3263	−3.61	22.27	2.06	0.88	−3.61	2.06	−15.01	3.76	1.71	0.44	2
ESTP	37.2713	−4.8662	81.14	13.05	1.56	0.59	83.16	1.34	63.44	3.12	1.45	0.18	9
GORA	37.4805	−3.0398	72.71	6.85	1.30	0.38	74.46	1.12	73.28	5.36	1.18	0.14	5
HORN	37.8200	−5.2800	58.06	21.19	1.07	0.4	57.56	0.94	40.15	2.28	0.92	0.1	14
JAND	38.22	−3.97	6.49	48.64	1.72	0.33	31.52	1.80	1.03	3.75	1.61	0.32	3
MELI	35.2899	−2.9392	66.87	8.24	1.43	0.6	63.11	1.50	67.51	3.27	0.95	0.09	3
SELV	37.2383	−3.7277	59.01	14.65	1.04	0.56	52.48	0.81	48.33	4.56	0.86	0.12	6
SESP	38.1208	−2.5452	66.28	28.69	1.68	0.63	72.26	1.70	47.35	1.38	1.77	0.11	14
SFS	36.4656	−6.2055	−1.27	28.41	1.10	0.99	−1.27	1.10	17.03	7.91	0.87	0.41	2
VELZ	37.5838	−1.9880	69.66	12.87	1.45	0.48	66.45	1.40	64.94	2.64	1.39	0.08	8

For (m) errors give two times the standard deviation of individual values; for (w) they give the error of the weighted mean.

former collision ridge (Internal Zone) was broken up and dispersed, and the crust behind this region was thinned by extension. In the northern and southern portions of the subduction zone, the westward movement slowed down as Iberian and African lithosphere was encountered and the emplacement of the Internal Zone was accommodated by shortening in the continental margins. The central portion of the subducting trench continued its westward migration and the continued subduction-zone rollback induced extension beneath the Alboran Sea. On the other hand, several other models consider different geometries and dip direction for the subducting slab: the above models invoke eastward subduction of oceanic lithosphere rolling back to the west (Lonergan and White, 1997; Gutscher et al., 2002); others consider an extinct subduction oriented northwards (e.g., Zeck, 1996). Recent analyses of body-wave dispersion at Ceuta (Bokelmann and Maufroy, 2007) indicate very different dispersion characteristics of events arriving from the West from those arriving from the East, which suggests the presence of an oceanic slab beneath the Alboran Sea.

3. Data and method

In this study, we used seismic data recorded by 13 permanent broadband stations of the Instituto Andaluz de Geofisica (IAG), and by 3 broadband seismic stations of the ROA-UCM-GEOFON (Real Observatorio de la Armada in San Fernando—Universidad Compute Madrid-Geofon). The station locations are reported in Fig. 1 and Table 1.

Locations and centroid times of teleseismic events used to extract the data from the continuous record were taken from the Harvard catalogue, http://www.seismologyharvard.edu/CMTsearch.html and arrival times of theoretical SKS phases at the stations were calculated using the theoretical Earth model IASP91 (Kennett, 1995) with the IASP91TTIM software (Buland and Chapman, 1983; Kennett and Engdahl, 1991). From the teleseismic events covering the period 2001–2006, we selected events occurring at distances larger than 85° and of magnitude (Mw) larger than 5.7. The selected events are shown in Fig. 2, with a global projection centered on southern Spain and preserving the azimuths. For the distance range between 130 and 165° we also selected SKKS phases. A careful visual inspection of the data allowed us to keep about 207 seismograms from 67 teleseismic events.

For each selected event, we calculated the two splitting parameters, that is, the azimuth of the fast axis ϕ and the delay time δt between the fast and slow component of the shear waves. We performed these measurements using SplitLab (Wüstefeld and Bokelmann, 2007; Wüstefeld et al., 2008), which utilizes three different techniques simultaneously: the rotation-correlation method (e.g. Bowman and Ando, 1987), that is maximizing the cross-correlation between the radial and transverse component of the SKS phase, the minimum energy method (Silver and Chan, 1991), that is minimizing the energy on the transverse component, and the minimum eigenvalue method (Silver and Chan, 1991). Fig. 3 shows an example of the application of these techniques for an event that arrives from the North at station ACBG. Under good measurement conditions, i.e. good signal-to-noise ratio and a favorable backazimuth, these methodologies give similar splitting parameters. The comparison between the different methods is helpful for characterizing cases of small δt where seismograms do not show clear SKS splitting, the so-called Null measurements, and for

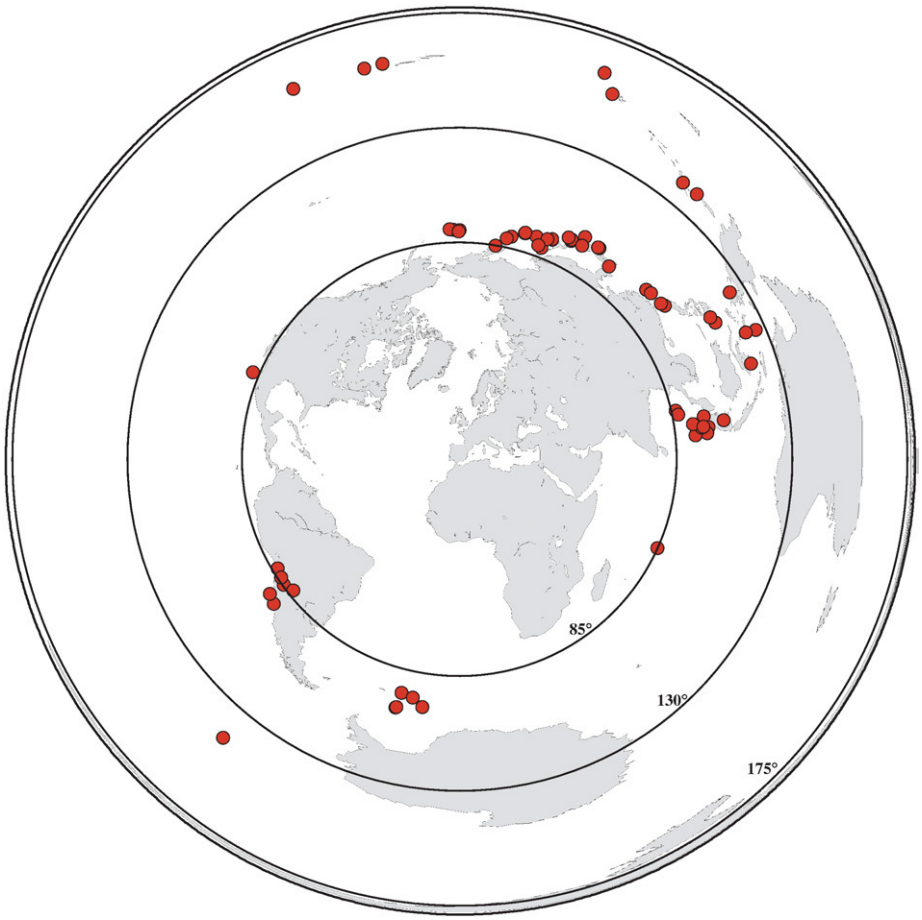

Fig. 2. Spatial distribution of earthquakes used in this study in a projection that preserves backazimuths, centered on the Alboran. The 85° (minimum distance for SKS splitting measurement) and 130° of epicentral distance are also shown.

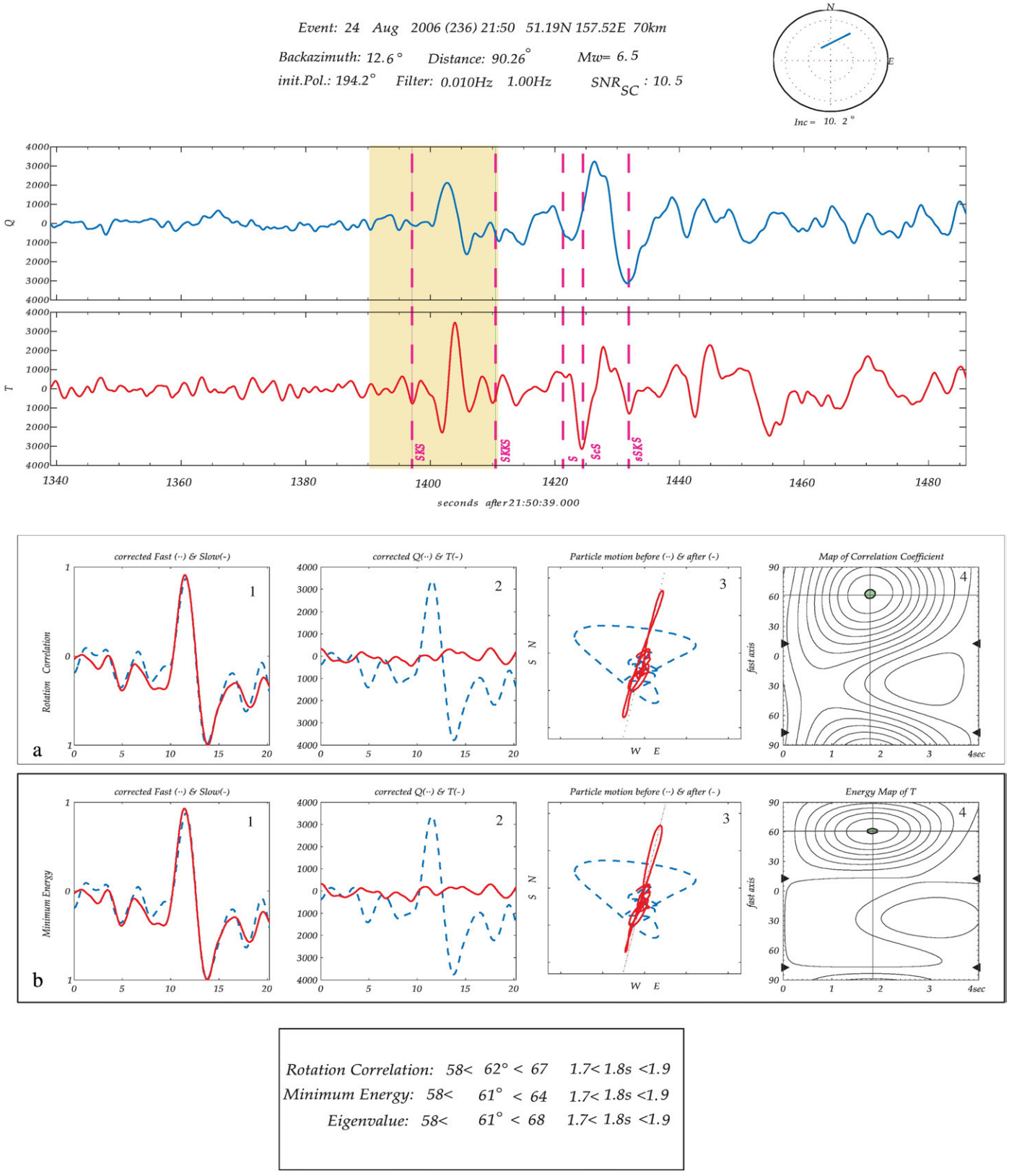

Rotation Correlation:	58<	62° <	67 1.7< 1.8s <1.9
Minimum Energy:	58<	61° <	64 1.7< 1.8s <1.9
Eigenvalue:	58<	61° <	68 1.7< 1.8s <1.9

Fig. 3. Example of data processing using SplitLab software (Wüstefeld et al., 2008) at ACBG station. (top) The upper panel shows the event information and the initial radial and transverse components. Dashed lines are the predicted phase arrival times from IASP91; the shaded area is the selected window for the shear-wave splitting processing. (middle) Figures for inspecting the performance are shown with four plots for the rotation-correlation method in panel a) and four plots for the minimum energy method in panel b). From left to right: 1) fast and slow components (dashed and continuous lines, respectively), corrected for the calculated splitting delay time; 2) corrected radial and transverse components (dashed and continuous lines, respectively), note that the energy on the transverse component is well removed after anisotropy correction; 3) the particle motion in the horizontal plane (dashed) becomes linear after the correction for anisotropy (solid); 4) contour plot for the maximum value of correlation coefficient and for the energy on transverse component as function of delay time and fast polarization angle. The shaded area marks the 95% confidence interval. (bottom) Numerical values that summarize the results for the three methodologies are given at the bottom, with their respective error ranges.

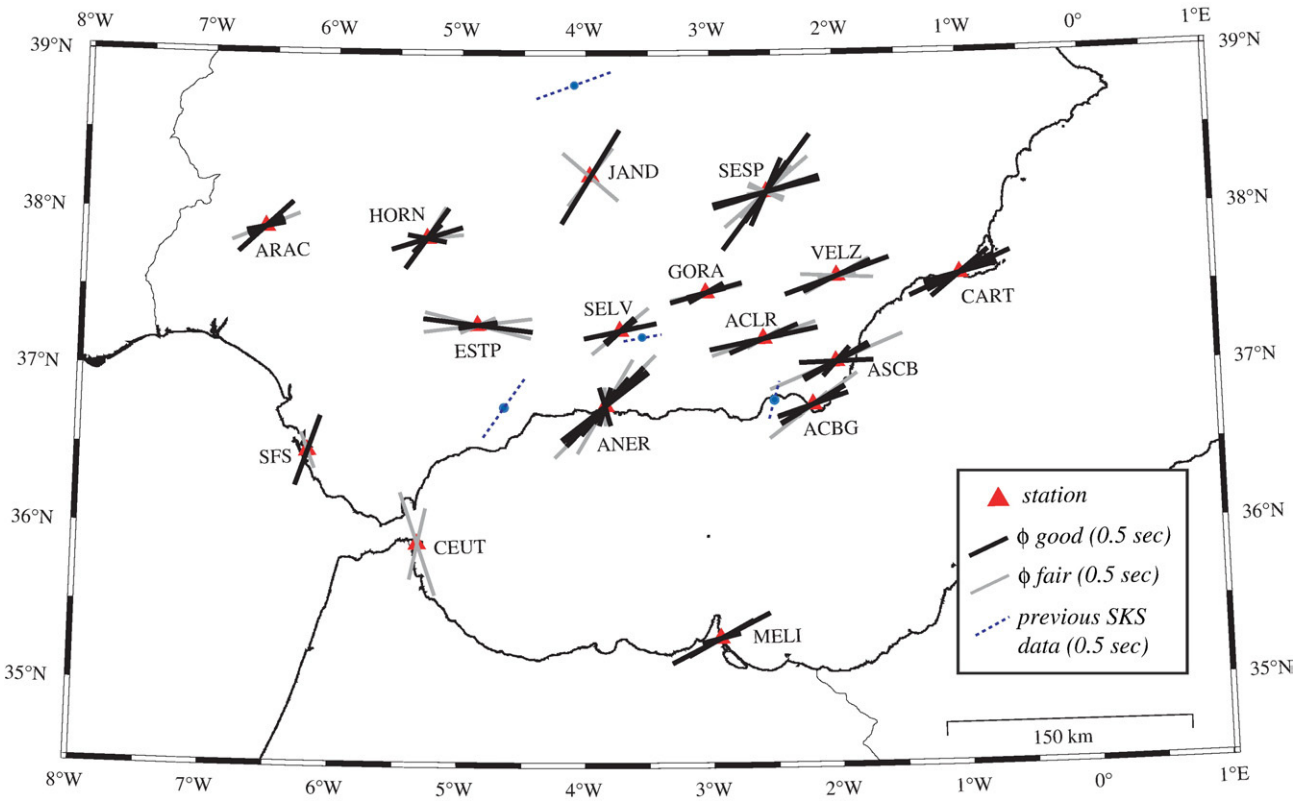

Fig. 4. Splitting results shown at the seismic stations used in the present study. Each measurement is characterized by a fast azimuth ϕ, and the length of the segment is proportional to the delay time δt. Good (thick dark lines) and fair (thin lines) are represented.

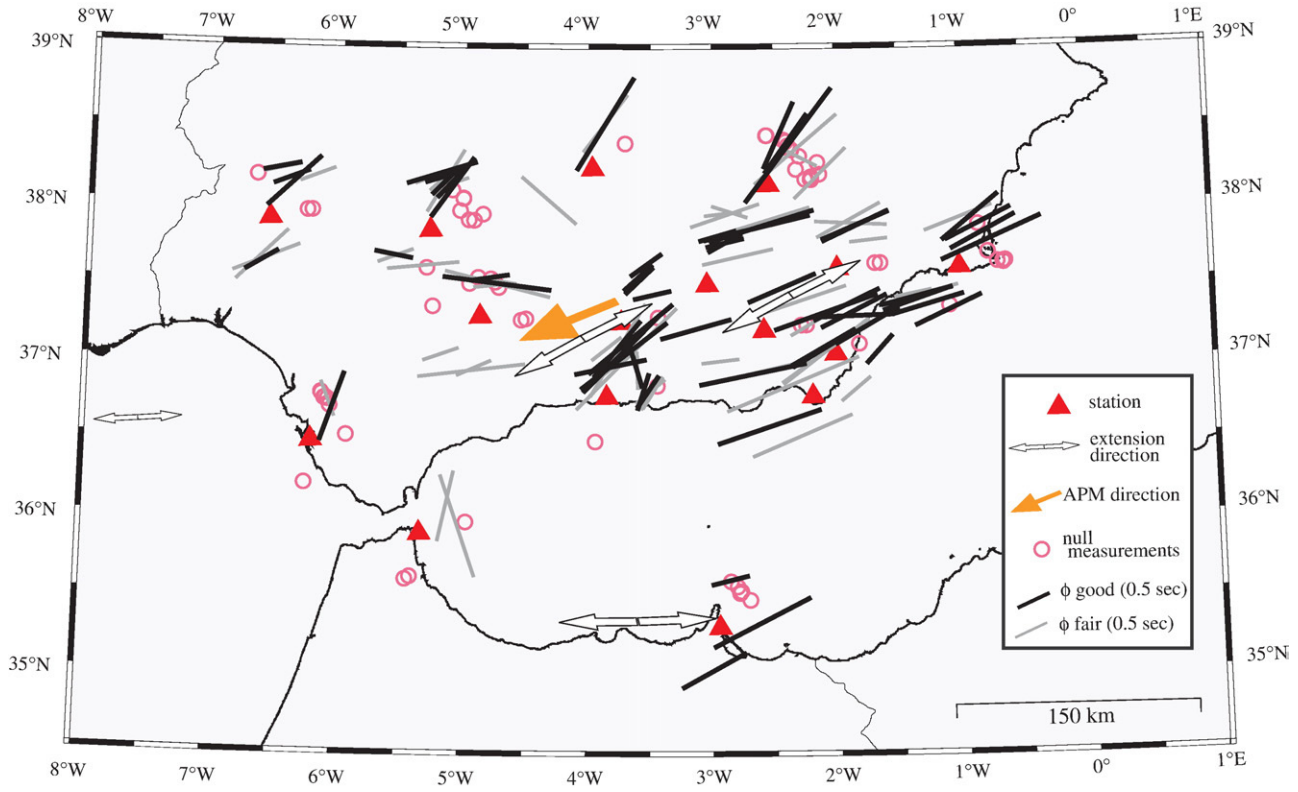

Fig. 5. Individual splitting measurements projected at 150 km depth along the ray paths. Good measurements are shown by thick lines, fair measurements by thin lines. Null measurements (events with no apparent splitting) are shown by circles. White arrows are average stress extension directions calculated by Stich et al. (2006), the dark arrow shows absolute plate motion direction for the model HS3-Nuvel-1A (Gripp and Gordon, 2002).

discriminating them from cases of existent but weak splitting. Null measurements occur when the SKS phase is not split. This may happen when the medium is isotropic or when the backazimuth of the incoming SKS wave is parallel to either the slow or the fast directions in the anisotropic layer. In the case of a simple anisotropic medium, Null and non-Null measurements have to be consistent with each other. For simplicity in the discussion and pictures we present only measurements obtained with the minimum energy method. Table 1 gives resulting splitting parameters (ϕ and δt) for each seismogram.

We qualified the splitting results as "good", "fair", and "poor" as proposed by Barruol et al. (1997), i.e., depending on the quality of the seismograms, on the signal-to-noise ratio of the initial phase, on the amount of energy on the transverse component, on the correlation of the two split waveforms, and on the elliptical particle motion before anisotropy correction and its linearization after correction. Waveforms with good or fair quality generally provide similar results with and without filtering, indicating that results do not overly depend on the filter parameters. We generally choose to not filter the data unless required to remove high frequencies and/or long-period noise.

We will initially assume that the anisotropy is characterized by layer (s) with horizontal symmetry axes. Dipping axes of symmetry (or some orthorhombic symmetry systems) can cause systematic variations of splitting parameters as functions of backazimuth. However the small number of observations at each station precludes testing such cases.

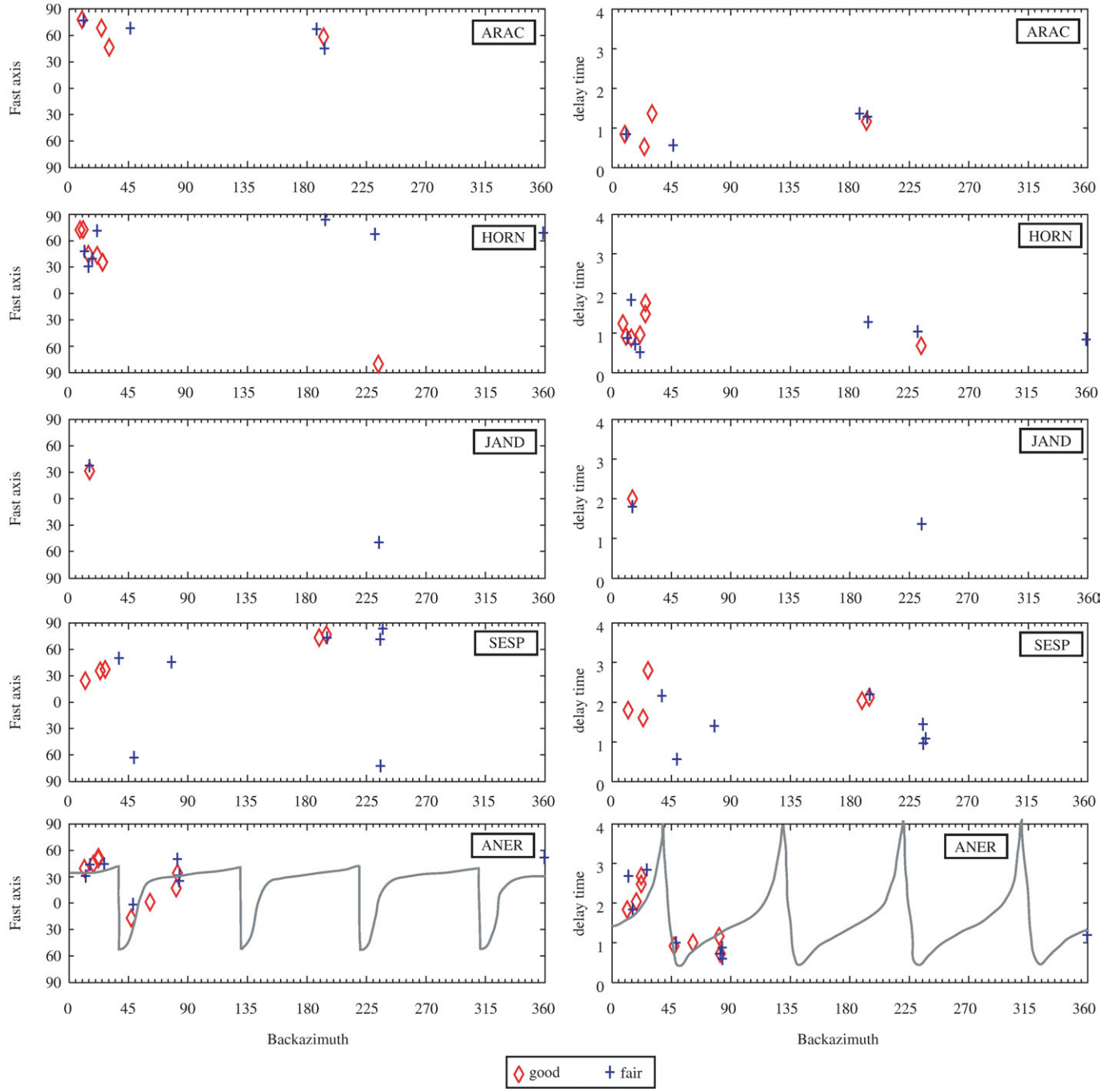

Fig. 6. Backazimuthal distribution of SKS splitting for stations SESP, JAND, HORN, ARAC, and ANER that are not easily explained by a single anisotropic layer. The panels for ANER also show the prediction for the best-fitting two-layer model. See text for explanation.

4. Results of SKS splitting

The individual splitting measurements (see Table 2, given in the Electronic supplement) are plotted in Fig. 4 at the various stations to evaluate the coherence of the results. Lines show the fast anisotropy directions ϕ, obtained from the minimum energy method, and their lengths are proportional to the splitting delay time δt. "Good" data are shown by thick dark lines, and "fair" data by thin lines; "poor" data are not plotted. Most stations in the Eastern Betics, CART, VELZ, ACBG, GORA, ACLR and ASCB show a homogeneous ϕ trending roughly N70°E and high delay times of around 1.5 s. Given the weak spreading of fast direction measurements ϕ at stations in that region, and the spatial coherence, the splitting observed at those stations is likely originating within a single anisotropic layer that is well-constrained by a suitable number of measurements. We record a similar trend for the station MELI in Northern Africa, where the fast direction is N68°E with a delay time of roughly 0.95 s. Interestingly, ϕ is nearly North–South at stations SFS and CEUT, i.e., parallel to the trend of the Gibraltar arc. At each of these two stations unfortunately, measurement conditions were relatively difficult, and there are only two measurements available at CEUT from 3 yr of data analyzed, (N12°E, δt=1.44 s and N19°W δt=2.68 s), and two non-Null measurements at SFS (N19°E, δt=1.80 s and N21°W δt=0.4 s).

Diaz et al. (1998) used data from temporary stations and found a fast direction oriented N80°E at a station in the southern part of the Variscan Iberian Massif. In the Betics, they observed a NNE–SSW trend in the eastern part that changes to E–W in the central part, near Granada, and again NNE–SSW near the coast of Malaga interpreted in terms of their particular lithospheric geodynamic settings. Schmid et al. (2004) studied the station CART, in the eastern part of Betic, and MELI in the north of Africa, finding fast directions in the Betic trend, oriented N70°E and N56°E respectively.

At a number of stations, there is a clear backazimuthal dependence of the splitting parameters, like at stations ARAC, HORN, JAND, SESP, and ANER. Such a backazimuthal dependence of splitting parameters may be explained either by invoking vertical variation of anisotropy, e.g. by the presence of two (or more) anisotropic layers, or by lateral variations of anisotropy. First, we address the case of lateral heterogeneity. In order to better visualize the lateral sampling of the anisotropy measurements and the regional-scale stability of the anisotropy parameters beneath the stations, we choose to project the individual splitting measurements of good and fair quality along their incoming rays to a depth of 150 km (Fig. 5). Although the splitting of the SKS waves is not well-located vertically, this representation is helpful since it plots the splitting parameters closer to the location where they were acquired. The measurements with well-constrained anisotropy ("good") are presented as thick dark lines while measurements of lower quality ("fair") are shown by thin lines. In addition, Fig. 5 presents the Null measurements by open circles. In the eastern and internal Betics, this figure clearly indicates smooth spatial variation of the anisotropic structures beneath most stations (with the exception of ANER, see discussion below). Such a pattern was less clear in Fig. 4. It suggests that the variation is not caused by noise in the observations. It is apparently due to real anisotropic variations at depth. This suggests that the upper mantle beneath the Internal Betics is dominated by a single anisotropic layer, with smoothly varying fast directions. Station ESTP located in the Subbetic domain shows a homogeneous distribution of the fast directions that led us to conclude that this part is characterized by a single layer. We will address the nature of this anisotropy and its smooth spatial variation in detail below.

The splitting parameters observed at stations ARAC, HORN and JAND near the transition to the Variscan Iberian Massif, SESP in the Prebetic units, and ANER in the Internal Betics, are not fully explained by lateral variation of splitting. These 5 stations are characterized by an apparent backazimuthal variation of the splitting parameters as shown in Fig. 4. The projection at depth of the individual splitting measurements (Fig. 5) suggests strong lateral variations at small scale-length. Such a rapid variation is not easily explained by lateral variation since the Fresnel zone of SKS phases in the upper mantle that quantifies the width of the zone over which the SKS 'average' the structure, is 100 to 200 km wide for SKS waves with 10 s period. For these 5 stations, we show the detailed ϕ and δt backazimuthal variation in Fig. 6. A single anisotropic layer would produce a constant fast direction ϕ, independent of backazimuth, as well as a constant splitting delay δt. With the possible exception of station ARAC, such a simple single layer does not explain the observations at these stations. However, the stations are characterized by varying amounts of data, partly due to the different running periods of the stations. Data at station JAND were available only from July 2006 and therefore provide only few SKS measurements. Nevertheless, the station exhibits a general NE trend except for the event on day 237 (year 2006, see Table 2 Electronic supplement) with backazimuth of 234° that shows a different ϕ. The small number of data cannot constrain the results for that station. For ANER, there is a nearly North–South trend for such events that arrive from ENE, but data with NNE backazimuth show NE–SW fast directions. The stations HORN, SESP and ARAC exhibit a good number of data which will allow the discussion of a possible two-layer case that we will present below.

5. Discussion

A striking feature in the anisotropy pattern observed in this study is that the Eastern Betics seems to be well-described by a single and rather homogeneous anisotropic layer, whereas a more complex anisotropic model likely involving lateral and vertical variations of anisotropy seems to be present in the upper mantle beneath stations in the North, and perhaps the West and the South. The Eastern Betics show indeed a smooth lateral variation of anisotropy, whereas stations in the Western and Southern part of this region indicate much stronger lateral variations in the splitting parameters. There are also strong lateral variations associated with the transition from the Betic to Variscan Iberia, in addition to two-layer anisotropy as we will show below, as is required at some of the stations at least.

5.1. Eastern Betics

Fast directions are oriented ENE–WSW in the Eastern Betics, and there is a smooth spatial variation clearly visible in Fig. 5 that is more or less parallel to the mountain belt. The anisotropy in that region is easily explained by a single anisotropic layer. The average splitting delay time in that region is about 1.5 s, which is consistent with a layer that is 150 km thick assuming the typically used value of 4% anisotropy in the upper mantle (Mainprice and Silver, 1993; Mainprice et al., 2000). Tomographic models for the region, (e.g. Blanco and Spakman, 1993), show a pronounced low-velocity anomaly in the upper mantle under the Betics between 30 and 100 km depth that is also apparent and even more pronounced in the Pn tomographic model of Calvert et al. (2000a). This area is also the locus of a pronounced high attenuation anomaly of Sn waves (Calvert et al., 2000b). This may suggest that continental mantle material under the Betics has been replaced by asthenospheric material. Geochemical studies favor such a hypothesis by suggesting an edge delamination that could have occurred under the Betics (Duggen et al., 2005). If the lithosphere has indeed been removed, this should suggest that the deformation recorded by the seismic anisotropy under the Betics is associated rather with hot and thus relatively low-viscosity material. At larger depths, however, velocities are again relatively high in tomographic models (e.g., Blanco and Spakman, 1993) down to the transition zone, including the zone of very deep seismicity around 600 km depth (Buforn et al., 1997).

The ENE–WSW fast directions observed in the Eastern Betics are nearly parallel to the absolute plate motion direction, which is 239°

and 2 cm/yr for the motion model Nuvel1A relative to the hotspot reference system HS3 (Gripp and Gordon, 2002). Although the Eurasian plate motion vector is slow and therefore still matter of debate, a simple deformation model related to plate motion of the Iberian/Eurasian plate over the deeper mantle might thus explain the anisotropy. In this context, the gradual rotation of fast direction along the coast might be explained reasonably by invoking a deviation of mantle flow around the Iberian lithosphere, following similar suggestions of Bormann et al. (1996) for central Europe and of Barruol et al. (1997) and Fouch et al. (2000) for North America. This might also explain the minor difference of 10° between the average fast direction in the Eastern Betics and the absolute plate motion direction.

On the other hand, the observed fast directions in the Eastern Betics also show an interesting correlation with crustal features which is not expected in the case of plate motion induced asthenospheric anisotropy. The convergence direction between the African and the Iberian/Eurasian plate is NNW–SSE, and the current style of deformation in the crust is predominately left-lateral strike–slip faults with a NE–SW trend (e.g. Alhama de Murcia, Palomares and Carboneras faults). Vauchez and Nicolas (1991) suggested that in many collisional belts the dominant motion is strike–slip parallel to the main trend of the belt. In this case, both crustal and mantle fabrics may reflect these movements, and the entire lithosphere develops a fabric and becomes anisotropic. They attribute this anisotropy to a dominant mantle flow parallel to the mountain belt during orogeny. Such a structure is well illustrated in the Ronda peridotite massif where pervasive structures and fabric in the lithospheric and asthenospheric mantle are well preserved (Vauchez and Garrido, 2001). The present-day extension direction inferred by Stich et al. (2006), using moment tensors of crustal earthquakes, is N240°E, which is indeed parallel to the inferred fast polarization directions. The anisotropy is thus also consistent with a notion of vertically coherent deformation of crust and mantle as initially proposed by Silver and Chan (1988, 1991), except that we are dealing with hot deformed mantle in this region, and thus probably with current deformation, rather than fossil deformation remaining from the creation of continental lithosphere. For the close-by Gulf of Cadiz region, Stich et al. (2005) have shown that the stresses imposed by the Africa–Iberia plate convergence have the same geometry in the crust and the mantle. The convergence thus imposes a similar lateral boundary condition over a considerable depth range. Crust and mantle in the Betics may thus both be constrained to deform in a similar fashion. The observed anisotropy under the Eastern Betics could be thus caused by a combination of this kind of vertically coherent deformation, and absolute-motion-related deformation, both producing a seismic anisotropy such as the observed one. The relative importance of each is not constrained though. Interestingly, a model of slab rollback is also consistent with such coherence between crustal and upper mantle deformation. The retreat to the WSW of the Alboran slab may have induced a large transcurrent deformation in the mantle beneath the eastern Betics but also in its crust.

5.2. Variscan belt

The northernmost stations of our study area are situated on or near the Variscan Iberian Massif. The fast anisotropy directions we observe at these stations are trending more NE–SW than those recorded by stations in the Betics that trend more ENE–WSW. These directions do not appear to correspond to orientations of geological structures in the Variscan basement, since the latter trend more or less NW–SE in the Northwest portion of Iberia and East–West in eastern Spain. While we do not obtain those “Variscan” directions for our northernmost stations that are near the southern end of the Variscan belt, they are in fact observed further North, in the center of Variscan Iberia (Silver and Chan, 1988; Schmid et al., 2004), where they are roughly E–W. Three of our northernmost stations show a wide range of fast orientations (Figs. 5 and 6). Different anisotropy parameters are obtained for measurements arriving from the North and South. This is not easily explained by lateral heterogeneity, unless all these stations are located above a geological suture zone so that events arriving from the North and the South could experience a different medium. Since these stations are indeed near the Betics deformation front, we wish to further test both hypotheses for the northernmost stations, namely the ‘lateral heterogeneity hypothesis’ and the ‘two-layer anisotropy hypothesis’. Fig. 5 illustrates the ‘lateral variation hypothesis’, where splitting results were projected along the incoming rays to 150 km depth. In this view, fast directions that show up to the North of the stations, within the Iberian Variscan Massif, are generally associated with NE–SW fast direction, while results generally show more East–West trending fast directions, for southern backazimuth i.e., close to the general Betics trend. This is particularly clear at station SESP, and it may indicate that the events arriving from the south are experiencing the same anisotropic structure as the stations located further south in the Internal Betics. This would suggest that SESP may lie close to an important boundary between lithospheric blocks. Among the northern stations of our study area, ARAC shows little backazimuthal dependence of the anisotropy parameters: NE–SW fast directions are visible both to the North and to the South of the station.

On the other hand, we may assume a two-layer model for each of these four northern stations, to try to explain the observed variation of the splitting parameters apparent in Fig. 6. Constraining the four parameters of a two-layer model requires a relatively good backazimuthal coverage (see Walker et al., 2007), which we do not have. We therefore decided to apply a similar approach as Fontaine et al. (2007) for the SKS splitting obtained at oceanic island stations, by considering the area as homogeneous enough to group the individual splitting measurements together into a single “virtual” station. We processed measurements obtained from the four stations together, since they have similar backazimuthal coverages. Different from the other three stations, SESP is located within the Betic Cordillera, in the so-called Pre-Betic. Nevertheless splitting parameters are more like those of the stations at the limit, e.g. HORN, rather than the other station on the Betics.

If there were several anisotropic layers present at depth, mantle deformation would not necessarily mimic crustal deformation. A tectonic decoupling somewhere within the lithosphere might explain why anisotropic directions in the area are different from the trend of the mountain belt. Seismic reflection profiles in the south-western portion of the Iberian Massif show that the Moho is discontinuous (Simancas et al., 2003), particularly under the Ossa-Morena and Central Iberian Massif. In fact, the Moho is probably a decoupling zone between the mantle and the crust in the area.

Following the approach defined by Silver and Savage (1994), we therefore tested two-layer models by varying ϕ and δt in the upper and lower layer by increments of 2° and 0.2 s, respectively, and compared the expected backazimuthal variations with our observations. We use the statistical technique presented in Walker et al. (2005) to judge the significance of the variance reduction over the best-fitting one-layer model. Testing all possible two-layer models (Fig. 7), we find that the best-fitting models belong to three groups of models, 1) those having NE–SW fast directions in both layers, 2) those having NE–SW for the upper layer and NW–SE for the lower layer, and 3) vice-versa. While the best model formally falls into the second category, we cannot rule out the other two cases, including the one of a shallower layer with NW–SE fast azimuths, that would indeed correspond to the trend of the Variscan basement in its southern portion. This ambiguity is in part due to the backazimuthal distribution of the events being rather limited, but more fundamentally since a second layer with exactly perpendicular orientation to the first one only varies the splitting delay but does not produce a backazimuthal variation of fast direction and splitting delay. We note that the splitting delay associated with the lower layer is quite small (0.2 s). While the additional variance reduction (39%) associated with this weak second layer is slightly statistically significant, we choose to

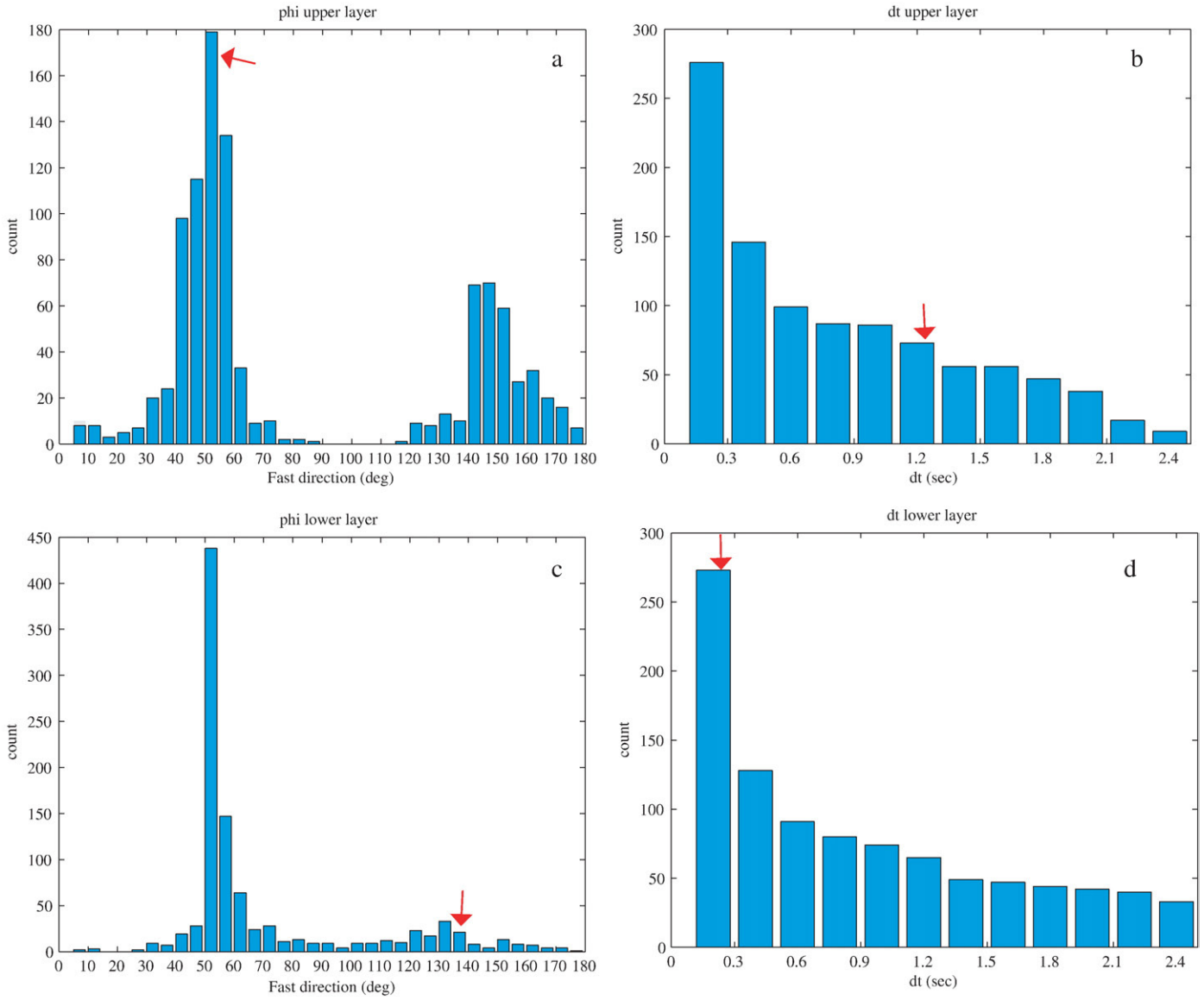

Fig. 7. Statistical analysis of two-layer modelling for the joint data set of 4 stations in the north (ARAC + HORN + JAND + SESP): parameters for the 1000 best-fitting models are shown as histograms for a) fast direction in upper layer; b) delay time in the upper layer c) fast direction in the lower layer; d) delay time in the lower layer. The arrows show the optimum values for each model, ϕ=N52°E and ϕ=N136°E for a) and c) respectively, and δt=1.2 s and δt=0.2 s for b) and d) respectively.

not attribute much significance to this. The backazimuthal variation that is present in the data may likely represent a complexity that is perhaps better characterized by an anisotropy that varies laterally.

5.3. Gibraltar arc: constraints on geodynamic models

Fast directions in Southernmost Spain, close to Gibraltar show rather distinct orientations from those in the Internal or External Betics: ϕ trends more or less North–South at the two stations CEUT and SFS. Station ANER near Malaga provides evidence for higher complexity and perhaps multi-layer anisotropy. We have therefore performed a two-layer modeling as detailed above but consider only the results obtained at this station. The thousand best two-layer models obtained for ANER give a best-fitting model with fast direction ϕ for the upper layer of N28°E and for the lower layer of N68°E (Fig. 8), and splitting delays 1.0 and 0.6 s. This result suggests that this station lies in a region of transition between the eastern Betics where ϕ trend ENE (i.e., close to the ANER lower layer ϕ) and the Gibraltar arc where ϕ trend close to NS (i.e., close to the ANER upper layer ϕ). Interestingly, the close NS trend of the upper layer seems also to coincide with the N–S line of intermediate-depth earthquakes (Morales et al., 1999; Calvert et al., 2000b). Nevertheless, we note that for the fast directions in the two layers, the maxima of the histograms in Fig. 8 are only 20° apart. Even though the statistical improvement is slightly significant, we defer a deeper discussion of a possible two-layer anisotropy until data from more stations around ANER become available.

We consider both Pn and SKS anisotropy measurements, which provide different and complementary depth sampling (e.g., Pera et al., 2003). SKS waves travel almost vertically and are not able to localize the precise depth range of the anisotropy, except that a layer of more than 100 km thickness is required to explain the observed splitting delay times (Mainprice and Silver, 1993; Ben Ismaïl and Mainprice, 1998), and that it should be in the upper mantle. On the other hand, Pn travels horizontally just below the Moho, and thus constrains anisotropy at that depth level. Pn models for the area have been produced by Calvert et al. (2000b) and by Serrano et al. (2005) which give rather similar results in the area of interest. In each case, arrival times of regional events have been used to determine isotropic and anisotropic velocity variations. The agreement of anisotropic fast directions from Pn and SKS are in fact remarkable on the Spanish side

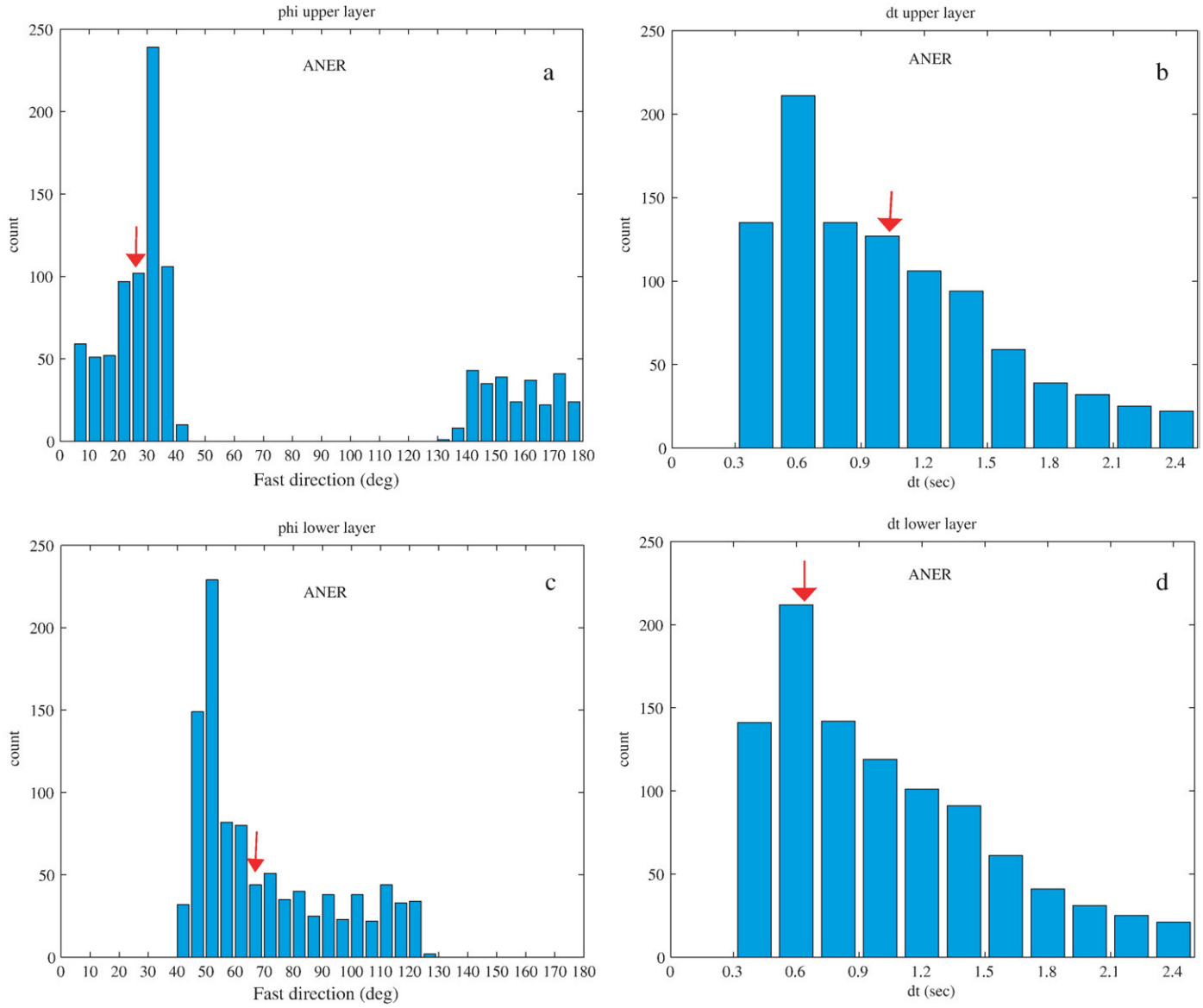

Fig. 8. Statistical analysis of two-layer modelling for station ANER: parameters for the 1000 best-fitting models are shown as histograms for a) fast direction in upper layer; b) delay time in the upper layer; c) fast direction in the lower layer; d) delay time in the lower layer. The arrows show the optimum values for each model, ϕ=N28°E and ϕ=N68°E for a) and c) respectively, and δt=1.0 s and δt=0.6 s for b) and d) respectively.

of the Alboran arc (Fig. 9). Not only are these fast directions parallel in the eastern Betics, but they seem to rotate together with the large-scale geological structures of the Alboran arc, and parallel with the coast, in a similar fashion for the shallowest and somewhat deeper mantle. The model may perhaps suggest that this parallelism is not present on the African side of the Gibraltar arc where fast Pn trend NS to NNW–SSW and fast split SKS trend NE–SW. The model is less well-constrained in that area, but if the feature is real, this may suggest a complete decoupling between the sub-Moho and the deeper anisotropy. However, the similarity between Pn and SKS fast directions may reflect different tectonic processes at depth, particularly in the vicinity of a subduction zone. Indeed, if there is subduction in the area, as has often been argued (e.g., Gutscher et al., 2002), Pn may be affected by the anisotropy above the slab, whereas SKS might be sensitive to the anisotropy below, above, and possibly within the slab. Fast split directions parallel to the slab is a rather common feature in subduction zones, both above and below the slab. This has been found for instance in New Zealand (Marson-Pidgeon and Savage, 2004) and in Northern Italy (Mele et al., 1998). Trench-parallel fast directions, may be explained either by invoking trench-parallel flow (e.g., Russo and Silver, 1994), or by invoking a hydrated mantle wedge above the slab (Jung and Karato, 2001). The degree of hydration of the mantle wedge and of magnitude of the applied stress above a subduction zone appears to have a strong influence on the style of seismic anisotropy (e.g., Jung and Karato, 2001; Kaminski and Ribe 2002): Slab-parallel seismic fast axes from SKS can in principle be explained either by slab-parallel flow in an anhydrous mantle wedge or by slab-normal compression in a hydrous mantle wedge. Such a pattern of anisotropy may show apparently erratic behaviour in some places; this may perhaps help to explain the complexity that we find at station ANER.

Deep structure and dynamics beneath the Alboran area has been widely debated throughout the last decades and a wide variety of geodynamic models has been proposed for the area. These models can be categorized by the way material is recycled into the mantle. If mantle lithosphere has been removed as has been proposed in the

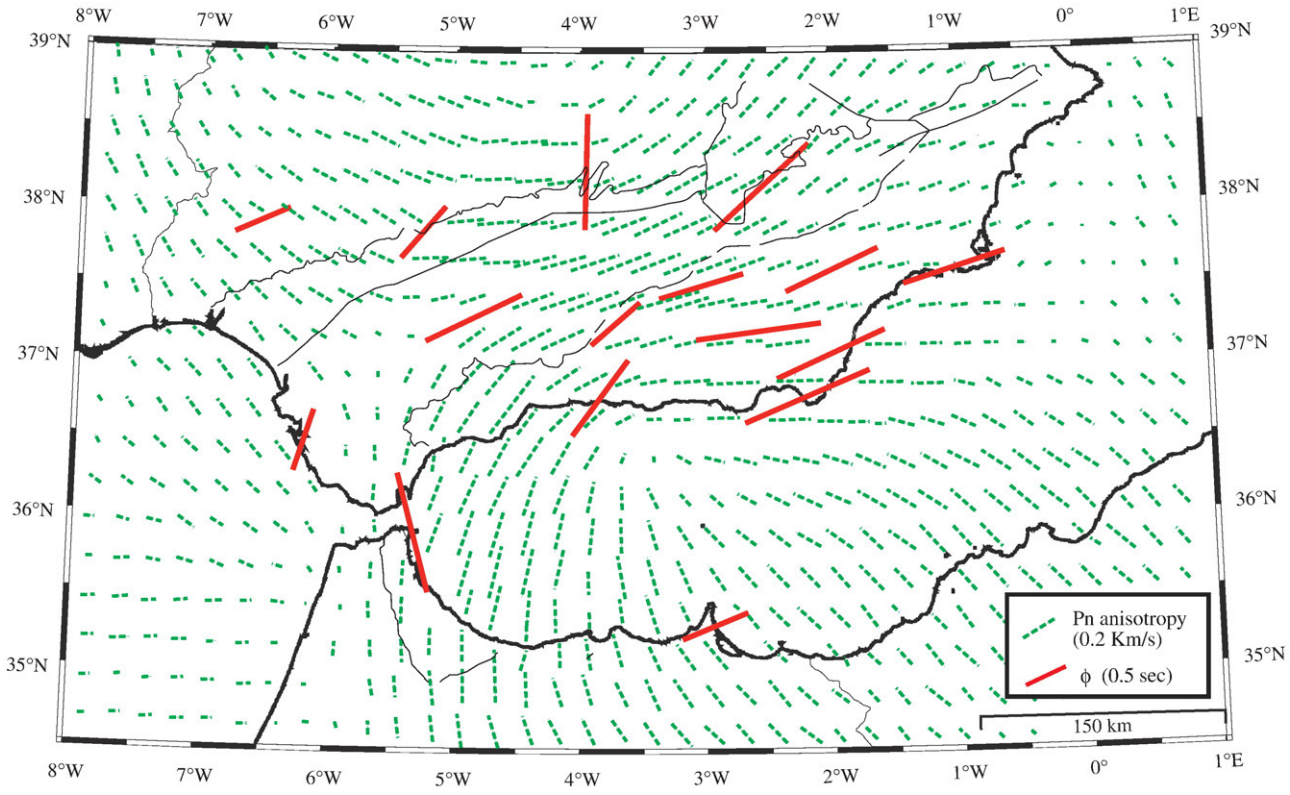

Fig. 9. Comparison of SKS fast directions (weighted-mean values from this study) with Pn-fast directions (redrawn from Calvert et al., 2000b). See text for explanations.

convection-removal hypothesis (Platt and Vissers, 1989) and the delamination model (e.g., Seber et al., 1996a), this would require the removed material to be replaced by asthenospheric material. This replacement would correspond to a flow that is directed radially inwards. An idealized convective-removal model would in fact imply that such a flow would be acting radially inwards from all directions. One should not expect to observe a radial flow from all directions though, since any asymmetry or heterogeneity would easily lead to an asymmetric flow, more like that to be expected in a delamination model. However, a radial flow would necessarily exist somewhere, to replace the material that has been recycled into the mantle. This flow would produce anisotropic fast directions that are oriented radially. Fig. 5 shows however, that the flow is oriented more or less tangentially to the Alboran Sea region. The required radial flow is thus not observed. This suggests that convective-removal and delamination models are unlikely to explain the anisotropy observations. On the other hand, subduction to the Northwest, as proposed by Zeck (1996), would require a rollback to the South to produce trench-parallel flow. Focal mechanisms of intermediate-depth seismicity are consistent with this, but hypocenters do not show a dip toward the North. In fact, they do not show a clear Benioff zone at all, but a line of seismicity dipping steeply to the South. For that same area, teleseismic and regional tomographic studies indicate a pronounced high-velocity anomaly located beneath the Alboran Sea (e.g. Blanco and Spakman, 1993; Calvert et al., 2000b; Seber et al., 1996a). Calvert et al. (2000b) produced a tomographic model that showed a robust high-velocity anomaly beneath the west Alboran Sea and west and central Betics between 100 and 150 km. Assuming that these positive velocity anomalies indicate a region of cooler mantle, the most likely interpretation is that it indicates the presence of lithospheric mantle in view of the coherent continuation of the anomaly at depth. The positive anomaly extends from lithospheric depths beneath the Strait of Gibraltar and southern Spain to depths of about 350–400 km beneath the Alboran Sea, and it is interpreted as a lithospheric body that has descended into the upper mantle. More recently, waveform studies (Bokelmann and Maufroy, 2007) have indicated dispersed body-wave arrivals propagating through the mantle under the Alboran Sea, that favor the presence of a subducted slab under the Alboran Sea, still containing a continuous low-velocity crustal layer. Wortel and Spakman (2000) also proposed a slab structure isolated in the mantle below the Betic-Alboran region at 200 km depth and that seems to be connected with deep seismicity at depths of about 640 km. Lonergan and White (1997) proposed that there was a subduction zone beneath the Alboran Sea that is now extinct. They suggested that the ancient subducting slab in the Western Mediterranean was split into two fragments, the eastern one of which has continued to roll back toward the south-east, generating the Tyrrhenian Sea and forming the present-day Calabrian arc. The other slab fragment rolled back to the west, generating the Alboran Sea and the Betic-Rif orocline. Our SKS splitting observations, together with the previously published Pn results, show a spectacular rotation following the curvature of the roll back and of the mountain chain. If the SKS fast directions are to be explained by a rotation similar to that shown by the Pn observations, this would be explained most easily by a toroidal mantle flow under the subducting lithosphere that shows rollback toward the west. There is an interesting similarity with the Calabrian arc in Southern Italy, for which shear-wave splitting results have been presented by Civello and Margheriti (2004) and more recently by Baccheschi et al. (2007). The asthenospheric toroidal flow induced by the Tyrrhenian slab roll back is presently beneath Calabria (Civello and Margheriti, 2004; Baccheschi et al., 2007) but may have left some imprint in the mantle all along its Neogene travel path from southern France (Barruol et al., 2004) to Sicily (Lucente et al., 2006). Seismic anisotropy beneath the Betics is likely related to a similar phenomenon, and thus to the large-scale dynamics of ocean opening in the Southwestern Mediterranean.

6. Conclusions

We have studied upper mantle seismic anisotropy in Southern Spain and around the Gibraltar arc. Our observations suggest a consistent splitting direction parallel to the mountain belt in the Internal Betics, a more northerly direction at stations located further north in the transition with the Variscan Iberia, and a rotation of fast split directions toward NS azimuths around the Gibraltar arc.

The Eastern Betics anisotropy observations are well explained by a single layer of anisotropy with a fast anisotropic direction trending ENE, with smooth and small variations in space. In the transition region between the Variscan and the Betics, the anisotropy shows backazimuthal variations of splitting parameters. Models of two-layer anisotropy and lateral heterogeneous anisotropy have been tested, and a strong lateral change in anisotropy is likely for the transition region toward the Variscan Iberian Massif. Close to Gibraltar, fast directions are oriented close to N–S at CEUT and SFS and this suggests a gradual rotation around the arc. Combining Pn and SKS anisotropy, geological features and tomographic images allow us to discuss the various families of geodynamic models. Our SKS measurements are difficult to reconcile with geodynamic models based on delamination or convective removal. The observations instead favor models of subduction and rollback of the western Mediterranean slab.

Acknowledgements

We warmly thank Andreas Wüstefeld for his useful help in the use of SplitLab software, and Alain Vauchez, Daniel Stich, Carlos Garrido and Francisco Vidal for fruitful discussions. We also thank Martha Savage and an anonymous reviewer for their comments and corrections. SplitLab is available at http://www.gm.univ-montp2.fr/splitting/ together with its user guide, the related publications and the SKS World splitting database. Figures are created using the GMT software of Wessel and Smith (1995). This study was possible thanks to the effort of collecting high-quality broadband seismic data of the IAG-UGR and ROA-UCM-Geofon networks. We received support through Spanish project CGL2005-04541-C03-01-BTE, European Commission project NEAREST (GoCE-037110) and Junta de Andalucia RNM104 and through the project Topo-Iberia CSD2006.

Appendix A. Supplementary data

Supplementary data associated with this article can be found, in the online version, at doi:10.1016/j.epsl.2008.06.024.

References

Baccheschi, P., Margheriti, L., Steckler, M.S., 2007. Seismic anisotropy reveals focused mantle flow around the Calabrian slab (Southern Italy). Geophys. Res. Lett. 34, L05302. doi:10.1029/2006GL028899.

Balanyá, J.C., García-Dueñas, V., 1988. El Cabalgamiento cortical de Gibraltar y la tectónica de Béticas y Rif, presentado en II Congreso Geológico de España. Simposium sobre Cinturones Orogénicos.

Barruol, G., Mainprice, D., 1993. A quantitative evaluation of the contribution of crustal rocks to the shear wave splitting of teleseismic SKS waves. Phys. Earth Planet. Inter. 78 (3–4), 281–300. doi:10.1016/0031-9201(93)90161-2.

Barruol, G., Silver, P.G., Vauchez, A., 1997. Seismic anisotropy in the eastern US: deep structure of a complex continental plate. J. Geophys. Res. 102 (B4), 8329–8348.

Barruol, G., Deschamps, A., Coutant, O., 2004. Mapping Upper mantle anisotropy beneath SE France by SKS splitting indicates a Neogene asthenospheric flow induced by the Apenninic slab rollback and deflected by the deep Alpine roots. Tectonophysics 394, 125–138. doi:10.1016/j.tecto.2004.08.002.

Ben Ismaïl, W., Mainprice, D., 1998. An olivine fabric database: an overview of upper mantle fabrics and seismic anisotropy. Tectonophysics 296 (1–2), 145–157.

Blanco, M.J., Spakman, W., 1993. The P-wave velocity structure of the mantle below the Iberian Peninsula: evidence for subducted lithosphere below southern Spain. Tectonophysics 221, 13–34.

Bokelmann, G.H.R., Maufroy, E., 2007. Mantle structure under Gibraltar constrained by dispersion of body waves. Geophys. Res. Lett. 34, L22305. doi:10.1029/2007GL030964.

Bormann, P., Grünthal, G., Kind, R., Montag, H., 1996. Upper mantle anisotropy beneath Central Europe from SKS wave splitting: effects of absolute plate motion and lithosphere asthenosphere boundary topography? J. Geodynamics 22 (1–2), 11–32.

Bowman, J.R., Ando, M., 1987. Shear-wave splitting in the upper-mantle wedge above the Tonga subduction zone. Geophys. J. R. Astron. Soc. 88, 25–41.

Buforn, E., Coca, P., Udías, A., Lasa, C., 1997. Source mechanism of intermediate and deep earthquakes in southern Spain. J. Seismol. 1, 113–130.

Buland, R., Chapman, C.H., 1983. The computation of seismic travel times. Bull. Seismol. Soc. Am. 73, 1,271–1,302.

Calvert, A., Sandvol, E., Seber, D., Barazangi, M., Roecker, S., Mourabit, T., Vidal, F., Alguacil, G., Jabour, N., 2000a. Geodynamic evolution of the lithosphere and upper-mantle beneath the Alboran Region of the western Mediterranean—constraints from travel-time tomography. J. Geophys. Res. 105, 10871–10898.

Calvert, A., Sandvol, E., Seber, D., Barazangi, M., Vidal, F., Alguacil, G., Jabour, N., 2000b. Propagation of regional seismic phases (Lg and Sn) and Pn velocity structure along the Africa–Iberia plate boundary zone: tectonic implications. Geophys. J. Int. 142, 384–408.

Civello, S., Margheriti, L., 2004. Toroidal mantle flow around the Calabrian slab (Italy) from SKS splitting. Geophys. Res. Lett. 31, L10601. doi:10.1029/2004GL019607.

Comas, M.C., Platt, J.P., Soto, J.I., Watts, A.B., 1999. The origin and tectonic history of the Alborán Basin: insights from Leg 161 results. In: Zahn, R., Comas, M.C., Klaus, A. (Eds.), Proc. ODP, Sci. Results. Ocean Drilling Program, College Station, TX, pp. 555–579.

De Larouzière, F.D., Bolze, J., Bordet, P., Hernández, J., Montenat, C., Ott d'Estevou, P., 1988. The Betic segment of the lithospheric Trans-Alboran shear zone during the Late Miocene. Tectonophysics 152, 41–52.

Dewey, J.F., Helman, M.L., Turco, E., Hutton, D.H.W., Knott, S.D., 1989. Kinematics of the western Mediterranean, in: Conference on Alpine tectonics. In: Coward, M.P., Dietrich, D., Park, R.G. (Eds.), Geological Society of London Special Publications, London, pp. 265–283.

Diaz, J., Gallart, J., Hirn, A., Paulssen, H., 1998. Anisotropy beneath the Iberian Peninsula: the contribution of the ILIHA-NARS broad-band experiment. Pure Appl. Geophys. 151, 395–405.

Duggen, S., Hoernle, K., Van den Bogaard, P., Garbe-Schonberg, D., 2005. Post-collisional transition from subduction- to intraplate-type magmatism in the westernmost Mediterranean: evidence for continental-edge delamination of subcontinental lithosphere. J. Petrol. 46, 1155–1201.

Faccenna, C., Piromallo, C., Crespo-Blanc, A., Jolivet, L., Rossetti, F., 2004. Lateral slab deformation and the origin of the western Mediterranean arcs. Tectonics 23, TC1012. doi:10.1029/2002TC001488.

Fernández-Ibáñez, F., Soto, J.I., Zoback, M.D., Morales, J., 2007. Present-day stress field in the Gibraltar Arc (western Mediterranean). J. Geophys. Res. 112, B08404. doi:10.1029/2006JB004683.

Fontaine, F.R., Barruol, G., Tommasi, A., Bokelmann, G.H.R., 2007. Upper-mantle flow beneath French Polynesia from shear wave splitting. Geophys. J. Int. 223. doi:10.1111/j.1365-246X.2007.03475.x.

Fouch, M.J., Fischer, K.M., Parmentier, E.M., Wysession, M.E., Clarke, T.J., 2000. Shear wave splitting, continental keels, and patterns of mantle flow. J. Geophys. Res. 105 (B3), 6255–6275.

Galindo-Zaldívar, J., Jabaloy, A., González-Lodeiro, F., Aldaya, F., 1997. Crustal structure of the central sector of the Betic Cordillera (SE Spain). Tectonics 16, 18–37.

Garcia-Dueñas, V., 1969. Les unités allochtones de la zone Subbétique,dans la transversale de Grenade (Cordillères Bétiques, Espagne). Rev. Geogr. Phys. Geol. Dyn. 2, 211–222.

Garcia-Hernandez, M., Lopez-Garrido, A.C., Rivas, P., Sanz de Galdeano, C., Vera, J.A., 1980. Mesozoic paleogeographic evolution of the External Zones of the Betic Cordillera. Geol. Mijnb. 59, 155–168.

Godfrey, N.J., Christensen, N.I., Okaya, D.A., 2000. Anisotropy of schists: contribution of crustal anisotropy to active source seismic experiments and shear wave splitting observations. J. Geophys. Res. 105, 27991–28007.

Gripp, A.E., Gordon, R.G., 2002. Young tracks of hotspots and current plate velocities. Geophys. J. Int. 150, 321–361.

Gutscher, M.A., Malod, J., Rehault, J.P., Contrucci, I., Klingelhoefer, F., Mendes, V.L., Spakman, W., 2002. Evidence for active subduction beneath Gibraltar. Geology 30, 1071–1074.

Jung, H., Karato, S., 2001. Water-induced fabric transitions in olivine. Science 293, 1460–1463. doi:10.1126/science.1062235.

Kaminski, E., Ribe, N.M., 2002. Timescales for the evolution of seismic anisotropy in mantle flow. Geochem. Geophys. Geosystem 3, 1051. doi:10.1029/2001GC000222.

Kennett, B.L.N., 1995. Seismic traveltime table. In: Ahrens, T.J. (Ed.), Global Earth Physics. A Handbook of Physical Constants. AGU Ref. Shelf. AGU, Washington, DC, pp. 126–143.

Kennett, B.L.N., Engdahl, E.R., 1991. Travel times for global earthquake location and phase identification. Geophys. J. Int. 105, 429–465.

Lonergan, L., White, N., 1997. Origin of the Betic-Rif mountain belt. Tectonics 16, 504–522.

Lucente, F.P., Margheriti, L., Piromallo, C., Barruol, G., 2006. Seismic anisotropy reveals the long route of the slab through the western-central Mediterranean mantle. Earth Planet. Sci. Lett. 241, 517–529. doi:10.1016/j.epsl.2005.10.041.

Luján, M., Crespo-Blanc, A., Balanyá, J.C., 2006. The Flysch Trough thrust imbricate (Betic Cordillera):a key element of the Gibraltar Arc orogenic wedge. Tectonics 25, TC6001. doi:10.1029/2005TC001910.

Mainprice, D., Silver, P.G., 1993. Interpretation of SKS-waves using samples from the subcontinental lithosphere. Phys. Earth Planet. Inter. 78, 257–280. doi:10.1016/0031-9201(93)90160-B.

Mainprice, D., Barruol, G., Ben Ismail, W., 2000. The seismic anisotropy of the Earth's mantle: from single crystal to polycrystal. In: Karato, S.I. (Ed.), Earth's Deep Interior: Mineral Physics and Tomography from the Atomic to the Global Scale. . Geodyn. Ser. AGU, Washington, D.C., pp. 237–264.

Mainprice, D., Tommasi, A., Couvy, H., Cordier, P., Frost, D.J., 2005. Pressure sensitivity of olivine slip systems: implications for the interpretation of seismic anisotropy of the Earth's upper mantle. Nature 433, 731–733.

Marson-Pidgeon, K., Savage, M., 2004. Shear-wave splitting variations across an array in the southern North Island, New Zealand. Geophys. Res. Lett. 31, 21602. doi:10.1029/2004GL021190.

Mele, G., Rovelli, A., Seber, D., Hearn, T., Barazangi, M., 1998. Compressional velocity structure and anisotropy in the uppermost mantle beneath Italy and surrounding regions. J. Geophys. Res. 103 (B6). doi:10.1029/98JB00596.

Morales, J., Serrano, I., Jabajoy, A., Galindo-Zaldívar, J., Zhao, D., Torcal, F., Vidal, F., González Lodeiro, F., 1999. Active continental subduction beneath the Betic Cordillera and the Alborán Sea. Geology 27, 735–738.

Nicolas, A., Christensen, N.I., 1987. Formation of anisotropy in upper mantle peridotites—A review. In: Fuchs, K., Froideveaux, C. (Eds.), Composition Structure and Dynamics of the Lithosphere Asthenosphere System. AGU, Washington D.C., pp. 111–123.

Ott D'Estevou, P., Montenat, C., 1985. Evolution structurale de la zone bétique orientale (Espagne) du Tortonian a l'Holocene. C. R. Acad. Sci. Paris 300, 363–368.

Pera, E., Mainprice, D., Burlini, L., 2003. Petrophysical properties of the upper mantle beneath the Torre Alfina area (Northern Apennines, Central Italy). Tectonophysics 370, 11–30.

Platt, J.P., Vissers, R.L.M., 1989. Extensional collapse of thickened continental lithosphere: a working hypothesis for the Alboran Sea and Gibraltar Arc. Geology 17, 540–543.

Platt, J.P., Soto, J.I., Comas, M.C., Leg 161 Shipboard Scientific Party, 1996. Decompression and high-temperature–low-pressure metamorphism in the exhumed floor of an extensional basin, Alboran Sea, western Mediterranean. Geology 24 (5), 447–450.

Platt, J.P., Soto, J.I., Whitehouse, M.J., Hurford, A.J., Kelley, S.P., 1998. Thermal evolution, rate of exhumation, and tectonic significance of metamorphic rocks from the floor of the Alboran extensional basin, western Mediterranean. Tectonics 17, 671–689.

Platt, J.P., Whitehouse, M.J., Kelley, S.P., Carter, A., Hollick, L., 2003. Simultaneous extensional exhumation across the Alborán Basin: implications for the causes of late orogenic extension. Geology 31, 251–254.

Rosenbaum, G., Lister, G.S., 2004. Neogene and Quaternary rollback evolution of the Tyrrhenian Sea, the Apennines and the Sicilian Maghrebides. Tectonics 23, TC1013. doi:10.1029/2003 TC001518.

Royden, L.H., 1993. Evolution of retreating subduction boundaries formed during continental collision. Tectonics 12, 629–638.

Russo, R., Silver, P., 1994. Trench-parallel flow beneath the Nazca Plate from seismic anisotropy. Science 263, 1105–1111.

Savage, M.K., 1999. Seismic anisotropy and mantle deformation: what have we learned from shear wave splitting? Rev. Geophys. 37, 69–106.

Schmid, C., Van der Lee, S., Giardini, D., 2004. Delay times and shear wave splitting in the Mediterranean region. Geophys. J. Int. 159, 275–290.

Seber, D., Barazangi, M., Ibenbrahim, A., Demnati, A., 1996a. Geophysical evidence for lithospheric delamination beneath the Alboran Sea and Rif-Betics mountains. Nature 379, 785–790.

Serrano, I., Hearn, T.M., Morales, J., Torcal, F., 2005. Seismic anisotropy and velocity structure beneath the southern half of the Iberian peninsula. Phys. Earth Planet. Inter. 150 (4), 317–330.

Sieminski, A., Liu, Q., Trampert, J., Tromp, J., 2007. Finite-frequency sensitivity of body waves to anisotropy based upon adjoint methods. Geophys. J. Int. 171, 368–389. doi:10.1111/j.1363-246X.2007.03528.x.

Silver, P.G., Chan, W.W., 1988. Implications for continental structure and evolution from seismic anisotropy. Nature 335, 34–39.

Silver, P.G., Chan, W.W., 1991. Shear wave splitting and subcontinental mantle deformation. J. Geophys. Res., 96, 16429–16454.

Silver, P.G., Savage, M., 1994. The interpretation of shear-wave splitting parameters in the presence of two anisotropic layers. Geophys. J. Int. 119, 949–963.

Simancas, J.F., Carbonell, R., Gonzalez Lodeiro, F., Perez Estaun, A., Juhlin, C., Ayarza, P., Kashubin, A., Azor, A., Martınez Poyatos, D., Almodovar, G.R., Pascual, E., Saez, R., Exposito, I., 2003. Crustal structure of the transpressional Variscan orogen of SW Iberia: SW Iberia deep seismic reflection profile (IBERSEIS). Tectonics 22 (6), 1062.

Stich, D., Ammon, C.J., Morales, J., 2003. Moment tensor solutions for small and moderate earthquakes in the Ibero-Maghreb region. J. Geophys. Res. 108, 2148. doi:10.1029/2002JB002057.

Stich, D., Mancilla, F., Morales, J., 2005. Crust–mantle coupling in the Gulf of Cadiz (SW-Iberia). Geophys. Res. Lett. 2, L13306. doi:10.1029/2005GL023098.

Stich, D., Serpelloni, E., Mancilla, F., Morales, J., 2006. Kinematics of the Iberia-Maghreb plate contact from seismic moment tensors and GPS observations. Tectonophysics 426, 295–317.

Turner, S.P., Platt, J.P., George, R.M.M., Kelley, S.P., Pearson, D.G., Nowell, G.M., 1999. Magmatism associated with orogenic collapse of the Betic-Alboran Domain. SE Spain. J. Petrol. 40, 1011–1036.

Vauchez, A., Nicolas, A., 1991. Mountain building: strike parallel motion and mantle anisotropy. Tectonophysics 185, 183–201.

Vauchez, A., Garrido, C., 2001. Seismic properties of an asthenospherized lithospheric mantle: constraints from lattice preferred orientations in peridotite from the Ronda Massif. Earth Planet. Sci. Lett. 192, 245–259.

Vinnik, L.P., Makeyeva, L.I., Milev, A., Usenko, A.Yu., 1992. Global patterns of azimuthal anisotropy and deformations in the continental mantle. Geophys. J. Int. 111, 433–447.

Walker, K.T., Bokelmann, G.H.R., Klemperer, S.L., Bock, G., 2005. Shear-wave splitting around the Eifel hotspot: evidence for a mantle upwelling. Geophys. J. Int., 163, 962–980.

Walker, K.T., Bokelmann, G.H.R., Klemperer, S.L., Bock, G., the Eifel plume team, 2007. Seismic anisotropy in the asthenosphere beneath the Eifel region. In: Ritter, J.R.R., Christensen, U.R. (Eds.), Mantle plumes — a multidisciplinary approach. Springer-Verlag, VIII, pp. 439–464.

Wessel, P., Smith, H.F., 1995. New version of the Generic Mapping Tools released. EOS, Trans. Am. Geophys. Un. 76, 329.

Wortel, M.J.R., Spakman, W., 2000. Subduction and slab detachment in the Mediterranean–Carpathian region. Science 290, 1910–1917.

Wüstefeld, A., Bokelmann, G.H.R., 2007. Null detection in shear-wave splitting measurements. Bull. Seismol. Soc. Am. 97 (4), 1204–1211.

Wüstefeld, A., Bokelmann, G.H.R., Zaroli, C., Barruol, G., 2008. SplitLab: a shear-wave splitting environment in Matlab. Comput. Geosci. doi:10.1016/j.cageo.2007.1008.1002.

Zeck, H.P., 1996. Betic-Rif orogeny:subduction of Mesozoic Tethys lithosphere under eastward drifting Iberia, slab detachment shortly before 22 Ma, and subsequent uplift and extensional tectonics. Tectonophysics 254, 1–16.

Zeck, H.P., Kristensen, A.B., Williams, I.S., 1998. Post-collisional volcanism in a sinking slab setting-crustal anatectic origin of pyroxene-andesite magma, Caldear Volcanic Group, Neogene Alborán volcanic Province, southeastern Spain. Lithos 45, 499–522.